PUSHING THE FRONTIERS OF SUPERCONDUCTING RADIO FREQUENCY SCIENCE: FROM THE TEMPERATURE DEPENDENCE OF THE SUPERHEATING FIELD OF NIOBIUM TO HIGHER-ORDER MODE DAMPING IN VERY HIGH QUALITY FACTOR ACCELERATING STRUCTURES

A Dissertation

Presented to the Faculty of the Graduate School

of Cornell University

in Partial Fulfillment of the Requirements for the Degree of

Doctor of Philosophy

by

Nicholas Ruben Alexander Valles

January 2014

PUSHING THE FRONTIERS OF SUPERCONDUCTING RADIO
FREQUENCY SCIENCE: FROM THE TEMPERATURE DEPENDENCE OF
THE SUPERHEATING FIELD OF NIOBIUM TO HIGHER-ORDER MODE
DAMPING IN VERY HIGH QUALITY FACTOR ACCELERATING
STRUCTURES

Nicholas Ruben Alexander Valles, Ph.D.

Cornell University 2014

This thesis investigates the three frontiers of superconducting radio frequency
(SRF) science: Gradient, Continuous wave beam power, and High quality factor
structures. On the first front, the full temperature dependence of the superheat-
ing field - which sets the ultimate gradient limit for SRF cavities was measured
for the first time for niobium. It was found that the Ginsburg-Landau result near
T_c is consistent with measurements within measurement uncertainty to even
low temperatures. The beam power frontier was extended by designing a mul-
ticell cavity for the Cornell Energy Recovery Linac (ERL) with strongly damped
higher-order modes. Simulations show that an ERL constructed of these cavi-
ties can support high beam current in excess of 300 mA, ~30 times higher than
in ERLs currently in operation. Finally, measurements of the prototype main
linac cavity for the Cornell ERL demonstrate that the fundamental accelerating
mode of the cavity in a fully equipped cryomodule can achieve quality factors in
excess of 6×10^{10} at 1.8 K and 16.2 MV/m, a result more than tripling the design
specification. This prototype structure also set a world record of $Q_0 = 1 \times 10^{11}$ at
1.6 K, for a cavity installed in a fully equipped cryomodule, and introduces the
possibility of a new class of extremely high efficiency SRF accelerators.

BIOGRAPHICAL SKETCH

Nick was born at a young age in Berrien Springs, Michigan. He spent his youth in Southern California until entering Andrews University where he completed his B.S. in Physics and B.S. in Mathematics in 2008. He earned his M.S. in Physics at Cornell University in 2011 and finished his Ph.D. in Physics in 2013.

Along the way, he met and married a lovely lady named Anneke and they are now living in Southern California.

To my wife, Anneke, who is my constant companion through life's adventures.

ACKNOWLEDGEMENTS

No man is an island

- John Donne

I would like begin my acknowledgements by honoring the memory of Kathy. I hope that this thesis serves as a small tribute to the mysteries she might have unraveled.

The document you are reading would not exist without a large investment of time and effort from many, many people.

I would like to thank, my wife, Anneke, who has been by my side throughout this process. Any of my accomplishments are a direct result of her continual support. I also appreciate my parents, grandparents and family members for stressing the importance of education and teaching, challenging, and supporting me through my intellectual journey.

A deep thanks goes to Ozzie Nevarez, who inspired my nascent interest in physics, and the professors at Andrews University who cultivated my abilities.

My adviser, Matthias Liepe, deserves immeasurable appreciation for his patience, guidance, stunning physical insight, encyclopedic knowledge of the universe of SRF, and persistence in forming me into the physicist I am today. Undoubtedly, my graduate school career would not have been a success without him.

Zachary Conway also deserves special recognition for taking me under his wing as a fledgling graduate student and teaching me the techniques necessary to conduct SRF research, as does Valery Shemelin for our many fruitful discussions about electromagnetic simulations.

My graduate student colleagues and friends Sam Posen, Dan Gonnella, Daniel Hall and Yi Xie, who served as fellow researchers in training, lunchtime

debate partners and competitors in innumerable[1] games of Glory to Rome made my graduate experience at Cornell a full one, as did the friendship of the Adams, Sutter and Liepe families.

I would also like to recognize my committee members, James Sethna and David Rubin, as well as the many technicians, researchers and professors I have worked with on the Cornell Energy Recovery Linac Test Horizontal Test Cryomodule program: Adam Bartnik, Ivan Bazarov, Sergey Belomestnykh, Mike Billing, Paul Bishop, Benjamin Bullock, Eric Chojnacki, Brian Clasby, James Crittenden, Holly Conklin, John Dobbins, Ralf Eichhorn, Brendan Elmore, Fumio Furuta, Andriy Ganshin, Mingqi Ge, Greg Kulina, Terry Gruber, Don Hartill, Don Heath, Vivian Ho, Georg Hoffstaetter, Roger Kaplan, Tim O'Connell, Chris Mayes, Jared Maxson, Hasan Padamsee, Colby Shore, Karl Smolenski, Peter Quigley, Dave Rice, Dan Sabol, James Sears, Eric Smith, Maury Tigner, Vadim Veshcherevich, and Dwight Widger, as well as John Kaminski and the excellent machinists that turned designs into reality.

---

[1]Not actually innumerable, just a lot.

TABLE OF CONTENTS

LIST OF TABLES

LIST OF FIGURES

LIST OF ABBREVIATIONS

ADC   Analog to Digital Converter
BBU   Beam Breakup
BCP   Buffer Chemical Polish
BCS   Bardeen, Cooper and Schrieffer
CAD   Computer-aided Design
CBP   Centrifugal Barrel Polish
CERN   Conseil Européen pour la Recherche Nucléaire
          [European Organization for Nuclear Research]
CMM   Coordinate Measuring Machine
DAC   Digital to Analog Converter
EP   Electro-polish
ERL   Energy Recovery Linac
FEL   Free Electron Laser
FPGA   Field-programmable Gate Array
GL   Ginzburg-Landau
HERA   Hadron-Electron Ring Accelerator
HOM   Higher-Order Mode
HPR   High-Pressure rinse
HTC   Horizontal Test Cryomodule
ILC   International Linear Collider
LCLS   Linac Coherent Light Source
LHC   Large Hadron Collider
LINAC   Linear Accelerator
LLRF   Low-level RF
MLC   Main-Linac Cryomodule
PLL   Phase-locked loop
RF   Radio Frequency
RRR   Residual Resistivity Ratio
SRF   Superconducting Radio Frequency
TE   Transverse Electric
TM   Transverse Magnetic
TTF   Telsa Test Facility
XFEL   X-Ray Free Electron Laser

LIST OF SYMBOLS

B	Magnetic flux density
$B_c(0)$	Critical magnetic field at 0 K
B_{c_1}	Lower critical magnetic field
B_{c_2}	Upper critical magnetic field
B_{pk}	Peak (maximal) surface magnetic field
B_{sh}	Superheating field
$c = 299\,792\,458$ m/s	The speed of light in free space
D	Electric flux density
$e = 2.71828\ldots$	Euler's number
E	Electric field intensity
E_{acc}	Accelerating electric Field
$E_g \equiv 2\Delta(0)/(k_B T_c)$	Normalized energy gap of a superconductor
E_{pk}	Peak (maximal) surface electric field
$E_S \equiv \Delta(0)/(k_B T_c)$	Normalized energy gap of one electron in a Cooper pair used in SRIMP calculations
f	Frequency of electromagnetic wave
G	Geometry factor of RF structure
H	Magnetic field intensity
i	Imaginary unit, $\sqrt{-1}$
$\Im$	Imaginary part
k	Wavenumber
$k_B = 1.38 \times 10^{-23}$ J/K	Boltzmann constant
K	Kelvin (SI unit of temperature)
ℓ_{tr}	Normal conducting electron's mean free path
m	Mass (usually of the electron)
n	Density of electron gas
P_{diss}	Dissipated power
$q = 1.60217657 \times 10^{-19}$ C	Charge of the electron
Q	Quality Factor
Q_0	Intrinsic Q of a resonator
Q_{ext}	External Q, generally of a coupler

Q_L	Loaded Q of resonator and coupler
(R/Q)	Shunt impedance (monopole) [Ω]
$(R/Q)_\perp$	Transverse shunt impedance [Ω/cm^{2m}]
$(R/Q)'_\perp$	Transverse shunt impedance [Ω]
R_0	Residual resistance
R_{BCS}	BCS resistance
R_s	Surface resistance
$\mathfrak{R}$	Real part
S	Fermi surface area
$S_F \equiv 4\pi(3\pi^2 n)^{2/3}$	Fermi surface normalization factor
t	Time
$t \equiv T/T_c$	Normalized temperature
T	Temperature
T_c	Critical temperature of a superconductor
U	Stored energy
v	Velocity
v_F	Fermi velocity
V	Voltage
$\beta = v/c$	Velocity normalized to the speed of light
β	Coefficient relating Δf and $\Delta\lambda$
γ	Relativistic Lorentz factor
$\gamma = 0.57721\dots$	Euler-Masheroni constant
γ_c	Electronic specific heat coefficient
Γ	Gamma function
δ	Skin-depth of a conductor
$\Delta(0)$	Half the binding energy of a Cooper pair
Δf	Frequency shift
$\Delta\lambda$	Change in penetration depth
ϵ	(Complex) Permittivity of material
$\epsilon_0 \equiv 1/\left(\mu_0 \cdot c^2\right)$ $= 8.9\dots \times 10^{-12}$ F/m	Permittivity of free space
ε	Electronic charge in CGS units (esu)

$\zeta(s)$	Euler-Riemann zeta function
η	(Complex) Wave impedance
θ	Polar angle
κ_{GL}	Ginzburg-Landau parameter
λ_{GL}	Ginzburg-Landau penetration depth
λ_L	London Penetration depth at 0 K
λ_{tr}	Argument to Gor'kov χ function
μ	(Complex) Permeability of material
$\mu_0 \equiv 4\pi \times 10^{-7}\,\mathrm{N/A^2}$	Permeability of free space
ν	Frequency of electromagnetic wave
ξ_0	BCS coherence length
ξ_{GL}	Ginzburg-Landau penetration depth
ξ_S	Coherence length used in SRIMP
$\pi \equiv \tau/2 \approx 3.14159\ldots$	Ratio of a circle's circumference to its diameter
ρ	Electrical resistivity
σ	Electrical conductivity
$\tau = 6.283185\ldots$	The ratio of circle's circumference to radius
ϕ	Azimuthal angle
χ	Gor'kov χ function
ψ	Digamma function, derivative of Γ
ω	Angular frequency
$\hbar = 1.0546 \times 10^{-34}\,\mathrm{J \cdot s}$	Reduced Planck's Constant

CHAPTER 1

INTRODUCTION TO RF SUPERCONDUCTIVITY

Particle accelerators have been at the forefront of scientific investigation for almost 100 years. Beginning in the early 1920s, particle accelerators began to probe the interior structure of matter. From their small beginnings–table top devices providing energies below one MeV–accelerators have grown to span hundreds of kilometers at sites across the globe. The largest particle accelerator in the world, currently the Large Hadron Collider (LHC) located at the European Organization for Nuclear Research with a circumference of 27 km, accelerates proton beams to 4 TeV and recently discovered the long postulated Higgs boson. [Aad12] The LHC is at the forefront of high energy physics, and represents a broad class of accelerator applications, namely machines designed to produce and study particle collisions.

Once circular synchrotrons of sufficiently high energy were developed (a few tens of MeV), researchers began to observe radiation emitted from the accelerated particle beam. Ever inventive in their naming conventions, researchers dubbed this phenomena "synchrotron radiation." Today many accelerators have been designed with the express purpose of generating this radiation, and have application in medicine, nuclear science, and industry.

Light sources are the second class of accelerator application, and currently are pushing the photon flux and energy frontier leading to a wide variety of new discoveries. Cornell's Energy Recovery Linac (ERL) is an example of a next generation light source that will open up completely new areas of scientific inquiry.

Regardless of the application, all large-scale modern particle accelerators rely on RF structures to transfer energy from the RF source to the electron beam. This chapter is an introduction to the physics of standing wave accelerating cavities and shows that the introduction of superconductivity to these devices enables the creation of a completely new class of machines for scientific research.

1.1 Radio Frequency Cavities

The workhorse of modern accelerators is the RF cavity, which can be of the standing wave or travelling wave variety. While each structure is suitable for certain applications, [Mil86] the following discussion will focus on standing wave structures.

A cavity can be thought of as a modified waveguide, so to understand these structures we will start with Maxwell's equations in free space, then introduce the changes needed to realize a working standing wave accelerating cavity.

In the time domain, Maxwell's equations in free space have the differential form

$$\nabla \times \vec{E} = -\frac{\partial \vec{B}}{\partial t}, \tag{1.1a}$$

$$\nabla \times \vec{H} = \frac{\partial \vec{D}}{\partial t}, \tag{1.1b}$$

$$\nabla \cdot \vec{D} = 0, \tag{1.1c}$$

$$\nabla \cdot \vec{B} = 0, \tag{1.1d}$$

where $\vec{E}$ is the electric field intensity, $\vec{B}$ is the magnetic flux density, $\vec{H}$ is the magnetic field intensity, and $\vec{D}$ is the electric flux density. [Jac98] In free space,

the densities and intensities are related via:

$$\vec{B} = \mu_0 \vec{H}, \tag{1.2a}$$

$$\vec{D} = \epsilon_0 \vec{E}, \tag{1.2b}$$

where μ_0 is the permeability of free space and ϵ_0 is the permittivity of free space.

Assuming that the electric and magnetic fields vary harmonically with time dependence $\exp(-i\omega t)$, where ω is the angular frequency of the field and t is time, the substitutions $\vec{E} \exp(-i\omega t) = \mathbf{E}$, $\vec{H} \exp(-i\omega t) = \mathbf{H}$, can be made in Equation 1.1 and Equation 1.2 to yield the Helmholtz equation in the frequency domain:

$$\left(\nabla^2 + \frac{\omega^2}{c^2} \right) \begin{pmatrix} \mathbf{E} \\ \mathbf{H} \end{pmatrix} = 0, \tag{1.3}$$

where $c = 1/\sqrt{\epsilon_0 \mu_0}$. A general technique to solve Equation 1.3 involves expanding $\mathbf{E}$ and $\mathbf{H}$ in terms of orthogonal eigenfunctions. [Sla50]

A waveguide can be idealized as a region of space enclosed by a perfect conductor. Supposing the waveguide has constant cross-sectional geometry along the z-axis so that it varies with $\exp(i\mathbf{k} \cdot \mathbf{z})$, where $\mathbf{k}$ is the wavenumber, the Laplacian operator can be separated into transverse and longitudinal components $(\nabla_\perp^2 \equiv \nabla^2 - \frac{\partial^2}{\partial z^2})$, to yield the relationship:

$$\left[\nabla_\perp^2 + \left(\frac{\omega^2}{c^2} - k^2 \right) \right] \begin{pmatrix} \mathbf{E} \\ \mathbf{H} \end{pmatrix} = 0, \tag{1.4}$$

with the boundary conditions at the perfect conducting wall

$$\mathbf{n} \times \mathbf{E} = 0, \tag{1.5a}$$

$$\mathbf{n} \cdot \mathbf{H} = 0, \tag{1.5b}$$

3

where **n** is a vector normal to the surface.

To illustrate the characteristics of the solution to these equations, consider the simple case of a pillbox cavity, that is a cylindrical structure of a finite length enclosed by perfectly conducting walls. The solutions to this boundary value eigen equation come in two types, or modes. Transverse magnetic (TM) modes have magnetic fields with no component along the z-axis, and transverse electric (TE) modes have electric fields with zero component along z.

Quantity	TM Fields	TE Fields
E_z	$\psi_{mn} \cdot \cos\left(\dfrac{p\pi z}{d}\right)$	0
H_z	0	$\psi_{mn} \sin\left(\dfrac{p\pi z}{d}\right)$
$\mathbf{E_t}$	$-\dfrac{p\pi}{d\gamma_{mn}^2} \sin\left(\dfrac{p\pi z}{d}\right) \nabla_\perp \psi_{mn}$	$-\dfrac{i\omega_{mn}\mu}{\gamma_{mn}^2} \sin\left(\dfrac{p\pi z}{d}\right) \hat{z} \times \nabla_\perp \psi_{mn}$
$\mathbf{H_t}$	$\dfrac{i\epsilon\omega_{mn}}{\gamma_{mn}^2} \cos\left(\dfrac{p\pi z}{d}\right) \hat{z} \times \nabla_\perp \psi_{mn}$	$\dfrac{p\pi}{d\gamma_{mn}^2} \cos\left(\dfrac{p\pi z}{d}\right) \nabla_\perp \psi_{mn}$
ψ_{mn}	$E_0 J_m(\gamma_{mn}\rho) \cdot \exp(im\phi)$	$E_0 J_m(\gamma_{mn}\rho) \cdot \exp(im\phi)$
γ_{mn}	$\dfrac{x_{mn}}{R}$	$\dfrac{x'_{mn}}{R}$
ω_{mn}	$\dfrac{1}{\sqrt{\mu\epsilon}} \sqrt{\left(\dfrac{x_{mn}}{R}\right)^2 + \left(\dfrac{p\pi}{d}\right)^2}$	$\dfrac{1}{\sqrt{\mu\epsilon}} \sqrt{\left(\dfrac{x'_{mn}}{R}\right)^2 + \left(\dfrac{p\pi}{d}\right)^2}$

Table 1.1: Resonant modes in an ideal pillbox cavity. Modes are identified with indices (m, n, p) indicating the number of oscillations in the azimuthal (ϕ), radial (ρ), and longitudinal (z) coordinates. In cylindrical coordinates, $\nabla_\perp \equiv \nabla - \partial_z$. Values x_{mn} and x'_{mn} are n^{th} root of the mth Bessel function and its derivative respectively. E_0 is the amplitude of the electric field.

Table 1.1 presents the closed form solution for electric and magnetic fields of a pillbox cavity with radius R, and length d, filled with a lossless material with permittivity ϵ and permeability μ. [Jac98] As in other problems involving cylindrical symmetry, solutions rely on the Bessel function, $J_m(x)$, [Abr70] which

can be defined by the series

$$J_m(x) = \sum_{\alpha=0}^{\infty} \frac{(-1)^\alpha}{\alpha! \Gamma(\alpha + m + 1)} \left(\frac{x}{2}\right)^{2\alpha+m}. \tag{1.6}$$

The electric and magnetic vector fields for the mode with the lowest resonant frequency, called the fundamental mode, in a pillbox structure with beam tubes are presented in Figure 1.1. The equations given in Table 1.1 for an ideal pillbox cavity do not exactly describe the field, since the beam tubes introduce a small perturbation. Nevertheless, in this structure, and other more complicated geometries, the concepts of TE and TM modes provide a good approximation to the actual fields in the cavity.
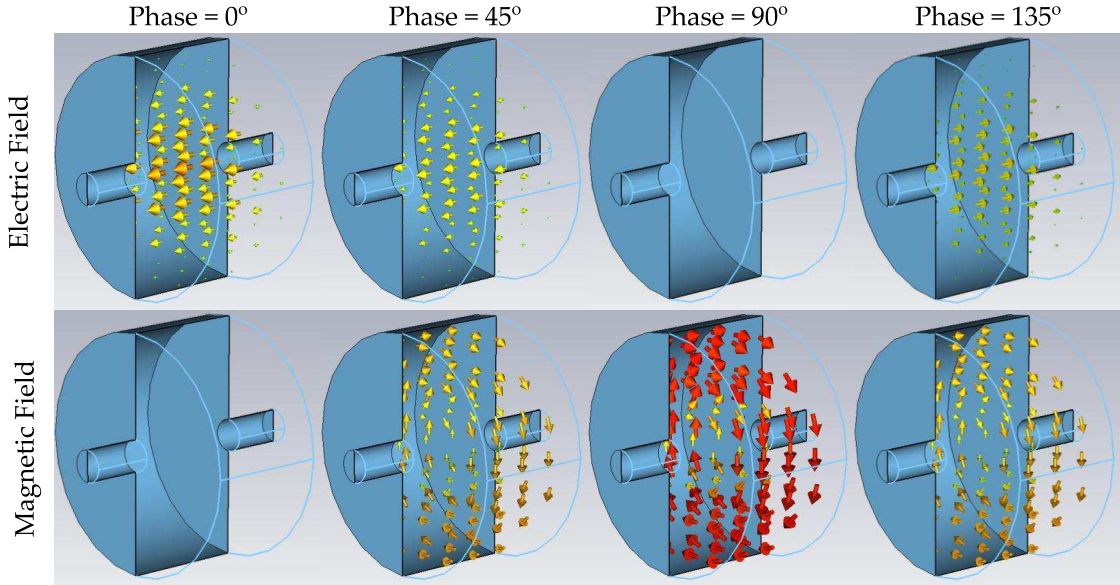
Figure 1.1: Electric and magnetic fields for the TM_{010} mode of a pillbox cavity with beam tubes over time. Field patterns at phases $180°$, $225°$, $270°$, and $315°$ are the same as above with the vector direction reversed.

The TM class of modes have an electric field component pointing along the z-axis, and so, by adding an aperture to the front and end plate, a charged particle beam passing through the structure can be accelerated by transferring energy from the cavity to the beam. For this mode, a relativistic ($\beta \equiv v/c = 1$) charged

particle traveling along the cavity's beam axis will pass through an effective potential difference, V, given by

$$V = \int \mathbf{E}(x = 0, y = 0, z) \exp\left[i(\omega z/c + \phi)\right] \cdot d\hat{z}, \tag{1.7}$$

where ϕ is the phase of the electric field at the time the particle enters the cavity. The real part of this value gives the accelerating voltage, $V_{acc} \equiv \mathfrak{R}[V]$. The accelerating electric field gradient, E_{acc}, calculates the energy gain for a structure with active accelerating length, L, according to

$$E_{acc} \equiv \frac{V_{acc}}{L}, \tag{1.8}$$

and can be maximized by proper choice of ϕ.

The mathematical formulation of standing wave solutions assumes the cavity's material is made of perfectly conducting material. Realistic structures have finite conductivity, leading to an important figure of merit characterizing the energy losses in the walls of a structure. The quality factor, Q_0, is defined in terms of the energy stored in a cavity, U, and the power dissipated in the cavity walls, P_{diss} according to

$$Q_0 \equiv \frac{\omega U}{P_{\text{diss}}}, \tag{1.9}$$

and has the physical interpretation that the energy stored in a cavity will decrease by a factor of $1/e$ with a time constant of Q_0/ω. The energy stored in a structure can be computed via

$$U = \frac{1}{2\mu_0} \iiint_\Omega |\mathbf{B}(x, y, z)|^2 \, d\Omega = \frac{1}{2}\epsilon_0 \iiint_\Omega |\mathbf{E}(x, y, z)|^2 \, d\Omega \tag{1.10}$$

where Ω is the volume of the cavity. [PKH98]

Modes of accelerating structures also have impedances analogous to those encountered in circuit theory. One of the most common figures of merit for

monopole modes of the form TM$_{0mp}$, R/Q, is defined as

$$\frac{R}{Q} = \frac{|V|^2}{2\omega U},$$ (1.11)

and physically couples the energy stored in the cavity with the effective potential difference a particle sees as it passes through the structure. [PKH98] The factor of two is a convention used in the circuit theory analysis, though other authors may use different definitions.

The final figure of merit is the geometry factor, G, which is a parameter coupling the quality factor of a structure with its surface resistance, R_s. Because the power dissipated in the cavity walls in Equation 1.9 can be written as

$$P_{diss} = \frac{1}{2\mu_0^2} R_s \iint_A |\mathbf{B}|^2 \, dA,$$ (1.12)

where A is the surface area of the cavity. Using Equation 1.10, one can write

$$Q_0 = \frac{\omega\mu_0}{R_s} \cdot \frac{\iiint_\Omega |\mathbf{B}|^2 \, d\Omega}{\iint_A |\mathbf{B}|^2 \, dA}.$$ (1.13)

The geometry factor is then defined as

$$G \equiv R_s \cdot Q_0 = \omega\mu_0 \cdot \frac{\iiint_\Omega |\mathbf{B}|^2 \, d\Omega}{\iint_A |\mathbf{B}|^2 \, dA},$$ (1.14)

which is only dependent on the shape of the cavity, independent of material properties.

1.1.1 Non-fundamental mode resonances

Higher-order modes

A given accelerating structure can support an infinite number of eigen modes, depending on possible values of m, n, and p. As the eigenvalues (frequencies)

of these modes are larger than the fundamental mode, they are referred to as higher-order modes (HOMs). These modes may cause unwanted phenomena, such as beam instability or emittance growth, in an accelerating structure, so they should be understood thoroughly.

Figure 1.2 presents electric field maps for TM higher-order modes at the center of a pillbox cavity. Modes are often referred to as monopole ($m = 0$), dipole ($m = 1$), quadrupole ($m = 2$), sextupole ($m = 3$), or octupole ($m = 4$), depending on their number of azimuthal variations; this nomenclature is frequently used in this thesis.
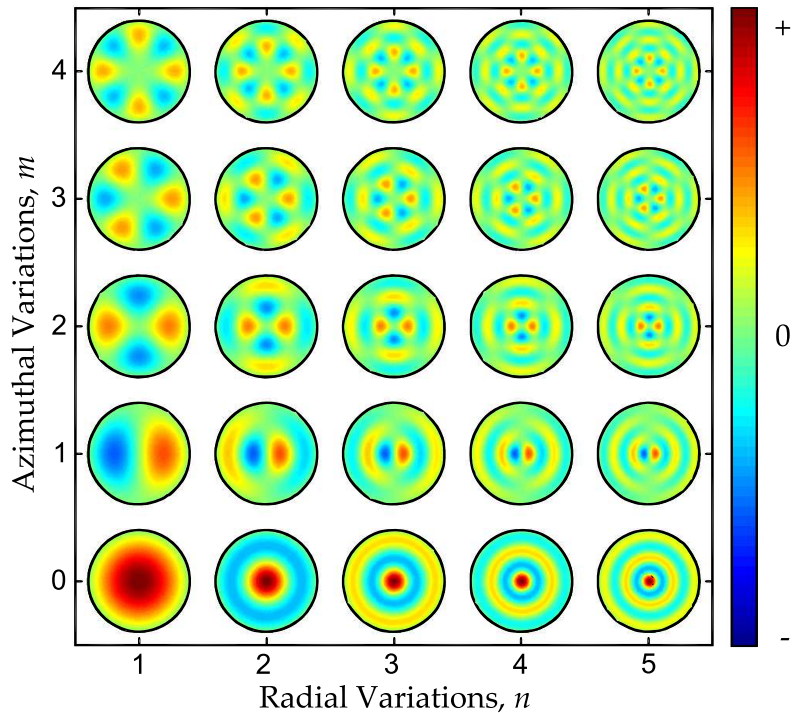
Figure 1.2: Electric field component E_z at the center of a pillbox cavity for TM higher-order modes for various values of m and n.

For modes having a non-zero number of azimuthal variations, $E_z = 0$ along the beam axis. This means that Equation 1.7 is identically zero, so the impedance of the mode via Equation 1.11 also vanishes. To remedy this situation, a trans-

verse voltage, $V_\perp$, is defined for modes with $m > 0$ a distance r_0 parallel to the beam axis.

To derive $V_\perp$, it is convenient to consider the modes excited by a relativistic particle ($\beta = 1$) travelling parallel to the beam axis, but offset a distance r_0 in the direction of the HOM's polarization axis, chosen to be in the x-direction. The beam will couple to the z-component of the electric field. The voltage induced by the longitudinal field scales (for small values) with radius, r, as

$$V(r) = \left(\frac{r}{r_0}\right)^m \cdot V(r_0), \tag{1.15}$$

where $V(r_0)$ is defined as in Equation 1.7, substituting $x = r_0$, and the scaling arises from the leading term of the series in Equation 1.6. [Sch11]

The particles are deflected by the multipole field, receiving a transverse kick, $\Delta p_\perp$, given by the Panofsky-Wenzel theorem, [PW56]

$$\Delta p_\perp = i\frac{q}{\omega}\frac{dV}{dr}. \tag{1.16}$$

Carrying out the differentiation connects the transverse and longitudinal voltage via

$$V(r)_\perp = \frac{c\Delta p_\perp}{q} = i\frac{c}{\omega r_0} \cdot \left(\frac{r}{r_0}\right)^{m-1} V(r_0), \tag{1.17}$$

$$V(r_0)_\perp = i\left(\frac{c}{\omega r_0}\right) \int E_z(r_0, z) \exp\left(i\omega\frac{z}{c}\right) dz, \tag{1.18}$$

where ω is the angular frequency of the mode, and the second equation uses $r \rightarrow r_0$. Analogous to the longitudinal R/Q defined in Equation 1.11, the transverse value, $(R/Q)'_\perp$ is simply

$$\left(\frac{R}{Q}\right)'_\perp \equiv \frac{|V_\perp|^2}{\omega U}, \tag{1.19}$$

which is valid for all multipole modes, and used in 3D electro-magnetic simulation codes such as ACE3P. [LLNK09] Note $(R/Q)'_\perp$ has dimension Ω.

9

A 2.5D electromagnetic code[1] CLANS2 [MY99] uses a slightly different definition of transverse impedance. In CLANS2,

$$\left(\frac{R}{Q}\right)_\perp \equiv \frac{|V(r_0)|^2}{2\omega U r_0^{2m}}, \tag{1.20}$$

and has units of Ω/cm^{2m}. The benefit of this definition is that $(R/Q)_\perp$ is independent of offset for small values of r_0. This quantity appears unprimed, because it is the standard definition used in most of this work.

Mode splitting in multi-cell structures

In addition to HOMs obtained from azimuthal, longitudinal, or radial variations, the formation of an accelerating structure composed of several resonators (e.g. several pillbox cavities, each of which is a cell, connected by coupling holes or irises) also introduces additional modes, due to the cell-to-cell interaction. This can be modelled in terms of oscillators coupled with springs, or via a circuit model, as illustrated in Figure 1.3. A structure comprised of N cells will have N modes in the TM_{010} passband. [Lie01] The eigenfrequencies of the ath modes in a given passband have the form

$$\omega_a = \omega_0 \sqrt{1 + 2k_c \left[1 - \cos\left(\frac{a\pi}{N}\right)\right]}, \tag{1.21}$$

which depend on the cell-to-cell coupling factor, k_c, assumed constant between cells in the above equations. [Lie01] Figure 1.4 presents the relative field amplitude for the fundamental passband of a 7-cell cavity.

In addition to mode splitting between cells in a structure, it is also possible to introduce additional modes by the coupling of multicell structures with

---

[1]CLANS2 models 2D structures, but accounts for azimuthal variations of multipole modes for cylindrically symmetric structures, giving it the extra 1/2 dimension.
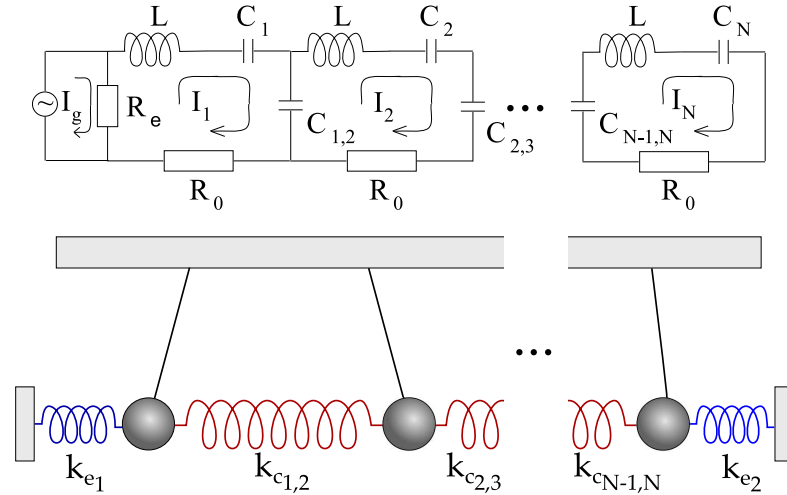
Figure 1.3: Top: Circuit model of coupled cavities modeled as RLC circuits driven by a current source with capacitive coupling. [Lie01]. Bottom: Coupled pendula model illustrating the different coupling of cavities in at the end of a cavity string with those coupled to cavities on both sides.

one another. [Lie01] In general this coupling is extremely weak for the fundamental mode because beam tubes are chosen so that the fundamental mode is strongly attenuated outside of a given resonant structure. Higher-order modes may propagate out of a given cavity and couple with those of other cavities.

At this point, the basic theory of electromagnetic fields in resonant cavities has been introduced. Next, attention is turned to the benefits of coupling this technology with superconducting science.

1.2 Introduction to Superconductivity

Superconductivity is a phenomena that was first discovered by Kamerlingh Onnes in 1911, wherein he measured the temperature dependent resistance of a column of mercury at very low temperatures. He found that below 4.2 K,
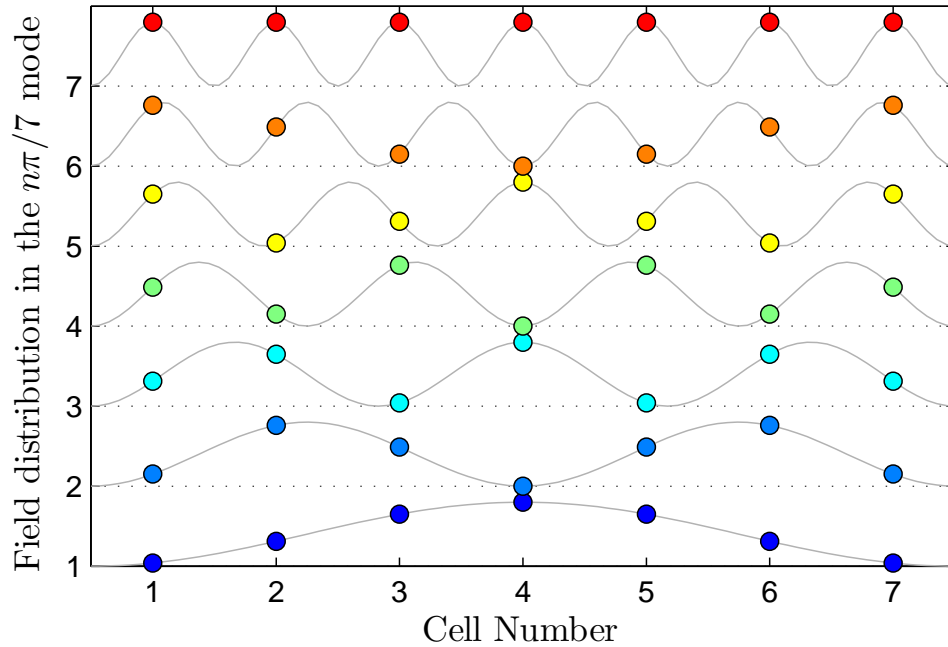
Figure 1.4: Amplitude distribution of modes 7-cell cavity's fundamental pass-band. The $7\pi/7$ mode has equal amplitude in all cells, and is used as the fundamental accelerating mode.

the resistance of the mercury dropped sharply from $\approx$0.1 Ω to less than 1 $\mu\Omega$ of resistance (a value too small to measure with his instruments). [Onn11] Figure 1.5 shows the first measurement of a superconducting sample, a feat for which Onnes received the Nobel Prize in Physics, just two years later. [Nob13a]

Subsequent measurements of the resistivity of superconductors to direct current showed that the ratio of the resistivity in the superconducting state to the normal conducting state was less than 2×10^{-16}. [Bro61] Thus, in DC, a superconductor can be considered a perfect conductor, and the physics of perfect conductors can shed insight into the workings of superconductors without delving into the full microscopic theory; more about the theory will be presented in chapter 2. The arguments below follow the presentation in Padamsee's "RF Superconductivity for Accelerators." [PKH98]
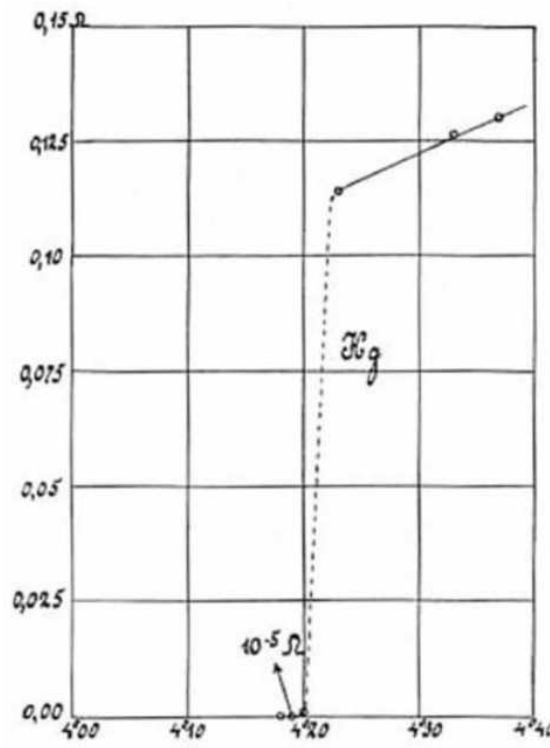
Figure 1.5: First experimental evidence of superconductivity, measured in a mercury sample by H. Kamerlingh Onnes. [Onn] Horizontal axis is temperature and vertical axis is resistance. Plot shows that within 0.01 K below 4.2 K, the resistance jumps from more than 0.1 Ω to less than 10^{-6} Ω. The discontinuity at 4.2 K was unexpected and pointed to a new phase of matter.

Inside a perfect conductor that is exposed to an electric field, $\vec{E}$, the electrons will be accelerated according to

$$m\frac{\partial \vec{v}}{\partial t} = -q\vec{E},$$
(1.22)

where m and q are the mass and charge of an electron and $\vec{v}$ is its velocity. Assuming the conductor has an electron density of n, the current density is $\vec{j} = -nq\vec{v}$, meaning that Equation 1.22 can be written as

$$\frac{\partial \vec{j}}{\partial t} = \frac{nq^2}{m}\vec{E}.$$
(1.23)

13

Using the result of Equation 1.23 in Equation 1.1a one arrives at the result

$$\frac{\partial}{\partial t}\left(\nabla \times \vec{j} + \frac{nq^2}{m}\vec{B}\right) = 0. \tag{1.24}$$

For static fields, there is no displacement current and $\nabla \times \vec{B} = \mu_0 \vec{j}$, so applying this relation to Equation 1.24 yields

$$\left(\nabla^2 - \frac{1}{\lambda_L^2}\right)\vec{B} = 0, \tag{1.25}$$

where λ_L is the London penetration depth

$$\lambda_L \equiv \sqrt{\frac{m}{\mu_0 nq^2}}, \tag{1.26}$$

which gives the distance into the perfect conductor at which the magnetic flux density drops by a factor of $1/e$, when exposed to an external uniform magnetic field.

Superconductors exhibit one important difference compared with perfect conductors: the ability to expel magnetic flux from the material bulk, when cooled below its critical temperature, T_c. This phenomena, illustrated in Figure 1.6, is known as the Meissner effect after one of its discoverers, Walther Meissner. [MO33] This effect cannot be explained by assuming perfect conductivity. Instead, it requires that not only Equation 1.24 be satisfied, but its argument be identically zero:

$$\nabla \times \vec{j} + \frac{nq^2}{m}\frac{\partial \vec{B}}{\partial t} = 0, \tag{1.27}$$

which is known as the second London equation. [LL35]

The London equations predict the current density and magnetic field only exist within a penetration depth, λ_L of the surface layer of a superconductor. These equations do not theoretically address the underlying physics, which rely

14
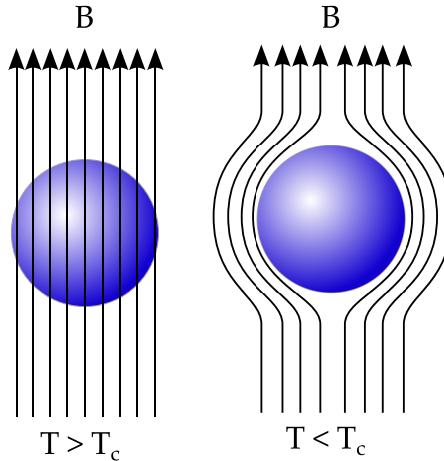
Figure 1.6: Illustration of the Meissner effect. At left, a superconductor at a temperature above T_c is positioned in a uniform magnetic field. Shown at right is the same setup after cooling the material below T_c, which causes flux to be expelled from the bulk of the superconductor.

on a microscopic explanation, and as such do not explain such phenomena as flux pinning, but do adequately provide a broad explanation of empirical results.

Superconductivity arises from the pairing of electrons due to a weak attractive potential caused by lattice distortions as electrons pass through a material. [BCS57] This changes the density of states present in a normal conductor to one in which an energy gap, E_g, appears between states with paired electrons and vacant states. As such, it costs energy to break up electron pairs, known as Cooper pairs, and the superconducting state is energetically favorable.

It is important to note that the pairing between electrons is not a tight one, as is the pairing between an electron and an atomic nucleus. Cooper pairs have correlated spin and momenta as between particles having $(\vec{p}, \uparrow)$ and $(-\vec{p}, \downarrow)$. [PKH98] The rough distance of coherence between the pairs can be calculated.

The condensing electrons are those with momenta sufficient to place their

15

energy near the Fermi energy $k_B T_c$. This allows one to write

$$k_B T_c = \delta \left(\frac{p^2}{2m} \right) = \frac{p}{m} \delta p, \tag{1.28}$$

$$\delta p = \frac{k_B T_c}{v_F}, \tag{1.29}$$

where the Fermi velocity $v_F \equiv p/m$ has been introduced. The minimal spatial extent of the pair, ξ, is limited by the Heisenberg uncertainty principle, $\xi \cdot \delta p = \hbar$ to yield

$$\xi = \frac{\hbar v_F}{k_B T_c}. \tag{1.30}$$

While the actual definition of coherence length varies based on which theoretical frame work is being used (see Appendix A for a full discussion), Equation 1.30 provides a qualitative description of the correlation length between paired electrons.

With the qualitative properties of superconductors introduced, the interface between accelerator physics and superconductivity will be explored.

1.2.1 Superconductivity applied to accelerating structures

Modern accelerating structures rely on oscillating RF fields. The discussion in the previous section holds true for static fields, but modifications are necessary to treat the RF case. The first needed modification is to note that in an RF field, the conductivity of Cooper pairs is not infinite, due to their inertial mass.

One of the most significant benefits of RF superconducting structures is their extremely small, yet finite, surface resistance. The surface impedance can be calculated by assuming that the conductivity is due to normal conducting elec-

trons, σ_n, and superconducting electrons, σ_s. The surface impedance, Z_s, due to an RF oscillation of frequency ω is

$$Z_s = R_s + iX_s = \sqrt{\frac{i\omega\mu_0}{\sigma_n - i\sigma_s}}. \tag{1.31}$$

where R_s is the resistance of the structure and X_s is the reactance. [PKH98] Assuming the conductivity of the superconducting electrons is much greater than those of the normal conducting electrons, the real and imaginary parts of the impedance becomes

$$R_s = \frac{1}{2}\sigma_n\omega^2\mu_0^2\lambda_L^3, \tag{1.32}$$

$$X_s = \omega\mu_0\lambda_L. \tag{1.33}$$

It is important to note that λ_L is temperature dependent, which can change R_s by orders of magnitude from temperatures near T_c to the low temperatures used in SRF operation. In general $R_s \gg X_s$ for superconductors. [PKH98] The actual values of surface resistance depend on superconductor properties, but as Figure 1.7 demonstrates, surface resistance on the order of nano-Ohms is achievable, yielding quality factors in excess of 10^{10}.

Quality factors of normal conducting metals such as copper are of the order of 10^4. [Poz05] Electromagnetic energy stored in these structures quickly dissipates in the cavity walls. Dissipated power absorbed in the cavity walls can cause melting or other structural compromises if sufficient cooling is not present. In general, normal conducting accelerating structures can only support high gradient operation in brief pulses. For example the Next Linear Collider, a high energy accelerator proposal utilizing normal conducting technology, would employ RF pulses of lengths on the order of hundreds of nanoseconds at a repetition rate of 120-180 Hz. [RAB+95]
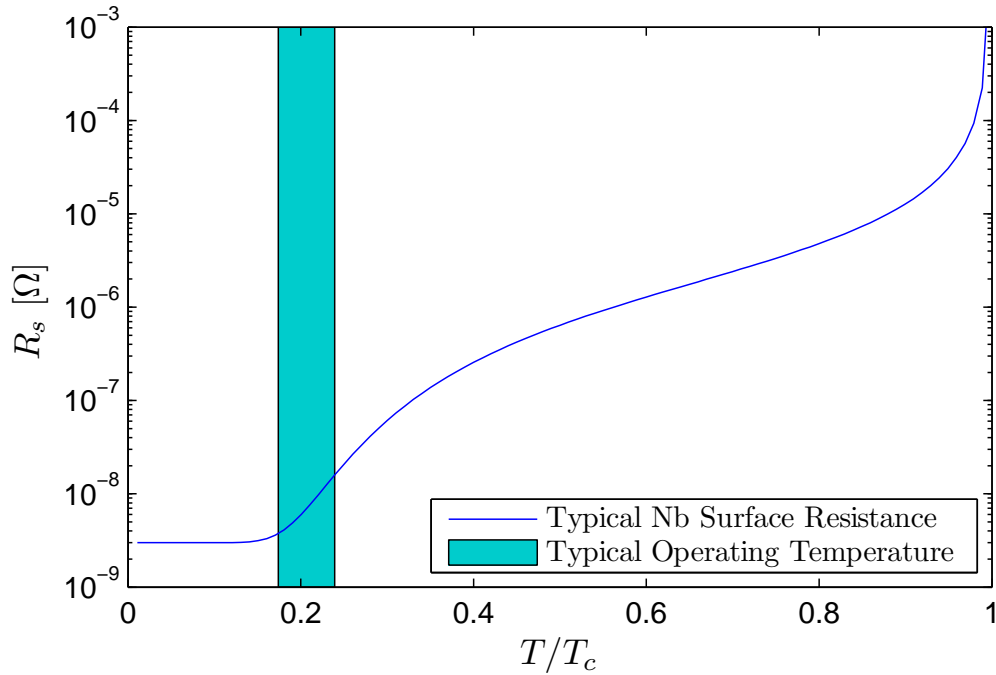
Figure 1.7: Typical RF surface resistance of superconducting niobium (assuming a residual resistance of 3 nΩ) at 1300 MHz calculated from BCS theory with SRIMP. [Hal70b] The blue region shows the region of temperatures usually chosen for superconducting accelerators.

In contrast, superconducting RF structures, with their extremely small surface resistances, regularly achieve quality factors in excess of 10^{10} at high gradients. The power loss in the walls is reduced by orders of magnitude, allowing continuous wave operation of accelerators at high gradients.

A brief back of the envelope calculation demonstrates the benefits of superconductivity in accelerators operating in continuous wave mode: A multicell cavity operating at an accelerating gradient of 20 MV/m with a frequency of 1300 MHz stores just under 20 J of energy in the structure. A copper cavity at room temperature, having $Q_0 = 10^4$ would dissipate 15 MW of power in the cavity walls, leading to power densities that could not be removed by a cooling system. The same structure, composed of superconducting niobium, operating at 1.8 K, would only dissipate approximately 15 W of power. Even including

18

the inefficiency of power extraction at cryogenic temperatures, which requires about 1000 W of wall power for each Watt removed at 1.8 K, superconducting RF structures provide huge energy savings, and the realization of scientific devices that are infeasible without the technology.

1.2.2 RF Characterization of Superconducting Cavities

One of the primary benefits of utilizing superconductors in accelerating structures is the extremely high quality factors. A technique is needed to accurately measure this figure of merit for resonant cavities. The theory behind RF measurements of superconducting resonators is well understood, so below the basic features are highlighted, following [PKH98].

Supposing energy, U is stored in a cavity with resonant angular frequency, ω, losses will cause the energy to decay as a function of time, t, according to

$$\frac{dU}{dt} = -\frac{U}{\tau_L(t)}. \tag{1.34}$$

In the above equation, the time constant, τ_L, for dissipation of energy in the cavity is defined as

$$\tau_L(t) = \frac{\omega}{Q_L(t)}, \tag{1.35}$$

and can be measured with a power meter. The loaded quality factor of the structure, Q_L, takes into account the overall quality factor due to multiple sources of losses, such as the cavity wall (Q_0) and the power coupled out via RF input coupler (Q_e), and field probe (Q_t). These quantities are related as

$$\frac{1}{Q_L} = \frac{1}{Q_0} + \frac{1}{Q_e} + \frac{1}{Q_t}. \tag{1.36}$$

By design, the losses to the field probe are small and can usually be neglected. The quantity of interest is Q_0, since it is an intrinsic property of the resonator independent of coupling scheme. For this reason, Q_0 is often called the intrinsic quality factor.

The coupling between the RF input coupler and the cavity is characterized through a coupling constant $\beta = Q_0/Q_e$. This constant can be measured by turning off input power to the cavity and measuring power levels reflected from the cavity coupler at several points in time to calculate

$$\beta_e = \frac{1}{2\sqrt{\frac{P_i}{P_e}} - 1}, \tag{1.37}$$

$$\beta_i = \frac{1 \pm \sqrt{\frac{P_r}{P_i}}}{1 \mp \sqrt{\frac{P_r}{P_i}}}, \tag{1.38}$$

whose average yields β. In Equation 1.38, the upper sign is used when $\beta > 1$ and the lower sign when $\beta < 1$. [PKH98] The definitions of P_i, P_e, and P_r come from the reflected power trace, as illustrated in Figure 1.8.
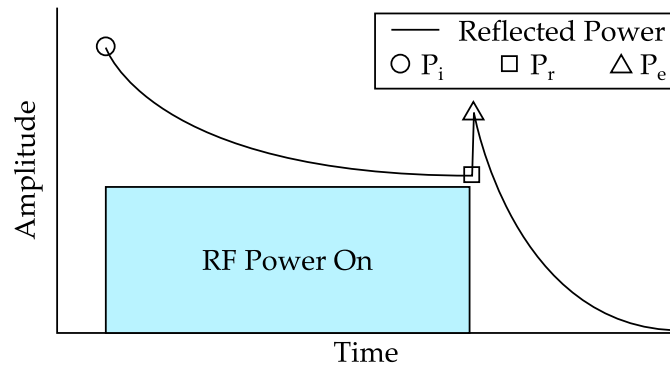
Figure 1.8: Reflected power signal as a function of time for an under-coupled cavity. Geometric symbols mark the points on the trace giving values used in Equation 1.37 and Equation 1.38. The box labelled "RF Power On" marks the time period in which the cavity is driven on resonance with constant drive power.

The intrinsic quality factor is given by

$$Q_0 = \omega \cdot \tau_L \cdot (1 + \beta). \tag{1.39}$$

Software was developed to automate the data taking process, [GVL12] greatly simplifying the characterization of superconducting resonators.

The accelerating gradient can be determined by measuring the power coupled out of the cavity with a field probe, P_t, with very weak coupling Q_t, to a mode with shunt impedance (R/Q). Recalling the relation $P = V^2/R$, the voltage in the structure is given by

$$V = \sqrt{2 \cdot P_t \cdot \left(\frac{R}{Q}\right) \cdot Q_t}, \tag{1.40}$$

where the factor of 2 arises from use of the circuit definition of (R/Q). For a cavity driven at a constant power, P_f, from an input coupler with Q_{ext} coupling to the mode, the voltage in the cavity is given by

$$V = \frac{2 \cdot \beta_e}{1 + \beta_e} \cdot \sqrt{2 \cdot P_f \cdot \left(\frac{R}{Q}\right) \cdot Q_{ext}}. \tag{1.41}$$

The accelerating gradient is obtained by dividing by the appropriate length, as discussed in Equation 1.8.

It is also possible to relate the peak surface electric or magnetic field (which usually occur at different locations) and the stored energy in the structure, U, via electromagnetic constants k_e and k_m obtained from field solving codes. They are related via

$$E_{pk} = k_e \cdot \sqrt{U}, \tag{1.42}$$

$$B_{pk} = k_m \cdot \sqrt{U}. \tag{1.43}$$

1.3   Superconducting Properties of Niobium

To date, niobium is the only superconducting material that has been utilized in the accelerating structures of large-scale projects. There are many reasons for this, including its (relatively) high critical temperature, its mechanical properties including ductility and high thermal conductivity, and the S-wave nature of its superconductivity. The benefits of each of these properties will each be discussed in turn.

The first benefit of niobium is that of all pure substances, it has the highest critical temperature, as shown in Table 1.2. Generally speaking, for type-I superconductors, the maximum magnetic field a superconductor can support in the Meissner state is proportional to the critical temperature. Specifically, a superconductor with critical temperature T_c, operating at a temperature T, can support magnetic surface fields that increase as $T/T_c \rightarrow 0$. This has direct consequences for accelerators in that materials capable of supporting higher fields require less real estate to operate at high energies. An additional benefit of choosing to use a superconductor with a higher T_c is the fact that cryogenic systems become more technologically challenging at low temperatures, making installation and operation costs prohibitively expensive for large installations.

In addition to the benefits of its high critical temperature, niobium has several properties that make it suitable for forming into accelerating structures. It is ductile, and can be rolled, pressed or hydroformed into cavity shapes. Furthermore, it can be produced in high purity ingots, with low resistivity at cryogenic temperatures. A parameter characterizing the purity of the niobium in terms of the ratio of its room temperature and cryogenic resistivity, the residual resistiv-

Element	T_c [K]	$B_c(0)$ [mT]	$\dfrac{2\Delta(0)}{k_B T_c}$	$\xi_0 = \dfrac{2}{\pi} \cdot \dfrac{\hbar v_F}{2\Delta(0)}$ [nm]	λ_L [nm]
Ga	1.1	5.1	3.5	-	-
Al	1.2	10.5	3.3	1600	16
In	3.4	29.3	3.6	40	360
Sn	3.7	30.9	3.5	230	34
Hg	4.2	41.2	4.6	-	-
Pb	7.2	80.3	4.38	83	37
Nb	9.2	198	3.6-3.85	38	39

Table 1.2: Superconducting properties of selected elements. Data is presented in order of increasing critical temperature, T_c, and shows that the critical field at 0 K, $B_c(0)$, increases as T_c increases. Other properties presented are the normalized energy gap at 0 K, $\Delta(0)/k_B T_c$, BCS coherence length, ξ_0, and London penetration depth, λ_L. Niobium has the benefit of having the highest critical temperature of this group of materials, and in this case data for extremely clean niobium has been presented, making it almost type-I. No coherence length and penetration depth data is available for bulk samples of Ga and Hg. Data sources: Critical temperature, [Roh04, MGC63] critical field, [Eis54] energy gap, [Kit86, TM80, NM75] coherence length and penetration depth. [MS69, Poo99]

ity ratio (RRR), defined as

$$RRR \equiv \frac{\rho(T_{warm})}{\rho(T_{cold})}. \tag{1.44}$$

Typical temperatures selected are T_{warm} = 300 K and T_{cold} = 4.2 K,[2] and high purity niobium routinely has bulk RRR in excess of 300. [PKH98] A benefit of large RRR is a high thermal conductivity, allowing power to be efficiently extracted from the RF surface into the cryogenic bath. Other mechanical properties of niobium are presented in Table 1.3.

Superconductivity in niobium is mediated by electrons travelling together in spherical orbits, but in opposite directions. This is referred to as S-wave su-

---

[2]Although niobium is a superconductor, and thus has no resistance below 9.2 K, a resistivity can be measured by supplying a magnetic field large enough to cause the bulk niobium to transition into the normal conducting state.

Parameter	Value	Unit	symbol
Electrical resistivity at 296 K	160	$n\Omega \cdot m$	ρ
Electronic specific heat coefficient	7.4×10^2	$J \cdot m^{-3} \cdot K^{-2}$	γ_c
Grain Size	~ 50	μm	—
Tensile Strength	~ 100	MPa	—

Table 1.3: Typical properties of high purity niobium used in particle accelerators. Resistivity and specific heat values from [GR03] and [FSS66], where as grain size and tensile strength are specifications for niobium sheets from the XFEL project quoted in [PKH98].

perconductivity. In contradistinction to D-wave superconductors, which have paired electron orbitals resembling a four leaf clover,[3] S-wave superconductors are isotropic, eliminating the influence of grain orientation from having strong effects on superconductivity. Intermediate temperature superconductors have superconducting properties that are dependent on the orientation of the wavefunction current. Of the superconductors that are described by BCS theory, or its extensions, Magnesium Diboride (MgB$_2$, T_c = 39 K) [BLP$^+$01] exhibits both Type-I and Type-II superconductivity, having two energy gaps depending on whether the current is travelling parallel to or perpendicular to the ab-planes of the material. [BS05] This anisotropy poses theoretical and technological barriers to implementation in superconducting structures, that can be avoided by using S-wave superconductors such as niobium, or Nb$_3$Sn.

1.4 Future accelerators

A complete understanding of the science of superconductivity is necessary to push the field of microwave superconductivity toward its fundamental limits. The two frontiers are the energy frontier, characterized by large gradients, and

---

[3]The first discovered D-wave superconductor was CeCu$_2$Si$_2$. [SAB$^+$79]

the power frontier, characterized by extremely high quality factors. It is the purpose of this thesis to elucidate the connection between these two frontiers for niobium material.

1.4.1 Pulsed High Gradient Accelerators

In 1964 a group of physicists postulated the existence of an undiscovered particle as the mechanism behind inertial mass of matter. [EB64, Hig64, GHK64] In the intervening 49 years, a collaboration of more than 2,000 scientists working at CERN designed the world's largest particle accelerator to detect this massive particle, a key discovery leading to the key theorists receiving the 2013 Nobel Prize in Physics. [Nob13b]

Though the Higgs boson has been detected, a great many questions about the underlying fabric of the universe remain: Are there undiscovered principles of nature? What is dark matter and dark energy? At high energies, do all forces become one? Does the universe exhibit supersymmetry? Hints at solutions to these problems are being provided by the Large Hadron Collider, but further illumination requires precision measurements possible with higher energy machines such as the International Linear Collider. [Pan05]

To achieve a center-of-mass energy of 500 GeV, the 30.5 km long accelerator sections consisting of niobium superconducting cavities must operate in pulsed mode at average gradients of 31.5 MV/m, corresponding to surface magnetic fields of about 135 mT. [The13a] Can the gradient be increased further to push to even higher energy regimes? What is the intrinsic limitation to operating these niobium structures at very high gradients? These questions are further explored

in chapter 2 by exploring a fundamental limitation to surface magnetic fields on superconducting niobium, the magnetic superheating field.

1.4.2   High Efficiency CW Accelerators

In recent years, many applications of CW accelerators have been proposed. Science projects such as free-electron lasers (LCLS-II at SLAC [BBD$^+$12]), proton based CW linac machines (Project-X at Fermilab [OSB$^+$12]) and accelerator driven systems (ADS being investigated at multiple locations worldwide [Age99]) all rely on SRF technology pushing the efficient limit. These machines do not require extreme gradients to minimize total costs, as illustrated by cost estimates for LCLS-II presented in Figure 1.9 and Figure 1.10, but instead are optimal when running at medium gradients with accelerating cavities having very high fundamental mode Q_0.

In addition to the high Q_0 frontier, high efficiency particle accelerators are also pushing the beam current/power frontier. The Cornell Energy Recovery Linac, pictured in Figure 1.11, is a proposed source of ultra-bright, very fast repetition rate x-rays with high coherence. [BBB$^+$11] The science case for the Cornell ERL is expansive, encompassing disciplines such as planetary physics, material science, energy storage and molecular visualization to the atomic scale. [BBD$^+$10] This science will only be possible with major progress in continuous wave acceleration of high beam current.

The x-rays generated at 1.3 GHz repetition rate by the Cornell ERL will be produced by passing a 100 mA, 5 GeV electron beam though specially designed undulators, [Tem08] resulting in high quality photons at a very high repeti-
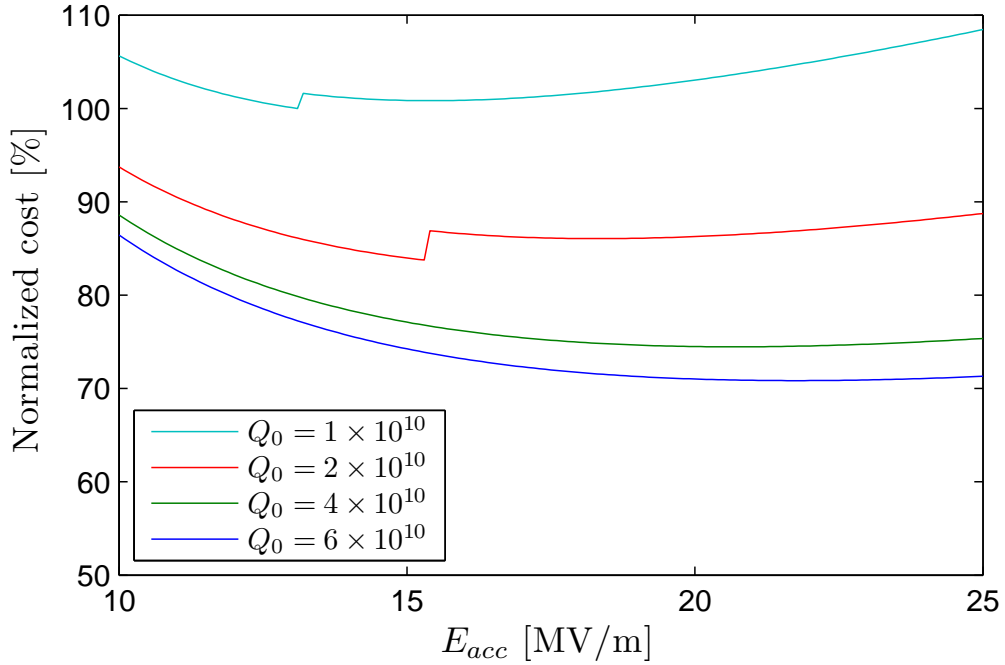
Figure 1.9: Normalized cost vs accelerating gradient for LCLS-II, including cryomodules, cryoplant and RF power for given SRF cavity Q_0.

tion rate. The ERL will have spectral brightness orders of magnitudes higher than other synchrotron based light sources, [BBD+10] and even yield coherent flux similar that of FEL devices as shown in Table 1.4. Though FELs produce very high intensity light, the less intense, but much higher repetition rate of photons produced by the Cornell ERL allows non-destructive testing of samples and ultra-fast science via "tickle and probe" methods [DGB+11] for investigations such as time-resolved synchrotron radiation excited optical luminescence. [SR07]

The prospect of a high current ERL has spurred significant research and development. The successful operation of the light source requires maintaining the ultra-low emittance of the high-current beam. Reaching the Cornell ERL specified beam current of 100 mA requires more than an order of magnitude improvement over the previous ERL current record [TBD+05]. This can be accom-
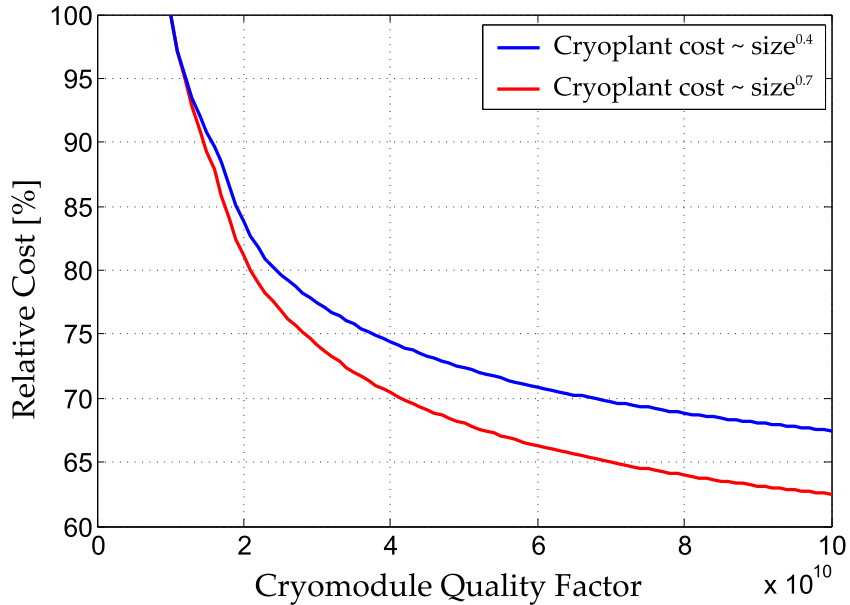
Figure 1.10: The operational cost for the LCLS-2 vs cryomodule quality factor. Specific costs depend on the precise scaling of the cryoplant cost as a function of the size of the cryogenic low temperature load, but the value is likely between the plotted curves.

Parameter	LCLS @ SLAC	X-FEL @ DESY	ERL @ Cornell	Units
Photons/pulse	10^{12}	10^{12}	1.5×10^6	ph*/0.1%
Repetition Rate	1.2×10^2	4.0×10^3	1.3×10^9	Hz
Flux	1.2×10^{14}	3.3×10^{16}	2.0×10^{15}	ph/s/0.1%
Coherent Fraction	74	89	37	%
Coherent Flux	2.2×10^{13}	2.9×10^{15}	4.8×10^{14}	ph/s/0.1%
Source Size	33	29.7	9.0	μm
Divergence	0.4	0.4	2.3	μrad
Pulse width	0.02	0.1	2	ps
Spot size at 100 m	75	72	226	μm

Table 1.4: Comparison of beam properties generated from FELs and the Cornell ERL for λ = 1.5 light, reproduced from [BBD+10]. Sources: LCLS [Emm09], XFEL [MT01], ERL [BBD+10].
*Units above use ph as an abbreviation for photon.

plished by careful design of the main linac accelerating structures (discussed in chapter 3) as well as producing cavities with extremely high fundamental mode Q_0 (while simultaneously suppressing the quality factors of HOMs) at the working gradient to limit the size of the cryogenic plant (discussed in chapter 4).

28
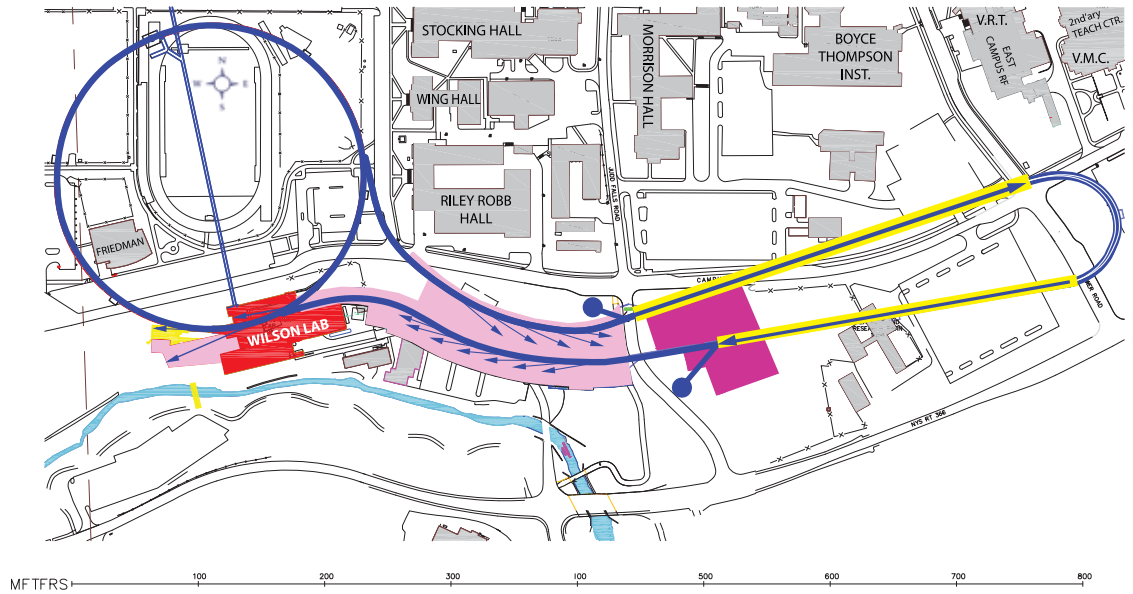
Figure 1.11: An overhead view of the site layout for Cornell's ERL. The accelerator uses part of the Cornell Electron Storage Ring (CESR) as a return arc, and extends tunnels to allow for two accelerating sections where electron beams are simultaneously accelerated and decelerated. [BBB+11]

Contributing to the success of the ERL main linac project in these two capacities is a central objective of this thesis, and, as mentioned at the beginning of this section, has applications far beyond a single project.

1.5 Summary and Organization of this Dissertation

Superconducting RF science lies at the nexus between accelerator physics and material science, perfectly positioned to address questions related to both the gradient frontier of high energy particle accelerator projects as well as research challenges in developing very efficient superconducting accelerating structures. The pages ahead address the material science of S-Wave superconductors by investigating the superheating field of niobium (chapter 2), optimal accelerating

structure design for the main linac of next generation ERL light source, capable of supporting threshold beam current well in excess of 100 mA (chapter 3), and conclusively demonstrate that prototype tests of the Cornell ERL main linac cavity show that extremely high quality factors are not only possible, but due to new material insights, can be expected (chapter 4). The conclusions that can be drawn from this work is discussed as well as highlighting opportunities for future investigation (chapter 5).

CHAPTER 2

MATERIAL STUDIES: THE SUPERHEATING FIELD OF NIOBIUM

What is the maximum gradient that can be obtained for a perfect accelerating structure? This question is of central importance in designing accelerators that push the energy frontier, and of course is material dependent. For superconducting structures, the theoretical answer is that the Meissner state can only meta-stably persist up to the magnetic superheating field before undergoing a phase transition.[1] While the superheating field is understood near a material's critical temperature, T_c, the temperature dependence is still an open question.

This work is important because SRF accelerators utilize niobium, and operate far from temperatures where rigorous results apply. This chapter investigates the temperature dependence of the superheating field of niobium, for surface preparations commonly used in large-scale accelerators.

The chapter begins by discussing the basic critical fields of superconductors, including the superheating field. Focusing on the superheating field, various theories are discussed followed by a review of measurements done prior to this work.

Next, new experimental measurements on the temperature dependence of the superheating field of niobium are presented for two different surface treatments. The presentation includes a description of the methodology used to obtain the data and subsequent analysis. The chapter concludes by showing that, for niobium, the experimental measurements of the superheating field results

---

[1]The maximum surface magnetic field in an SRF cavity is proportional to the accelerating electric gradient produced by the cavity, so throughout this chapter the concepts of maximum magnetic field and electric gradient are used interchangeably.

over a broad range of temperatures is well described by a linear dependence on $(T/T_c)^2$, in agreement with of Ginsburg-Landau Theory near T_c.

2.1 Introduction to the Theories of Superconductivity

As discussed in section 1.2, superconductivity is a phenomena characterized by the ability to conduct direct current with zero attenuation. The superconducting phase persists below critical points. For the purposes of this chapter, the critical points of interest are external or applied magnetic fields that initiate a phase transition out of the superconducting state at certain critical field values.

There are several approaches to understanding the behavior of superconductors near critical points. The simplest model is a phenomenological one, based on the theory of phase transitions, put forth at the very beginning of the 1950's by V. L. Ginsburg and L. D. Landau, which could explain the behavior of superconductors without examining their microscopic properties. [GL50] (An English translation appears in [Lan65])

A microscopic theory of superconductivity was not known until 1956 when L. N. Cooper demonstrated that electrons near the Fermi surface of a material could form an instability in the presence of an arbitrarily weak attractive potential. [Coo56] The following year, J. Bardeen, L. N. Cooper and J. R. Schrieffer incorporated this calculation into a full framework microscopically describing the phenomena of superconductivity from the interaction between the electrons and phonons in a vibrating crystal lattice, which is known as BCS theory. [BCS57]

In 1959, L. P. Gor'kov demonstrated that the Ginsburg-Landau (GL) equa-

tions could be obtained from the microscopic considerations of BCS theory. [Gor59] This work set the GL equations on strong theoretical footing, and has allowed the model to confidently be applied to the properties of superconductors near the critical temperature.

2.1.1 Interaction of Superconductors and Magnetic Fields

Supposing a superconductor in a constant magnetic field is cooled below its critical temperature, then the magnetic field will be expelled from the bulk of the superconductor, a phenomena known as the Meissner effect. [MO33] This is accomplished by superconducting electrons establishing a magnetization cancelling the applied field in the bulk of the material.

Due to the Meissner effect, the magnetic field in a superconductor is limited to a small region close to the surface, characterized by a penetration depth, λ_L, which is the region in which supercurrents flow. The Ginsburg-Landau coherence length, ξ_{GL} is related to the spatial variation of the superconducting order parameter.[2] In addition, GL theory uses a penetration depth, λ_{GL} that is related to λ_L, ξ_0, and the purity of the superconductor. [OMFB79][3] The ratio of these GL characteristic length scales yields the dimensionless Ginsburg-Landau (GL) parameter,

$$\kappa_{GL} \equiv \frac{\lambda_{GL}}{\xi_{GL}}. \tag{2.1}$$

This parameter, κ_{GL}, separates superconductors into two broad categories;

---

[2]A plethora of length scales will be bandied about in the following pages. For a quick reference of these lengths and their definitions, see Appendix A.

[3]Fortunately for pure superconductors, λ_L is nearly equal to λ_{GL} meaning the arguments are qualitatively correct either way.

those with $\kappa_{GL} < 1/\sqrt{2}$ are called Type-I superconductors and those with $\kappa_{GL} > 1/\sqrt{2}$ are called Type-II superconductors.[4] Though the distinction will be dealt with more thoroughly later in this chapter, roughly speaking, Type-I superconductors exist in either the fully superconducting state or in the normal state. Type-II superconductors can exist in a mixed state wherein normal conducting lines or vortices penetrate a superconducting bulk.

Pippard improved upon the superconductor model that only assumed local electron interaction to take into account non-local effects. [Pip53] He argued that superconducting wavefunctions should have a characteristic dimension, ξ_0.[5] If only electrons around $k_B T_c$ of the Fermi energy can be involved in the dynamics around the critical temperature, and they have a momentum range $\Delta p \approx k_B T_c / v_F$, where v_F is the Fermi velocity, then the approximate coherence length should, by the uncertainty principle be

$$\Delta x \sim \frac{\hbar}{\Delta p} \quad \rightarrow \quad \xi_0 \sim \frac{\hbar v_F}{k_B T_c}. \tag{2.2}$$

Assuming a pure material has a BCS coherence length, ξ_0, Pippard showed [Pip53] that if impurities introduce scattering centers giving an electron mean free path of ℓ_{tr} and modify the coherence length as

$$\frac{1}{\xi_p} = \frac{1}{\xi_0} + \frac{1}{\ell_{tr}}, \tag{2.3}$$

where ξ_p is the modified coherence length of the impure material.

In the Pippard approximation, the penetration depth λ_p, as a function of electronic mean free path becomes

$$\lambda_p(\ell) = \lambda_L \sqrt{1 + \frac{\xi_0}{\ell_{tr}}}, \tag{2.4}$$

---

[4] Pure niobium is a weakly Type-II material, with $\kappa_{GL} \approx 1$.
[5] ξ_0 is the BCS coherence length.

where λ_L is the London penetration depth of the material with no scattering sites, which is valid near $T = 0$. [Pip53]

The results in Equation 2.3 and Equation 2.4 are quoted to provide a qualitative sense of the physical interactions. The quantitative results used in later calculations are the zero temperature Ginsburg-Landau length scales related to the BCS parameters, and have the forms

$$\xi_{GL} = \pi e^{\gamma} \sqrt{\frac{7\zeta(3)}{48}} \sqrt{\chi(\lambda_{tr})} \cdot \xi_0, \tag{2.5}$$

and

$$\lambda_{GL} = \frac{\lambda_L}{\sqrt{2R(\lambda_{tr})}} \sqrt{1 + \frac{\pi e^{-\gamma}}{2} \cdot \frac{\xi_0}{\ell_{tr}}} \tag{2.6}$$

where, the undefined functions and constants are discussed in Appendix A. [OMFB79]

The ratio of these two length scales yields the purity dependent, zero temperature Ginsburg-Landau parameter

$$\kappa_{GL} = \frac{e^{\gamma}}{\pi} \sqrt{\frac{24}{7\zeta(3)} \cdot \frac{1}{R(\lambda_{tr})}} \cdot \frac{\lambda_L}{\xi_0} \cdot \left(1 + \frac{\pi e^{-\gamma}}{2} \cdot \frac{\xi_0}{\ell_{tr}}\right). \tag{2.7}$$

Before delving into the full Ginsburg-Landau theory, simply energy balance arguments are laid out to motivate why there are two types of superconductors and what the essential difference is between them. The superconducting state is more ordered than the normal conducting state because of the Cooper pairing of electrons near the Fermi energy. Subjecting a material to a DC magnetic field causes supercurrents to flow in the layer within a penetration depth of the superconducting surface to cancel out interior fields, which raises the free-energy of the superconductor, F_s, which depends on the applied field. When F_s is equal

to the free energy of the normal conducting state, F_n, flux enters the supercon-
ductor, of volume V_s, and a phase transition occurs.

The magnetic critical field, B_c, is defined as the applied field at which the free
energy of the superconducting and normal conducting state is equal. [Kit86] It
can be calculated via

$$F_n = F_s(H = 0) + \frac{1}{\mu_0} V_s \int_0^{B_c} B \, dB, \tag{2.8}$$

which is applicable for Type-I superconductors in steady-state conditions.[6]

Supposing the energy density of superconductors is suppressed over a co-
herence length ξ_0, the free energy per unit area would be increased by

$$\frac{1}{2\mu_0} B_c^2 \xi_0. \tag{2.9}$$

If magnetic field, B_e is admitted to penetrate the material a distance λ_L, the free
energy is lowered by

$$-\frac{1}{2\mu_0} B_e^2 \lambda_L, \tag{2.10}$$

giving a net boundary energy per unit area of

$$\frac{1}{2\mu_0} \left(\xi_0 B_c^2 - \lambda_L B_e^2 \right). \tag{2.11}$$

The sign of this energy will depend on the length scales, ξ_0 and λ_L. Type-I su-
perconductors, with positive surface energy, only permit the Meissner state as
the low energy state. In contrast, type-II superconductors can benefit from a
negative surface energy gain by allowing flux tubes into the bulk of a supercon-
ductor, entering a mixed state of superconducting bulk and normal conducting
vortices.

---

[6]The following pages discuss critical magnetic fields in terms of the B-field, which is mea-
sured in Tesla and more commonly used in accelerator physics, rather than the H-field, which
is measured in A/m. In free space and non-magnetic materials they are related via $B = H/\mu_0$,
where μ_0 is the permeability of space.

In the next section, critical fields of superconductors will be discussed within the context of the phenomenological, or Ginsburg-Landau, model of superconductivity.

2.1.2   Ginsburg-Landau Theory

Now that the difference between type-I and type-II superconductors has been motivated, the Ginsburg-Landau (GL) framework will be discussed. This phenomenological approach, "a triumph of physical intuition," [Tin04, Chap. 4] introduces a pseudo wavefunction, $\psi(\mathbf{r})$ with the property that $|\psi(\mathbf{r})|^2$ represents the local density of superconducting charge carriers, $n_s(\mathbf{r})$, at any point in space $\mathbf{r}$.

Following the derivation of the Ginsburg-Landau equation in [Eds12], consider the free energy density, f_s, which is composed of several parts:

$$f_s = f_n + f_{pot} + f_{kin} + f_B, \tag{2.12}$$

where f_n is the free energy of the normal state, f_{pot} is the potential energy density, f_{kin} is the kinetic energy of the particles with mass M and charge q, which couple to the magnetic vector potential, $\mathbf{A}$,[7] and f_B is the magnetic energy density. These terms can be written explicitly to give

$$f_s = f_n + \underbrace{\alpha|\psi|^2 + \frac{\beta}{2}|\psi|^4}_{f_{pot}} + \underbrace{\frac{1}{2M}\left|\left(\frac{\hbar}{i}\nabla + q\mathbf{A}\right)\psi\right|^2}_{f_{kin}} + \underbrace{\frac{1}{2\mu_0}|\nabla \times \mathbf{A}|^2}_{f_B}. \tag{2.13}$$

The variables can be normalized via, $\psi \rightarrow \sqrt{M/\mu_0} \cdot \psi$, $\alpha \rightarrow (\hbar^2/M) \cdot \alpha$, $\beta \rightarrow (\mu_0\hbar^2/M^2) \cdot \beta$, and $\mathbf{A} \rightarrow \hbar\mathbf{A}$. Normalizing the free energy density as $f = \hbar^2/\mu_0 \cdot$

---

[7]The magnetic field can be expressed as the curl of the vector potential: $\mathbf{B} = \nabla \times \mathbf{A}$. [Jac98]

$(f_s - f_n)$, yields the dimensionless equation:

$$f = \alpha|\psi|^2 + \frac{\beta}{2}|\psi|^2 + \frac{1}{2}\left|(\nabla + iq\mathbf{A})\psi\right|^2 + \frac{1}{2}|\nabla \times \mathbf{A}|^2. \tag{2.14}$$

The goal of Ginsburg-Landau theory is to find ψ and $\mathbf{A}$ that minimize Equation 2.14.

Before discussing the Ginsburg-Landau equations, a few words should be said about the coefficients: α and β are temperature dependent expansion coefficients with the property that α changes sign at the critical temperature such that it is positive in the normal state and negative in the superconducting state. Expanding $\alpha(T)$ in a Taylor series around T_c yields

$$\alpha(T) = \alpha(T_c) + \alpha' \left(T - T_c\right). \tag{2.15}$$

By assumption of the sign change in α at T_c, $\alpha(T_c) = 0$, showing that α scales linearly with temperature, and where

$$\alpha' \equiv \frac{1}{T_c}\frac{d}{dT}\alpha(T)\bigg|_{T=T_c}. \tag{2.16}$$

For a potential well to exist, $\beta > 0$, and is typically taken as a constant or slowly varying function of temperature. By convention, $t \equiv T/T_c$.

Taking variational derivatives of Equation 2.14, ($\psi \to \psi + \delta\psi$ and $\mathbf{A} \to \mathbf{A} + \delta\mathbf{A}$) and minimizing yields the Ginsburg-Landau equations:

$$\alpha\psi + \beta|\psi|^2\psi + \frac{1}{2}(\nabla + iq\mathbf{A})^2\psi = 0, \tag{2.17}$$

$$\mathbf{J} = \frac{iq}{2}(\psi^*\nabla\psi - \psi\nabla\psi^*) - q^2|\psi|^2\mathbf{A},, \tag{2.18}$$

where Ampere's law, $\mathbf{J} = \nabla \times \mathbf{B} = \nabla \times (\nabla \times \mathbf{A})$, has been used to obtain the supercurrent density, $\mathbf{J}$.

The temperature dependence of the two length scales discussed above can be calculated in the Ginsburg-Landau framework. [Tin04] The (normalized) GL penetration depth is given by

$$\lambda_{GL} = \sqrt{\frac{\beta}{q^2|\alpha|}} = \sqrt{\frac{\beta}{q^2|\alpha'|}} \cdot \frac{1}{\sqrt{1-t}}, \tag{2.19}$$

and the (normalized) GL coherence length is given by

$$\xi_{GL} = \frac{1}{\sqrt{2|\alpha|}} = \frac{1}{\sqrt{2|\alpha'|}} \cdot \frac{1}{\sqrt{1-t}}, \tag{2.20}$$

to yield the (approximately) temperature-independent Ginsburg-Landau parameter in the clean limit

$$\kappa_{GL} \equiv \frac{\lambda_{GL}}{\xi_{GL}} = \sqrt{\frac{2\beta}{q^2}}. \tag{2.21}$$

Critical Magnetic Fields

In the absence of external magnetic fields, $\mathbf{A} = \mathbf{0}$, and Equation 2.14 can be minimized with respect to $|\psi|^2$ to find the depth of the potential well is largest for $|\psi|^{*2} = -\alpha/\beta$. The thermodynamic critical field is the magnetic field, B_c, required so that the free energy vanishes:

$$f_s - f_n = -\frac{B_c}{2\mu_0} = \alpha|\psi|^{*2} + \frac{1}{2}|\psi|^{*2} = -\frac{1}{2}\frac{\alpha^2}{\beta}, \tag{2.22}$$

giving $B_c = \mu_0 \sqrt{\alpha^2/\beta}$, where this relation uses un-normalized values of α, and β so that B_c has units of Tesla.[8] Empirically, the scaling of the critical field goes as

$$B_c(T) = \cdot B_c(0)\left[1 - t^2\right], \tag{2.23}$$

where $B_c(0)$ is the thermodynamic critical field at zero temperature. Though B_c only has physical significance in type-I superconductors, it is also convenient to express other critical fields for type-II superconductors in terms of B_c.

---

[8]Other critical fields in this section will also use SI units. In this case $B_c = \Phi_0/(2\sqrt{2}\xi\lambda)$, where Φ_0 is the flux quantum.
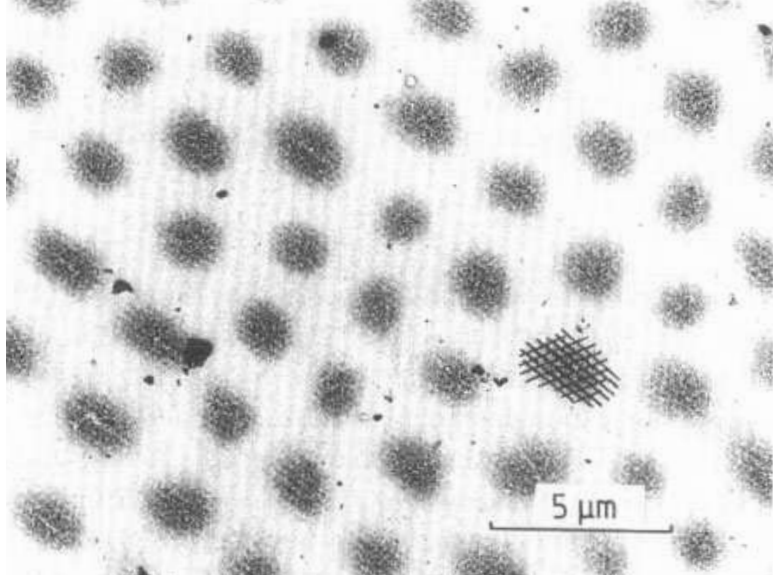
Figure 2.1: Flux line decoration of a high-purity Nb foil 0.16 mm thick at 1.2 K, with an applied field of 17.3 mT which is above B_{c_1} for the foil. Dark islands are vortex lines embedded in a Meissner phase. [Bra95]

For type-II materials, the lower critical field, B_{c_1}, is the field at which the Gibbs energy of the system is equivalent whether a magnetic flux line (vortex) is inside or outside the superconductor. As such, this is the lowest field at which a superconductor can enter a mixed state, illustrated in Figure 2.1. There is not an exact closed form solution of B_{c1} in terms of κ_{GL}, but for $\kappa \gg 1$, it can be approximately given by

$$B_{c_1} = \frac{\Phi_0}{4\pi\mu_0\lambda_{GL}^2} \log(\kappa_{GL}), \tag{2.24}$$

where $\Phi_0 = h/(2e) \approx 2.07 \times 10^{-15}$ T·m is the flux quantum. [Tin04]

The dependence of B_{c_1} on κ_{GL} can be computed numerically from the Ginsburg-Landau equations. [HA63][9] An approximate expression relating B_{c_1} and B_c,[10] through the dependence on the Ginsburg-Landau parameter κ_{GL} was

---

[9]The reader is cautioned that the author of this paper interchanges the usual definition of B_{c_1}, the lower critical field, and B_{c_2}, the upper critical field, in his derivation.

[10]As mentioned, while B_c does not have physical significance for type-II superconductors, however B_c is approximately the geometric mean between B_{c_1} and B_{c_2}. [Tin04]

given by Merrill [Mer68] as

$$B_{c_1} = \frac{\log(\kappa_{GL}) + 0.08}{\sqrt{2}\kappa_{GL}} B_c, \tag{2.25}$$

while another approximation given by Hein [Hei99] is

$$B_{c_1} = \frac{\log(\kappa_{GL}) + 0.497}{\sqrt{2}\kappa_{GL}} B_c. \tag{2.26}$$

A comparison of B_{c_1} obtained through numerics and these approximations are presented in Table 2.1.

κ_{GL}	B_{c_1}/B_c via GL	B_{c_1}/B_c via Hein	B_{c1}/B_c via Merrill
0.3	1.68	—	—
$2^{-1/2}$	1.00	0.150	—
1	0.817	0.351	0.0566
2	0.547	0.421	0.2733
5	0.315	0.298	0.239
10	0.201	0.198	0.169
20	0.124	0.123	0.109
50	0.0622	0.0624	0.0565

Table 2.1: B_{c_1} vs κ_{GL}: Computed and calculated results. The second column is obtained by solving the Ginsburg-Landau equations numerically. [HA63] The third column uses Equation 2.26 and the fourth column uses Equation 2.25. Hein's formulation is more accurate than Merrill's, but is only close to the GL result for $\kappa_{GL} > 5$.

The mixed state where normal conducting vortices interpenetrate a superconducting bulk can only exist in magnetic fields above B_{c_1}, but below the upper critical magnetic field, B_{c_2}, at which state the material enters the normal conducting phase. [Bra95] The thermodynamic critical field and B_{c2} are related according to

$$B_c = \frac{B_{c_2}}{\sqrt{2}\kappa_{GL}}. \tag{2.27}$$

There is one more type of critical field, denoted B_{c_3} that is a surface effect first predicted by Saint-James and de Gennes. [dG65] Because real superconductors

are finite in size, the behaviour near the surfaces must be taken into account. For fields parallel to a superconducting surface, above B_{c_2} superconductivity can nucleate at a metal-insulator interfaces, though the bulk remains normal conducting.

Both theory and experiment have shown that for fields parallel to the surface of the bulk material of magnitude

$$B_{c_3} = 1.695 B_{c_2}, \tag{2.28}$$

a superconducting surface sheath of thickness ξ_{GL} persists, while the bulk is normal conducting. [FSS66] This field dominates a different type of phenomena compared with the other critical fields, because of the depth dependence of the state. For other critical fields, the superconductors have constant depth profiles, either being in the Meissner state or normal conducting state, where as between B_{c_2} and B_{c_3}, there is a transition from the superconducting to normal conducting state as depth increases.

For reference, Table 2.2 presents several values of critical fields for niobium found in the literature.

2.2 The Superheating Field

Critical fields mentioned thus far are in equilibrium conditions. Before a transition takes place, there is an energy cost to nucleate a fluxoid, which leaves open the possibility of a metastable state in which the energetically favorable transition has not occurred due to the activation energy barrier. This barrier vanishes at the superheating field, B_{sh}.

Critical Field	Value at 0 K [mT]	Reference
B_{c_1}	164	[Bah98]
B_{c_1}	174	[FSS66]
B_{c_1}	184	[Fre68]
B_c	180	[CKK$^+$05]
B_c	198	[Fre68]
B_c	200	[FSS66]
B_c	200	[Bah98]
B_{c_2}	390	[Fre68]
B_{c_2}	400	[FSS66]
B_{c_2}	410	[CKK$^+$05]

Table 2.2: Critical magnetic field values of clean niobium, having large mean free path.

Theoretically, surface magnetic fields up to the superheating field should be obtainable in SRF cavities before vortex entry will occur, and lead to excessive RF losses via vortex drag forces and quench the cavity. [PCL$^+$13] The superheating field thus sets the ultimate limit for the maximum surface magnetic field on the surface of an SRF cavity (and thereby limits the maximum achievable electric gradient).

Both Type-I and Type-II superconductors can persist in the Meissner state above their lower critical magnetic fields, B_c and B_{c_1} respectively. The precise relationship of the temperature dependence of B_{sh} is still a field of active experimental and theoretical research. Following the emperically observed behaviour of the critical field, which scales as $(1 - t^2)$ (see Equation 2.23), one can posit the temperature dependence of the superheating field has the following form:

$$B_{sh}(t) = c(\kappa_{GL})B_c(T = 0)\left[1 - t^2\right], \tag{2.29}$$

where $c(\kappa_{GL})$ is a function that may depend on temperature.

The superheating field coefficient, $c(\kappa_{GL})$, can be determined near T_c by solv-

43

ing the Ginsburg-Landau equations for a superconductor taking up the half-space $x > 0$. The free energy density of this system is

$$\delta = \left(\frac{1}{\kappa}\nabla f\right)^2 + \frac{1}{2}\left(1 - f^2\right)^2 + f^2 \mathbf{A}^2 + (\mathbf{B_a} - \nabla \times \mathbf{A})^2, \tag{2.30}$$

where $\mathbf{B_a}$ is the applied magnetic field. [DDBD96] The substitutions $\psi \to f$ and $\kappa_{GL} \to \kappa$ have been made, and the field inside the superconductor is $\mathbf{B} = \nabla \times \mathbf{A}$, where $\mathbf{A} = (0, A(x), 0)$. Minimizing the above equations with respect to f and A yields

$$\frac{1}{\kappa^2}f'' - A^2 f + f - f^3 = 0, \tag{2.31}$$

$$A'' - f^2 q = 0, \tag{2.32}$$

$$B = A', \tag{2.33}$$

where primes denote derivatives with respect to x.

Near T_c, B_{sh} has been determined by solving the above equations numerically. [MS67] A phase diagram of superconductors with critical fields discussed thus far is shown in Figure 2.2.

While there is not a closed form solution for the superheating field as a function of κ_{GL}, in limiting regions there are accurate representations. For small κ_{GL}, the [2,2] Padé approximate is given by

$$c(\kappa_{GL}) \approx \frac{2^{-1/4}}{\sqrt{\kappa_{GL}}} \frac{1 + 5.4447812\kappa_{GL} + 4.2181012\kappa_{GL}^2}{1 + 4.7818686\kappa_{GL} + 1.3655230\kappa_{GL}^2} \tag{2.34}$$

which is accurate to within 1% for $\kappa_{GL} \leq 1$. [DDBD96]

In the region $1 \ll \kappa_{GL}$, the superheating field coefficient (valid near T_c) has
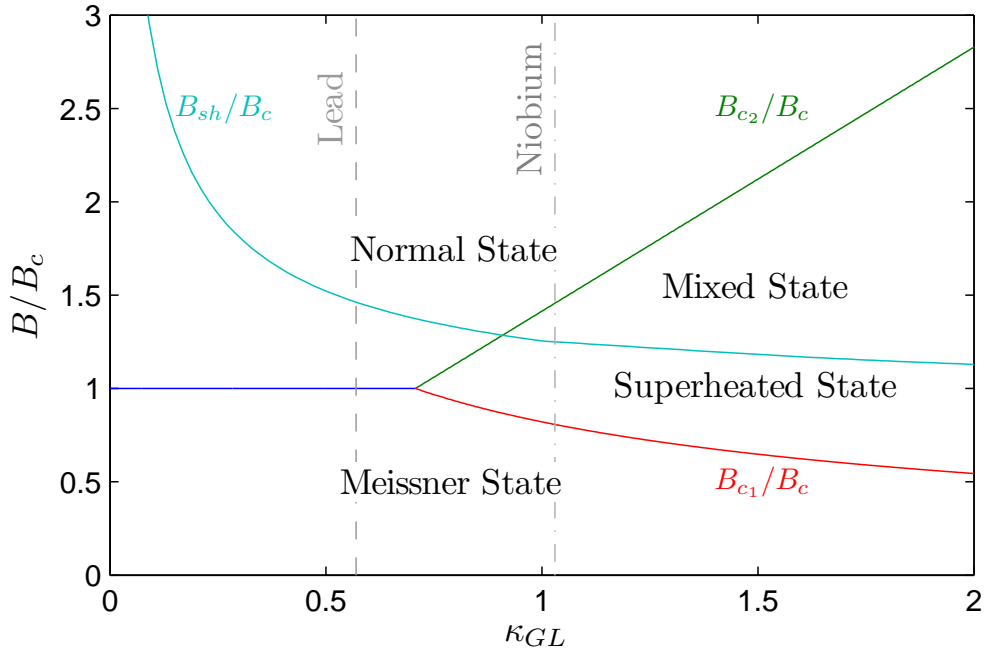
Figure 2.2: Phase diagram of normalized magnetic field vs κ_{GL} for superconductors in the intermediate κ_{GL} range at $T = T_c$. Note that above the Meissner state for both Type-I and Type-II superconductors, a metastable superheating state exists up to the superheating field that, in the equilibrium state, would be either a normal conducting or mixed state. The line showing the superheating field was solved numerically by Matricon and Saint-James. [MS67] Dashed lines mark typical values of κ_{GL} for clean Pb and Nb.

the form

$$c(\kappa_{GL}) \approx \frac{\sqrt{5}}{3} + \frac{8}{9}\left(\frac{2}{15}\right)^{1/4}\frac{z_0^{3/4}}{\sqrt{\kappa_{GL}}} \tag{2.35}$$

$$\approx \frac{\sqrt{5}}{3} + \frac{0.544755}{\sqrt{\kappa_{GL}}} \tag{2.36}$$

where $z_0 \approx 1.018793$ is the smallest number satisfying Ai'$(-z_0) = 0$; [TCS11] Ai(x) is the Airy function satisfying the differential equation $y'' - xy = 0$. [Abr70, p. 446]

The most recent and thorough treatment of Ginsburg-Landau equations solved them over a large range of κ to yield the superheating field, B_{sh}, taking

45

into account one- and two-dimensional perturbations causing the instability of the Meissner phase. [TCS11] This solution yields the correct values of the superheating field, which Equation 2.34 and Equation 2.35 approximate, in their realms of validity, to within a few percent.

The phenomenological approach gives insight into B_{sh} near T_c but to investigate its behaviour over a range of temperatures, a more physically complete theory is required. In general one expects the behavior of the critical fields as a function of temperature to behave qualitatively as illustrated in Figure 2.3. The essential feature of the figure is the demonstration that the typical SRF accelerator operating region is far from the region where GL theory is applicable, calling for a thorough theoretical and experimental treatment of the superheating field and its full temperature dependence.

In principle BCS theory allows a complete understanding of the temperature dependence of the superheating field. In practice, however, currently it is not known how to compute the superheating field within this context, nor even how to correctly formulate the problem. Thus, another simpler theory is necessary to make progress on this front.

To this end, two methods, the Eilenberger equations and Eliashberg theory, allow determination of the superheating field as a function of temperature. Eliashberg theory [GÉ68] requires the full information about the electronic structure of the superconductor and is very difficult to solve. The Eilenberger equations, [Eil68] while also very challenging to solve, have been the subject of significant recent theoretical progress, and thus provide the best theoretical understanding to date. The temperature dependence of the superheating field prefactor, $c(\kappa_{GL}, T)$, was solved in the high-κ limit for strongly type-II supercon-
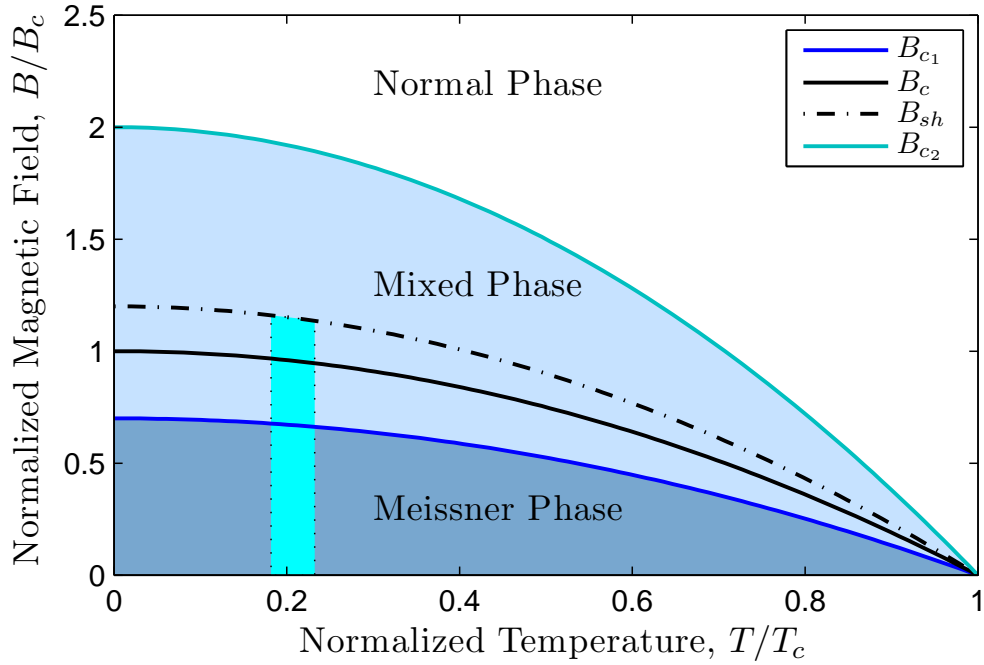
Figure 2.3: Qualitative temperature dependence of critical magnetic fields for a weakly Type-II superconductor. The cyan region enclosed in dotted lines denotes the typical operating temperature region of SRF cavities. Theoretically, surface magnetic fields up to the superheating field should be obtainable in SRF cavities before vortex entry will cause excessive RF losses and quench of the cavity.

ductors, and found that it increases with decreasing temperature, peaking at $T = 0.05T_c$, with an increase of more than 12% of the value at T_c. [CS08]

Niobium is a weakly type-II superconductor, meaning the high-κ results are not necessarily applicable, and a later study was able to solve these equations in the intermediate κ range, initially finding that it diverged from GL theory at low temperatures. [Tra11b] There was speculation that the discrepancy at low temperature was in fact caused by lack of convergence due to the small length scales needed to accurately model the problem, so experimental data was called for to test the initial theoretical results of the temperature dependence of the superheating field of niobium and arrive at a solid understanding of this ultimate

limit for SRF cavities at low temperatures.

2.3 Review of Superheating Field Experiments

Much of the experimental understanding of the superheating field has been through using the RF critical field (B_c^{RF}), or largest RF magnetic field that can be applied to a sample while it remains superconducting, as a proxy for the superheating field. The reason these fields may not be equivalent is that the critical RF field can be limited by material defects, local roughness, surface contamination or pre-quench heating causing superconductivity to quench at prematurely low fields. For a perfect sample, however, one would expect that the critical RF field is limited only by B_{sh} since that is a fundamental property of the material. Above this field, vortices enter the material, and large vortex drag in the RF field will generate excessive heating and leading to quench and phase transition, so fields above the superheating field with superconductor in a mixed state can not be reaching in GHz RF field cavities.

Finnemore et al. measured B_c, B_{c1} and B_{c2} for high purity samples of niobium using magnetization curves and noted that when measuring B_{c1}, "a final, steady-state value of the magnetization is sometimes obtained only after 10 or 20 sample translations. It is as if vibration assists the flux movement into or out of the sample." [FSS66] Though they did not assert that the field values in the Meissner state above the final measured B_{c1} were evidence of superheating, it seems likely. A similar set-up was used by Doll and Graf to measure the superheating in Sn samples [DG67], though their measurements were only over a small temperature range near T_c.

The first measurement confirming that the superheating field of niobium is greater than the thermodynamic critical field, B_c was reported in 1967 by Renard and Rocher [RR67]. They used magnetization curves of very pure Nb cylinders at 4.2K to demonstrate this fact, and set the stage for subsequent measurements.

2.3.1 Superheating measured near T_c as a function of κ

The superheating field near the critical temperature, T_c, has been measured for several Type-I materials, such as In, Sn, and Pb, as well as with a few alloys of SnIn and InBi that are Type-II. [YDM77] For these measurements, a superconducting Nb resonator was used to generate large RF magnetic fields on samples, defining B_c^{RF} as the field at which the resonator Q was degraded by dissipation in the sample. [YDM77]

A plot of the phase diagram along with several measurements of critical RF fields are presented in Figure 2.4.

Yogi did not study the temperature variation of the superheating field, and was only done at temperatures just under T_c, at RF frequencies ranging between 90 and 300 MHz.

Yogi used measurements of several types of materials with κ_{GL} near to T_c to try to determine the type of nucleation of normal conducting sites above B_{sh}. [YDM77] He used his data to compare several models: A "plane nucleation model" into the spherical samples will cause B_{sh} to scale with $(1-t)^{-1/12}$, [SBC70], where as "line nucleation model" would scale with $(1-t)^{-1/6}$, and point nucleation would scale with $(1-t)^{-1/4}$. [YDM77]
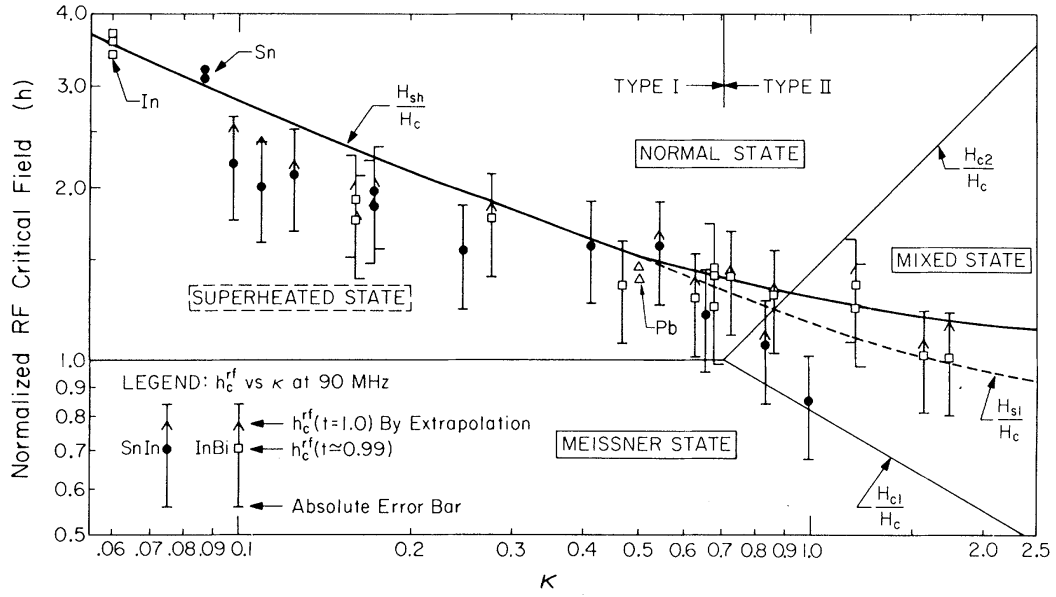
Figure 2.4: Normalized critical fields as a function of the Ginsburg-Landau pa-
rameter κ. Data points are for $h_c^{RF} = H_c^{RF}/H_c$ at $t = T/T_c = 0.99$ for
several metals and alloys ($B_c = \mu_0 H_c$). The dark curve is the calcula-
tion by Matricon and Saint-James of the superheating field. Figure
reproduced from [YDM77].

Yogi put forward the last two models, and his data at $T > 0.8T_c$ correlated
to his vortex line nucleation model, [YDM77] leading to it gaining early pop-
ularity. New theoretical work, [CS08] and experimental measurements shown
in this thesis contrast strongly with these results, definitely showing that the
line nucleation model is not correct. From [CS08], "... [Sethna and Catelani's]
result is in sharp contrast with the commonly used heuristic $H_{sh} \sim B_c/\kappa_{GL}$ of
Yogi et al. [YDM77] This heuristic, termed as the 'line nucleation model,' is not
a linear stability calculation but an energy balance argument that gives a non-
sensical estimate $H_{sh} < H_{c_1}$ for large κ_{GL}. The formulas success in describing
experiments suggests that there may be nucleation mechanisms (perhaps dis-
order mediated) that become more difficult to control in high-κ_{GL} materials but
it should be viewed as an experimental extrapolation, rather than a theoretical
bound, in guiding the exploration of new materials."

50

2.3.2 Temperature dependent measurements of B_{sh}

Measurements of RF critical field in Niobium resonators at 4.2 K were first made by Campisi and Farkas at SLAC. [CF84, Far84] Their pulsed measurements did not reach very large surface magnetic fields, obtaining ~130 mT in a niobium cavity. [Cam87][11]

Subsequent measurements of the RF critical field using accelerating structures were performed by Hays at Cornell. [HP95] In all cases they found that near T_c, the data followed the GL prediction near T_c, but the maximum fields achieved in the fully superconducting state were substantially lower then the phenomenological predictions for the superheating field at low temperatures (see Figure 2.5).

The important question to answer experimentally is if the $B_{sh}(T)$ curve presented in Figure 2.5 is fundamental (as supported by the heuristic "line nucleation model") or if other effects (surface defects or RF heating) prevented B_{sh} from being measured at lower temperatures.

In summary, the question as to the behavior of the critical RF magnetic field of niobium at temperatures far from T_c, such as accelerator environments, remained open. This provided an opportunity to determine the fundamental behavior of superconductors in the intermediate κ_{GL} range and simultaneously provide accelerator science with an upper bound for what is achievable with niobium SRF cavities.

At this point we conclude the historical survey, and present new experimental work in measuring the temperature dependence of the superheating field.

---

[11]Measurements were also made for Nb_3Sn and Pb.
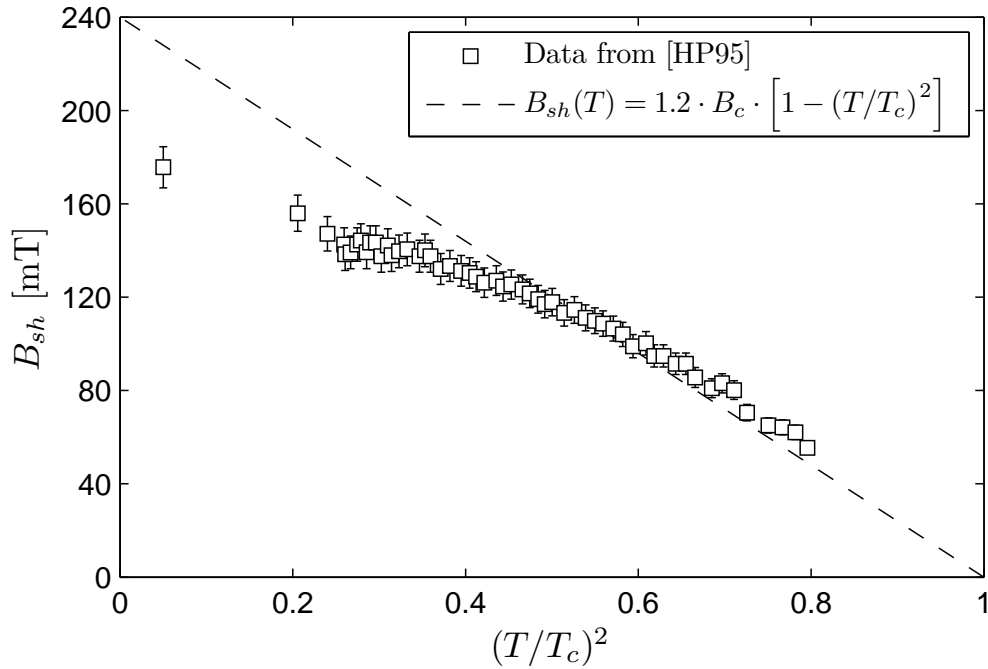
Figure 2.5: Measurements of the temperature dependence of B_{sh} from [HP95]. Witness samples receiving the same purifying heat treatment preparation as the cavity measured with pulsed RF power suggest the cavity has a very large mean free path.

2.4 Measuring Superheating with Pulsed RF

The superheating field of niobium can be measured by using high power pulses to drive a superconducting cavity and noting at what field level the cavity transitions from the superconducting to the normal conducting state [HP95]. The location of the quench origin can be determined by using oscillating superleak detectors [CHPS09]. If the quench is found to be global, then the limiting field is a fundamental property of the material, not simply caused by a localized defect, and suggest that the superheating field was reached. By placing thermometry on the outer cavity wall one can determine the temperature dependence of the superheating field and compare it with predictions.

By calculating the quality factor–a number proportional to how many RF cycles it takes to dissipate the energy stored in a system–during the pulse, one can pinpoint the time the cavity transitioned into the normal conducting state. The surface magnetic fields at the transition time yield the superheating field.

To accurately measure the superheating field, it is essential to determine precisely when the cavity transitions to the normal conducting state. Previous work has shown that a niobium cavity remains at least 90% superconducting as long as the intrinsic quality factor is greater than 2×10^6. [HPR95, HP95][12] It has been shown how to determine the quality factor as a function of time in several publications, [Far84, CF84, HPR95, HP95] but the argument is reproduced here for completeness.

A cavity with a resonant frequency, ω, driven on resonance by a single input coupler at power, P_f, reflects some power, P_r, and has some power coupled into the cavity, P_{in}. Part of the incident power wave increases the field in the cavity, U, and part of the power is dissipated in the cavity walls, $\omega U / Q_0$, (see Equation 1.9) where Q_0 is the intrinsic quality factor of the cavity. Conservation of energy gives:

$$P_f = P_r + P_{in}, \tag{2.37}$$

$$P_{in} = \frac{\omega U}{Q_0} + \frac{dU}{dt}, \tag{2.38}$$

where t is the time variable.

The reflected power is not a measured quantity in our experiment, so an-

---

[12]For high RRR material (RRR~300), normal conducting Q_0 at cryogenic temperatures are approximately 2×10^5. Assuming 20% of the material is normal conducting (90% has $Q_0 \gg 10^8$), the overall Q_0 will be 2×10^6. The quality factor drops very quickly once the material begins to become normal conducting (see Figure 2.6), so the exact value used here for Q_0 to determine the loss of superconductivity is not important, which is to say an essentially equivalent critical field would be measured with a different Q_0 threshold criteria such as 10^7 or 10^6. Thus the exact Q value used for the superconducting/normal conducting transition does not effect the results.

other expression relating P_r and P_f is needed. To get this additional relation, the argument made in Padamsee et al., Chap. 8 is followed. [PKH98].

Incident power, P_{in}, on the cavity is simply the difference between the forward P_f and reflected P_r waves. Supposing the cavity is driven on resonance with a coupler having an external quality factor Q_{ext}, the power that is absorbed by the cavity is given by

$$
P_{in} = 4 \frac{\dfrac{P_f}{Q_{ext}} \left(\dfrac{1}{Q_0} + \dfrac{1}{\omega_0 U} \dfrac{dU}{dt} \right)}{\left(\dfrac{1}{Q_{ext}} + \dfrac{1}{Q_0} + \dfrac{1}{\omega_0 U} \dfrac{dU}{dt} \right)^2},
\tag{2.39}
$$

which is obtained from considering the oscillator to have a complex frequency, with the imaginary part providing damping of the system. [PKH98, Eq. 8.34]

Using Equation 2.37 and Equation 2.38 in conjunction with Equation 2.39 results in

$$
P_r = P_f - P_{in} = P_f - \sqrt{\frac{4 P_f \omega_0 U}{Q_e}} + \frac{\omega_o U}{Q_{ext}},
\tag{2.40}
$$

and factoring gives the result:

$$
P_r = \left(\sqrt{P_f} - \sqrt{\frac{\omega_0 U}{Q_{ext}}} \right)^2.
\tag{2.41}
$$

This relation between P_r and P_f allows Q_0 to be expressed as a function of measurable quantities.

Using P_r from Eq. 2.41 in Eq. 2.37 yields the expression

$$
\frac{\omega U}{Q_0} = 2 \sqrt{\frac{\omega U P_f}{Q_{ext}}} - \frac{dU}{dt} - \frac{\omega U}{Q_{ext}}
\tag{2.42}
$$

54

The final expression relating Q_0 and time can be obtained by using the identity

$$\frac{d\sqrt{U}}{dt} = \frac{1}{2\sqrt{U}}\frac{dU}{dt},\tag{2.43}$$

to yield

$$\frac{1}{Q_0} = \frac{2}{\omega\sqrt{U}}\left(\sqrt{\frac{\omega P_f}{Q_{ext}}} - \frac{d\sqrt{U}}{dt}\right) - \frac{1}{Q_{ext}}\tag{2.44}$$

Equation 2.44 allows one to calculate Q_0 as a function of time from measurements of P_f and U. Finding the time when the quality factor of the cavity falls bellow 2×10^6 pinpoints when the cavity transitions into the normal conducting state. [HPR95]

Two examples of the application of these equations to pulsed RF measurements are presented in Figure 2.6 and Figure 2.7.

As a comparison between the two RF measurements shows, the superconducting to normal conducting transition field is not necessarily the maximum surface field measured. This is because under certain conditions it is still possible to load the resonator with more power than it dissipates, while it is in the normal conducting state. Therefore, Equation 2.44 is necessary to determine the precise transition time.

2.4.1 Experimental Methods to Distinguish B_{sh} from $B_{max,sc}^{RF}$

The superheating magnetic field is measured with a niobium resonator driven by a klystron capable of supplying 1.5 MW pulses with durations between 50-500 μs. These short, high power pulses are intended to minimize cavity heating as the electro-magnetic fields increase, so the temperature across the cavity wall is small.
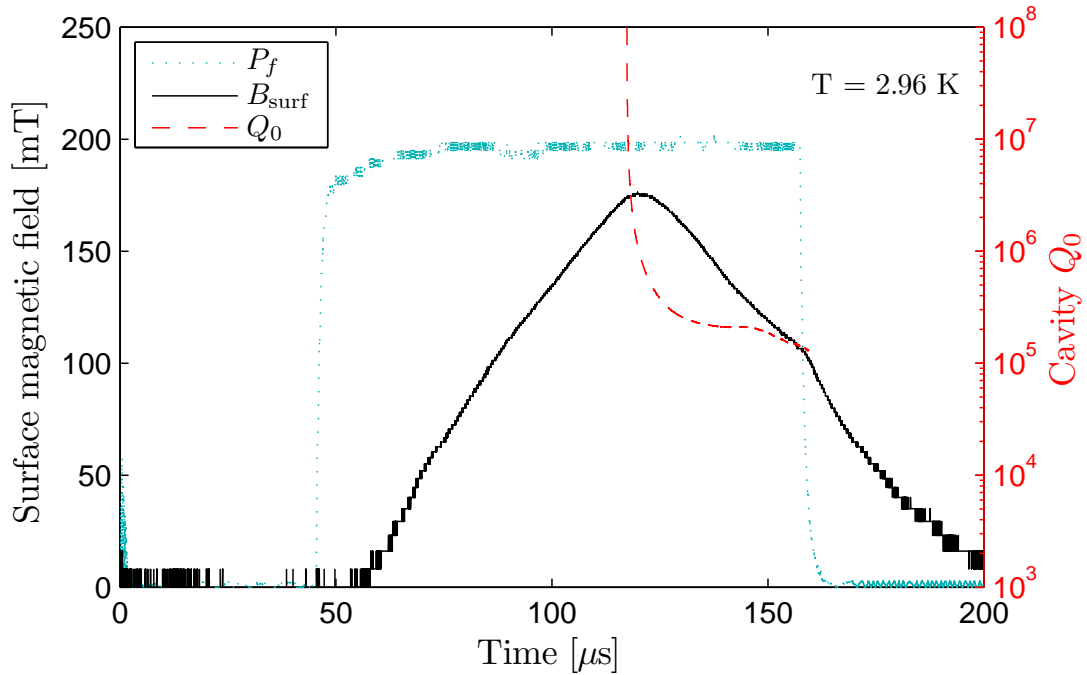
Figure 2.6: Superconducting to normal conducting transition field measurement at 2.96 K. The cavity's Q_0 shows the cavity enters the normal conducting state near the maximal measured surface field. Power supplied to the cavity by the klystron, P_f, is plotted in arbitrary units, but has peak magnitude of ~1 MW.

When the magnetic field on the cavity surface reaches the so-called quench field, $B^{RF}_{max,sc}$, the superconductor undergoes a phase transition into the normal conducting state.[13] There is no guarantee that this transition is initiated by exceeding the fundamental limitation of the superconductor, as many phenomena can reduce the peak performance of superconducting material. One hint as to the nature of the break down of superconductivity is the quench location.

If the break down down of superconductivity occurs in a localized region, it is most likely due to contamination on the surface or a material defect. If the quench occurs over a large region, it is likely that a fundamental limitation of the superconductor has been reached, so that $B^{RF}_{max,sc} = B_{sh}$.

---

[13]This transition dissipates a great deal of energy, and is often referred to as a quench.
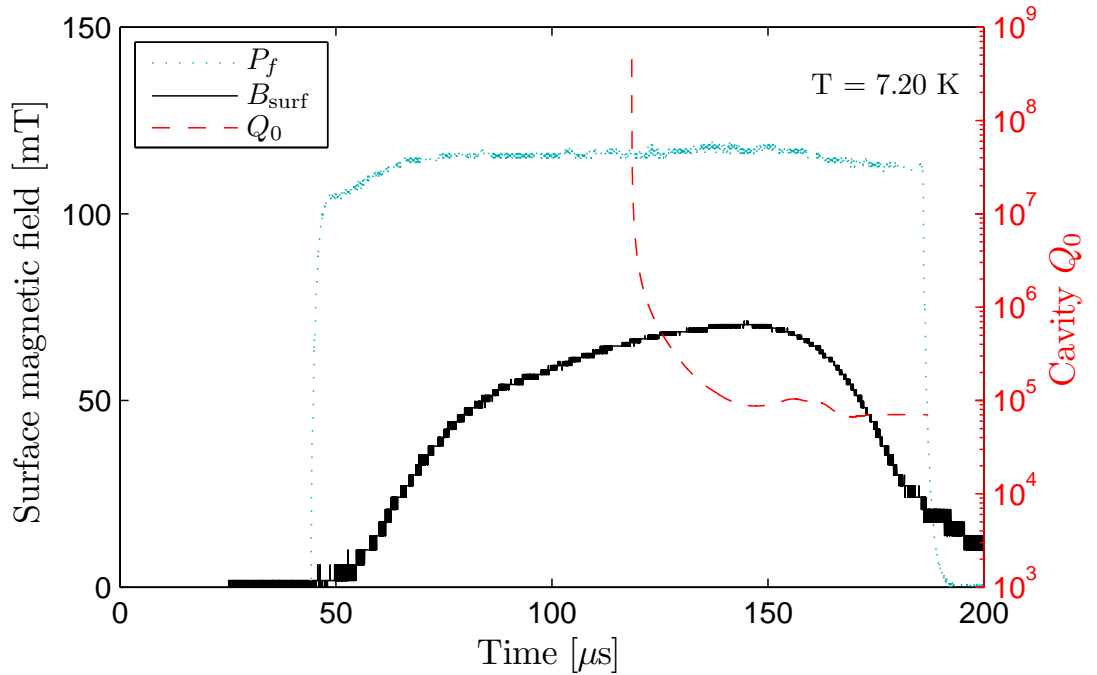
Figure 2.7: Superconducting to normal conducting transition field measurement at 7.20 K. The cavity's Q_0 shows the cavity enters the normal conducting state well below the maximum measured surface field. Power supplied to the cavity by the klystron, P_f, is plotted in arbitrary units, but has peak magnitude of ~1 MW.

The quench location can be determined by the use of oscillating superleak transducers (OSTs). [CHPS09] These devices are essentially capacitors that detect second sound waves in superfluid helium. Just as in superconductors, superfluids are bosonic condensates which at finite temperatures below a critical temperature (T_c = 2.172 for ^{4}He [DB98]) consists of both superfluid and normal fluid components. [Tis38] Figure 2.8 shows the temperature dependence of the superfluid fraction near the lambda transition, named for the characteristic shape caused by the discontinuity of specific heat at T_c. [KK35]

In addition to the first sound wave (velocity $\approx$ 230 m/s), [LF99] which is a longitudinal pressure-density wave, superfluid helium can support a second sound wave wherein temperature and entropy are conveyed through the fluid.
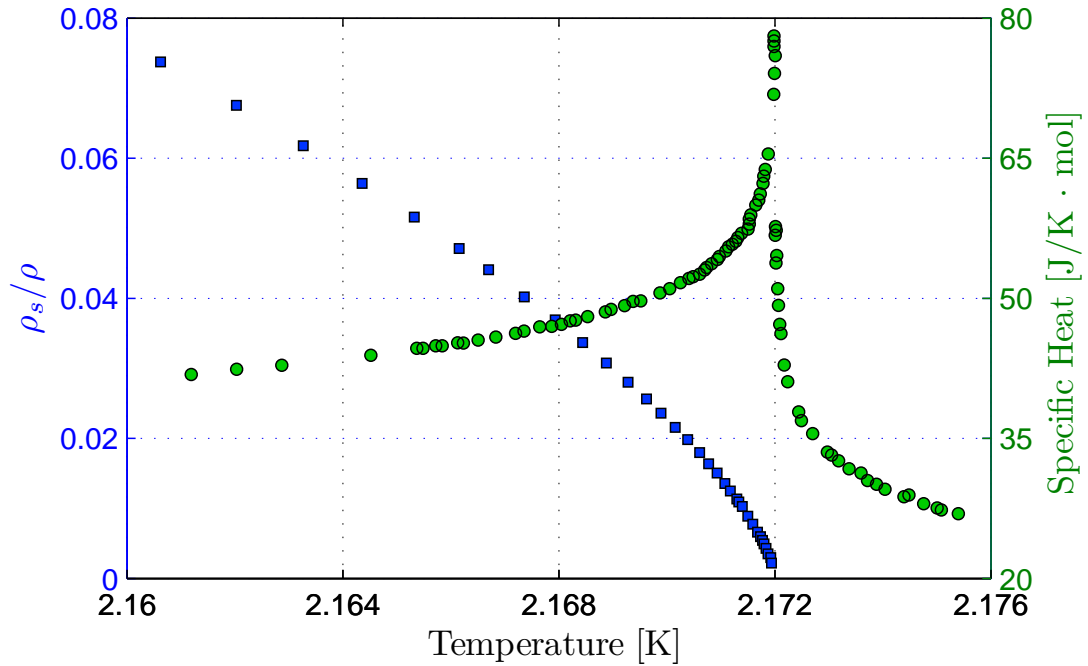
Figure 2.8: Superfluid fraction (□) and specific heat (○) of ^{4}He vs temperature.

[LFF47] The velocity of the second sound wave is temperature dependent (see Figure 2.9), but does not vary much in the region used for SRF research.

An OST is essentially a capacitor with a semipermeable membrane on one side that allows the superfluid component of helium to pass into the capacitor while screening out the normal fluid component. The change in capacitance when the 2nd sound wave arrives at the OST membrane can be measured on an oscilloscope. By measuring the time delay between the dissipation of cavity stored energy (quench) and the ringing of OSTs, trilateration can be performed to determine the original quench location at a certain region on the cavity wall.
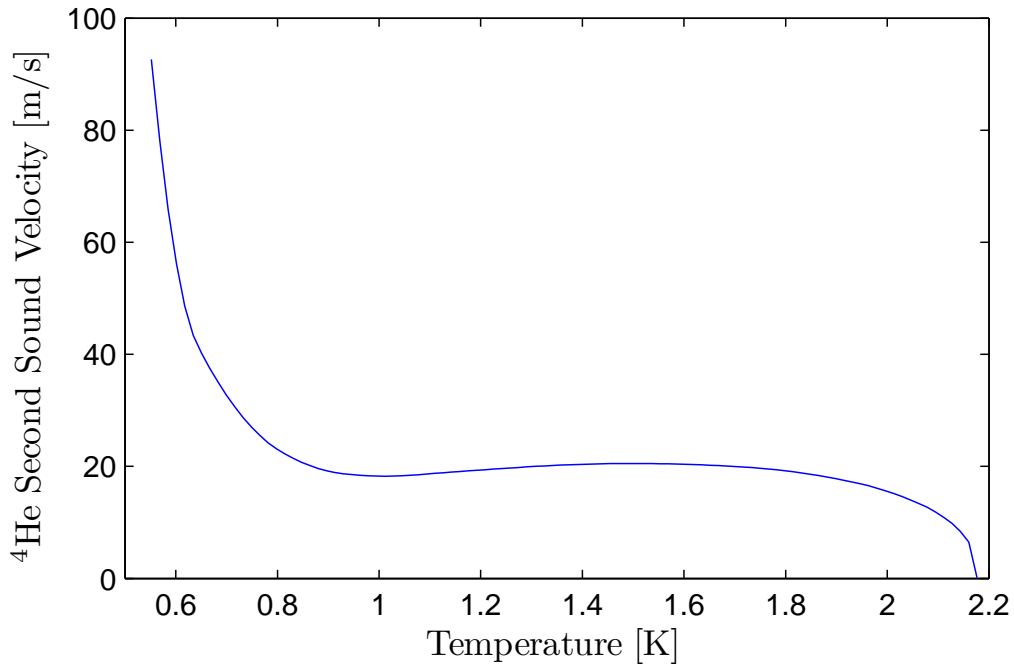
Figure 2.9: Velocity of Second Sound wave in ^{4}He from knots and coefficients of a spline fit given by Donnely. [DB98] In the temperature region used by SRF cavities (1.4 - 2.0 K) the second sound velocity is roughly constant.

2.4.2 RF measurement apparatus

A schematic of the test stand used to couple the RF power from the klystron into the cavity is shown in Figure 2.10. The antenna length controls the coupling to the cavity, and should be chosen to minimize the time needed to reach a given surface magnetic field.

The minimal time required to reach a given surface field level is calculated as follows: In equilibrium, the energy stored in the cavity, U ($\propto E^2 \propto B^2$), at a given input power level, P_f, is

$$U = 4\frac{P_f\omega}{Q_{ext}}\tau_L^2,\tag{2.45}$$

where ω is the angular frequency of the RF wave and the loaded time constant is

59
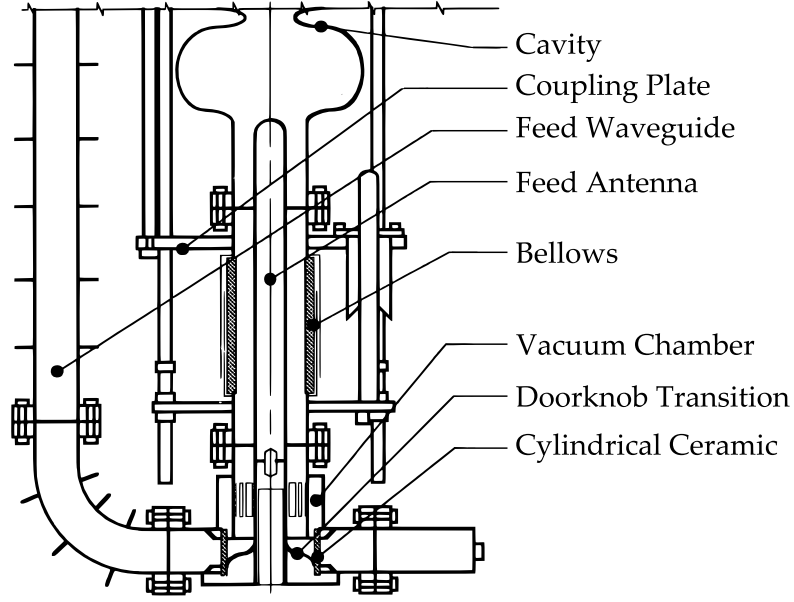
Figure 2.10: Schematic of high pulsed power insert, reproduced from [PKH98]. The insert is placed into a dewar, allowing the cavity's properties to be measured at cryogenic temperatures.

$\tau_L \equiv Q_L/\omega$ where Q_L is related to the coupler's quality factor, Q_{ext}, and intrinsic quality factor, Q_0, via

$$\frac{1}{Q_L} = \frac{1}{Q_{ext}} + \frac{1}{Q_0}. \tag{2.46}$$

During filling, the change in field is proportional to the difference of the current level, and it's equilibrium value, which is described by the relationship

$$\sqrt{U(t)} = \sqrt{U_0}\left[1 - \exp\left(-\frac{t}{2\tau_L}\right)\right]. \tag{2.47}$$

Eliminating τ_L and Q_L yields the time needed to reach an energy $U < U_0$:

$$t = -\frac{2Q_{ext}}{\omega}\left(1 + \frac{Q_{ext}}{Q_0}\right)^{-1}\log\left[1 - \sqrt{\left(1 - \frac{Q_{ext}}{Q_0}\right)^2 \frac{\omega U}{Q_{ext}P_f}}\right]. \tag{2.48}$$

The time needed to reach a given stored energy in the cavity as a function of antenna coupling is presented in Figure 2.11, showing that pulsed power measurements should be performed with Q_{ext} of 10^5–10^6.

60
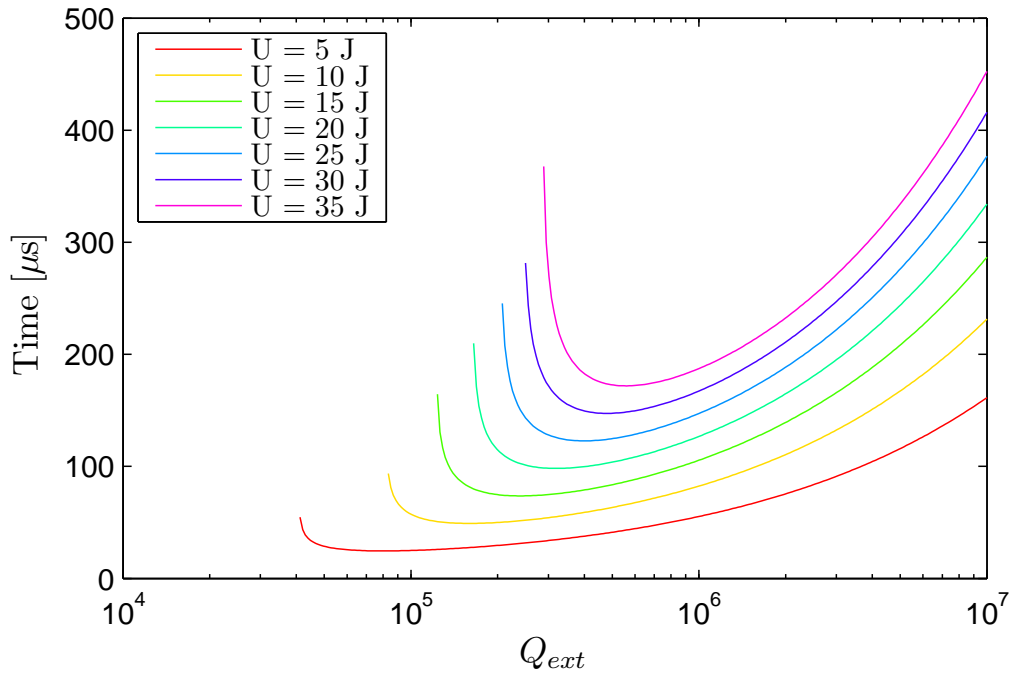
Figure 2.11: Time needed to store a given amount of energy in the cavity vs antenna coupling. Equation 2.48 was used with $\omega = 2\pi \cdot 1.3$ GHz, $Q_0 = 10^{10}$ and $P_f = 1$ MW. For comparison, in the cavity tested, LR1-3, 5 J $\approx$ 100 mT and 35 J $\approx$ 200 mT surface field.

Temperature Measurement

Temperatures of the cavity's RF surface is determined by Cernox thermometers on the outside wall. For short RF pulses, and high enough Q_0, the temperature gradient across the wall is very small. In addition, cooling grooves were milled on the outside of the cavity to reduce the wall thickness and increase the heat transfer to the liquid helium bath. For $Q_0 \sim 10^9$, the temperature difference between the inner and outer wall is ~0.2 K. [VCL09] However, if Q_0 drops to low values, the thermal gradient across the wall can become significant, preventing B_{sh} from being reached at the bath temperature since the inner wall is at a higher temperature.

2.4.3 Material Characterization via Q_0 vs Temperature

It is desirable to characterize the material properties of the Nb surface to enable correlation to superheating field results. This can be carried out by measuring the surface resistivity of the superconductor as a function of temperature.

Holding the accelerating gradient constant, by measuring the intrinsic quality factor, Q_0, as a function of temperature, the surface resistivity, R_s can be found by using the relationship in Equation 1.14, $R_s = G/Q_0$, where G is the geometry factor of the cavity. This method requires the accelerating gradient to be large enough to be out of the low field Q-slope region but not so large that medium- or high-field Q-slope artificially reduces the quality factor.

In general, the surface resistance is the sum of two contributions: the BCS resistance, which is temperature and frequency dependent, and the residual resistance, which is temperature independent. After obtaining the surface resistance, the material properties can be found by using a program SRIMP [Hal70b] which yields the AC surface resistivity of a superconductor from parameters using BCS theory. Further information about extracting superconducting properties from R_s vs temperature data is presented in Appendix C.

2.5 New Measurements of B_{sh}

A photograph of the niobium cavity, LR1-3, used in superheating field measurements is shown in Figure 2.12. The cavity was outfitted with 8 OSTs to act as quench detection and three Cernox temperature sensors attached to the outside surface of the cavity.
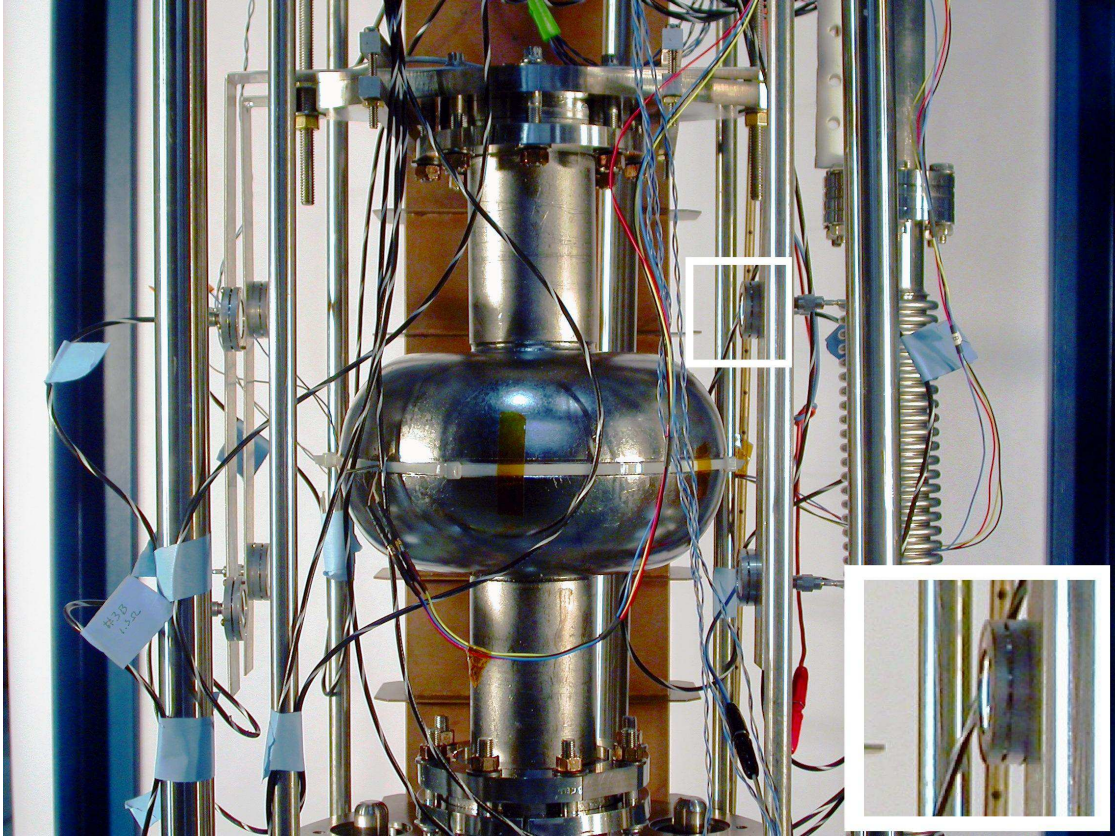
Figure 2.12: Photograph of 1.3 GHz cavity LR1-3 on pulsed power insert. The copper waveguide in the background can transport 1.5 MW RF pulses to the insert. There are eight OSTs forming the corners of a cube around the cavity. One OST is highlighted with a white box and an enlargement is shown in the lower right corner.

2.5.1 Material Preparation

Two different surface preparations of the cavity LR1-3 were used to probe the temperature dependence of the superheating field of niobium for different mean free paths. This cavity was chosen to explore B_{sh}, since it had previously achieved very high gradients. [GEPS07]

Preparation A consisted of out-gassing the cavity at 800°C for two hours, vertically electropolishing the cavity, high pressure rinsing it for two hours, and then cleanly assembling it on a waveguide test stand. Finally it was evacuated,

and baked at 120°C for 48 hours, a process known to mitigate the effects of high field Q-slope, [EP06] and decrease the electron mean free path of the RF surface layer.

Cavity preparation B consisted of out-gassing the cavity at 800°C for two hours, performing a 15 μm electropolish, high pressure rinsing the cavity for two hours then cleanly assembling the cavity. Preparation B did not include a 120°C bake. For each preparation, the cavity was tested under RF conditions to determine material properties and subsequently tested under high pulsed power to measure the temperature dependence of the superheating field.
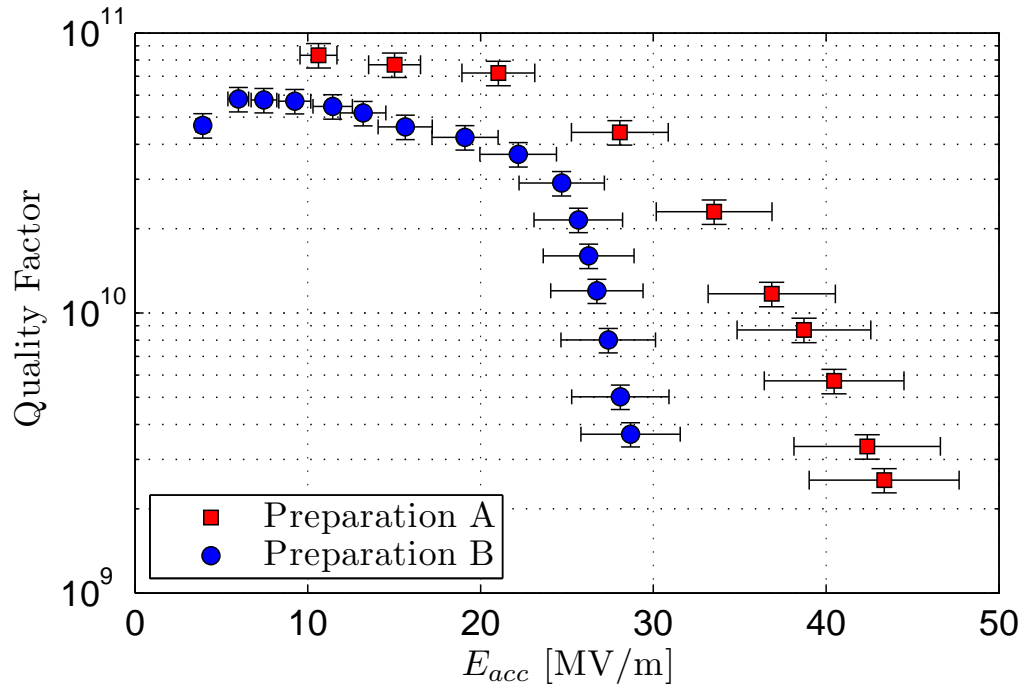
Figure 2.13: Quality factor versus accelerating gradient for different surface preparation methods, taken at (1.65 ± 0.05) K. Note that the 120°C treatment has the effect of increasing the quality factor at high gradients compared to the case without the 48 hour bake.

2.5.2   Continuous Wave Measurements

The cavity's properties were first tested in continuous wave (CW) mode. The intrinsic quality factor, Q_0, in both cases as a function of accelerating gradient is shown in Figure 2.13. Both measurements demonstrate a strong decrease in Q_0 (i.e. increase in surface resistivity) at high fields, though the cavity with Preparation A has a much higher quality factor above 30 MV/m. Neither measurement was quench limited, but limited by the power available from the RF amplifier driving the cavity.

The measurement of the quality factor vs temperature yielded the surface resistance plots presented in Figure 2.14 via the use of Equation 1.14. For LR1-3, $G = 283.1\ \Omega$.

The R_s versus temperature data was used to extract material surface properties using SRIMP, as discussed in Appendix C. The critical temperature was determined from pulsed superheating field measurements (presented in the next section) to reduce the number of free parameters in the data fit. Material properties consistent with both measurements are presented in Table 2.3.

Using the material properties to estimate the GL parameter, κ_{GL}, for Preparation A, $\kappa_{GL} = 3.52 \pm 1.56$, whereas for Preparation B, $\kappa_{GL} = 1.25 \pm 0.17$. Solving GL theory for the superheating field near T_c yields $c(\kappa_{GL}) = 1.04 \pm 0.06$ for Preparation A and $c(\kappa_{GL}) = 1.22 \pm 0.02$ for Preparation B.[14]

The results are summarized in Table 2.3, demonstrating that the properties of superconducting surface depends strongly on the material preparation. Prepa-

---

[14]The superheating field coefficient $c(\kappa_{GL})$ was calculated using interpolated values from 1D and 2D stability analyses. [Tra11a]
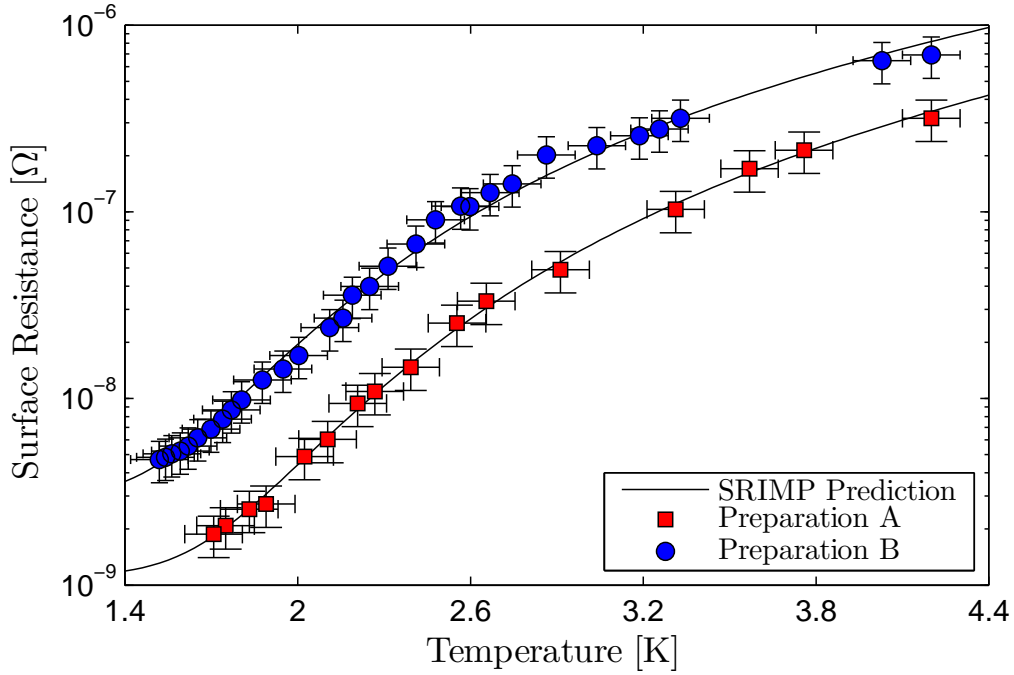
Figure 2.14: Surface resistance versus temperature for the two different surface preparation methods. The black lines are the result of the BCS prediction generated by parameters presented in Table 2.3. The superheating field coefficient was interpolated from 1D and 2D stability analyses performed by M. Transtrum. [Tra11a]

ration A yielded a surface with larger κ, which is to say that it is more strongly Type-II. Preparation B, however resulted in a surface with smaller κ, and the Niobium is closer to Type-I in this case.

A few comments about the material properties obtained by these fits should be mentioned: The energy gap, $2\Delta(0)/k_B$, of the niobium treated by Preparation A is larger than the reported value of 3.93 for pure niobium. [PKH98] The surface preparation, especially the baking process, has been shown to effect the energy gap, [Cio07] which could explain the difference in energy gap. The critical temperature of the sample significantly differs from the critical temperature of pure niobium, 9.22 K, but is consistent with the diffusion of oxygen into the superconductor, due to the low temperature bake. Assuming the degradation

SRIMP Surface Resistance Parameters			
Input Parameter	Preparation A	Preparation B	Unit
Frequency	1294.5	1294.5	MHz
T_c	8.8	9.2	K
λ_L	39.00	39.00	nm
ξ_0	38.00	38.00	nm
Fit Parameter			
E_g	4.384 ± 0.052	3.732 ± 0.044	—
ℓ_{tr}	12.04 ± 7.26	117.81 ± 71.06	nm
R_0	1.1 ± 0.1	3.0 ± 0.3	nΩ
Calculated Result			
λ_{tr}	2.784 ± 1.680	0.284 ± 0.172	—
$R(\lambda_{tr})$	1.057 ± 0.455	1.009 ± 0.130	—
λ_{GL}	52.17 ± 11.579	31.11 ± 2.079	nm
ξ_{GL}	14.83 ± 0.10	24.88 ± 0.06	nm
κ_{GL}	3.52 ± 1.56	1.25 ± 0.17	—
$c(\kappa_{GL})$	1.04 ± 0.06	1.22 ± 0.02	—

Table 2.3: Material properties used to fit surface resistance vs temperature data presented in Figure 2.14, with E_g, ℓ_{tr} and R_0 as fit parameters. The critical temperature was determined from superheating field measurements. The large uncertainty in ℓ_{tr} does not significantly effect $c(\kappa_{GL})$.

of RRR of the material is due to oxygen impurities in the RF surface layer, one calculates that the surface niobium contains 0.08wt% oxygen. Using data from De Sorbo, [DeS63] the critical temperature of the niobium is expected to be reduced to (8.98 ± 0.02) K, consistent with the measurement above.

Preparation B resulted in material properties consistent with what is expected from pure Niobium. This suggests that there is not significant oxygen contamination, which also agrees with the much larger electron mean free path in this sample.

After measuring the quality factor as a function of temperature, pulsed measurements of the superheating field were carried out.

2.5.3 Pulsed Measurements

Pulsed RF measurements of $B^R_{max,sc}F$ were carried out as described in subsection 2.4.2. Results of $B^R_{max,sc}F$ for both surface preparations are presented in Figure 2.15 and Figure 2.16.
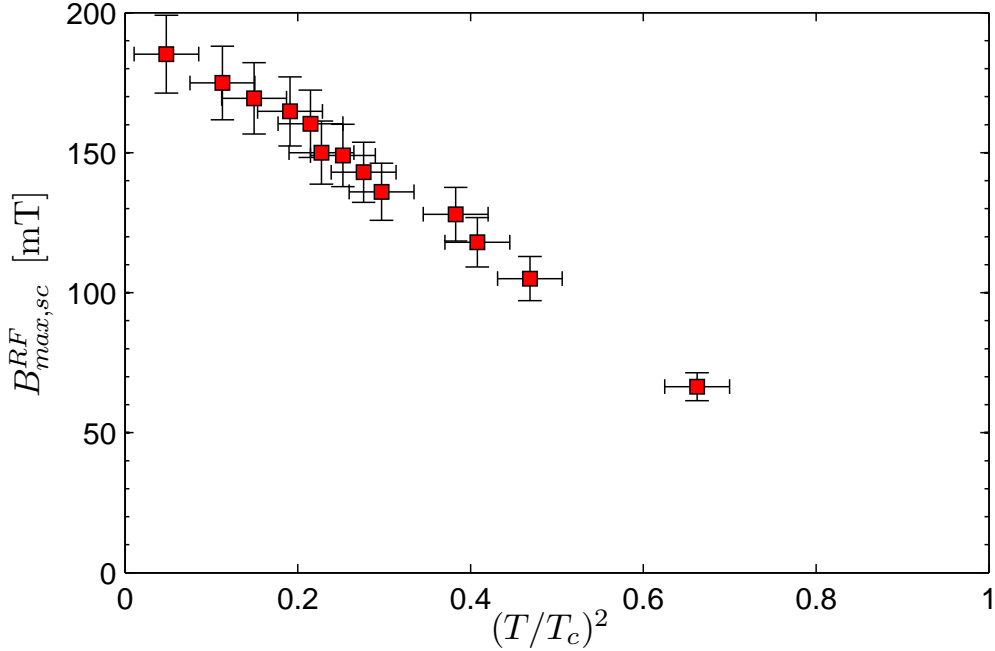
Figure 2.15: Measurements of the superconducting to normal conducting transition magnetic field of LR1-3 after receiving preparation A.

During the cavity test with preparation A, OST measurements showed that the quench occurred over the entire cavity surface at the same time. The global nature of the quench demonstrates $B^R_{max,sc}F$ was not limited by a localized surface defect. This means that neither point defect heating, field emission nor contamination was the source of field limitation, which suggests that the transition field measured was fundamental in nature, i.e. equal to the superheating field B_{sh}.

Measurements of the cavity with Preparation B showed the RF transition
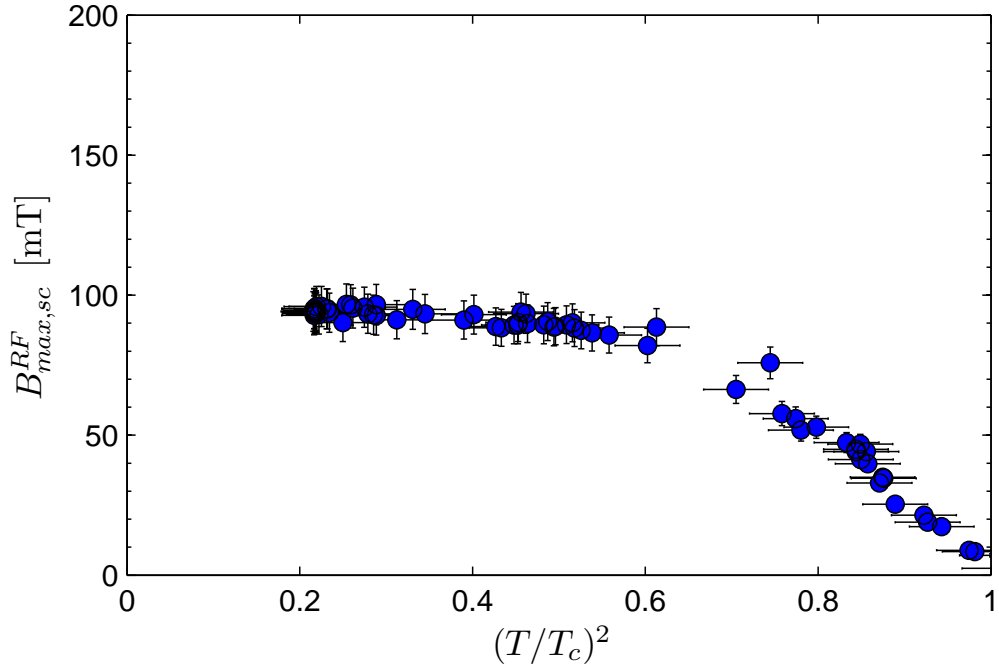
Figure 2.16: Measurements of the superconducting to normal conducting transition magnetic field of LR1-3 after receiving preparation B.

field plateau well above temperatures at which helium is superfluid and OSTs can determine quench origin. The steep quality factor deterioration at high fields, and associated heating of the inner cavity wall, likely prevented the superheating field from being reached at any except the highest temperatures.

Fitting the $B^{RF}_{max,sc}$ vs t^2 data near $t = 1$ yields two important pieces of information. First, since the superheating field vanishes at the material's critical temperature, the horizontal intercept yields a measurement of T_c. Secondly, near T_c, where the phenomenological model applies, the slope of the graph gives a direct measurement of $c(\kappa_{GL})$, independent of the material property calculations extracted from R_s vs T measurements and theoretical models.

A linear fit of $B^{RF}_{max,sc}$ vs $(T/T_c)^2$ was performed on each pulsed data set near

T_c, where $B_{sh} \approx B_{max,sc}^{RF}$. For preparation A:

$$\frac{B_{sh}(T)}{B_c(T=0)} = (0.99 \pm 0.03) \cdot \left[1 - (1.08 \pm 0.06)\left(\frac{T}{T_c}\right)^2 \right], \qquad (2.49)$$

whereas for Preparation B:

$$\frac{B_{sh}(T)}{B_c(T=0)} = (1.23 \pm 0.03) \cdot \left[1 - (1.01 \pm 0.04)\left(\frac{T}{T_c}\right)^2 \right], \qquad (2.50)$$

and in both equations $B_c(T=0) = 200$ mT for niobium. [FSS66] From the above fits, κ_{GL} can be extracted from $c(\kappa_{GL})$ using data from the phenomenological model. The results of this measurement are summarized in Table 2.4. It is important to note that both results are consistent with the result of the material property determination by BCS theory.

Superheating Field Measurements			
Parameter	Preparation A	Preparation B	Unit
T_c	8.8 ± 0.2	9.2 ± 0.2	K
$c(\kappa_{GL})$	1.04 ± 0.01	1.28 ± 0.06	–
κ_{GL}	3.49 ± 0.16	0.92 ± 0.15	–

Table 2.4: Properties extracted from $B_{max,sc}^{RF}$ vs t^2 measurements for two surface preparations. Interpolation of superheating field vs κ_{GL} data was used to extract κ_{GL} from the measured values of $c(\kappa_{GL})$.

The superheating field measurements for both surface preparations are plotted in Figure 2.17. Overlayed are predictions from the Ginsburg-Landau theory, for the material parameters extracted from the CW measurements, including the fit uncertainty.

As expected, measurements near T_c and the prediction by GL theory agree very well. The data for Preparation A shows the full temperature dependence of B_{sh}, something which which has not been measured before, and is a major achievement. If heating can be mitigated in the case of Preparation B, similar results may hold, as will be explored in subsection 2.5.5. This new information

that can be compared with the latest theoretical work calculating the tempera-ture dependence of B_{sh} for niobium (see subsection 2.5.4).
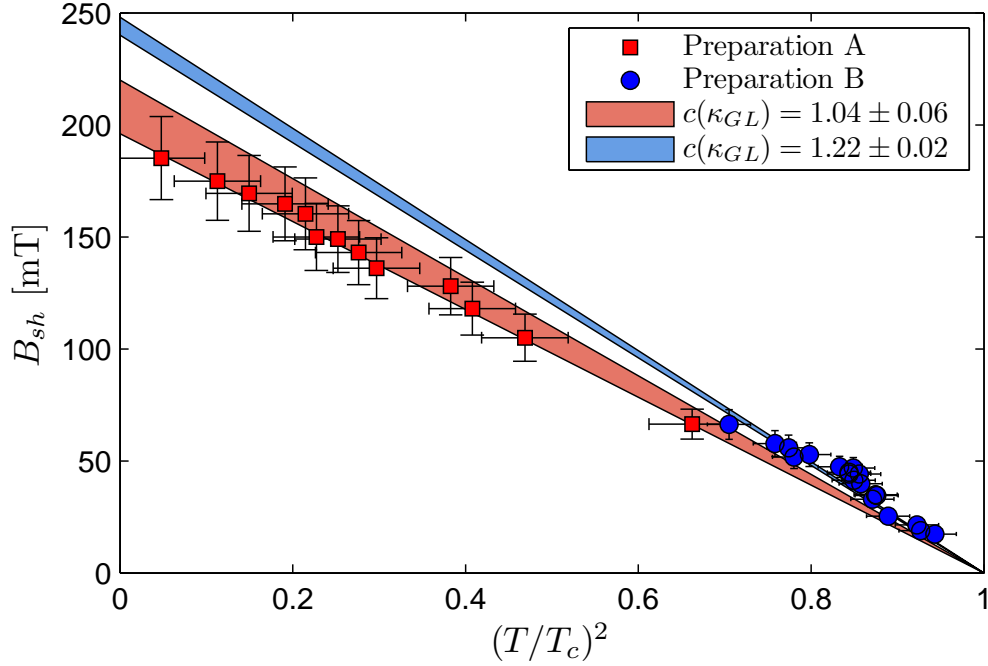
Figure 2.17: B_{sh} vs $(T/T_c)^2$ for both surface preparations. The cones present $c(\kappa_{GL}) \cdot B_c$, with experimental uncertainty, as calculated within GL theory for the material properties presented in Table 2.3.

These results show that surfaces treated by the standard high gradient cavity preparation strongly influence the superheating field. The mechanism in this study is related to the change in electron mean free path due to scattering sites in the RF layer, but in principle other effects could also change κ_{GL}. Specific to this case, the 120°C bake appears to make Nb more strongly Type-II and thereby reduce H_{sh}. This leads naturally to ask if an alternative to the 120°C bake that eliminates high field Q-slope while not reducing the material's mean free path can be developed.

2.5.4 Comparison with the Latest Theoretical Work

Transtrum et al. solved the temperature dependent Eilenberger equations were solved at moderate temperatures for material parameters consistent with preparation A. [Tra11a] A plot comparing the superheating field measurements and the Eilenberger prediction is presented in Figure 2.18. The accuracy of modelling the Fermi surface of niobium can be increased by including a higher the number of Matsubara frequencies (analogous to spherical harmonics) used in the calculation.
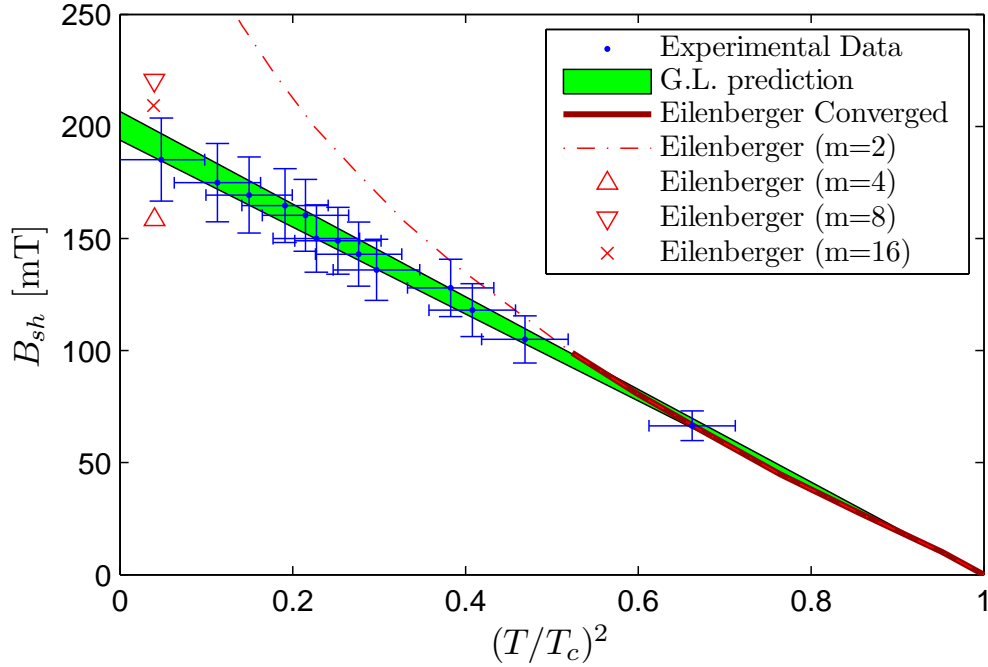
Figure 2.18: Comparison of the superheating field results of the cavity receiving Preparation A and the results of Eilenberger theory for $\kappa_{GL} = 3.5$ computed with a varying number of Matsubara frequencies, m. [Tra11b]

Alternating values of the Eilenberger calculation for increasing m at $t^2 = 0.05$ suggests that at this temperature, the superheating field for a $\kappa = 3.5$ material lies somewhere between 210-220 mT, just outside the uncertainty of pulsed RF

measurements.

Notice that for the $\kappa_{GL} \sim 3.5$ material, both the experimental data as well as Eilenberger theory show that B_{sh} vs t^2 is well described (within 7%) by a $(1 - t^2)$ temperature dependence, i.e. $c(\kappa_{GL} = 3.5)$ approximately temperature independent, down to $t \sim 0.2$.

2.5.5   DC Superheating Field Measurements

The previous section established that the temperature dependence of the superheating field of $\kappa_{GL} \sim 3.5$ niobium is consistent with the Ginsburg-Landau result near T_c. The main challenge with measuring B_{sh} for the case of Preparation B is substantial RF heating of the inner cavity wall by the high fields, exacerbated by the high field Q-slope. To mitigate this effect, this section presents a new method to measure the temperature dependence of a superheating field of an accelerator cavity in a way that is not susceptible to RF heating and small surface defects. This new technique utilizes DC fields to transition from the superconducting to normal conducting state and uses low level RF fields to probe this transition.

Experimental Apparatus

For the superheating field measurements in DC fields, LR1-3 received an additional 15-μm electropolish with the intention of obtaining $\kappa_{GL} \sim 1$ to yield a surface with a large superheating field.

DC critical field measurements of the re-entrant cavity LR1-3 used a solenoid to generate an increasing strength DC magnetic field at a certain location near

the cell's equator while maintaining a low RF field inside the cavity to observe at what field the cavity quenches, or transitions to the normal conducting state.

The solenoid has an inner coil diameter of 20 mm, an outer diameter of 33 mm and is 50 mm long. The wire used to construct the solenoid contains 54 superconducting NbTi filaments in a copper matrix (wire diameter is 0.45 mm), which is coated in FormVar. The solenoid has 1760 windings, giving 35200 turns/meter, and has a measured inductance of 2.28 H. A picture of the experimental setup is presented in Figure 2.19.
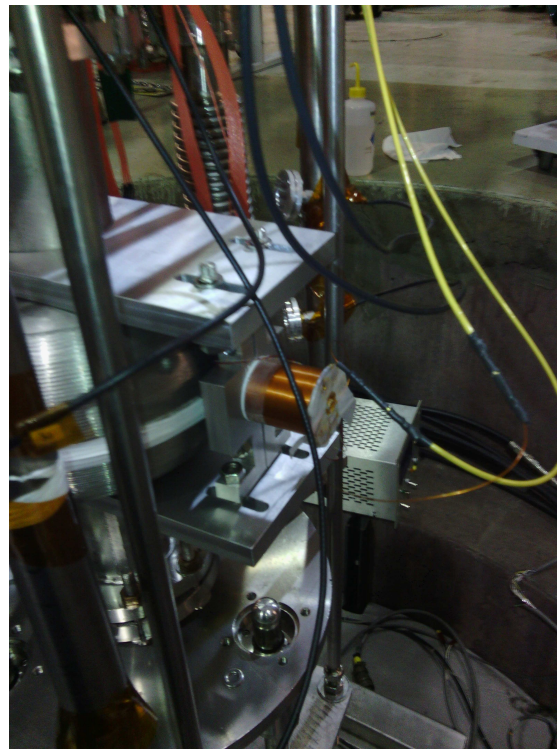
Figure 2.19: Solenoid used to generate the external magnetic field for DC super-heating field measurements installed outside LR1-3. A Hall probe mounted on the surface of the cavity measures the magnetic field produced by the solenoid

A probe mounted on the outer cavity wall measures the magnetic field on the surface of the cavity via the Hall effect. [Hal79] The sensor used, a LakeShore HGCT-3020, operates at temperatures as low as 1.5 K and can measure fields up

to 3 T. [Lak13] The active area of the hall sensor is a circle roughly 1.04 mm in diameter. The end of the solenoid was placed 3.0 mm from the the Hall probe, which was mounted directly on cavity's outer wall.

Measurements are made by quasi-statically increasing the strength of the external magnetic field until a phase transition occurs. A low level CW RF field is stored in the cavity, and can be used to determine the quench time.
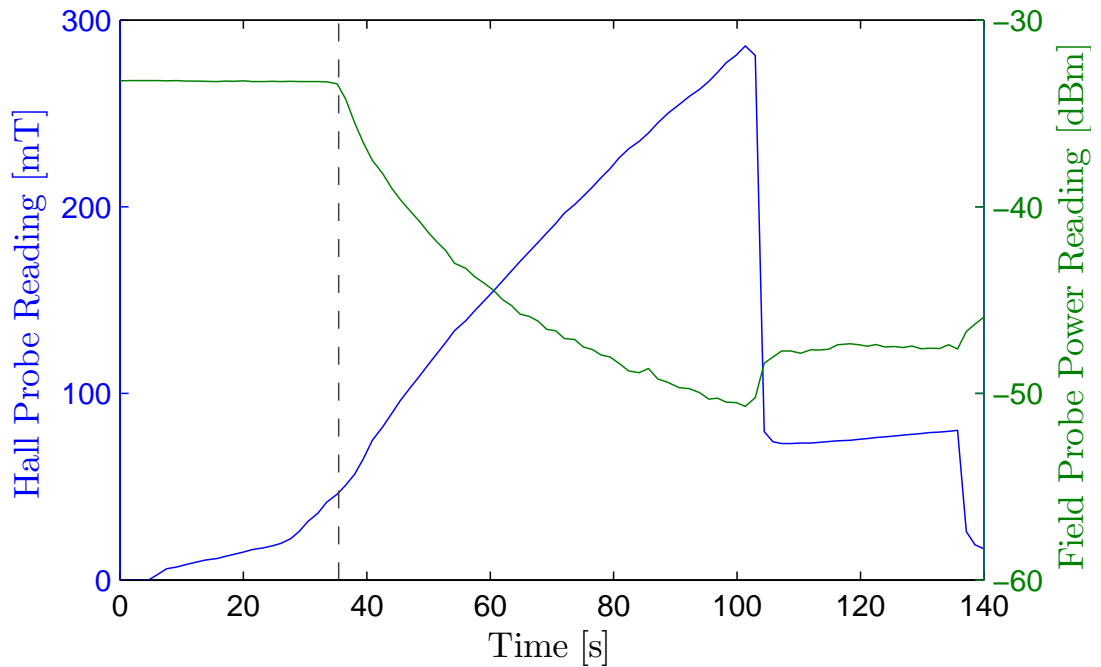
Figure 2.20: Measurement of the DC critical field at 7.0 K. At t = 35.2 s, marked by the gray dashed line, the field probe measures a drop in the stored magnetic energy in the cavity. At this time the Hall probe measures 50 mT. At t = 100 s, the magnet quenches, and at t = 136 s, the magnet power is shut off. The Hall probe measures magnetic flux of 19 mT after the solenoid is de-energized, suggesting that flux is trapped in the cavity wall.

When constant RF power is impingent on a superconducting cavity in steady state conditions, part of the incident power is reflected and part of the power is dissipated in the cavity walls. When the cavity leaves the Meissner state, the wall losses increase sharply, and the field in the cavity quickly dissipates.

Therefore, by measuring the cavity field as a function of time, the transition from the Meissner state can be identified. An example of a DC critical field measurement is presented in Figure 2.20.

Magnetostatic Simulations

The magnetic flux measured by the hall probe is not necessarily equivalent to the peak flux on the surface of the cavity. This is because in the superconducting state, the cavity wall prevents flux from entering the material, leading to the maximum magnetic field located a distance away from the solenoids' axis of rotational symmetry.
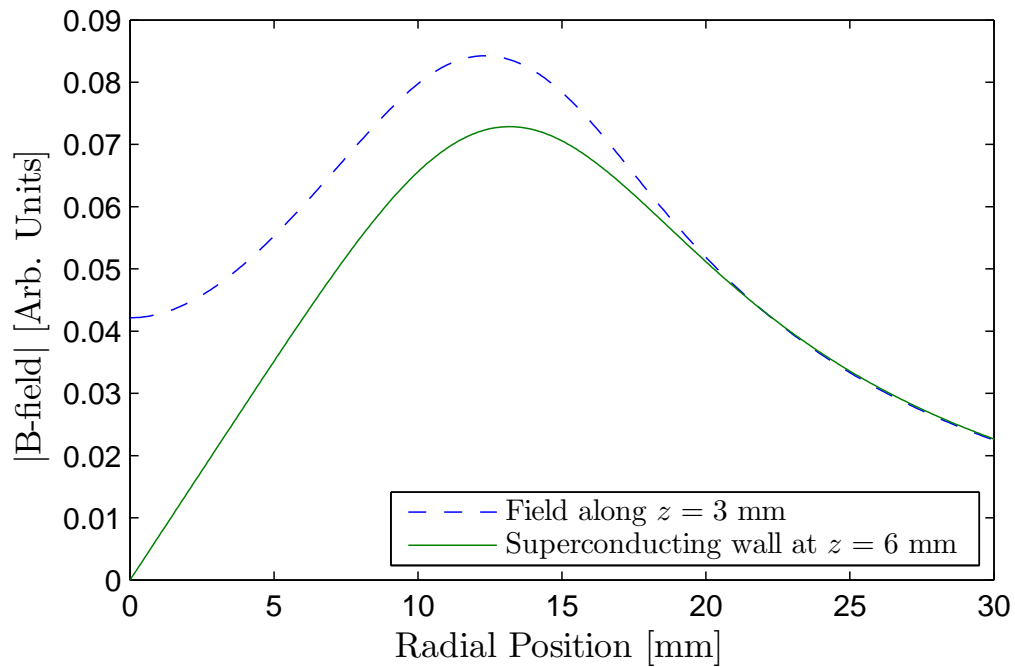
Figure 2.21: Magnetic field magnitude on a plane 3 mm and 6 mm from the end of a solenoid with a superconducting wall 6 mm from the end of the solenoid. The enhancement between the value measured by a hall probe at z=3 mm on the solenoid axis and the maximal field on the surface is ~ 1.7. The superconducting wall was modelled by enforcing the boundary condition $\vec{B}(r, \phi, z_0) \cdot \hat{z} = 0$ at z_0=6 mm.

Magnetostatic field modelling was performed with Radia [ECC97] to calculate the field enhancement on the cavity surface, which is the difference between the field measured on the hall probe and the peak magnetic field on the cavity surface. Figure 2.21 shows the magnetic field on a plane 3 mm and 6 mm from the end of a solenoid with a superconducting sheet at z = 6 mm modelling the superconducting cavity.

Uncertainty in Hall probe position must also be taken into account to obtain the correct surface magnetic field measurement. Supposing the active area of the probe has coordinates, (x_p, y_p, z_p), and the maximum magnetic field occurs at the surface of the cavity at position (x_M, y_M, z_M). The enhancement factor, η, is defined as

$$\eta = \frac{|\vec{B}(x_M, y_M, z_M)|}{|\vec{B}(x_p, y_p, z_p)|}. \tag{2.51}$$

The fundamental field limit will be reached when the inner RF surface ($\sim$ 100 nm), which is the portion of the cavity probed by the low level RF field, transitions from the superconducting state to the normal conducting state. This will not be the same value as measured by the Hall probe, since outer sections transition earlier as they are closer to the magnet and see higher magnetic fields. An enhancement factor must be computed to determine the DC magnetic field measured at the inner RF surface.

Figure 2.22 shows the enhancement factor for the probe at various distances from the solenoid's symmetry axis. For the case of the setup used to measure the DC superheating field, the probe is 2.75 ± 0.25 mm in front of the cavity's inner surface (wall thickness and sensor thickness), yielding an enhancement factor η = 1.9 ± 0.2.
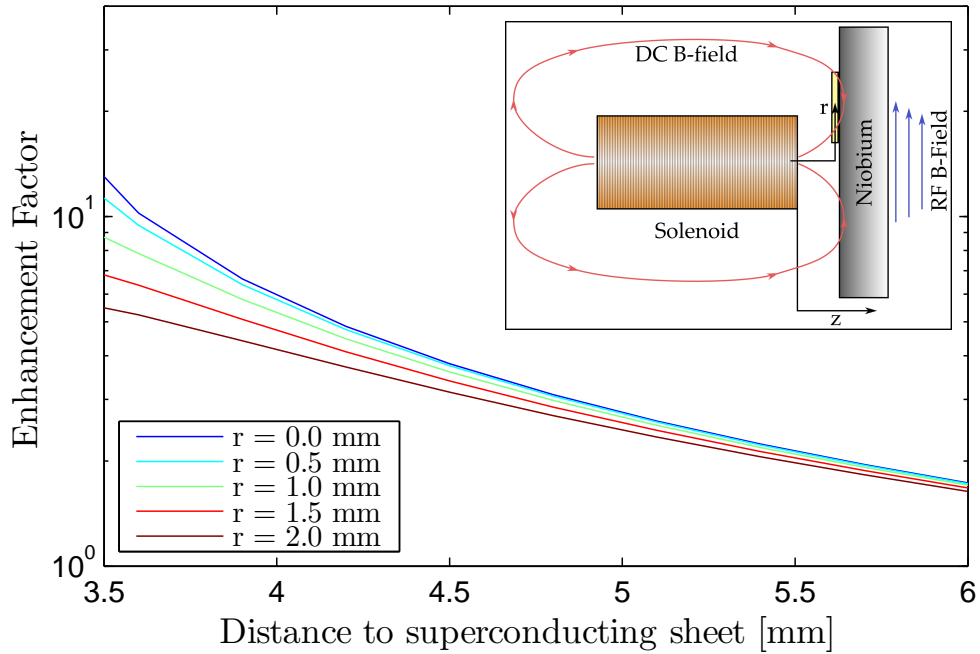
Figure 2.22: Enhancement factor as a function of distance between probe active area, z, and end of solenoid for various axial offsets, r, between the end of the solenoid and hall probe sensor, as illustrated in the inset. The sensor is assumed to lie at $z = 3$ mm, and the symmetry plane (i.e. superconducting surface) at $z > 3$ mm. The calculation assumes the field measures the largest value of the magnetic field anywhere in the probe's active area, which has a radius of 0.52 mm.

Measurements

LR1-3 was initially characterized by measuring Q_0 vs temperature at low fields between 4.2 and 8 K. These measurements are presented in Figure 2.23, and the corresponding BCS fit parameters are listed in Table 2.5.

The measured BCS values are roughly consistent with Preparation B in the RF superheating field measurement. This is to be expected as both times the cavity was electropolished without subsequent low temperature heat treatment. A major difference between the two cases is the fact that contamination due to a prior vacuum leak during the experiment caused the residual resistance to be
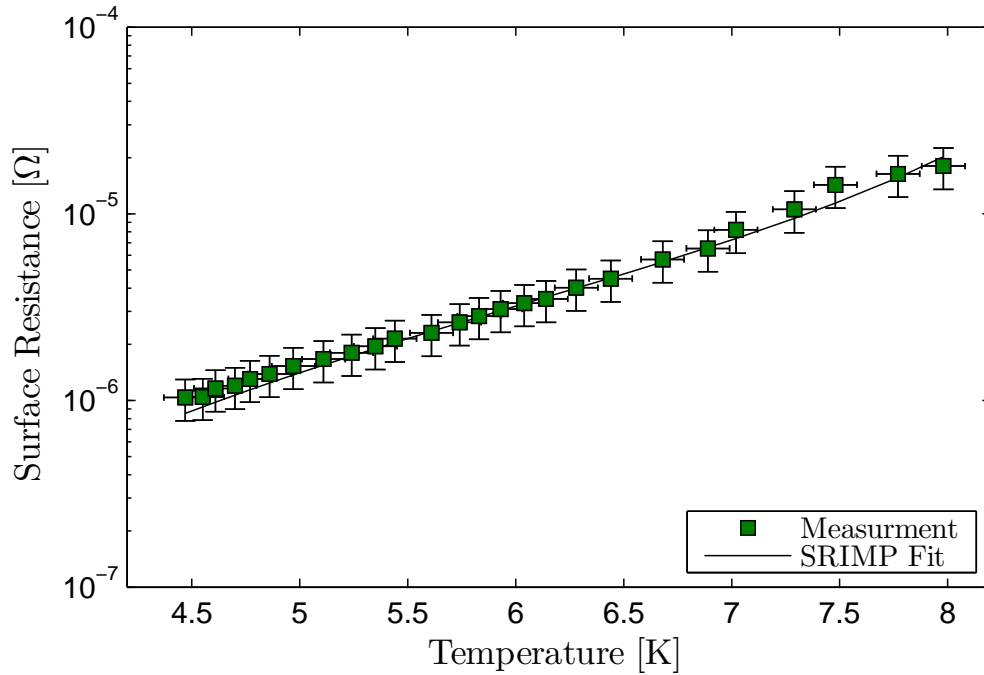
Figure 2.23: R_s vs T for LR1-3 prior to DC critical magnetic field measurements.

much larger in the DC measurement case.

Quality factor measurements were made before and after each DC critical field measurement. Measurements found that the surface resistance increased significantly after quenching the cavity with the solenoid due to trapped magnetic flux. High power pulsed RF quenches were able to release some trapped flux, but only warming the cavity above T_c returned the cavity's Q_0 to it's initial value.

The superconducting to normal conducting critical field was measured using the external DC magnetic field method at several temperatures, as presented in Figure 2.24. Both the magnetic field measurement by the Hall probe at phase transition and the calculated maximum magnetic field (using an enhancement factor, $\eta = 1.9 \pm 0.2$) on the cavity surface at that time are displayed.

Input Parameter	Value	Unit
Frequency	1300	MHz
T_c	9.20	K
λ_L	39.00	nm
ξ_0	38.00	nm
Fit Parameter	Value	Unit
E_g	4.408 ± 0.052	—
ℓ_{tr}	$2.94 \times 10^4 \pm 1.77 \times 10^4$	nm
R_0	$133. \pm 14.0$	$n\Omega$
Calculated Result	Value	Unit
λ_{tr}	0.001 ± 0.001	—
$R(\lambda_{tr})$	1.000 ± 0.001	—
λ_{GL}	27.59 ± 0.01	nm
ξ_{GL}	$28.05 \pm 3 \times 10^{-4}$	nm
κ_{GL}	$0.98 \pm 7 \times 10^{-4}$	—
$c(\kappa_{GL})$	$1.26 \pm 2 \times 10^{-4}$	—

Table 2.5: Material properties used to fit surface resistance vs temperature data presented in Figure 2.23, with E_g, ℓ_{tr} and R_0 as fit parameters. The critical temperature was measured separately. The small uncertainty of the calculated parameters are due to the large mean free path.

Fitting the maximum surface B-field, as a function of $t = T/T_c$, with the phenomenological prediction (assuming $c(\kappa_{GL})$ is temperature independent, which is justified by the close fit to the data).

$$B_{sh}(t) = c(\kappa_{GL}) \cdot B_c \cdot \left(1 - t^2\right), \qquad (2.52)$$

where $B_c = 200$ mT, [FSS66] yields the result $c(\kappa_{GL}) = 1.216 \pm 0.098$.

The agreement between the values of $c(\kappa_{GL})$ obtained from the superheating field measurements with the GL prediction using the material properties listed in Table 2.5, argues that, as for the superheating field measurement using RF fields, $B_{max,sc}^{DC} = B_{sh}$, for $\kappa_{GL} \sim 1$.

The DC field apparatus enabled measurement of B_{sh} without being limited by the RF heating of the inner wall. This result demonstrates that for
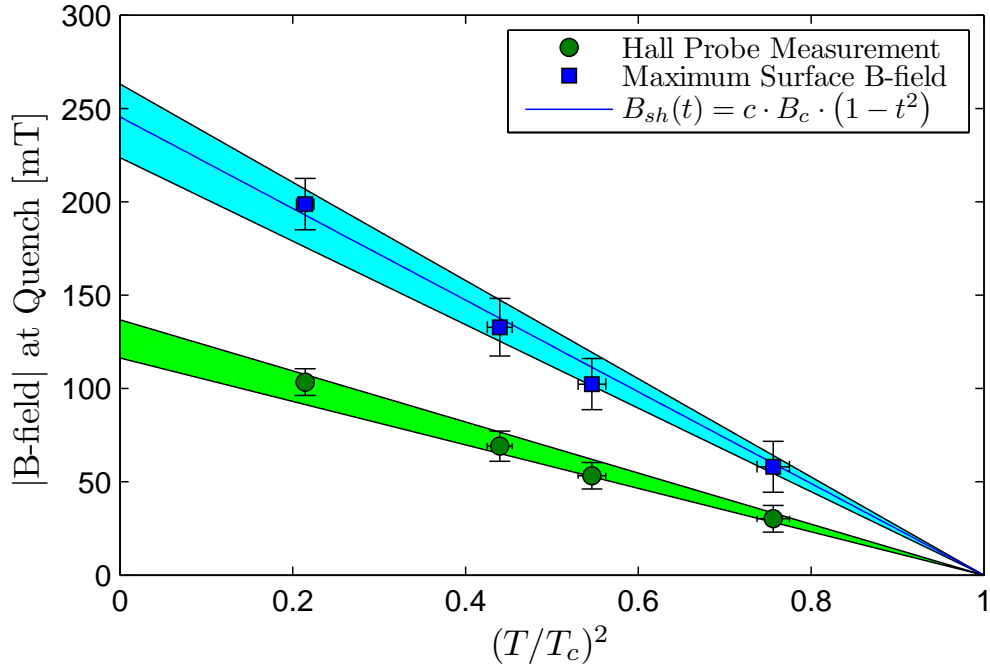
Figure 2.24: Hall probe reading and maximum surface magnetic field at the time of phase transition from the Meissner state to the mixed state versus temperature. The maximum field at the cavity surface is enhanced by a factor of $\eta = 1.9 \pm 0.2$ relative to the Hall probe reading. The blue line marks the best fit of the superheating magnetic field assuming $c(\kappa_{GL})$ is temperature independent. The green and blue colored regions denote fit uncertainty. In the plot $T_c = 9.2$ was used, consistent with critical temperature measurements obtained by resonant frequency tracking with the network analyzer.

$\kappa_{GL} \sim 1$ (consistent with Preparation B from the RF measurement), the Ginsburg-Landau result, using a temperature independent value for $c(\kappa_{GL})$ has applicability far from T_c, (within 5% of the measured value).

With this result, the temperature dependence of the superheating field of niobium was successfully measured for both surface preparations, and suggests that the superheating field of niobium is well described by the GL result near T_c.

2.6 Conclusion of Superheating Field Investigations

The work presented here demonstrates the first measurements of the temperature dependence of the superheating field as a function of material properties. The results show that while the Ginsburg-Landau model is known to not completely describe the superheating field mechanism at low temperatures, it fits the data well over a large temperature range for κ_{GL}=1–3 material compositions. This demonstrates that the Meissner state metastably persists to between 200–250 mT in Nb at low temperatures, dependent on material preparation, as long as thermal runaway due to RF heating can be mitigated.

The zero temperature superheating field values of 200–250 mT should be compared with the values of $B_{c_1}(T = 0) = 94\text{-}164$ mT (interpolated from Table 2.1 with $\kappa_{GL} = 1$–3), which demonstrates that the Meissner state persists metastably well above B_{c_1}.

Furthermore, these results show that niobium surfaces receiving the standard high gradient cavity preparation treatments have a reduced superheating field. The mechanism in this study is related to the change in electron mean free path due to scattering sites in the RF layer, but in principle other effects could also change κ_{GL} of the material. Specific to this case, the 120°C heat treatment appears to make Nb more strongly Type-II, by reducing the electronic mean free path, ℓ, and thereby reducing B_{sh}. This leads naturally to ask if an alternative to the 120°C heat treatment that eliminates high field Q-slope while not reducing the material's mean free path can be developed.

This trade off between ℓ and B_{sh} is explicitly shown in Figure 2.25. Though κ_{GL} is not shown on the figure, $\ell \to 0$ is the regime wherein niobium is strongly

type-II, and $\ell \to \infty$ is the regime in which niobium is closer to type-I. The fact that niobium's material properties can drastically change depending on preparation should be carefully considered in SRF design of niobium accelerators.
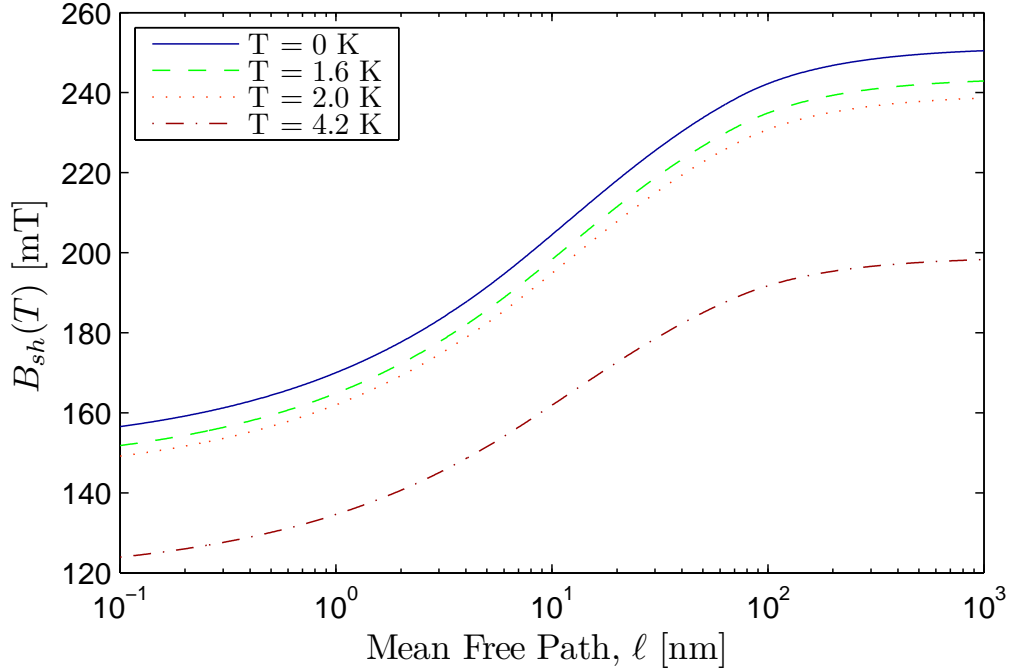
Figure 2.25: B_{sh} for niobium vs ℓ at several temperatures computed by $B_{sh}(t) = c(\kappa_{GL}) \cdot 200 \cdot \left[1 - t^2\right]$, where $t = T/T_c$, and $c(\kappa_{GL})$ is the GL result near T_c. Clean niobium has $\ell \to \infty$, with a maximum superheating field of about 250 mT at zero temperature. The 120°C heat treatment yields $\ell \sim 10$ nm, with a zero temperature superheating field of about 200 mT.

Theoretical progress on the temperature dependence of intermediate κ_{GL} materials are continuing with work on the Eilenberger equations, though there are still questions about the convergence of these results at very low temperatures. Thus, the work here provides much needed experimental data to help guide the further development of theory.

A new type of experimental apparatus was developed to measure the superheating magnetic field of niobium with strong Q-slope preventing pulsed RF

measurements. The apparatus utilizes a superconducting solenoid, and measurements demonstrated that the Ginsburg-Landau result for the superheating field of niobium near T_c is applicable over a large temperature range.

We now return to the question that ignited these investigations: "What is the maximum gradient that can be supported in a niobium SRF accelerating structure?" For typical high gradient accelerating structures, such as the TESLA cavity geometry, the ratio of peak magnetic field to accelerating gradient is 4.26 mT/(MV/m), [ABB$^+$00] meaning that at T=0 K, the largest gradient that can be supported in a niobium cavity, assuming the high field Q-slope can be overcome without the 120° heat treatment, is about 58.7 MV/m. With the heat treatment, the accelerating gradient is limited to ~47 MV/m. New cavity designs, such as the Low Loss ILC cavity, with B_{pk}/E_{pk} = 3.26 mT/(MV/m), [SKG$^+$05] may increase the maximal theoretical gradient to 69.2 MV/m, or 61 MV/m with the 120° heat treatment.

Finally, the question of whether the superheating field results can be reproduced for alternative materials such as Nb_3Sn or MgB_2 is of central importance. Work is progressing rapidly on the production of Nb_3Sn, [PL11] and initial study of samples of this material are an active field of research, with hints that this new material may allow the accelerating gradient to be doubled. [Pos13b, CS08]

MAIN LINAC CAVITY DESIGN FOR THE CORNELL ENERGY

RECOVERY LINAC

This chapter begins by introducing the idea behind an energy recovery linac (ERL) and explains why it necessitates the use of superconducting accelerating technology. Next, the phenomena of beam break-up is discussed, which is the primary obstacle to the realization of a high current ERL, followed by the methods used to design the main linac accelerating structure. Finally, validation of the design in 2D and 3D simulations are presented along with properties of the final structure.

3.1 Energy Recovery Linac Principles

As discussed in section 1.4, progress on many frontiers of X-ray science require very bright light sources with a large coherent fraction of the radiation. To this end, Cornell University has developed a next generation light source, that is brighter, and has a larger fraction of coherent X-rays than any existing storage ring based light source (see Figure 3.1).

The spectral brightness of a photon source, $\mathcal{B}$, is given by

$$\mathcal{B} = \frac{\mathcal{F}}{4\pi^2 \Sigma_x^T \Sigma_{x'}^T \Sigma_y^T \Sigma_{y'}^T},$$

(3.1)

where $\mathcal{F}$ is the spectral flux[1], and $\Sigma_{x,y}^T$ are the photon source sizes in the transverse directions and $\Sigma_{x',y'}^T$ are their divergences. [BBB$^+$11] Because the photon

---

[1]Flux is the rate at which electromagnetic energy is transferred through a surface, but in the synchrotron light source community, only the fraction of photons near the maximum in the intensity vs frequency function is considered yielding the units of spectral flux of [photons/s/0.1%BW].
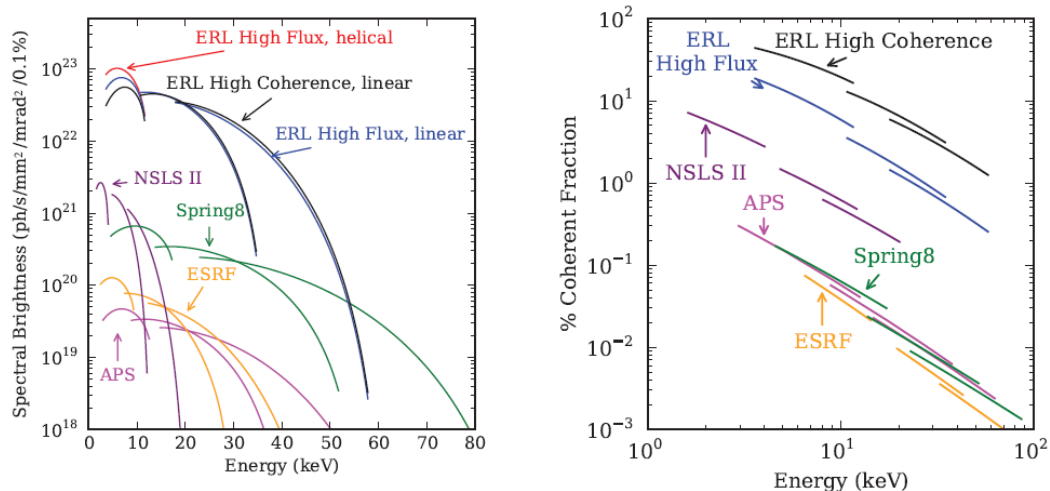
Figure 3.1: (Left) Average spectral brightness vs energy for several ERL operating modes, compared with brightnesses of other light sources. (Right) Coherence in X-ray sources. Figure reproduced from [BBB+11].

source size is given by the convolution of the radiation produced by a particle beam travelling through an undulator, a small electron beam emittance translates into a bright X-ray source. Energy recovery linacs are able to produce brighter X-rays, because the electron beam only cycles through the machine once (or a few times for multi-pass ERLs), compared with more than 10^5 times for synchrotron based sources, so the beam emittance never reaches its (larger) equilibrium value.

The specifications the Cornell ERL call for several operating modes, as presented in Table 3.1, with the high flux mode requiring a 5 GeV electron beam operating at 100 mA of current. The power required to accelerate this beam without energy recovery would be 5 GV·100 mA = 500 MW, which is about 70% of the average electrical power usage of Connecticut in 2011. [Adm13] Obviously, producing a standard linac requiring this level of power consumption is infeasible; to realize a linac with this beam power, a new type of accelerator is

Table 3.1: Beam parameters for Cornell ERL's operating modes. Geometric horizontal and vertical emittances (ε_x, ε_y), bunch duration (σ_z/c), and relative energy spread (σ_δ) in both the North Arc (NA) and South Arc (SA) insertion device. Values are obtained from start-to-end simulations. [BBB$^+$11] Normalized emittances for the 5 GeV beam are obtained by multiplying the emittances below by 10^4.

Parameter	High Flux	High Coherence	Short Bunch	Unit
Energy	5	5	5	GeV
Current	100	25	25	mA
Bunch Charge	77	19	19	pC
Repetition Rate	1300	1300	1300	MHz
ε_x (SA/NA)	31/52	13/34	21/66	pm
ε_y (SA/NA)	25/26	10/10	14/14	pm
σ_z/c	2.1/2.1	1.5/1.5	10/0.1	ps
σ_δ	1.9/1.9	0.9/1.0	9.1/9.3	10^{-4}

required, namely an energy recovery linac.

The principle of an energy recovery linac was first described by Maury Tigner in 1965. [Tig65] The initial proposal used two accelerating sections aimed at one another that would exchange energy from a high energy beam with a low energy beam using a superconducting standing wave cavity as the interchange medium, illustrated in Figure 3.2. After travelling through an accelerating section of length $N\lambda/2$, where N is an integer and λ is the wavelength of the RF power, the high energy beam travels a distance $n\lambda$, n another integer, to arrive at the second cavity section 180° out of phase. The high energy beam loses energy which is stored in the accelerating cavity, and used to accelerate fresh, low energy electron bunches. This allows the continuous production of high energy, low emittance particle beams, which (among other things) can be used to produce extremely bright light sources.

One way the efficiency of an ERL operating at beam current I_b can be quantified with an "RF to beam multiplication factor", η, which is the ratio of the beam
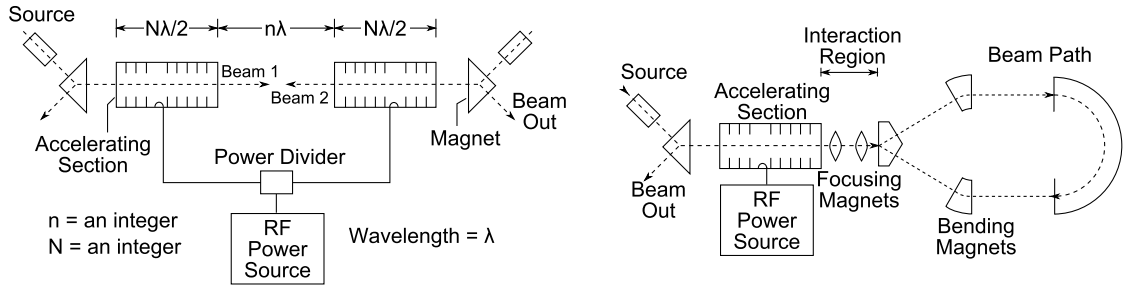
Figure 3.2: (Left) Low energy particles are produced by each source, and accel-
erated to full energy from phase locked accelerating sections. After
passing through an interaction region of length $n\lambda$ the high energy
beam enters accelerating section 180° out of phase, leaving energy
in the standing wave structure, and is dumped at low energy. The
energy transferred to the cavity is used to accelerate new particle
bunches. (Right) Modified scheme using a single accelerating sec-
tion for energy recovery. Figure based on diagrams from [Tig65].

power, P_{beam} at the point X-rays are generated to the RF power incident on the
accelerating cavities, P_{RF}, and is given by

$$\eta = \frac{P_{beam}}{P_{RF}} \approx \frac{I_b E_f}{I_b E_{inj} + q \cdot P_{RF,linac}}, \tag{3.2}$$

where E_f is the final beam energy, E_{inj} is the injected beam energy, q is the charge
of the electron, and $P_{RF,linac}$ is the power incident on the main linac cavities.
[MDK03] The approximation is exact in the case of no losses in the RF cavity,
but is very close in most circumstances and is almost exact for superconducting
structures, which have quality factors above 10^{10}.

For the Cornell ERL with injection energy of about 10 MeV, full energy of
5 GeV, and average linac RF power per cavity of 2 kW for each of the 386 cavities,
the multiplication factor $\eta \approx 282$ so only 0.3% of the beam energy would be
needed to be supplied by the RF system.

The 10-operational cost of an ERL is minimized by using moderate gradi-
ents in the 15-20 MV/m range. [BBB+11] Swapping energy between low and
high energy bunches requires the cavities to always store energy, necessitating

continuous wave operation. The ohmic losses in a normal conducting cavity ($Q_0 \approx 2 \times 10^4$) would be on the order of megawatts/cavity, so superconducting technology ($Q_0 \approx 2 \times 10^{10}$) is required to keep these losses to approximately 10 W/cavity. This allows the total operational power needs for the Cornell ERL to be under 15 MW–a quantity that can easily be supplied by the existing power grid.

The parameters of the superconducting linac for the Cornell ERL are listed in Table 3.2. For reference, the aerial view of the accelerator linac is presented in Figure 1.11.

Table 3.2: SRF parameters of the Cornell ERL.

Parameter	Value
Accelerator Type	e^- linac
Frequency	1300 MHz
Temperature	1.8 K
Cavity Type	7-cell
Operational Gradient	16.2 MV/m
Q_0(16.2 MV/m)	2×10^{10}
Cavities	386
Cryomodules	64
Peak RF power/cavity	5 kW
Average RF power/cavity	2 kW

3.2 Main Linac Cavity Design Considerations

As discussed above, a continuous wave superconducting Energy Recovery Linac is required to produce a high-energy, low-emittance electron beam at the high repetition rates required for cutting edge X-ray science. Though there are many challenges that must be overcome to realize such a machine, the primary challenges for the main accelerating structure is that the cavities must be ex-

tremely efficient, having $Q_0 > 2 \times 10^{10}$ at 1.8 K, and the linac must be able to support threshold current in excess of the 100 mA design specification while preserving the small beam emittance created at the injector. The beam properties can be limited by the effect of strong higher-order modes (HOMs) in main linac cavities. Thus, the accelerating structures comprising the main linac must balance two opposing goals to achieve its science mission: obtain a very large Q_0 of the accelerating mode while making the Q_0 of all HOMs very small.

Successful cavity design depends on maximizing the threshold current of a very low emittance electron beam through the linac at the lowest cost. Since cryogenic power expenses account for more than 50% of the electrical costs for the ERL facility, it is important to examine the sources of power loss and their scaling with machine parameters.

For a cryogenic cavity, power losses can be separated into static and dynamic losses, both of which should be minimized for the ERL. The static losses are due to heat transfer from radiation and conduction, and are minimized through proper cryomodule design. Dynamic losses are due to the operation of the RF structure.

Heat produced by an SRF cavity is absorbed by the cryogenic system. The surface area of the cavity, and thus heat load per unit length scales inversely with the fundamental mode frequency. This consideration motivates operation at high frequencies.

The surface resistance of the cavity R_s has two contributions, the losses due to BCS resistance, R_{BCS}, and the residual resistance, R_0. Following Equation 1.9,

the power dissipated in the linac, P_{diss} per unit length, L, can be written as

$$\frac{P_{\mathrm{diss}}}{L} = \frac{2\pi f U}{Q_0 L},$$

(3.3)

where U is the stored energy in the cavity operating at frequency f. Using Equation 1.11 and Equation 1.14, one finds that the power dissipated per unit length, at a fixed voltage, depends on

$$\frac{P_{\mathrm{diss}}}{L} \propto \frac{R_{BCS} + R_0}{f}.$$

(3.4)

Because R_{BCS} increases with the square of the resonant frequency, low frequency operation is favorable when this component of R_s is large. However, at low temperatures the BCS component is negligible compared to the (roughly) frequency independent residual resistance–typical values are between 5-10 nΩ–and favors high frequency operation when this is the dominant factor. These considerations lead to the conclusion that AC cooling power is minimized for frequencies between 500 and 1500 MHz. [LK06]

An operating frequency of 1300 MHz was chosen for three main reasons: First, the upper end of the frequency range has small cavity surface area, reducing the chances of contamination during assembly. Second, higher frequencies allow smaller electron bunch charges to be used for the same beam current, which is important because smaller bunch charges help to mitigate space-charge effects and allow smaller beam emittances. Third, much work has been done developing 1300 MHz technology for the International Linear Collider and the European XFEL, so using these mature technologies reduces research and development costs by capitalizing on the availability of RF sources such as klystrons and solid state amplifiers.

The number of cells for the cavity were chosen as a compromise between maximizing linac fill factor, which increases with number of cells and reduces

the number of components such as input couplers, and the ability to sufficiently damp high Q modes that lead to beam break-up (BBU), which decreases with number of cells. Simulations suggested a good compromise between these two goals was obtained with 7-cells.

A major challenge in ERL main linac cavity design, the interaction between the particle beam and HOMs are discussed in the next section.

3.2.1   Higher-order mode/beam Interaction

Proper cavity design is a crucial challenge for the Cornell ERL because trapped modes (modes that decay slowly) can cause deleterious effects on a particle beam, limiting the threshold current through the structure. As a particle beam travels through a structure, it leaves electromagnetic energy behind, which are referred to as wakefields. Wakefields can be visualized in the time domain as shown in Figure 3.3.

In the frequency domain, energy is stored in any higher-order mode that can couple to the electron beam. In an accelerator, the particle bunch train excites certain modes resonantly and decay at a rate inversely proportional to their respective quality factors, Q_L. These modes can impart kicks to subsequent bunches and can lead to an instability causing beam-breakup (BBU). In addition to the quality factor, the strength an HOM couples to the beam will determine whether or not it ultimately leads to BBU.

In analogy to electrical circuits, the 'resistance' or coupling strength of a mode can be defined as either the longitudinal impedance (see Equation 1.11)
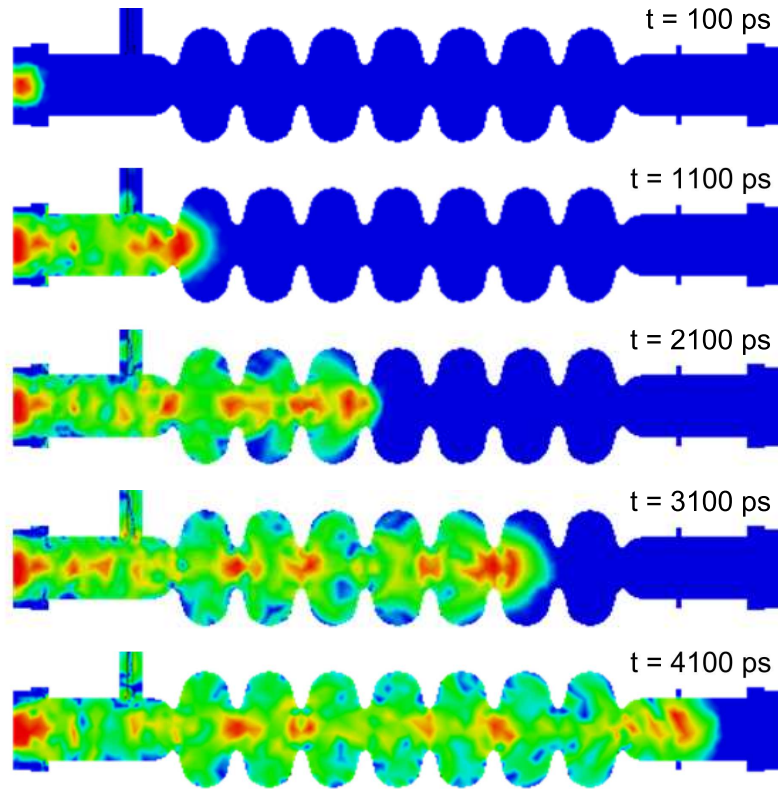
Figure 3.3: Wakefields from a 1.5 cm long bunch* as it traverses an accelerating structure. High intensity electric field is red and no field is blue. Calculation was performed using SLACs time domain solver T3P, [Xia97, KCG+10] running in parallel on 720 nodes at NERSC. [Nat] The full calculation took ~1000 computer-hours.

*Bunch charge was 25 times larger than the 0.6 mm bunch that will be used in the ERL, due to memory limitations.

for monopole modes or the transverse impedance in Equation 1.20 for non-monopole modes,[2] as was discussed in section 1.1.1. Non-monopole modes are only excited by a beam travelling off-axis.

Following [Wie95], the effect of an HOM on a charge, q, travelling with relative velocity $\beta = \mathbf{v}/c$ can be calculated. The transverse variation of the longitudinal field of a HOM, having transverse electric and magnetic fields $\mathbf{E}_\perp$ and $\mathbf{B}_\perp$,

---

[2]Non-monopole modes have zero field component along the axis so the voltage integral in Equation 1.7 vanishes.

imparts a transverse momentum kick

$$\mathbf{p}_\perp = \frac{q}{\beta} \int \left[\mathbf{E}_\perp + \frac{1}{c}(\mathbf{v} \times \mathbf{B})_\perp \right] dz. \tag{3.5}$$

The transverse vector potential $\mathbf{A}_\perp$ can be used to write $\mathbf{E}_\perp = -\partial_t \mathbf{A}_\perp$ and $\mathbf{B} = (\nabla \times \mathbf{A})_\perp$ to yield

$$\frac{\partial \mathbf{p}}{\partial t} = -\frac{q}{c} \nabla_\perp \int \mathbf{E}_z \, dz, \tag{3.6}$$

yielding the Panofsky-Wenzel theorem that was used to derive Equation 1.20, [PW56] which relates a mode's coupling strength to the transverse momentum kick a particle bunch receives.

The interaction between higher-order modes and the electron beam are of primary concern for ERL operation. Next, the effect of monopole, dipole and quadrupole modes are investigated.

Monopole Effects

Monopole HOMs, having non-zero field components along the beam axis, have the effect of introducing longitudinal instabilities into an ERL beam by changing the bunch energy, as has been studied in [SH06]. The threshold current, $I_{th,long}$ before longitudinal effects lead to BBU in an ERL is given by

$$I_{th,long} = \frac{2E}{\eta t_r \omega_\lambda \left(\frac{R}{Q} \right)_\lambda Q_\lambda}, \tag{3.7}$$

where E is the energy of the beam, t_r is the return time around the loop for an on-energy particle and η is the 'slip factor'. The slip factor relates the time offset ΔT of a particle with energy offset ΔE as

$$\Delta T = \eta t_r \frac{\Delta E}{E}. \tag{3.8}$$

The 6-dimensional ray tracing formalism, which relates an initial particle position $X(0)$ with its final position $X(s)$ after passing through elements having a transfer matrix, R, [Cha99] via

$$
\underbrace{\begin{bmatrix} x(s) \\ x'(s) \\ y(s) \\ y'(s) \\ l(s) \\ \Delta P(s)/P_0 \end{bmatrix}}_{X(s)} = \underbrace{\begin{bmatrix} r_{11} & r_{12} & r_{13} & r_{14} & 0 & r_{16} \\ r_{21} & r_{22} & r_{23} & r_{24} & 0 & r_{26} \\ r_{31} & r_{32} & r_{33} & r_{34} & 0 & r_{36} \\ r_{41} & r_{42} & r_{43} & r_{44} & 0 & r_{46} \\ r_{51} & r_{52} & r_{53} & r_{54} & 1 & r_{56} \\ 0 & 0 & 0 & 0 & 0 & 1 \end{bmatrix}}_{R} \cdot \underbrace{\begin{bmatrix} x(0) \\ x'(0) \\ y(0) \\ y'(0) \\ l(0) \\ \Delta P(0)/P_0 \end{bmatrix}}_{X(0)}, \tag{3.9}
$$

demonstrated that longitudinal BBU primarily depends on the r_{56} element which couples path length differences, l, with momentum deviations $\Delta P/P$. As long as $|r_{56}| < 10$ m, longitudinal BBU is not a danger ($r_{56} \approx 0$ for all ERL operating modes, and is less than 0.6 m at all points in the ERL lattice in operating mode C). [BBB+11] Therefore, longitudinal threshold current can be mitigated with proper optics design of the accelerator, and is not a cavity design concern.

This theoretical result was compared with particle tracking simulations of the Cornell ERL lattice, performed with with BMAD, [Sag06] accounting for the 4 strongest monopole modes. Simulations agreed with theory, and predicted that for a mode with $f = 3857.63$ MHz, $Q_L = 13728$ and $(R/Q) = 31$ Ω, $I_{th,long} \sim 8.6 \times 10^4$ mA, in the case of an ERL consisting of a single cavity and single HOM. Again, monopole BBU is not a danger for the Cornell ERL operating at 100 mA.

Dipole Effects

Dipole HOMs couple beam displacement and subsequent kick after one pass through the ERL. Instead of leading to energy spread, dipoles introduce transverse kicks to the bunch which can lead to beam loss at current substantially smaller than in the longitudinal BBU case.

The basic mechanism of transverse BBU is that a dipole mode applies a transverse kick to a beam, which then returns to the same cavity with transverse offset, leading to beam oscillation. Since the longitudinal voltage depends on offset (see Equation 1.18), the oscillating beam drives the mode more strongly, leading to an exponential instability.

The transverse voltage of dipole modes depends on offset, in contrast to monopole modes, whose longitudinal voltage does not depend on offset. This difference implies that a transverse oscillation will not drive a monopole mode unless the frequency of the HOM is a harmonic of the bunch repetition rate. On the other hand, a dipole mode can be driven if its frequency is a harmonic of the beam's oscillation frequency. Since the mode itself causes the transverse oscillation, it will automatically oscillate at the resonant frequency, which is why it is possible to get transverse beam breakup at any HOM frequency.[3]

A model of a single loop ERL consisting of one cavity with a single HOM

---

[3]Transverse beam breakup is analogous to closing a feedback loop with negative gain, highlighting the inherent instability of the system. There is dependence on the return phase, which is why beam breakup equations depend on return time.

was investigated theoretically with the use of a transport matrix, T, defined as

$$\begin{bmatrix} x(s) \\ x'(s) \\ y(s) \\ y'(s) \end{bmatrix} = \underbrace{\begin{bmatrix} T_{11} & T_{12} & T_{13} & T_{14} \\ T_{21} & T_{22} & T_{23} & T_{24} \\ T_{31} & T_{32} & T_{33} & T_{34} \\ T_{41} & T_{42} & T_{43} & T_{44} \end{bmatrix}}_{T} \cdot \begin{bmatrix} x(0) \\ x'(0) \\ y(0) \\ y'(0) \end{bmatrix}, \qquad (3.10)$$

to arrive at an analytic result for the threshold current. [HBS07][4] The result is

$$I_{th,dipole} = -\frac{2\omega}{q \cdot (R/Q)_{\perp,\lambda} \cdot Q_\lambda \omega_\lambda} \frac{1}{T_{12}^* \sin \omega_\lambda t_r}, \qquad (3.11)$$

where q is the bunch charge and in this case $(R/Q)_{\perp,\lambda}$ has units Ω/m^2,[5] and T_{12}^* depends on the polarization angle of the HOM, θ_λ, according to

$$T_{12}^* = T_{12} \cos^2 \theta_\lambda + (T_{14} + T_{32}) \sin \theta_\lambda \cos \theta_\lambda + T_{34} \sin^2 \theta_\lambda. \qquad (3.12)$$

Initial simulations of the Cornell ERL lattice demonstrated that $I_{th,dipole}$ in a realistic ERL can be substantially lower than the 100 mA design current, depending on assumptions about the HOM properties. [BH04] This is consistent with simulations and observations of BBU in the Jefferson Laboratory prototype ERL beginning at under 10 mA for modes having $Q_L > 10^6$, $(R/Q)'_\perp \sim 30\Omega$. [TBD$^+$05] Achieving 100 mA current in the Cornell ERL requires an order of magnitude reduction in dipole HOM strength and requires a very careful cavity design.

The realistic case of an ERL consisting of hundreds of cavities with many unique modes per cavity must be treated with particle tracking simulations, since coherent effects between cavities can introduce large corrections to the

---

[4]R/Q in this equation has been converted from the form presented in [BH04] to one consistent with later work in subsection 3.2.2.

[5]Various R/Q definitions having units of Ohms, Ohms/m, and Ohms/m^2 can be converted to one another by multiplication of $k = \omega/c$, a point first brought to my attention by V. Yakolev. [Yak11]

single cavity result in Equation 3.11. Unlike the monopole BBU case, the lattice optics properties can not always be adjusted to mitigate transverse dipole effects, so special care must be taken in cavity design to eliminate the effects of dipole HOMs that could limit $I_{th,dipole}$ below the 100 mA design specification. This will be discussed more thoroughly in subsection 3.2.2.

Quadrupole Effects

The effect of quadrupole modes leading to transverse BBU effects was explored in [SH07]. The theory for quadrupole transverse kicks depends on the beta functions[6] of the accelerated and returning beam in the horizontal and vertical directions, β_{1x}, β_{2x}, β_{1y}, β_{2y}, and the difference in betatron oscillations,[7] $\Delta\psi_x$, $\Delta\psi_y$, caused by the quadrupole kick.

The analytic result of threshold current, $I_{th,quad}$, in an ERL consisting of a single cavity with a single quadrupole mode is

$$I_{th,quad} = -\frac{E\omega_\lambda}{qc} \frac{\gamma r_0^4}{2\left(\frac{R}{Q}\right)_\lambda Q_\lambda \epsilon_n} \frac{1}{(\beta_{x1}\beta_{x2}\sin 2\Delta\psi_x + \beta_{y1}\beta_{y2}\sin 2\Delta\psi_y)} \frac{1}{\sin \omega_\lambda t_r}, \qquad (3.13)$$

where E is the beam energy, γ is the Lorentz factor of the beam, ϵ_n is the normalized emittance of the beam, and r_0 is the distance perpendicular to the beam axis at which $(R/Q)_\lambda$[8] is measured. [SH07] For reference, the beta functions of the beams travelling through accelerating sections in the Cornell ERL are presented in Figure 3.4. Simulations of a full linac with quadrupole HOMs having quality factors of $\sim 10^9$ yielded $I_{th,quad} > 100$ mA for a 5 GeV electron beam, even in a full

---

[6]The beta function is related to the to the transverse size of the particle beam. [ES93]
[7]Betatron oscillations are transverse oscillations exhibited by a particle offset from the on-orbit path. [Wil00]
[8]$(R/Q)_\lambda$ has units of Ohms.
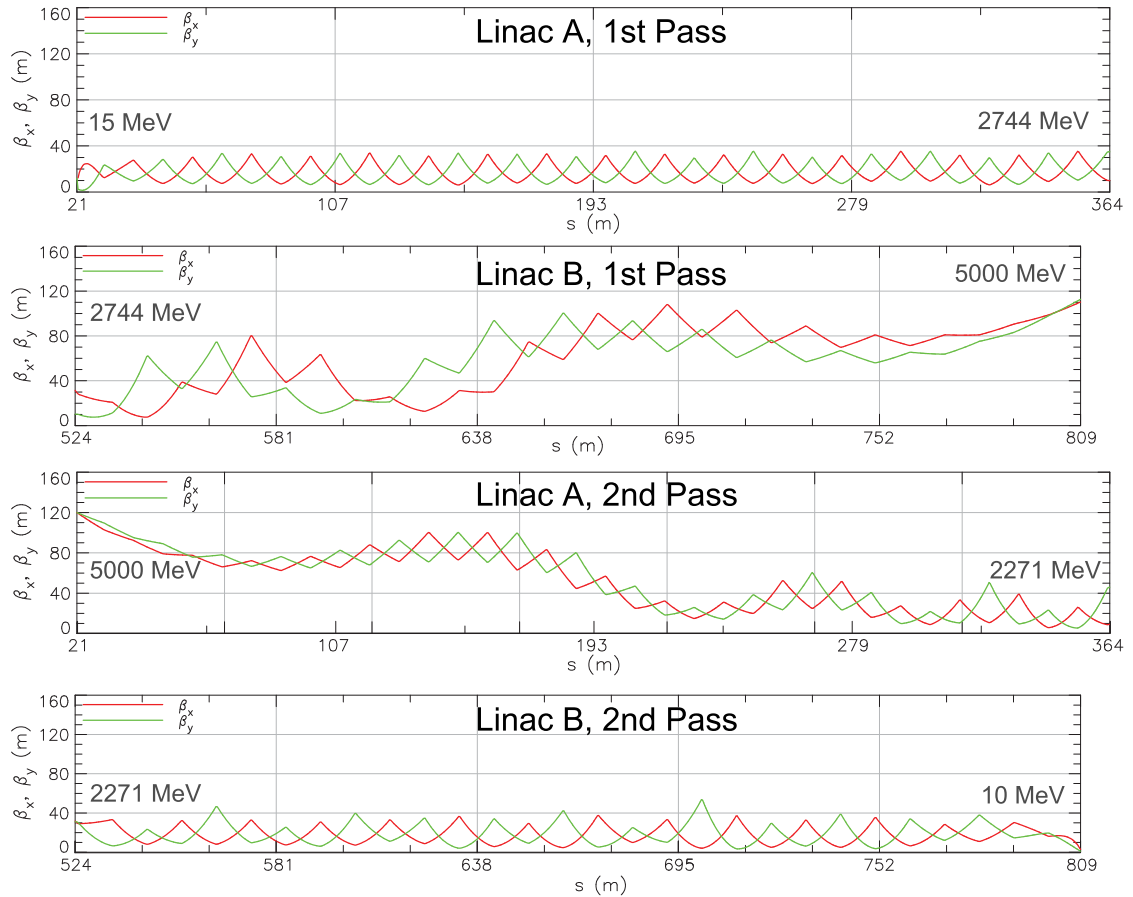
Figure 3.4: Beta functions of the electron beam in both linacs in acceleration and deceleration stages. The linac is broken into two portions. The initial and final energies at each stage of the linac is noted on each plot. Plots reproduced from [BBB+11].

ERL lattice where all cavities have the same resonant frequency.[9] The threshold current is several times higher than the 100 mA design specification for realistic frequency spread, so quadrupole modes with $Q_L \sim 10^9$ are acceptable. [BBB+11]

---

[9]This is an unrealistic, worst-case, assumption. Relative spread in the quadrupole mode frequency, which is virtually guaranteed from fabrication variation, would increase $I_{th,quad}$.

3.2.2 General Scaling Factors

The first step of any optimization relies on obtaining an appropriate goal function. For the design of the Cornell ERL main linac cavities, the goal function must reflect the need to obtain a large threshold current, I_{th}, through the ERL, and recognize that an analytic solution is not available. A single strong HOM can cause beam breakup. Coherent effects between several strong HOMs can reduce the threshold current even further. Thus, maximizing I_{th}, through the accelerator before beam instability sets in is the primary objective of the optimization.

Given many higher-order modes in hundreds of accelerating cavities forming the linac, I_{th} can only accurately be determined by statistical particle tracking. Since particle tracking is an expensive calculation, we sought an analytic parameterization of the threshold current that shares the same scaling properties of the more expensive calculation.

To determine scaling of this parameter, particle tracking was performed with BMAD [Sag06] on the Cornell ERL lattice. [May09] Each cavity in the lattice was defined as having a single higher-order mode. The HOM's quality factor, Q, R/Q,[10] and frequency, f, (with an assumed relative cavity-to-cavity frequency spread,[11] σ_f/f of 5×10^{-3}) was varied over range of values.[12]

Figure 3.5 presents the beam tracking results when an HOM's frequency and R/Q is varied. The plots demonstrate that $I_{th} \propto (R/Q)^{-1}$ and $I_{th} \propto f$, [VL10a] over

---

[10]For a multipole of order m, BMAD uses R/Q units of Ω/m^{2m}.

[11]The frequency spread has the effect of placing HOMs at slightly different frequencies from one cavity to another, as occurs in a realistic machine. BMAD uses a random Gaussian distribution with a root-mean-squared value of σ_f.

[12]This range of σ_f/f is typical of variations introduced by fabrication differences.
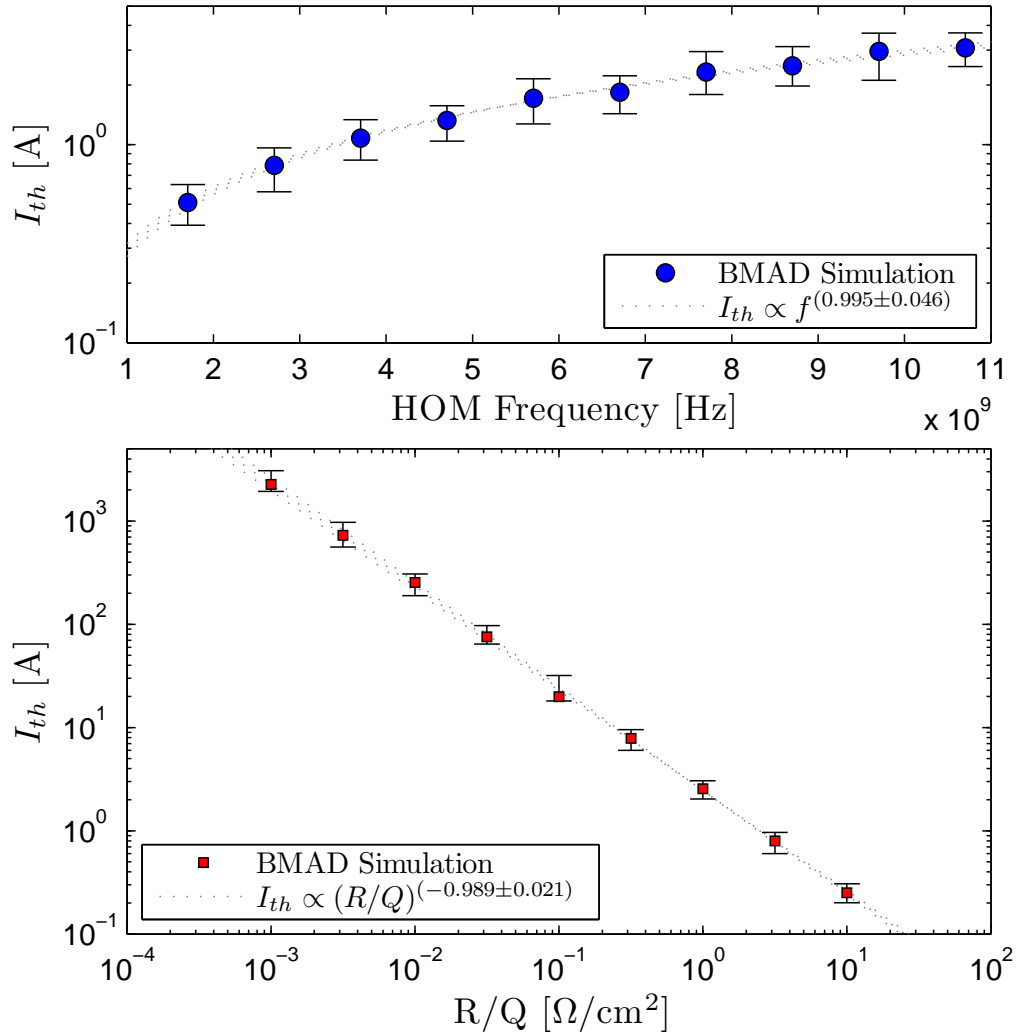
Figure 3.5: Scaling of the threshold current for the Cornell ERL lattice populated with cavities having a single HOM with nominal properties of $f = 1.7$ GHz, $R/Q = 5$ Ω/cm^2, $Q = 10^4$ and a cavity-to-cavity frequency spread of 5×10^{-3}. Markers denote average current, upper/lower error bar denotes the current achieved by the top/bottom 10% of simulated ERLs. Dotted lines show the best fit power-law dependence of each parameter on I_{th} with 95% certainty.

the entire simulated range, in agreement with Equation 3.11. The scaling of I_{th} with quality factor is more complicated, since it depends on the cavity-to-cavity relative frequency spread. [HB04]
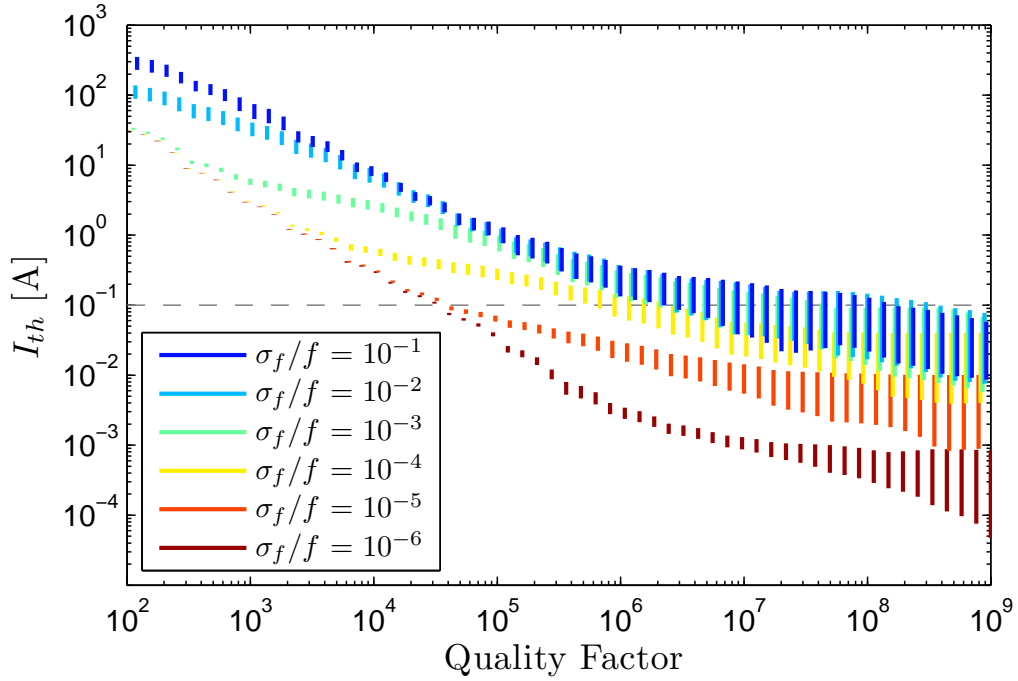
Figure 3.6: Scaling of the threshold current for the Cornell ERL lattice populated with cavities having a single HOM with nominal properties of $f = 3.236$ GHz, $R/Q = 10$ Ω/cm^2, and varying Q and cavity-to-cavity frequency spread. The vertical extent of each line is the range of threshold currents supported by the middle 80% of simulated ERLs. The dashed line is the Cornell ERL specification of 100 mA.

Figure 3.6 presents the dependence of I_{th} on Q and σ_f/f. It is apparent that I_{th} has different power-law scaling in the low- and high-Q regimes. At low Q ($< f/\sigma_f$), all cavities act coherently. For $Q > f/\sigma_f$, only some cavities act coherently, which for typical HOM properties is the relevant region (typical $\sigma_f/f \sim 10^{-3}$ suggests the coherent range only applies for $Q < 10^3$, far below typical HOM quality factors).

Power-law fits were determined in the two regions and are presented in Table 3.3. The low-Q region scales approximately as $1/Q$, whereas the high-Q region scales roughly as $1/\sqrt{Q}$. As the Q increases, the single cavity result in Equation 3.11 no longer holds and coherent effects begin to dominate. The scal-

ing of the top 90% of simulated ERLs for σ_f/f is presented in Figure 3.7, demonstrating this effect.
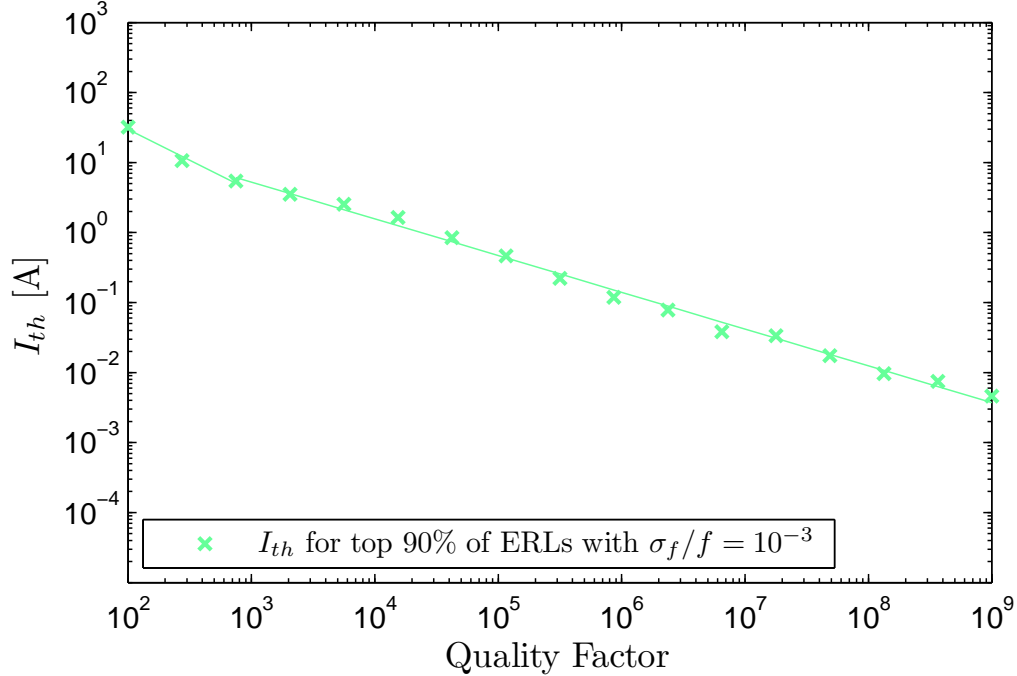
Figure 3.7: I_{th} scaling of the top 90% of simulated ERLs vs Q for $\sigma_f/f = 10^{-3}$. Linear fits were performed in two regions separated by $Q > f/\sigma_f$, showing that the high-Q region scales roughly as $Q^{-1/2}$.

Table 3.3: Scaling of I_{th} in the low- and high-Q regime. Table entries are the exponent in $I_{th} \propto Q^\alpha$, with a 95% confidence interval. Threshold current is the current supported by the top 90% of simulated ERLs. For $\sigma_f/f > 10^{-3}$, the low-Q range is not in the data range since σ_f is too large, and the entire range was used to determine the high-Q scaling.

σ_f/f	$Q < \sigma_f/f$	$\sigma_f/f < Q$
10^{-6}	-1.030 ± 0.033	-0.529 ± 0.079
10^{-5}	-0.933 ± 0.100	-0.461 ± 0.050
10^{-4}	-0.878 ± 0.186	-0.460 ± 0.039
10^{-3}	-0.724 ± 0.452	-0.529 ± 0.027
10^{-2}	—	-0.622 ± 0.045
10^{-1}	—	-0.666 ± 0.068

In determining an objective function, one should consider that typical fabrication errors give $\sigma_f/f \sim 10^{-3}$. In this region, for $Q > 10^3$,[13] I_{th} scales as $Q^{-1/2}$.

---

[13]Modes with very low Q are not important for the simulation since their threshold current is

Taking the simulations into account, the threshold current for a given dipole HOM, λ, in a realistic machine scales approximately as

$$I_{th,\lambda} \propto \frac{f_\lambda}{(R/Q)_\lambda \cdot \sqrt{Q_\lambda}}.$$ (3.14)

The objective function to be minimized then would be the worst HOM in the structure, where worst is defined as having the largest value of

$$\xi_\lambda \equiv \frac{(R/Q)_\lambda \cdot \sqrt{Q}}{f_\lambda}.$$ (3.15)

3.2.3 Geometric and electromagnetic constraints

Optimization constraints arise from physical manufacturing and preparation concerns as well as features affecting accelerator performance. Geometrically, cavity fabrication considerations limit the maximum radius of curvature in cell to three times the sheet metal width. [Cho09] Niobium sheets pressed into cells are 2 mm thick, requiring radii of curvature to be greater than 6 mm.

A standard cleaning procedure for preparing contaminant-free accelerating structures is high-pressure rinsing. Drainage concerns require cavity wall slopes of at least 5° from the horizontal to prevent water from pooling.

Electromagnetic considerations involve surface electric and magnetic fields on the structure's walls. The ratio of the peak surface electric field, E_{pk}, to the accelerating electric field, E_{acc}, should be kept to a low value to reduce the risk of field-induced emission of electrons from dust particles on the cavity surface. Field emission is particularly deleterious in CW operation since it can limit the

---

very large.

104

usable gradient by causing an additional cryogenic heat load and unacceptable radiation levels. The decision was made to limit $E_{pk}/E_{acc} \leq 2.1$.[14]

Previous work has demonstrated that the cryogenic heat load (inversely proportional to $G \cdot R/Q$) is related to the ratio of the peak magnetic field, B_{pk}, to the peak electric field. [She09a] Maintaining, $B_{pk}/E_{acc} \leq 4.2$ was chosen to keep dynamic losses within the operating capacity of the cryogenic plant, and is consistent with a structure having a fundamental mode $Q_0 \geq \times 10^{10}$.

With the objective function and constraints defined, the next concern is solving the complex, multi-optimization problem as efficiently as possible.

3.3   Approach to Accelerating Structure Design

As discussed previously, strong HOM damping is required for beam stability, and thus a major driver of the accelerating structure design. There are many schemes to damp HOM power including antenna and waveguide couplers that extract power, as well as beamline absorbers. [Mos89, CA99] The best solution depends on beam parameters. Since the Cornell ERL requires very strong broadband damping–extracting about 200 W of monopole power/cavity, assuming no monopole modes are driven resonantly [BBB+11]–the following damping scheme has been selected:

HOMs are absorbed in beamline dampers placed at either end of the cavity at an intermediate temperature ($\sim$ 80 K), as illustrated in Figure 3.8. The beam pipes have a diameter such that all monopole and dipole HOMs are above the

---

[14]This number is similar to ILC cavities, and is about as low as possible for a cavity iris radius of 35 mm. [She09a]

cut-off frequency and can propagate out of the cavity to the absorbers. Beam-line higher-order mode absorbers at the end of each beam pipe are cylindrically symmetric, and contain a ring of lossy dielectric material 1.5 cm thick, that couples to HOMs. This design provides broadband HOM damping and avoids the need for antenna or waveguide HOM couplers.

Figure 3.8: CAD model of the Cornell ERL 7-cell cavity with HOM absorbing loads. In the CAD model, the cavity is shown in light grey, the HOM load fixtures are colored light blue, and the beamline absorbing rings are dark grey. Only 1/2 of each HOM load was modelled. Symmetry planes at the center of the absorber were set to either magnetic or electric boundary conditions to simulate HOMs in a cavity within a long cavity string.

The initial 7-cell cavity geometry minimized the cryogenic losses due to the fundamental mode, and served as the starting point for complete cavity optimization [She09b]. The final design requirement was to obtain an accelerating structure for use in the linac that can support currents well in excess of the 100 mA specification.

This cavity shape optimization problem is challenging because a 7-cell cavity geometry can be constructed with at least 96 free parameters. Furthermore, computing the HOM spectrum and performing particle tracking are very time consuming operations.

To make the problem manageable, it was divided into pieces, which will be discussed in the following subsections:

- The center cell geometry was optimized to be stable under inevitable ma-

chining perturbations, while still maintaining low cryogenic losses due to the fundamental mode.

- End cells were optimized to effectively couple HOMs to the absorbers.

- The solution was verified by performing particle tracking in an ERL constructed of realistic cavities with small shape imperfections.

Center Cell Design

The center cells of an elliptical shaped, $\beta = 1$ cavity are responsible for both the properties of the fundamental accelerating mode and the dispersion relations of the higher-order mode passbands. They are shaped by two ellipses connected by a tangent line (see Figure 3.9) and can be described by 8 parameters. Only 6 parameters are free, since the length must be fixed to half a wavelength of the RF frequency to synchronize relativistic particles, and one parameter must be used to tune the cavity to the desired frequency. It is possible to generate cell geometries that have very similar fundamental mode properties–resonant frequency, geometry factor, G, R/Q, peak field ratios E_{pk}/E_{acc} and H_{pk}/E_{acc}–while having very different higher-order mode characteristics.

The initial center cell design minimized dynamic cryogenic losses due to the fundamental mode, which is equivalent to minimizing the power lost in cavity walls, P_c, at a given stored field energy, U, which is proportional to square of the operating voltage, V_c. If the cavity has a the geometry factor, G, defined as

$$G = Q_0 \cdot R_s = \frac{\omega \mu_0 \int_\Omega |\mathbf{B}|^2 \, d\Omega}{\int_S |\mathbf{B}|^2 \, dS}, \qquad (1.14 \text{ revisited})$$

where the top integral is performed over the cavity volume, Ω, with a bounding surface, S, and R_s is the average surface resistance of the cavity, the dissipated

107

power is minimized by maximizing $G \cdot (R/Q)$. This can be seen directly via

$$Q_0 = \frac{\omega U}{P_c} = \frac{2\omega U}{V_c^2} \cdot \frac{V_c^2}{2P_c}, \tag{3.16}$$

$$\frac{G}{R_s} = \left(\frac{R}{Q}\right)^{-1} \cdot \frac{V_c^2}{2P_c}, \tag{3.17}$$

$$\frac{P_c}{V_c^2} = \frac{R_s}{2G \cdot (R/Q)}. \tag{3.18}$$

Unfortunately, the design minimizing cryogenic losses due to the fundamental was very unstable in regard to cell shape imperfections due to machining variation, causing the beam breakup parameter to increase by several orders of magnitude, even when the error size is much smaller than currently achievable machining tolerances [VL09].

The instability in the original cell shape was due to some HOM passbands spanning a narrow frequency range. This is a sign of small coupling between the cells of the coupled multicell structure for these modes (analogous to having coupled pendulums with weak coupling). Due to the weak coupling, these modes and their field profiles along the cavity are very sensitive to small cell shape imperfections (equivalent to having coupled pendulums with different individual oscillating frequencies and resulting changes in coupled modes). This can have huge impact on mode damping, since it depends on field strengths in end cells of cavity since HOM loads are at cavity ends.

Simulating cavities with small shape imperfections indeed showed that and gave BBU currents far too low even with unrealistically small shape imperfections of $\pm 1/16$ mm.

To mitigate this effect, new center cells were designed with a slightly modified cell shape (including an increased iris aperture), which resulted in an in-

creased width of the initially narrow higher-order mode passbands, while preserving the properties of the fundamental mode's $R/Q \cdot G$ to within 5%. Increasing the passband width and cell-to-cell coupling makes the field distribution of the HOMs in a multicell cavity less sensitive to small dimensional variations. [VL09] This is accomplished by choosing cell geometries which have a large frequency spread between the passband's 0-mode, and the π-mode, as illustrated in Figure 3.9.
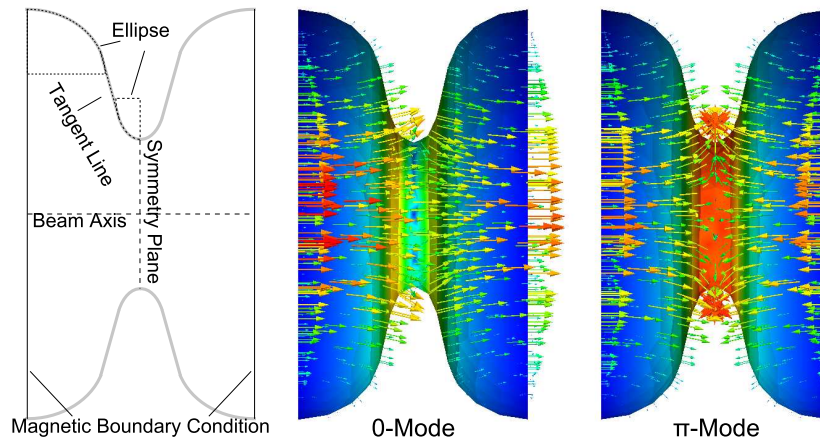
Figure 3.9: From left to right, center cell geometry, lowest mode in a passband having zero phase difference between cells, and the highest mode in a passband with π-phase difference between the cells. Vectors are electric field lines and colors correspond to electric field magnitude

The width of the first few HOM passbands are presented in Table 3.4. The geometrical properties of the final center cell shape are presented with the full optimization results in section 3.3.

Simulations demonstrated that cavities with the modified cavities were much more robust in regard to machining variation and that realistic cell imperfections (0.5 mm) did not lead to strong changes in the HOM damping and thus decrease the BBU current.

Table 3.4: Comparison of the frequency difference, Δf, between the 0-mode and π-mode of several higher-order mode passbands between the original center cell design and modified design. Notice the significantly increased width of the 3rd and 6th passband in the modified center cell shape.

Passband [GHz]	Original Δf [MHz]	Modified Δf [MHz]
1.8	192	188
1.9	95	73
2.5	31	107
2.7	277	277
3.1	55	47
3.4	10	20

Table 3.5: Initial and final center cell geometric figures of merit. Cyrogenic losses are slightly increased. The geometry factor and E_{pk}/E_{acc} are for the fundamental mode. Key: Eq.=Equator, Horiz.=Horizontal, Vert.=Vertical. The last four dimensions are half-axes of ellipses, measured in cm. Table reproduced from [VL09].

Parameter	Initial	Optimized	Unit
$R/Q \cdot G$	15576	14837	Ω^2
E_{pk}/E_{acc}	2.00	2.06	—
Wall angle	85	77	Degree
Iris Radius	3.500	3.598	cm
Eq. Horiz.	4.399	4.135	cm
Eq. Vert.	3.506	3.557	cm
Iris Horiz.	1.253	1.235	cm
Iris Vert.	2.095	2.114	cm

The center cell geometry found a good compromise between maximizing $R/Q \cdot G$ for the fundamental mode and reducing sensitivity to cell shape errors.

The center cells control the general features of the higher-order mode spectrum, so the next part of the design process is to ensure that the end cells efficiently couple HOMs to the absorbers where their energy can be extracted.

End-cell Optimization

As mentioned above, the half-end cells couple the higher-order modes to the beam line absorbers, thereby directly controlling HOM quality factors.

The end cell design includes a transition to a large beam pipe diameter (110 mm) that allows all higher-order monopole and dipole modes to propagate out of the cavity toward the beam pipe absorber. The two end cells are asymmetric, which helps to prevent trapped modes by breaking symmetry and shifting modes toward one end or the other. [Sek12] An iris reduction between the end cell and beam tubes (see Figure 3.8)helps to maintain a large R/Q, while the large beam pipe still allows HOMs to propagate out of the structure, a technique successfully employed in other designs [SBG⁺03, Mit91].

Each end cell geometry consist of an inner-half cell identical to the center cell shape, and modified design of the outer half cell. It was parameterized by six free variables per side. The end cell geometry is formed of two ellipses having four parameters each (ellipse centers and half-axes), and two more ellipses form an iris constriction flanging out to the beam pipe. Smoothness requirements constrain one ellipses' end points, as well as it's tangent.

The optimizer varied the half-axes of the three ellipses denoted by the symbols ▲, ●, and ◆ in Figure 3.16. The vertical position of the ellipse whose center is denoted by ▲ was also varied, adding a degree of freedom, but tuning requirements limited constrained a degree of freedom yielding six total.

Physical requirements yield system constraints: (1) The cavity frequency must be 1300 MHz, (2) The cryogenic losses due to the fundamental mode must be maintained to within 5% of the baseline design, (3) $E_{pk}/E_{acc} < 2.1$, which

is essential to reduce the risk of field emission, (4) wall angles must be more than 2.5° away from vertical to allow for proper chemical treatment and high pressure rinsing, (5) the radius of curvature of the design must be greater than 6 mm everywhere, as sharp bends are technologically challenging to produce, and undesirable from an electromagnetic perspective [VL09].

Optimization Algorithm

The ERL main linac cavity geometry was optimized in 2D (see Figure 3.10) simulating both the fundamental mode and dipole higher-order modes. The eigenmodes were solved with 2D finite element codes CLANS for the fundamental monopole mode and CLANS2 for dipole modes [MY99]. The beamline higher-order mode absorber was also included in the simulation, with half of the absorber on either side of the cavity. A realistic lossy dielectric for the absorbing loads was simulated with a permeability of μ_0 and a permittivity of $\epsilon = (50 - 25i)\epsilon_0$, corresponding to measured values of a carbon-loaded silicon carbide absorber [Cho10].
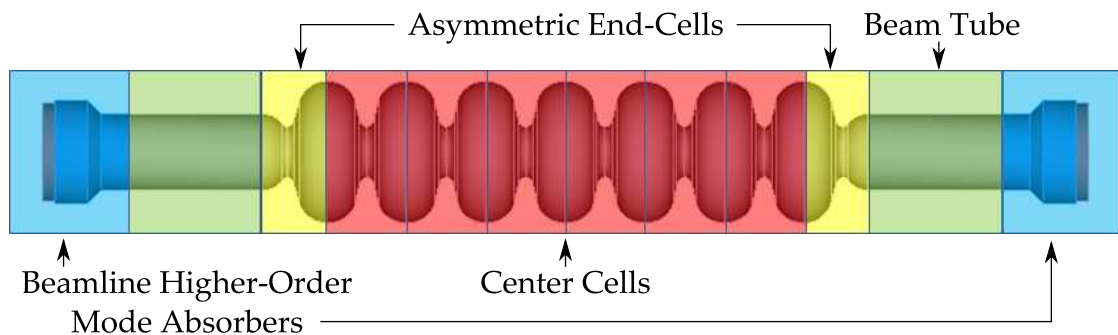
Figure 3.10: Model of the 7-cell cavity highlighting the major areas requiring design consideration. Center cells are relatively insensitive to fabrication variation, end cells couple HOMs to absorbers, the beam tubes maximize linac fill factor without excessively damping the fundamental mode, and the HOM loads extract HOM power from the cavity.

Each HOM passband was calculated using the four possible combinations of electric and magnetic boundary conditions at the symmetry plane of the HOM loads to simulate an infinitely long chain of identical cavities. This is more realistic than open boundary conditions because open boundary conditions are only applicable in the case of an isolated cavity, not one in a long chain of cavities. Thus, the HOMs computed here much more accurately reflect what one could expect in the main linac made out of a large number of cavities.

The optimization routine minimized the worst BBU parameter, ξ_λ, as defined in (Equation 3.15) for dipole HOMs from 1.5–10.0 GHz, which for the 4 boundary conditions meant computing the figures of merit for 1692 HOMs per iteration [VL10b]. The optimization is challenging because geometry changes that reduce the strength of one HOM can drastically increase the strength of another HOM. Thus, the problem is to find end cell shapes that simultaneously minimizes the highest BBU parameters of all the HOMs, which is an intrinsically non-analytic problem.

To simplify the optimization, the simultaneous minimization of N-HOMs was treated as the analytic problem of minimizing the worst HOM, under the non-analytic constraint that each BBU parameter of all other dipole modes in the spectrum be less than the maximal BBU parameter of all the modes $\equiv M$.[15] Minimization improves the BBU parameter by controlling the worst mode; all other modes are required to fall below M for the point to be in the search space. This process effectively minimizes all the HOMs simultaneously. Furthermore, should the control HOM be below another mode that had a smaller value earlier in the optimization, the optimization switches to control the new mode. Thus the non-analytic problem is decomposed into an analytic problem with a non-

---

[15]Personal communication with J. Sethna

analytic constraint.

The constrained optimization was carried out in parallel on 256 processors[16] with a simplex algorithm. MatLab code containing the basic structure of the objective function is presented below.

```matlab
function worst_RQQf = Cornell_ERL_Cavity_Objective_Function(y)
% Objective function for end cell optimization

        kill_flag = 0;        % Set to 1 if a test fails

% Scale the parameters to eliminate the interval constraints
% Get initial input from desire 'real coordinate guess', x, transform
% initial_input = atanh(2./(p2-p1).*(x-p1)-1)
    p1 = 1.0*ones(size(y)); % Default min_params
    p2 = 4.5*ones(size(y)); % Default max params
    x = (p2 - p1).*(tanh(y) + 1)/2 + p1;

% Load run settings including:
%       Prefix for geometry files
%       Which passbands to calculate
%   Number of modes to calculate/passband
    [prefix, pass_bands, modes] = ...
        Cornell_ERL_Cavity_read_run_settings('./run_settings.txt');

% # of passbands to calculate as well as # of boundary conditions
    num_passbands = length(pass_bands);
    bcs = 4;

% Check if end-cell parameters generate a suitable geometry:
%       Curvature constraints must fall within suitable limits
%       Cavity geometry must be tunable to 1300 MHz
%       Peak electric and magnetic fields must be within limits
%       Cavity quality factor must be above 2e10
%
% If point is unsuitable, set 'kill_flag' to 1 and return penalty
% Else, return cavity geometry and tune spacing
    [kill_flag, penalty, geo, sp_lf, sp_rt] = ...
        Cornell_ERL_Cavity_check_params(y);

    if kill_flag
        worst_RQQf = penalty;
        return
    end

    % Write files so the EM solver can compute HOMs
    Cornell_ERL_Cavity_gen_CLANS2_files(...
                geo, prefix, num_passbands, bcs);
```

---

[16]Resources leased from Cornell's Center for Advanced Computing

```
43
44          % Submit HOM jobs to cluster.
45      dos('python submit_clans2_jobs.py');

46
47  % Wait for jobs to complete and extract data
48  % If too many fail to complete, assign run a penalty value
49          [f, QL, R_Q, kill_flag, penalty] = get_HOM_properties();

50
51          if kill_flag
52                  worst_RQQF = penalty
53                  return
54          end

55
56          results_vec = [f QL R_Q];
57          rqqfs = R_Q.*sqrt(abs(QL))./(freqs);
58          fullvals = [freqs', QL', R_Q', rqqfs'];

59
60  % Return the worst HOM for the mode in question
61  % If another mode becomes 25% stronger, control on that one instead
62  % Baseline metric is max(R_Q*QL./f)
63          worst_RQQf = Cornell_ERL_Cavity_control_mode(R_Q, QL, f);

64
65          % Save results in a folder with the current time
66          cache_folder = datestr(now, 30);
67          save([cache_folder 'param.txt'], ...
68                  'yp', 'xp', 'sp_lf', 'sp_rt', '-ASCII');
69          save([cache_folder 'HOM_results.txt'], ...
70                  'results_vec', '-ASCII');
71          save([cache_folder 'freqs.txt'], ...
72                  'freq_vec','-ASCII');

73
74          h = semilogy(freqs, rqqfs,'b.');
75          xlabel('Frequency [MHz]');
76          ylabel('(R/Q) QL^{1/2} f^{-1} [\Omega/cm^2/MHz]');
77          grid on;
78          save([folder 'fulldata.txt'], 'fullvals','-ASCII');
79          saveas(h, [cache_folder 'modeplot.fig']);
80          saveas(h, [cache_folder 'modeplot.png']);
81  end
```

The function `Cornell_ERL_Cavity_check_params` ensures that the geometry satisfies the constraint equations $g_i \leq 0$, and returns a penalty value in the case that constraints are broken. Following [Rao09], the penalty function, p, is assigned via

$$p = \xi^* + \sum_i a_i \cdot \max(0, g_i)^2, \tag{3.19}$$

115

where ξ^* is the previously computed worst BBU parameter, and a_i is a vector specifying how much constraint violations are penalized. The values of a_i were chosen to make typical constraint violations cause p to be about 10-20% larger than ξ^*.

A plot of the BBU parameter for all 1692 dipole modes are presented in Figure 3.11.
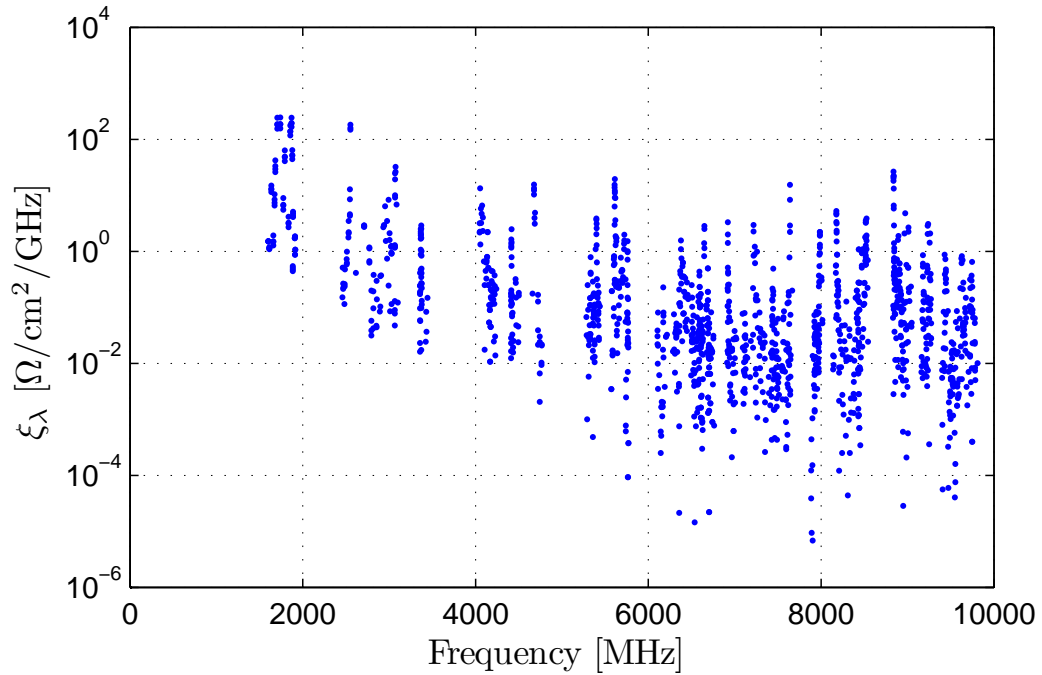
Figure 3.11: Beam breakup parameter versus frequency for the optimized main linac cavity. The 1692 modes are calculated for the four combinations of electric and magnetic boundary conditions.

The quality factor and R/Q of dipole modes are presented in Figure 3.12. Note that even though a few modes have large Q_L, their small values of R/Q mean they have only weak coupling to the beam, so these modes will not contribute strongly to beam breakup effects.

116
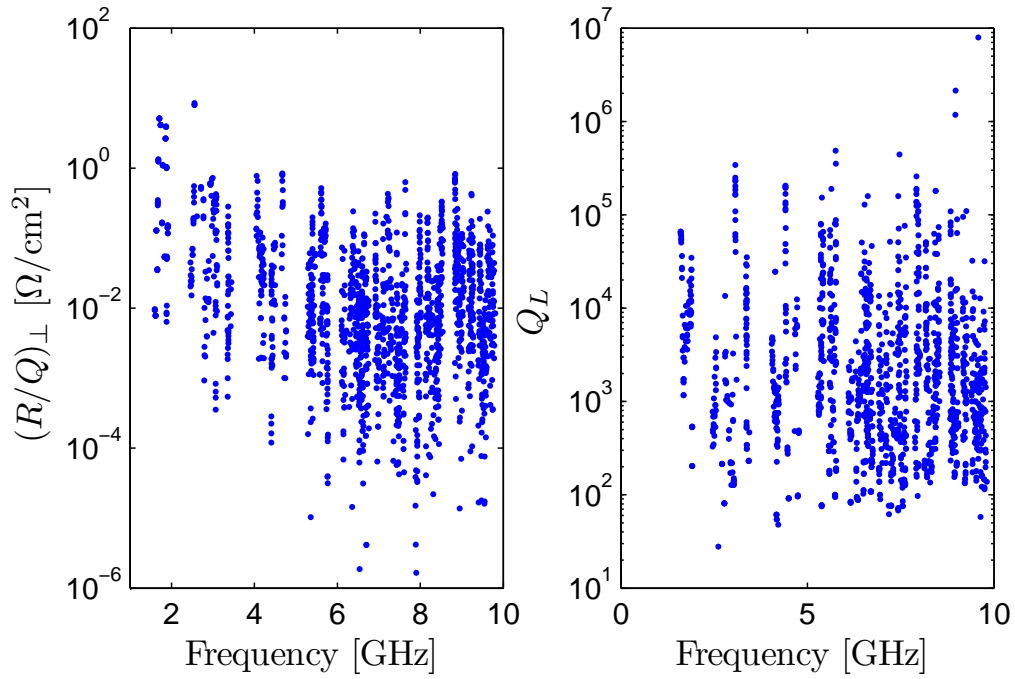
Figure 3.12: (R/Q) and Q_L values for dipole HOMs of the optimized cavity. The 1692 modes are calculated for the four combinations of electric and magnetic boundary conditions.

Optimization Results and Design Verification

After successfully optimizing the cavity end cells (the results are presented at the end of this section in Table 3.6) with respect to the beam breakup parameter, ξ, the performance of realistically shaped cavities had to be verified, since cavities cannot be fabricated exactly to the optimal geometry. Verification was accomplished by generating cavity geometries with each half-axis parameter, a_i, being replaced with $a_i + \delta_{max} U(-1, 1)$, where U is a uniformly distributed random variable between -1 and +1, and $\delta_{max} = \{0.125, 0.250, 0.500, 1.000\}$ mm is the machining tolerance.

For each σ, 400 unique cavity geometries were generated randomly, tuned for field flatness of the fundamental mode, and their higher-order mode spectra
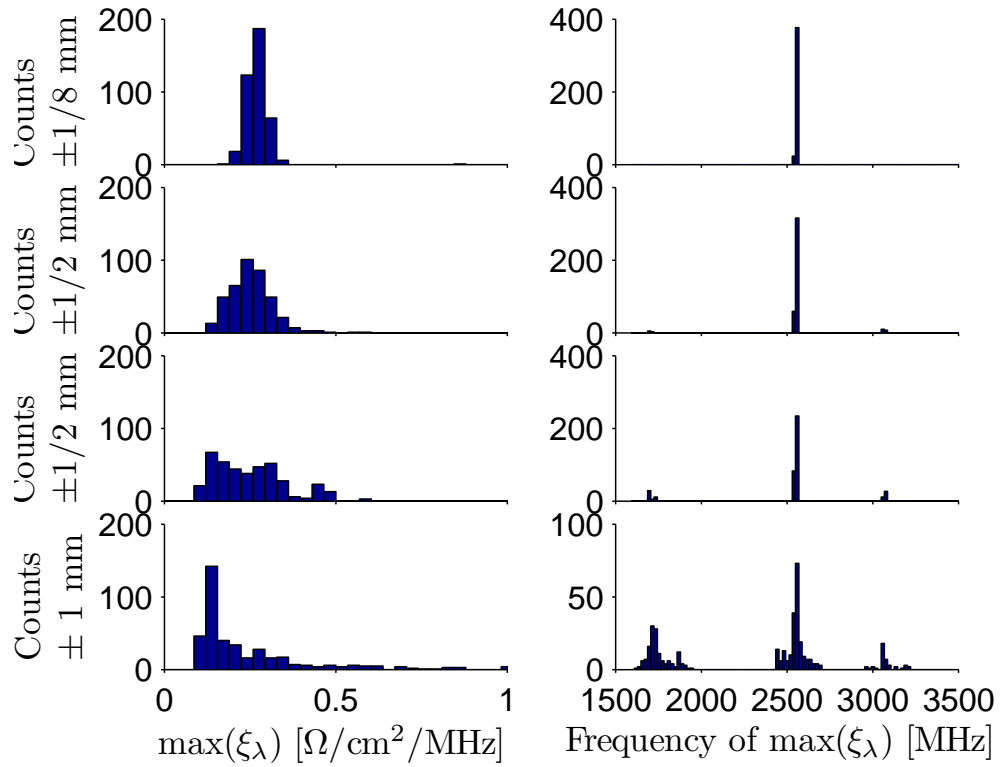
Figure 3.13: Histograms of the worst beam breakup parameters ξ_λ and the corresponding frequencies for randomly generated cavities with various machining tolerances. Each row contains data for a single machining tolerance. As the fabrication tolerances, δ_{max}, loosen, $\max \xi_\lambda$ increases and the frequency of the strongest mode in the ERL strays from the value it has in the ideal cavity. For larger tolerances, modes outside of the 2.5 GHz dipole passband begin to cause beam breakup.

were computed with CLANS2 (see Figure 3.13).

From this set of cavities, 100 ERLs were generated and simulated via particle tracking to determine the BBU current. Each cavity location in the simulated ERL lattice was populated with HOM properties (frequency, Q, and R/Q) from a randomly selected cavity (drawn without replacement) with realistic shape variations. The threshold current for each ERL was then computed with BMAD, and the results are displayed in Figure 3.14. [VKL11]
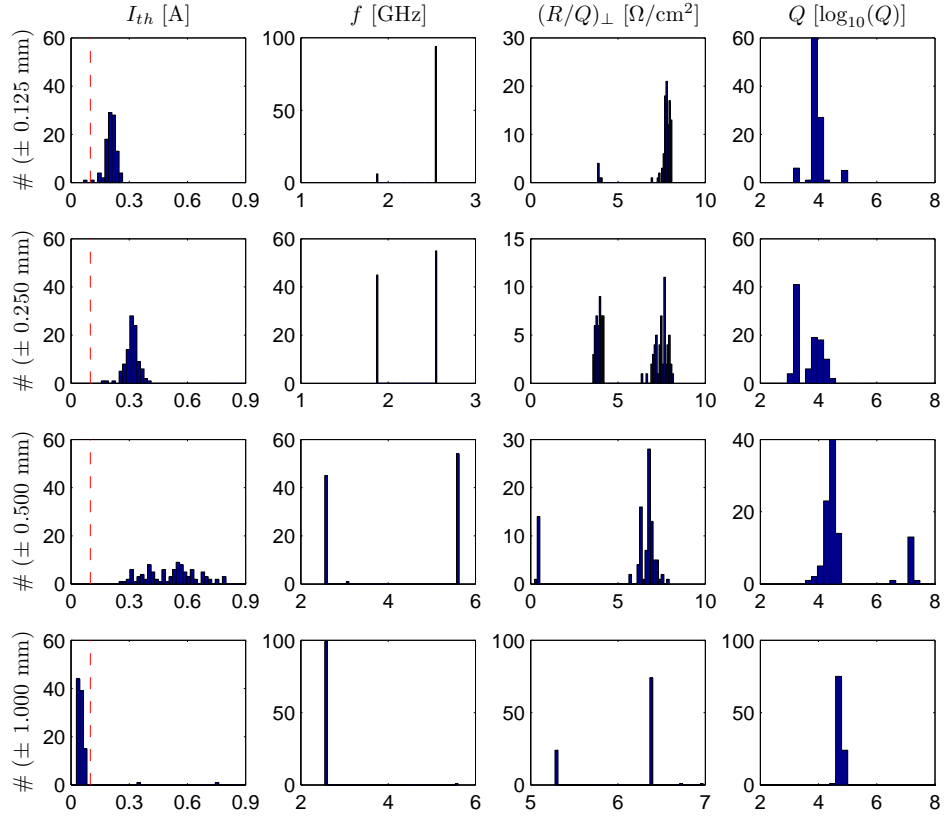
Figure 3.14: Histograms of BBU current and the properties of the HOM limiting the current computed by particle tracking for 100 simulated ERLs. The threshold current, frequency, $(R/Q)_\perp$, and quality factor of the mode causing BBU are displayed in the columns, and the rows correspond to the maximum machining tolerance for the runs. As the machining tolerances loosen, the HOM properties begin to diverge from their optimized values.

The relative cavity-to-cavity frequency spread of the HOMs in the 400 cavities was computed for the simulated fabrication variation dimensions, δ_{max}. Figure 3.15 compares the threshold current obtained by merely varying σ_f/f, with the frequency spread obtained from ERLs composed of unique cavities (characterized by maximum shape imperfection δ_{max}) with independent HOM properties.
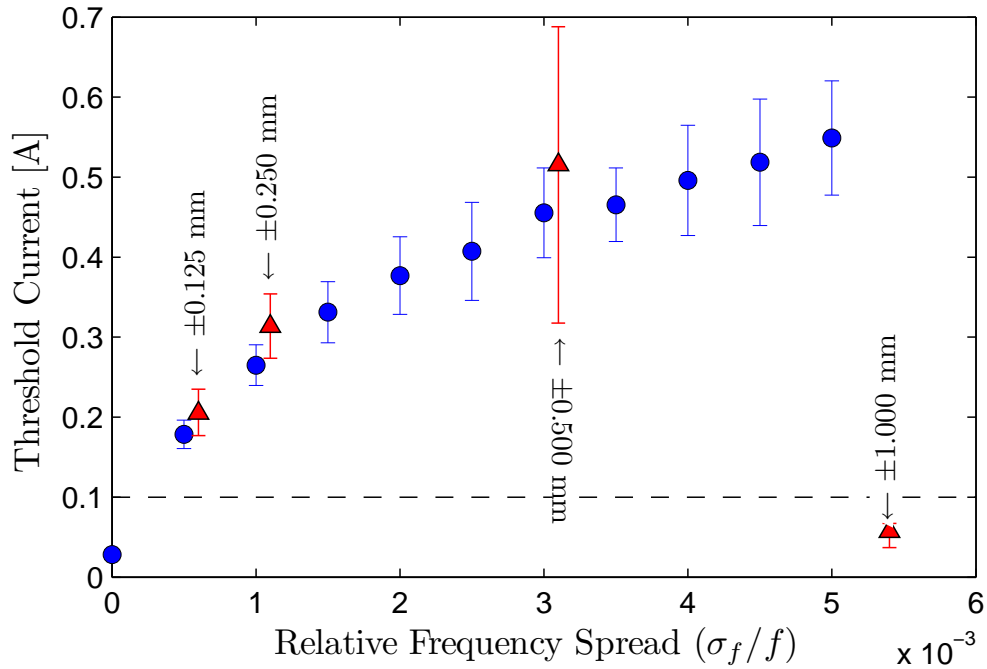
Figure 3.15: Average beam breakup current versus relative frequency spread for simulated ERLs. Blue circles mark the threshold current through an ERL with every cavity having the same nominal HOM frequency, Q, and R/Q values of 10 HOMs with the largest values of ξ_λ, as a function of relative cavity-to-cavity frequency spread. The red triangles denote the average threshold current for ERLs generated from realistically shaped cavities, having different frequencies, Qs and R/Qs from shape imperfections, and no artificial cavity-to-cavity frequency variation of these modes. The lower (upper) error bars mark the threshold current that 90% (10%) of the simulated ERLs can support. In all cases except the 1 mm variation size, simulated ERLs well exceed the design specification of 100 mA current, denoted by the dashed horizontal line.

For the simulated machining tolerances less than ±1.000 mm, the threshold current is well above the design specification of 100 mA, reaching an average value of over 500 mA for ±0.500 mm shape variations. To avoid, the large variability with ± 0.500 mm machining variation, the maximum allowable machining tolerance was set at for cavity fabrication is ±0.250 mm (though the cavity design is robust enough to tolerate even larger variations). This level of fabrication variation supports and current through the linac above 300 mA, triple

the design specification. In section 4.2, it will be demonstrated that tolerances between 0.250 - 0.500 mm are attainable in real cavities.

It is important to note that if the fabrication variation is too small (< 1/16 mm), the expected threshold current would not meet design specifications due to small cavity-to-cavity frequency spread causing many cavities to act coherently. Fortunately, experience with current fabrication technology demonstrates that precision is limited to just below our 0.250 mm specification, meaning suitable frequency spread is "built in" via the machining process.

After demonstrating that 2D shape variations resulted in ERLs able to support beam currents well in excess of 100 mA, the effect of 3D machining variation was investigated. The 3D cases took into account cell elliptical compression and stretching of the cell profile up to 1 mm as well as introducing bumps or pits on the cell surface with lengths up to 1 mm. and HOMs were calculated in 3D with ACE3P. Using these results, particle tracking was again performed. For these cases the mean threshold current expected for a realistic ERL was about 400 mA, and in all cases far exceeded the design specification. [XKL⁺11]
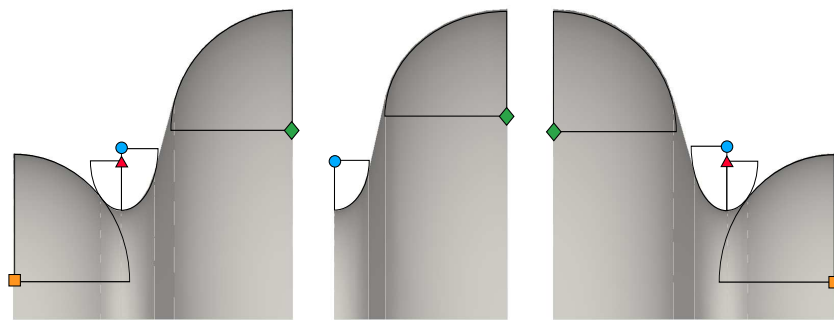
Figure 3.16: Illustration of the cell primitives for the left half end cell, the center cell, and the right half end cell. The values for each ellipse center denoted by the colored geometrical shape are presented in Table 3.6. The beam axis along the horizontal is the direction of increasing z.

The final ellipse properties are presented in Table 3.6, with Figure 3.16 illus-

Table 3.6: Ellipse properties for the optimized cell primitives used in the Cornell ERL 7-cell cavity. The properties of each ellipse in Figure 3.16 are: coordinates of the center of the ellipse (c_z, c_r), longitudinal half-axis h_z, and radial half-axis h_r. The origin of each cell's coordinate system lies along beam axis at the lower left corner of each shape. All values are in centimeters.

Ellipse	c_z	c_r	h_z	h_r
Center Cell				
🔵	0.0000	5.712	1.235	2.114
🔶	5.7652	6.731	4.135	3.557
Left End Cell				
🟧	0.00000	1.900	3.600	3.600
🔺	3.58665	5.695	1.127	2.095
🔵	3.58665	6.029	1.250	2.429
🔶	9.38034	6.238	4.146	4.050
Right End Cell				
🔶	0.00000	6.231	4.092	4.056
🔵	5.71111	6.001	1.253	2.401
🔺	5.55404	5.695	1.128	2.095
🟧	9.29776	1.900	3.600	3.600

trating the location of each ellipse.

At this point the 2D cavity geometry was optimized and verified to satisfy design design constraints with simulated BBU current in the 300 to 500 mA range for realistic shape imperfections, which pushes the threshold current limit three times above the requirement for the Cornell ERL.

Optimized Cavity Figures of Merit

The structural properties of the optimized Cornell ERL main linac cavity geometry are presented in the top portion of Table 3.7, which include results of mechanical simulations calculating the Lorentz-force detuning constant. [PL12b] Electromagnetic properties of the cavity's fundamental mode are shown in the middle of the table.

Table 3.7: Top: Structural properties and figures of merit for the optimized main-linac cavity for Cornell's ERL. Middle: Fundamental mode figures of merit. Bottom: Loss factors for the optimized main-linac cavity for Cornell's ERL, with a σ = 0.6 mm electron bunch from a 2D wakefield calculation with ABCI. [Chi94]

Structural Properties		
Parameter	Value	Unit
Type of accelerating structure	Standing wave	—
Accelerating Mode	TM_{010}, π-mode	—
Operating Gradient	16.2	MV/m
Intrinsic quality factor, Q_0 at 1.8 K	$> 2 \times 10^{10}$	—
Loaded quality factor, Q_L	6.5×10^7	—
Cavity half bandwidth	10	Hz
Cell Iris diameter	36	mm
Beam tube diameter	110	mm
Number of cells	7	—
Active length	0.81	m
$\Delta f / \Delta L$	16.0	kHz/μm
Lorentz-force detuning constant	1	Hz/(MeV/m)^2
Fundamental Mode Electromagnetic Properties		
Parameter	Value	Unit
Fundamental Frequency	1300	MHz
Cell-to-cell coupling	2.2	%
Geometry factor	270.7	Ω
R/Q (circuit definition)	387	Ω
E_{peak}/E_{acc}	2.06	—
H_{peak}/E_{acc}	4.196	mT/(MV/m)
Wakefield Loss Factors		
Parameter	Value	Unit
Total longitudinal loss factor	14.7	V/pc
Longitudinal loss factor from non-fundamental modes	13.1	V/pc
Transverse loss factor	13.7	V/pc/m

The loss factor of a beam travelling through the structure was calculated in 2D with a code ABCI. [Chi94] A 0.6 mm long Gaussian bunch was driven through a string of 4 accelerating cavities–which was the maximum number of cavities that could be simulated due to memory constraints–and the wakefield was calculated up to 150 GHz. The loss factors are summarized in the bottom

section of Table 3.7.

The longitudinal loss factor, $k_{\parallel}$, relates the average HOM monopole power, P_{avg}, generated by a beam current, I_b, consisting of bunch charges, q_b, according to

$$P_{avg} = k_{\parallel} \cdot q_b \cdot I_b. \tag{3.20}$$

For the Cornell ERL, P_{avg} = 13.1 V/pC · 77 pC · 200 mA = 200 W, would be expected for a large number of cavities with random HOM frequencies. This power can be lower or higher depending on how far the beam harmonics are from HOM frequencies. The design of the cavity ensures that no strong monopole modes are near beam harmonics of 2600 MHz, preventing overloading the HOM absorbers with monopole power.

3.3.1 High Power Coupler Design

The cavities in the ERL main linac will be operated at very high loaded quality factors, due to the large external coupling, Q_{ext}, of the high power input coupler. Because the energy transferred from the decelerated beam to the RF-cavity field is equal to the energy transferred from the RF field to the accelerated beam in an ideal ERL, there is virtually zero beam loading, and the optimal Q_{ext} only depends on the typical detuning, Δf, [BBB⁺11]

$$Q_{ext} = \frac{f_0}{2\Delta f}. \tag{3.21}$$

Estimates of the expected detuning suggest that 10 Hz is typical peak detuning of the cavities in operation, meaning Q_{ext} = 6.5 × 10⁷.

The main linac input coupler for the Cornell ERL main linac cavities is based on the TTF-III design, [DKM01, M⁺99] which was intended for pulsed linac operation, and modified to support up to 5 kW of reflected power in continuous operation. [VB09] The antenna is inserted into a port on the beam tube of the cavity that is at 2.0 K. The coupler contains two insulating alumina ceramics separating the cavity vacuum space from the 80 K space and the 300 K space. Figure 3.17 presents a cross-sectional view of the antenna.
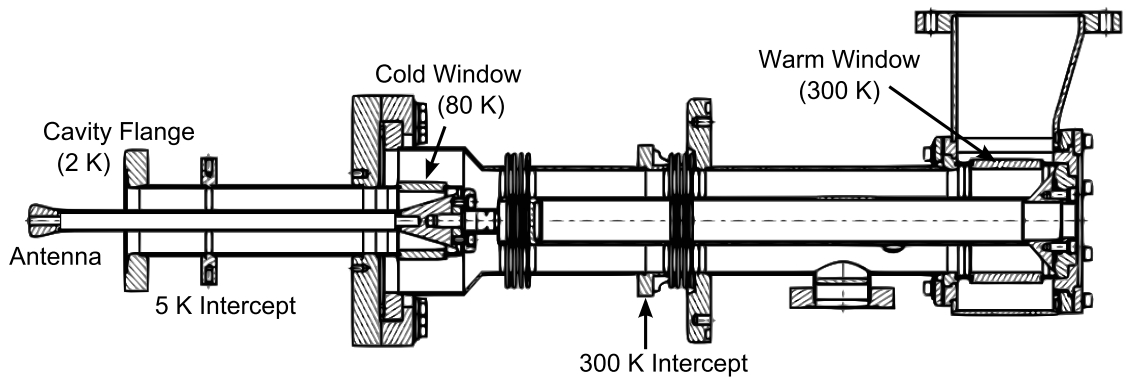
Figure 3.17: Cross-sectional view of the ERL main linac high power RF input coupler. Bellows allow the coupler to deflect up to 10 mm during cool-down. Each main linac cavity will be equipped with this type of coupler.

Subsequent simulations modelled the effect of the coupler on the cavity's properties. Alumina's electromagnetic properties vary on the type and purity of the ceramic, but are not lossy and over a wide range of frequencies (1 kHz–100 GHz) and have a dielectric constant between 7.0–10.0. [Aue96] Simulations modelling the entire structure treated the alumina as loss-free with $\epsilon = 9.3\epsilon_0$.

The first effect of the coupler that was investigated, was the time-dependent interaction between 3D RF fields near the input coupler antenna and the electron beam, discussed in the following section.

3.3.2 Compensation Stub Studies

Cavity microphonics will detune the cavities by more than one bandwidth during operation. This detuning will cause a time dependent change of the coupler kick on a passing electron bunch. Previous work suggested that a way to mitigate the overall kick and resulting emittance growth could be by including a symmetrizing compensation stub. [BH07] The coupler kick was calculated as a function of detuning and compensation stub length. [VLS11] The fact that these simulations are done as a function of detuning is of central importance because ERLs operating detuning is large ($\Delta f / f_{1/2} \geq 1$). Investigation began by mod-
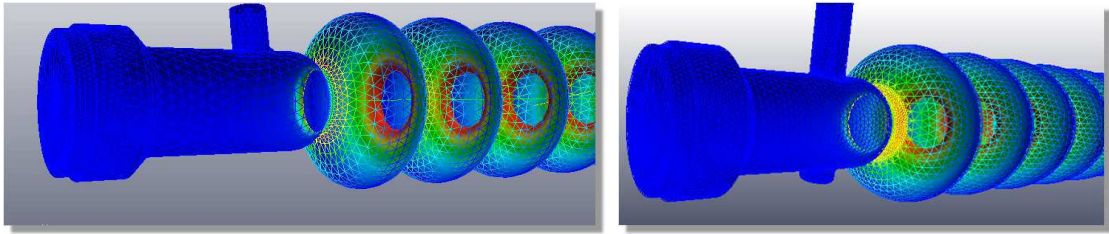
Figure 3.18: View of 7-cell cavity coupler region of a model without (left) and with (right) a compensation stub. Coloring corresponds to electric surface field intensity.

elling the cold portion of the antenna, which couples to the fundamental mode with $Q_{ext} = 6.5 \times 10^7$. Cavity geometries with and without a compensation stub are shown in Figure 3.18.

The height, H, of the compensation stub was varied, as shown in Figure 3.19, and the frequency dependence of the coupler kick was was simulated with S3P, [KCG$^+$10] as presented in Figure 3.20. Axial fields through the cavity on resonance are presented in Figure 3.21, showing the transverse components near the coupler region.

The theoretical basis for calculating of coupler kicks has been dealt with thor-
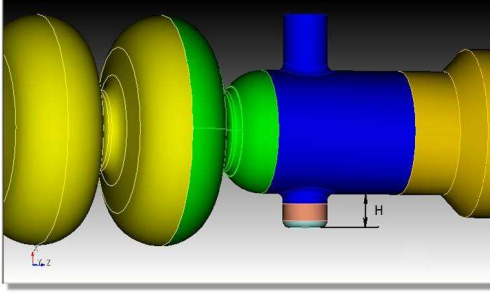
Figure 3.19: Coupler region of 7-cell cavity geometry. Orange cylinder illustrates method used to tune the length of the compensation stub, with a total height, H.
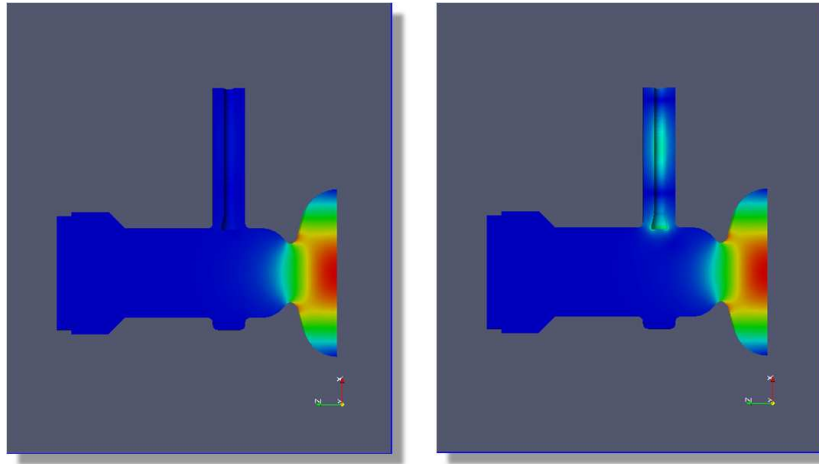
Figure 3.20: Coupler region of cavity showing electric field intensity for two frequencies. Left is on resonance for the 1300 MHz 7-cell structure and right is obtained by launching a wave through the fundamental power coupler with a frequency 14 kHz higher.

oughly in other sources [BH07]; here we just summarize a few key results for completeness.

As argued in [VLS11], given the z-component of the electric field, E_z along the beam axis of the cavity as a function of frequency, f, of the incident wave, the resonant frequency, f_0, is defined implicitly as the frequency that results in the maximal momentum gain to the beam:

$$P_z(f_0) = \max_f \left| \frac{q}{c} \int_{z=0}^{z=L} E_z(f; x = y = 0, z) \exp\left(\frac{f \cdot z}{c} \cdot \tau i \right) dz \right|, \qquad (3.22)$$

127
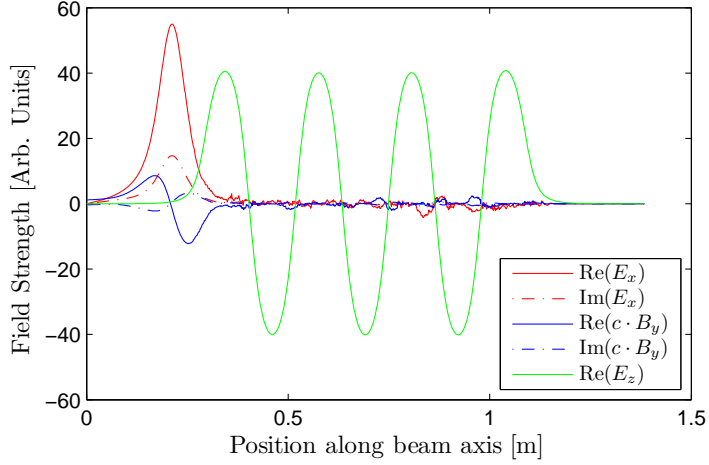
Figure 3.21: Axial fields through the cavity at 1300 MHz. E_z has been scaled down by a factor of 500 for clarity. There are non-zero transverse components of the electric and magnetic field near the coupler (around z = 0.14 m), which vanish further into the cavity. The phase was chosen such that $\text{Im}(E_z)$ vanishes.

where q is the bunch charge of the electron beam, and $\tau \equiv 2\pi$ is the corrected circle constant. [Pal01][17]

Since the longitudinal momentum transfer is proportional to the accelerating voltage in the cavity, one can use the general form of a resonator with near infinite Q_0 and loaded Q, Q_L to write:[18]

$$P_z(f) \propto V(f) \propto \left[\left(\frac{f_0}{f} - \frac{f}{f_0} \right)^2 + \frac{1}{Q_L^2} \right]^{-1/2}. \tag{3.23}$$

This equation can be used with the curve $P_z(f)$ to accurately determine both the resonant frequency and the loaded Q of the cavity.[19]

The normalized coupler kick to the bunch can be calculated by calculating the momentum imparted to the bunch given the field components along the

---

[17]The author in [Pal01] makes a compelling argument for the circle constant to be defined as 2π, but issue is taken with the strange symbol chosen in the article, and this section follows the suggestion of labelling this constant τ as put forth in [Har13].

[18]For a given frequency shift, δf, this statement is only true if $\delta f/f \ll 1$, since if f changes too much, the electron's transit time factor will change as well.

[19]The same mathematics is used in HOM analysis presented in Appendix B.

beam beam axis to give

$$\vec{P} = \begin{pmatrix} P_x \\ P_y \\ P_z \end{pmatrix} = \frac{q}{c} \begin{pmatrix} \int dz \left(E_x - cB_y \right) \exp \left(\frac{f \cdot z}{c} \cdot \tau i \right) \\ \int dz \left(E_y + cB_x \right) \exp \left(\frac{f \cdot z}{c} \cdot \tau i \right) \\ \int dz \, E_z \exp \left(\frac{f \cdot z}{c} \cdot \tau i \right), \end{pmatrix} \qquad (3.24)$$

where $\vec{E} = (E_x, E_y, E_z)$ and $\vec{B} = (B_x, B_y, B_z)$. The (frequency dependent) coupler kick is given by

$$\kappa(f) = \sqrt{\frac{P_x^2(f) + P_y^2(f)}{P_z^2(f)}}. \qquad (3.25)$$

The frequency dependence has been made explicit to demonstrate that the bunch kick is a function of detuning. In the simulations the cavity and coupler is symmetric about the xz-plane, meaning that P_y vanishes, so $\kappa = P_x/P_z$.

Note that κ is complex, and the real part of κ applies a kick to the bunch, where as the imaginary part causes the beam's emittance to increase. The kick is time dependent since the frequency change is due to microphonics that modulate at 10-100 Hz (in addition to the oscillation at the RF frequency). The rapid shifts are very difficult to correct with steering magnets, so should be mitigated in the coupler design.

Expected cavity x and y pitch errors in the fabricated ERL also contribute kicks to the beam, and simulations suggest the ERL's low emittance mode requires $|\kappa| < 1 \times 10^{-4}$. [May11] Coupler kicks should not exceed this threshold value.

Figure 3.22 compares the resonant frequency, as defined by frequency that gives largest longitudinal momentum transfer to the beam, with the frequency supplying minimal coupler kick. The kick strongly depends on the detuning
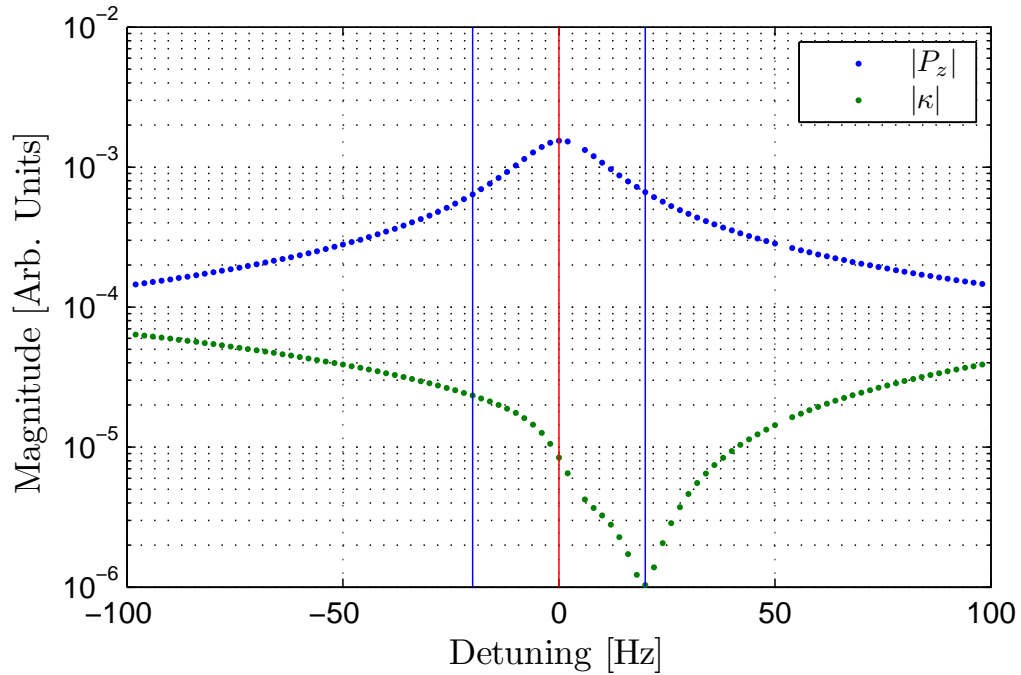
Figure 3.22: Magnitude of the longitudinal momentum gain and normalized coupler kick as a function of frequency for a geometry without a compensation stub. Red line marks resonant frequency of the cavity, and the blue lines mark ±20 Hz, which is expected microphonic detuning for the ERL.

of the cavity. Additionally, simulations show that detuning to lower frequencies leads to a larger kick than detuning to higher frequencies, an unanticipated result.

Microphonics, mechanical vibrations that couple to the electric field, [KSS67] are expected to introduce peak detuning of ±20 Hz. [BBB+11] The the coupler kicks at peak detuning and resonance was investigated.

The coupler kick as a function of frequency was computed for two geometries: one where the bottom of the symmetrizing stub was rounded with a radius of 3 mm, and one retaining the sharp edge of a simple cylindrical stub. For these geometries, 5 stub heights were simulated, along with the case of no stub at all.

The results of these simulations are presented in Figure 3.23.
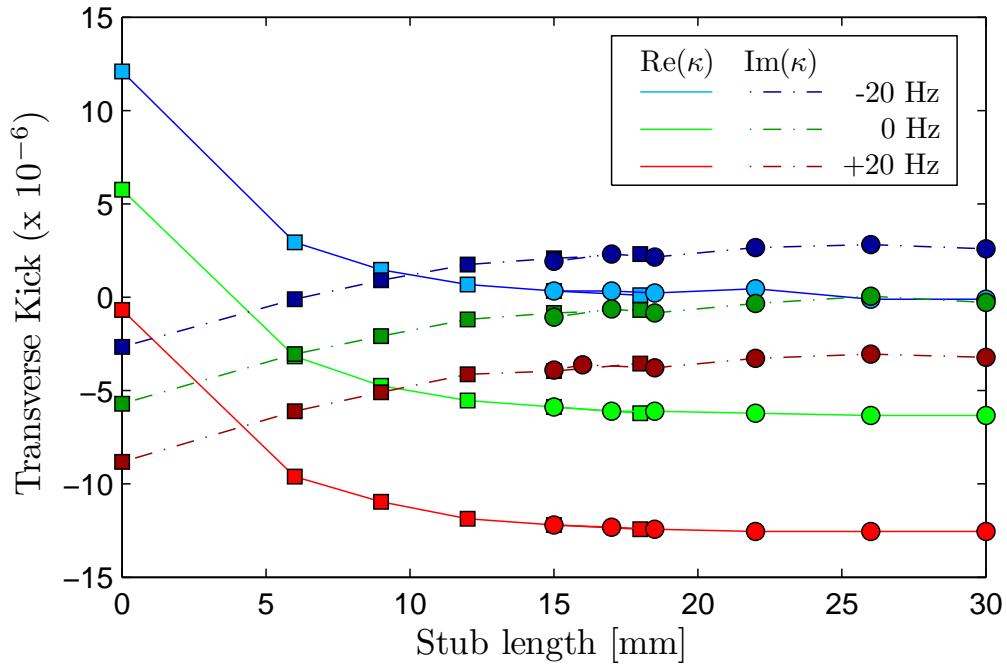
Figure 3.23: Real and imaginary components of transverse kick for -20, 0 and +20 Hz detuning. Circles, ∘, correspond to compensation stubs with 6 mm rounding at the bottom, and squares, □, show points without rounding–a necessary design choice to make short compensation stubs. Minimal kick occurs for about 10 mm deep stubs.

Figure 3.24 plots the maximum absolute values of the real and imaginary parts of κ for various stub lengths. The real component is minimized for $H =$ 6 mm, but the imaginary part is minimized for very large stub lengths.

Fortunately, the effect of these normalized kicks with $|\kappa| < 3 \times 10^{-5}$ are less than the expected, meaning that is sufficient to run successfully in the ERL's low emittance mode, which requires $|\kappa| < 1 \times 10^{-4}$, [May11] so the compensation stub is unneeded, and will not be included in the cavity design.

These investigations demonstrated that for the Cornell ERL main linac cavity a compensation stub is unnecessary, but even so, microphonics should be
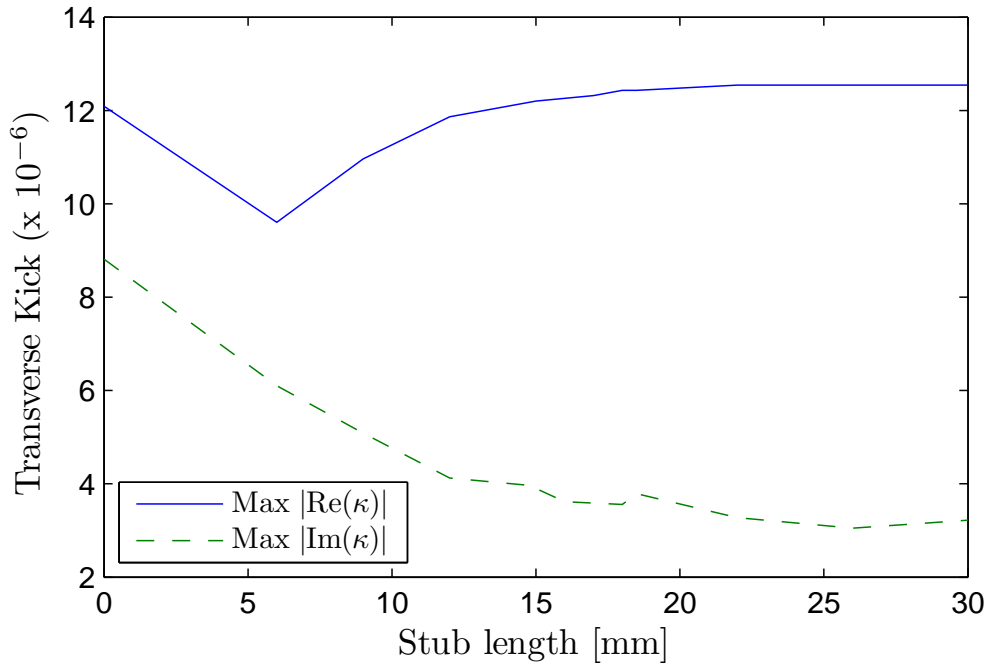
Figure 3.24: Maximum absolute values of the real and imaginary parts of the coupler kick, κ as a function of stub length over a detuning range of ±20 Hz.

kept small since they can cause the transverse kick to increase by more than an order of magnitude over the ±20 Hz bandwidth. This effect may be worse in accelerators with lower Q_{ext}, so for this type of machine, this effect should be investigated.

3.3.3   3D HOM Simulations

To investigate the influence of the high power coupler on the higher-order mode spectrum, simulations were performed with Omega3P. The center planes of the HOM loads and the rectangular waveguide port were set to either electric or magnetic boundary conditions. Several types of modes were located, finding monopole, dipole, quadrupole, sextupole and octupole HOMs as well as some

that strongly interact with the coupler.[20] Field patterns and properties of selected modes are presented in Figure 3.25.
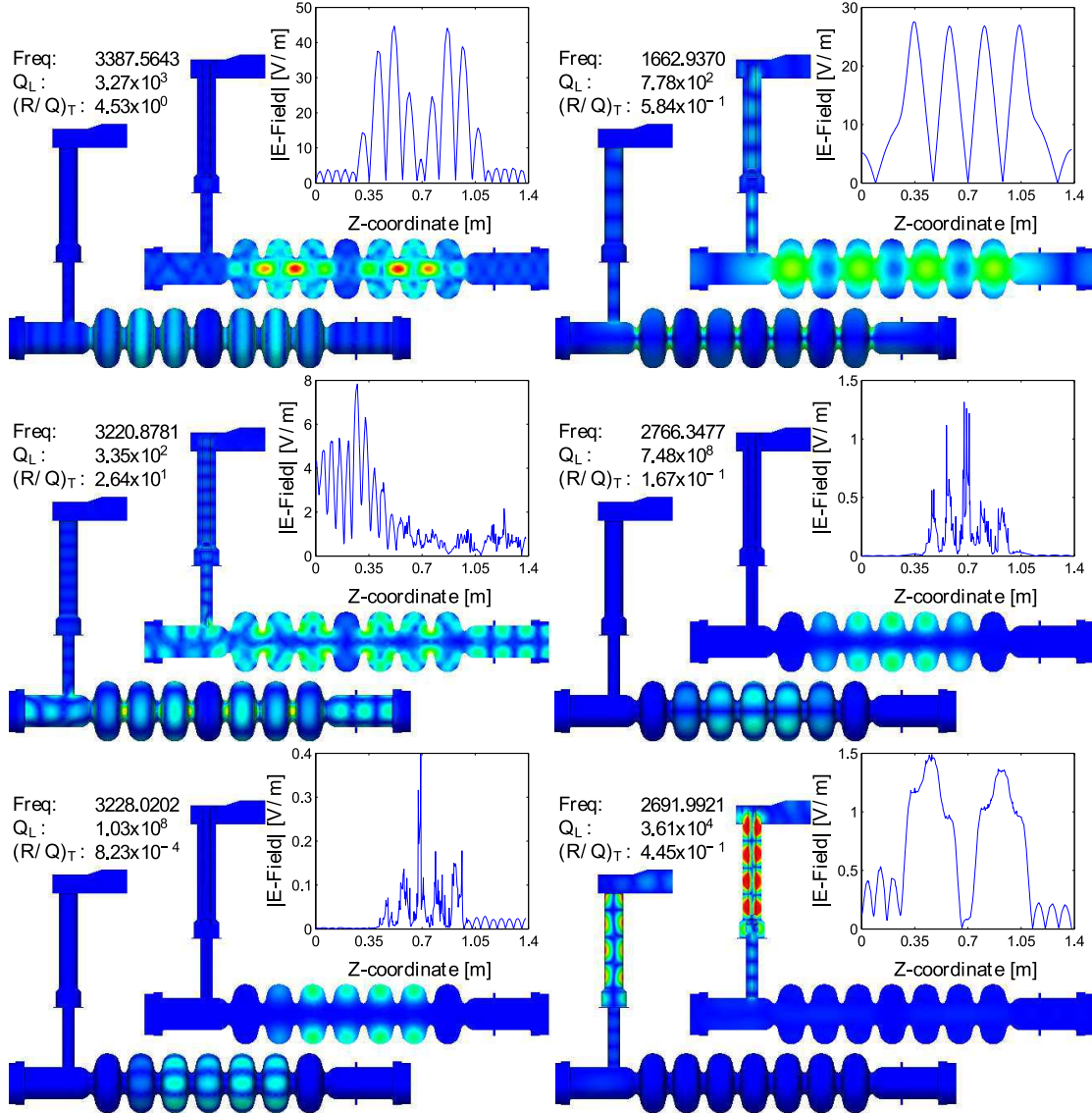
Figure 3.25: Electric field magnitude on cavity surface and mid-plane as computed by simulations with ACE3P. Frequency in MHz, quality factor and $(R/Q)'_\perp$ in Ohms (see Equation 1.19) is given for each mode along with the electric field profile along the cavity length with $r_0 = 1$ mm. From left to right, top to bottom, the mode types are monopole, dipole, quadrupole, sextupole, octupole and a mode contained in the coupler.

---

[20]These are somewhat artificial, created by the boundary condition at the end of the rectangular waveguide, and will probably be strongly damped for matched waveguide conditions.

A plot of the quality factors vs the frequency of the various types of higher order modes are presented in Figure 3.26. The frequencies of the modes agree with 2D simulations (discussed later in section 4.4, specifically Figure 4.42), but the significantly lower quality factors of quadrupole, sextupole and octupole modes suggest that these modes are only trapped if the cavity exhibits a high degree of symmetry. Symmetry breaking due to the coupler helps to concentrate HOM field near the beam tubes instead of near the center of the structure, increasing the coupling of these modes to the higher-order mode loads.
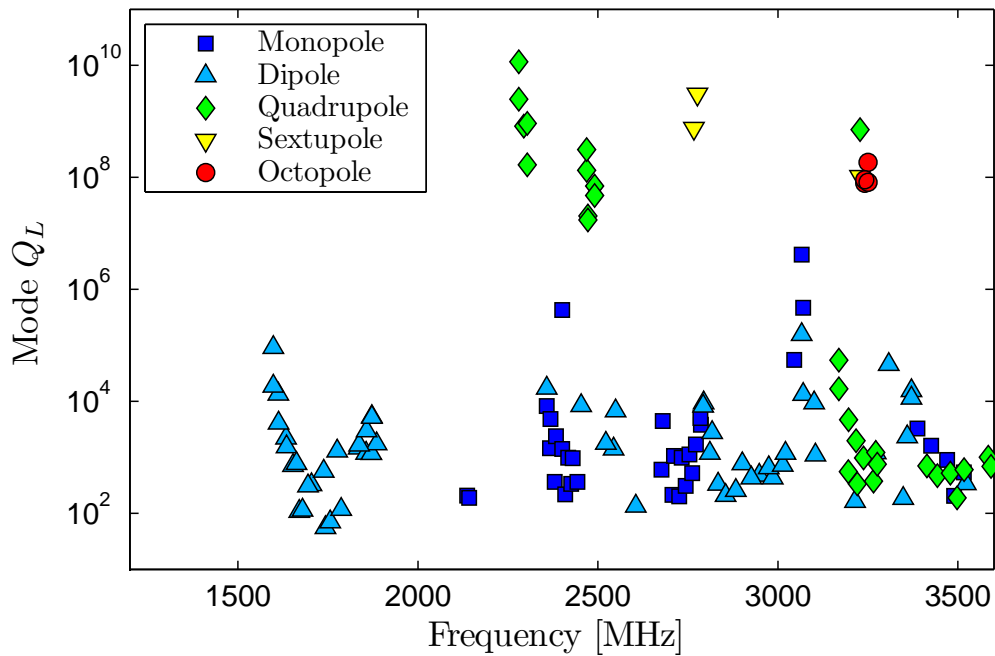
Figure 3.26: Higher-order modes in the ERL cavity with full input coupler geometry. Both electric and magnetic field boundary conditions were simulated to obtain modes expected in a full string of cryomodules.

3.4 Cavity Classes

Since BBU current can be lowered by multiple cavities acting coherently, by shifting the relative frequency of HOMs from cavity to cavity, the effective resonant kick given to the beam through the machine can be reduced. An increase in the threshold current has been seen when taking machining perturbations into account (recall Figure 3.15). Small dimensional errors change the shape of each cavity slightly and introduce a relative HOM frequency spread from cavity to cavity, and thus increase the threshold current.

It was shown in Figure 3.15 that simply relaxing machining tolerances to ever larger values to increase the frequency spread is not a way to increase the beam breakup current because too large shape perturbations (> 0.500 mm for the optimized cavity) can lead to trapped modes certain cavity shapes lead to trapped modes that will strongly reduce BBU current. [VL11] Instead, additional frequency spread can be introduced in a controlled way by designing multiple cavity center cell classes can be designed that have roughly the same fundamental mode properties, while having higher-order modes at different frequencies.

The additional cavities are made by selecting a new center cell design and optimizing the end cells for this center cell shape. By using several cavity shapes in the same ERL, having different HOM spectra, the relative cavity-to-cavity frequency spread of the cavities is increased.

The four parameters characterizing a center cell cavity were varied by ±5 mm in 1 mm steps, and the frequencies of 0- and π-modes, f_0 and f_π respectively, were calculated to obtain the first 6 dipole HOM dispersion curves
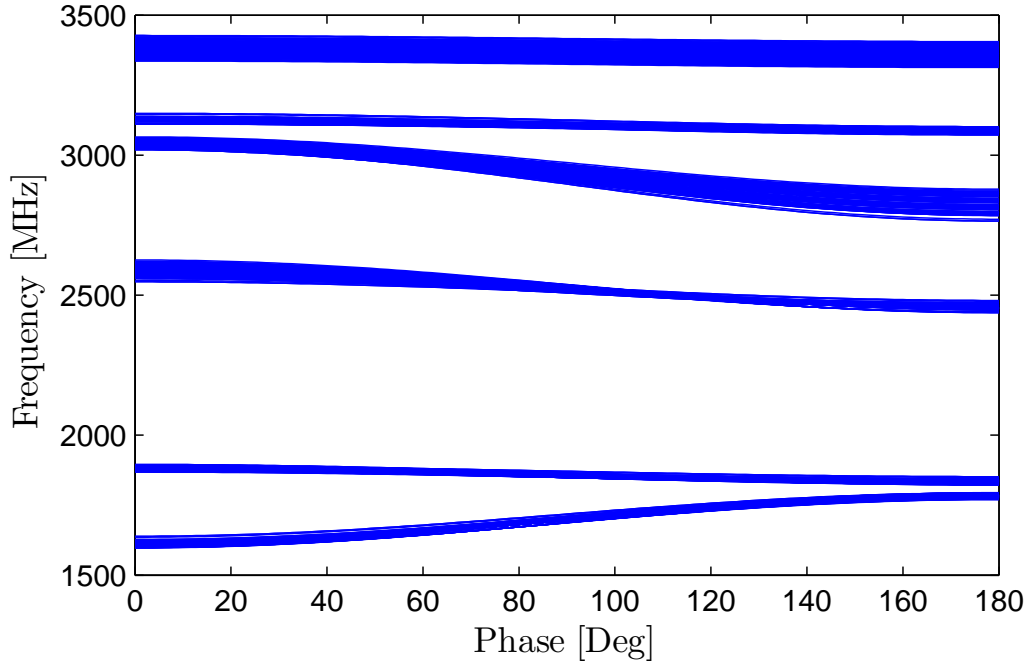
Figure 3.27: Dispersion curves for multiple center cell shapes, demonstrating that a large cavity-to-cavity frequency spread can be obtained while keeping similar fundamental mode properties.

for each geometry. Dispersion curves are calculated from these modes via

$$f(\phi) = f_0 \sqrt{1 + 2k_{cc}(1 - \cos\phi)}, \tag{3.26}$$

$$k_{cc} \equiv \frac{f_\pi^2 - f_0^2}{2f_0^2}, \tag{3.27}$$

where k_{cc} is the cell-to-cell coupling factor of the passband. [Lie01] Note that for electric coupling, the π-mode has a higher frequency than the 0-mode, where as for magnetic coupling, the reverse is true. [Sch11]

Dispersion curves are presented in Figure 3.27 for center cells that are within 5% of the optimized cavity's $R/Q \cdot G$ and H_{pk}/E_{acc}; E_{pk}/E_{acc} was maintained at 2.1. In addition, only cavity geometries with $|f_0 - f_\pi| > 20$ MHz were considered, since cavities with narrow passbands are not robust with respect to machining variation.

To maximize cavity-to-cavity frequency spread, $1, \ldots, n, \ldots, N$ cell shapes were chosen that cover a broad region of possible HOM frequencies. Suppose the dispersion curves of the $1, \ldots, m, \ldots, M$ suitable cavities have frequency vs phase characteristics given by $k_m(\phi)$. Furthermore, let $f_\phi^U \equiv \max_m[k_m(\phi)]$ and $f_\phi^L \equiv \min_m[k_m(\phi)]$. Ideally, center cell shapes should be chosen that are evenly distributed in intervals defined by the dispersion curve endpoints $[f_0^L, f_0^U]$ and $[f_\pi^L, f_\pi^U]$. This is equivalent to selecting the shapes which minimize the value of

$$\sum_{n=1}^{N} \min_{m \in M} \left\{ \sum_{\phi=0,\pi} \left[f_\phi^L + \frac{n-1}{N-1} \cdot \left(f_\phi^U - f_\phi^L \right) - k_m(\phi) \right]^2 \right\}. \tag{3.28}$$

A comparison of eight center cell shapes is presented in Figure 3.28 along with the first HOM passband dispersion curves. A relative cavity-to-cavity frequency spread of 4×10^{-3} is achievable with these shapes, suggesting a threshold current of ~ 450 mA is achievable for a linac constructed of modified geometry cavities.
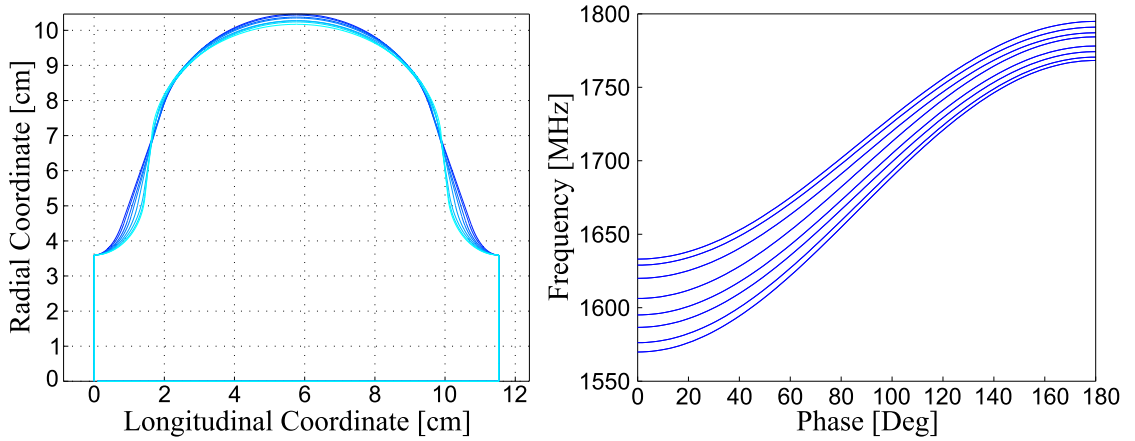
Figure 3.28: Left: Comparison of eight center-cell geometries. Right: Dispersion curves for the first HOM passband corresponding to the center cell geometries.

3.5 Conclusion of Cavity Design

This section has presented a systematic process used to design the main cavity for the 15 MeV to 5 GeV linear accelerating section of Cornell's ERL. Parallel computing was employed to the constrained optimization problem of mitigating the effect of higher-order modes in the cavity via the introduction of a beam breakup parameter, eschewing the need for costly particle tracking simulations at each iteration step.

The optimized cavity has been shown to be stable under small machining variations, verified by both 2D and 3D simulations. Particle tracking demonstrated that as long as dimensional variation introduced by the machining process are less than ±0.5 mm, machine current will exceed the design specification. Specifically, simulations of realistic ERLs comprised of cavities with unique HOM spectra show that threshold current in excess of 300 mA can be expected for the full machine, three times better than the 100 mA requirement.

Simulations incorporating 3D features such as the main linac coupler demonstrated also that quadrupole higher-order modes are sufficiently damped by beamline absorbers. The overall effect of the coupler is to break symmetry, which further assists in reducing the the Q of the otherwise trapped first two quadrupole passbands in the cavity via mixing to propagating modes in the beam tubes.

Overall the structure has been throughly verified to exceed the requirements for the Cornell ERL. In the next chapter, the fabrication and experimental qualification of the prototype of this structure is presented.

CHAPTER 4

PROTOTYPE CAVITY FABRICATION AND COMMISSIONING

This chapter discusses the process of taking the optimized cavity geometry design obtained in the previous chapter and turning it into a structure qualified to be used in an operational particle accelerator. Qualification consists of five steps: 1) Demonstrate that tight fabrication tolerances can be achieved. 2) Show that the fundamental mode has a very high intrinsic quality factor, Q_0. 3) Validate that higher-order modes are strongly damped. 4) Establish the proper operation of auxiliary components such as the RF input coupler, HOM beamline loads, and frequency tuner. 5) Study the mechanical properties of the cavity, showing that they are suitable for ERL operation.

This chapter begins by outlining the fabrication choices made for the Cornell ERL main linac cavity, the production of the first prototype cavity and the assembly, and installation methods used to measure the RF properties of the structure. Next, qualifications of the fundamental mode in vertical and horizontal tests are presented,[1] in which the cavity set a world record $Q_0 = 1 \times 10^{11}$ for a multicell cavity in a realistic accelerator environment, far exceeding the Cornell ERL Q_0 design specification of 2×10^{10}. Finally, the properties of the prototype cavity's higher-order mode (HOM) spectrum are measured and it is found that all measured dipole HOMs are strongly damped, suggesting that an ERL constructed from this type of 7-cell cavity should be able to support con-

---

[1]Vertical measurements are simple tests that can establish Q_0 of a resonator, but are unrealistic of the conditions within a particle accelerator. Horizontal testing probes the performance of a cavity in a similar configuration as in an operational accelerator.

tinuous beam current in excess of the 100 mA Cornell ERL design specification.

4.1 SRF Accelerating Cavity Fabrication Considerations

Modern particle accelerators relying on superconducting technology for their accelerating structures use niobium as the material for the RF surface layer. Many techniques exist to fabricate accelerating cavities with niobium RF surface layers, include forming structures from bulk Nb, explosion bonding a layer of Nb onto a Cu substrate, or various experimental techniques to deposit thin films of Nb onto metallic substrates, a process known as sputtering. [PKH98] All three methods have successfully been used to produce accelerating cavities, with explosion bonding Nb onto Cu used for the prototype cavities in HERA at DESY, [DEM+87][2] sputtering Nb on Cu for the superconducting cavities at LEP and the LHC at CERN, [Sla97, BCH+99] and bulk Nb cavities used at many sites around the world including at CEBAF at Jefferson Laboratory. [DIPK91] The design for Cornell's Energy Recovery Linac proposes to form the main linac accelerating structures out of sheet metal Nb, [BBB+11] a method that has been successfully demonstrated at many laboratories around the world, and is the proposed standard for the prospective International Linear Collider project. [SAE+13]

Bulk niobium material is available in high purity, typically with residual resistivity ratios (RRR) in excess of 300, and can be produced with either large or fine grain sizes (grain diameters >10 cm or ~50 μm respectively). [PKH98] While large grain material has been used to successfully fabricate SRF cavities with high quality factors at medium accelerating gradients (12-18 MV/m), [KMC+05,

---

[2]The cavities actually used in the HERA upgrade were made of bulk niobium. [DMM+95]

Myn07] all superconducting accelerator projects to date–such as the European XFEL at DESY, S-DALINAC at Darmstadt, and TRISTAN at KEK–have used fine grain material in their superconducting cavities. [Sin12, DEG⁺94, TFT87]

After manufacture, the niobium RF surface of cavities is typically treated chemically to minimize the surface resistance of the superconductor. Standard chemical treatments are electro-polishing (EP), buffer chemical polishing (BCP), or through removing material and regrowing an oxide layer with hydrofluoric acid. [GCPS05, vdHAP⁺07, ROGP12] It is also possible to obtain bulk removal and smooth surface finishes by treating cavities with centrifugal barrel polishing, a purely mechanical process. [CBJP11] All of these methods have been demonstrated to yield cavities with high intrinsic quality factors, Q_0, with no statistically significant difference between the performance of EP and BCP cavities at ~16 MV/m. [Val12] Because BCP treatment is simpler to implement than EP, and, coupled with a 48 hr 120°C heat treatment, has been shown to yield high quality factors at moderate fields, it was decided to treat the main linac cavities with BCP and low temperature heat treatment. [BBB⁺11]

4.2   Prototype Cavity Fabrication

The fabrication of the prototype 7-cell cavity (ERL 7.1) began in the Fall of 2011. The goals of the prototype cavity were threefold: Demonstrate that cavity fabrication tolerances of ±0.5 mm can be achieved, show a fundamental mode $Q_0 > 2 \times 10^{10}$ at the operating gradient and temperature, and check that there are no trapped (high Q_L) higher-order dipole modes in the cavity.

The first step of cavity fabrication was to stamp cells from fine grain niobium

sheet metal. This required male and female dies to be constructed to compensate for spring-back, a tendency of the deep drawn material to rebound from to the die geometry. [MK05] The dies were designed such that the cups, shown in Figure 4.1, after spring back would conform to the needed fabrication tolerances.

Figure 4.1: A pressed niobium half-cell before receiving rough trimming and being welded into a dumbbell structure.

A coordinate measuring machine (CMM), shown in Figure 4.2 was used to compare the stamped cell geometry with the nominal shape. The results of these measurements demonstrated that the cavity profile was well within the ±0.5 mm specification, with the largest deviations near the irises. The CMM measured the cell profile along four lines equally spaced azimuthally around the cavity. A measurement of a dumbbell profile is presented in Figure 4.3.

The deep drawn cells received a rough cut and were then electron-beam welded together into dumbbells, shown in Figure 4.4. The length of the cells were purposely longer than their final values because processes such as chemistry and weld shrinkages are not fully controlled, and must be corrected in the final fabrication step.

The resonant frequency of the dumbbells' TM_{010} 0- and π-mode was measured and used to determine how much material to remove from each equator. This process takes into account chemical etching and cryogenic shrinkage,

Figure 4.2: Apparatus used to measure cell shape profiles. The stylus contacts the niobium surface and can either measure distances along a profile line or raster over the entire surface to make a 3D representation of the cavity. Inset at top left is a topographical map of cell shape fabrication accuracy.

and calculates the total length of the dumbbell required so that the completed structure after electron beam welding will have the proper fundamental mode frequency and have equal field amplitude in each cell. [SC12] This is an important step in the process, since distortions in the cavity profile require cell-by-cell tuning that could potentially introduce dangerous higher-order modes into the cavity's spectrum leading to beam breakup phenomena limiting the current through the ERL. The apparatus used to measure the dumbbells' frequency is shown in Figure 4.5.

After the optimal lengths were determined, the excess length of material near the dumbbell equator was removed, and the dumbbells were placed in
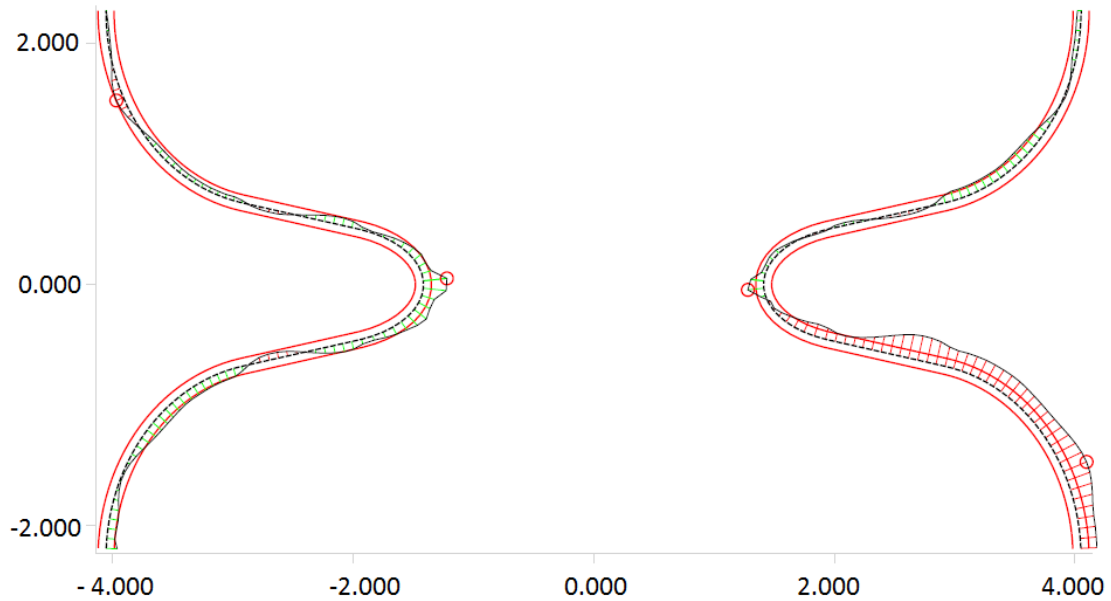
Figure 4.3: Measurements from CMM of a dumbbell cavity. The coordinate axes are in inches. Black dotted line denotes the nominal dumbbell shape. The red lines denote normal deviation from the nominal cavity shape of 0.125 mm, with 50x magnification. The red circles show the points of furthest deviation, either above the nominal value or below. The farthest discrepancy from the nominal value in this case is near the iris with a deviation of 0.38 mm.

nitric acid (30 min/side) to remove residual copper from the cells. The cells were then ultrasonically cleaned with a hot water (38 - 60°C) Liqui-Nox® solution for 15 minutes. Subsequently, the cups were rinsed to remove any soap residue and ultrasonically cleaned in hot de-ionized water for an additional 15 minutes, followed by a bulk BCP.

Each BCP used acid at an initial temperature between -20 and -17 °C. The BCP was complete when either 16 minutes had passed or the acid temperature increased to -9°C. After BCP, the oxide layer was allowed to regrow in de-ionized water for four hours, and was then dried with a stream of high pressure pure nitrogen gas for 1 hour and delivered for electron beam welding. [Car11]

After the dumbbells were welded to form the completed 7-cell structure, the

144

Figure 4.4: Cells after being welded to form dumbbells. These cells were subsequently measured to determine final trimming, and welded into a full cavity.

room temperature resonant frequency of the cavity's $TM_{010,\pi}$ mode was measured to be 1298.623 MHz, close to the pre-chemistry goal of 1298.985 MHz. [She11] A bead pull [Sch92] was performed to measure the field flatness[3] of the $TM_{010,\pi}$ mode and found the cavity was 95.7% field flat. These results demonstrate precise control over the fabrication process.

Following initial measurements, the cavity received a 150 μm BCP, followed by a 650°C bake for 12 hours. Subsequent tuning of the cavity[4] reached 95.1% field flatness with a resonant frequency of 1297.521 MHz. The room temperature, post-etch target frequency of 1297.425 MHz [She11] was obtained by a final 10 μm BCP. The field profile of the cavity is presented in Figure 4.6.

Next, the cavity was cleaned by high-pressure rinsing (HPR) with de-ionized water. During the HPR, the side port used for the high-power RF coupler was blanked off as well as one cavity flange to help maintain cleanliness of the SRF

---

[3]Field flatness is defined as the ratio of the average of the peak amplitudes in each cell over the maximum cell amplitude.

[4]Tuning is achieved by stretching and compressing the cells of a cavity.

Figure 4.5: A dumbbell inside the frequency measurement apparatus, used to determine how much material to trim from the equator region so that after welding the cavity has the proper resonant frequency. The screw allows the same force to be applied to each dumbbell, preventing unequal loading which could effect the measured resonant frequency. Image reproduced from [SC12].

surface while drying and assembly. After the initial 8 hour HPR, a field probe with $Q_{ext} = 3 \times 10^{11}$ was installed on the cavity, the top beam tube was sealed and the cavity was HPRed for an additional 8 hours.

The final assembly step after the second HPR was to connect a viking horn connector having the axial coupler ($Q_{ext} = 2 \times 10^{10}$) and vacuum connection to the cavity, thereby allowing evacuation of the cavity space. The cavity was braced and slowly evacuated until the vacuum was better than 10^{-6} Torr. The cavity was removed from the clean room, assembled onto a vertical test stand and received a low temperature heat treatment by baking the cavity at 120°C for
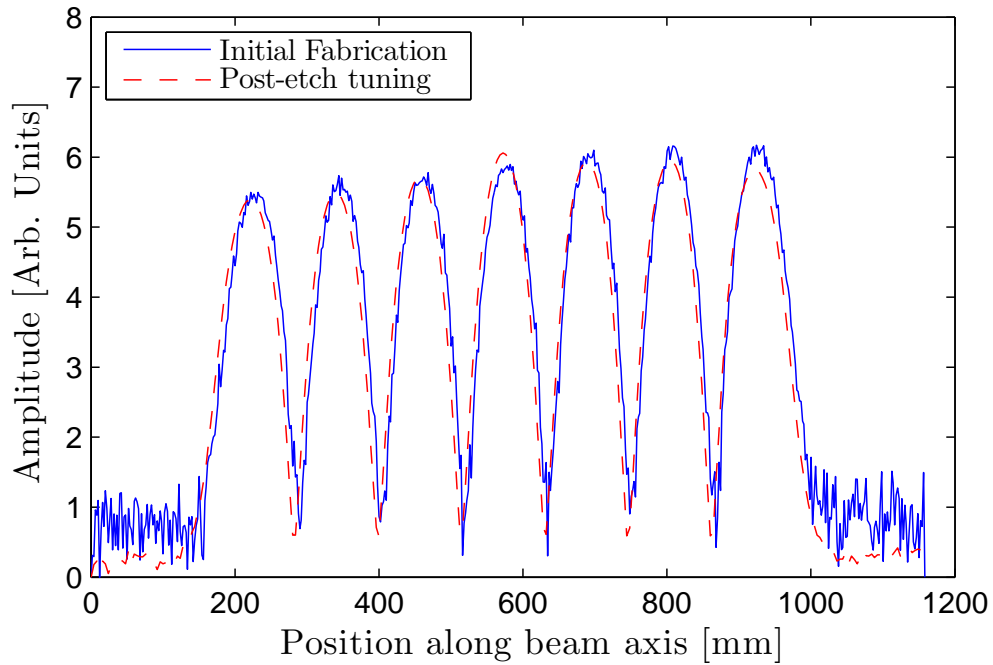
Figure 4.6: Field profile measurements of ERL7.1, before and after etching, demonstrating better than 95% field flatness in both cases. Measurements were performed by B. Bullock.
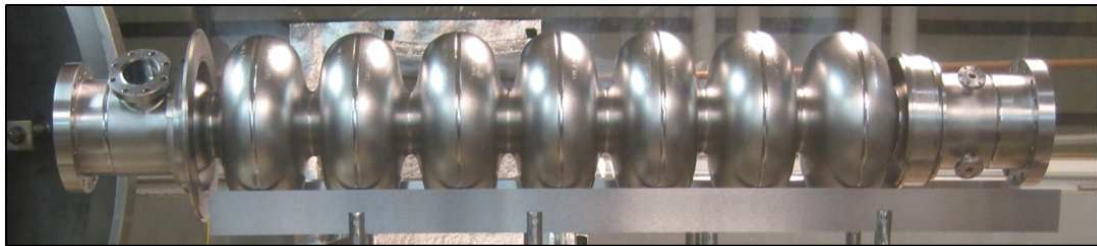
Figure 4.7: Fabricated prototype 7-cell cavity ERL 7.1 in a high temperature vacuum furnace after 650°C bake. The left beam tube shows the port for the high-power input coupler. The right beam tube shows the two ports for field probes. The normal to port A is parallel to the normal of the high-power input coupler, and port B is rotated by 90°.

48 hours.

4.3   RF Qualification Testing

The SRF properties of the cavity were tested in several stages. The first test was in a vertical dewar, followed by several tests in the horizontal orientation in a separate cryomodule. The vertical test is a simpler experiment, requiring less instrumentation and infrastructure compared with the horizontal test, so it was the first step along the path to qualification. It is also easier to cleanly assemble a cavity in the vertical orientation, so success in the vertical test can demonstrate that the cavity SRF surface is free of material defects that would otherwise limit the SRF performance of the fundamental accelerating mode of the cavity, but does not necessarily guarantee good performance in the full cryomodule tests. If there are other performance limiting phenomena, such as field emission or multipacting, detecting them at the vertical test stage helps to isolate which processes could be responsible, and mitigate them in subsequent fabrications or assemblies.

4.3.1   Vertical Test Qualification

The primary concern for the vertical test was to qualify the SRF properties of the fundamental mode of the cavity. To this end, all non-essential instrumentation was removed from the test stand, including OSTs and fixturing (in case the stainless steel trapped stray magnetic field). Temperature sensors, one on the top, center and bottom cells were installed on the outer cavity walls. A 500 W heater was attached to the bottom of the cavity assembly, which is used to reduce the magnitude of the temporal and spatial thermal gradients during cool down. The assembly of ERL 7.1 is presented on a test stand in Figure 4.8.

Figure 4.8: ERL 7.1 on experimental insert prior to vertical test.

After installing the cavity in the dewar, and pumping the cavity vacuum space to $< 1 \times 10^{-8}$ Torr, the cavity was quickly cooled down through the "Q-disease region" to prevent the nucleation of lossy hydrides on the SRF surface of the cavity. [PKH98] Once liquid helium began to accumulate–which occurs at 4.2 K at atmospheric pressure–the cavity was warmed up to above 10 K, and slowly cooled through the critical temperature at a rate of ~ 1 K/hr. During the transition through T_c, thermal gradients across the cavity were ~ 10 K/m.

A phase-lock loop system was used to measure the quality factor of the fundamental $TM_{010,\pi}$ mode vs accelerating gradient at 1.6, 1.8 and 2.0 K. The Q vs E measurements are presented in Figure 4.9. The cavity reached 26 MV/m with no radiation, which is an indication of a very clean assembly. Quality factor measurements were halted at 26 MV/m due to administrative limits. The cav-
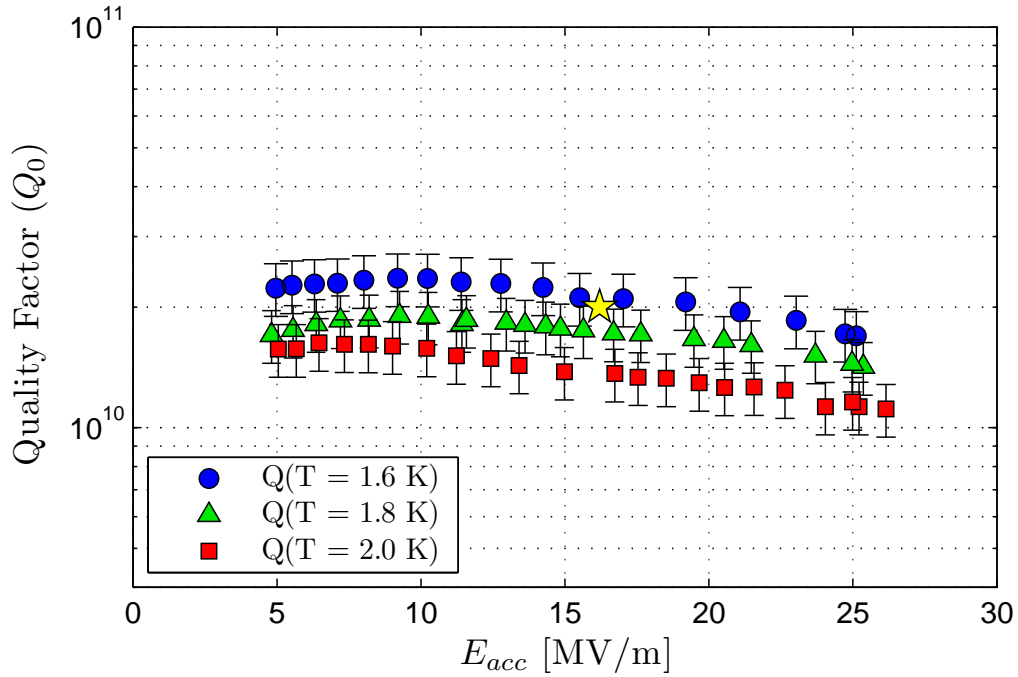
Figure 4.9: Quality factor vs accelerating electric field gradient for the proto-type 7-cell cavity ERL 7.1 at 1.6, 1.8, and 2.0 K in the vertical test. The star denotes the ERL quality factor specification of $Q_0(E_{acc} = 16.2 \text{ MV/m}) = 2 \times 10^{10}$ at 1.8 K, which was reached within measurement error.

ity did not reach a hard quench limit.

While cooling from 4.2 K down to 1.6 K, quality factor measurements were taken at intermediate temperatures. Using the geometry factor of the cavity presented in Table 3.7, the average surface resistance can be computed, and the average properties of the SRF layer can be determined. A comparison of the measured data with BCS theory is presented in Figure 4.10, and the material properties extracted from this data are shown in Table 4.1.[5] A full discussion of the definitions of the quantities presented in this table is presented in Appendix A.

[5]Error analysis for SRIMP fits are discussed in Appendix C. The uncertainties for parameters characteristic of those in the HTC tabulated in Table C.3.
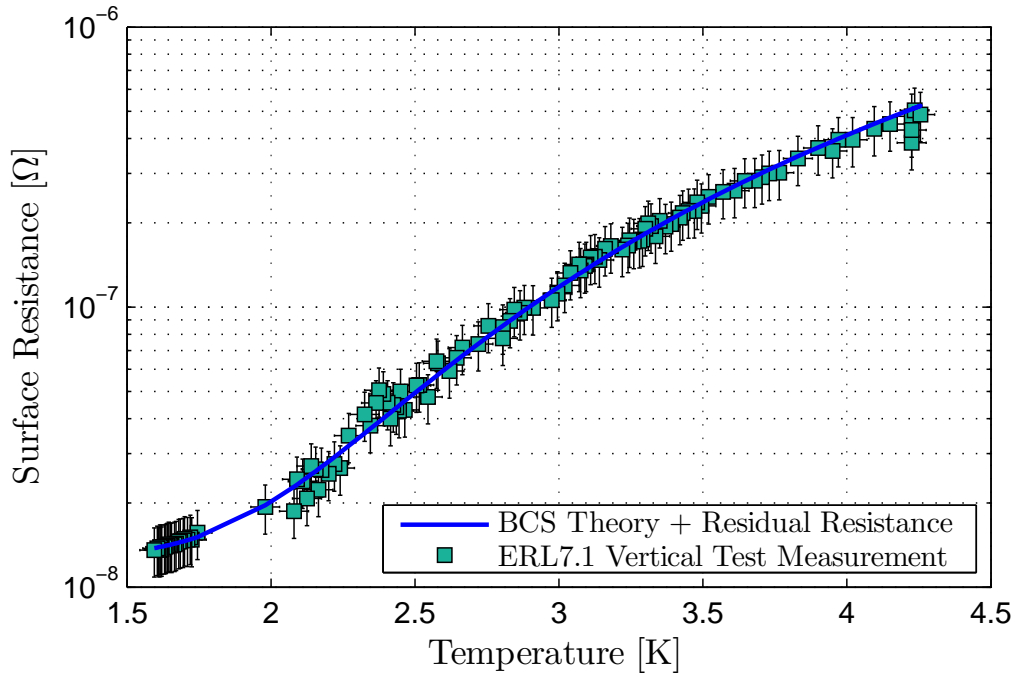
Figure 4.10: Surface resistance vs temperature for the vertical test of the proto-
type 7-cell cavity between 4.2 and 1.6 K. The material parameters
for this fit are presented in Table 4.1. (Can be compared with a later
result in Figure 4.15.)

The quality factor measured at the proposed operating temperature of 1.8 K
and gradient of 16.2 MV/m was slightly lower than the design specification,
but was consistent within measurement uncertainty, so deemed successful. The
prototype qualifications continued to the next stage: Testing in a horizontal cry-
omodule.

4.3.2 Horizontal Test Cryomodule Program

The horizontal test cryomodule (HTC) program seeks to demonstrate that
the prototype cavity meets the fundamental mode design specification of
$Q_0(\text{T}=1.8\text{ K}) = 2 \times 10^{10}$ at 16.2 MV/m, in a fully outfitted cavity, without deleteri-

Input Parameter	Value	Unit
Frequency	1300	MHz
T_c	9.20	K
λ_L	39.00	nm
ξ_0	38.00	nm
Fit Parameter	**Value**	**Unit**
E_g	3.836 ± 0.023	—
ℓ_{tr}	22.68 ± 10.98	nm
R_0	12.88 ± 0.49	nΩ
Calculated Result	**Value**	**Unit**
λ_{tr}	1.477 ± 0.715	—
$R(\lambda_{tr})$	1.038 ± 0.289	—
λ_{GL}	42.61 ± 6.15	nm
ξ_{GL}	18.16 ± 0.09	nm
κ_{GL}	2.35 ± 0.68	—
$c(\kappa_{GL})$	1.10 ± 0.05	—

Table 4.1: Surface superconducting properties extracted from the vertical test of prototype cavity ERL 7.1. Top: Fixed parameters used in the SRIMP calculation of BCS resistance. Middle: Fit parameters obtained by minimizing the residual sum of squares between the data in Figure 4.10 and SRIMP's calculation. Bottom: Calculated Ginsburg-Landau parameters at zero temperature and finite mean free path as given by equations in [OMFB79]. Note that $c(\kappa_{GL})$ is the coefficient used to determine the superheating field in Ginsburg-Landau theory.

ously effecting the higher-order mode properties that can lead to beam breakup, validating the cavity design. In addition, the HTC is a proving ground for the technology to be used in the main linac cryomodule, examining whether key systems such as helium cooling systems, RF input coupler, HOM loads, and cavity frequency tuner perform appropriately, validating the cryomodule design.

The HTC can be used to explore the question of whether the quality factor of SRF structures necessarily perform more poorly in the horizontal orientation than in vertical and if it is possible to mitigate low fundamental mode quality factors. In principle there should be no geometric sensitivity to the efficiency

of an RF superconductor, regardless of orientation. However, experiments at many laboratories around the world have demonstrated consistently higher Q_0 values in the vertical orientation than in the horizontal. [Hoc13] Measured differences could arise from effects such as cleanliness of assembly, the magnetic environment of the experiment, or perhaps the influence of thermal gradients during cooldown on the superconductor. The HTC experiments are in a position to investigate whether this phenomena is fundamental, or can be mitigated by tight control of the RF surface and cryogenic environment.

The horizontal test cryomodule is a vacuum vessel large enough to house a single ERL main linac 7-cell cavity and instrumentation. The cryomodule is designed to incorporate all the main systems that are needed in a full-size cryomodule (which will hold 6 cavities), and serve as an operational accelerating structure for subsequent beam tests. Figure 4.11 shows a longitudinal cross-section of the HTC as prepared in the three experimental phases.

The HTC experiment progressed in three stages: HTC-1 tests the prototype cavity with an on-axis, high Q_{ext} RF input coupler, and no HOM absorbers. The goal of this test was to replicate the results of an initial vertical test in a horizontal cryomodule, with the geometry exposed to RF energy as similar as possible to that of the vertical measurement. The axial RF input coupler allowed accurate measurement of the quality factor of the cavity via standard RF methods. In addition, the precise RF measurements can be benchmarked against other calorimetric methods of determining Q that must be used in future tests.

HTC-2 modified the RF input power scheme to the cavity, adding a side mounted high power (5 kW) RF input coupler ($Q_{ext} \approx 5 \times 10^7$) in addition to the axial probe. This stage allowed the coupler assembly process to be qualified,
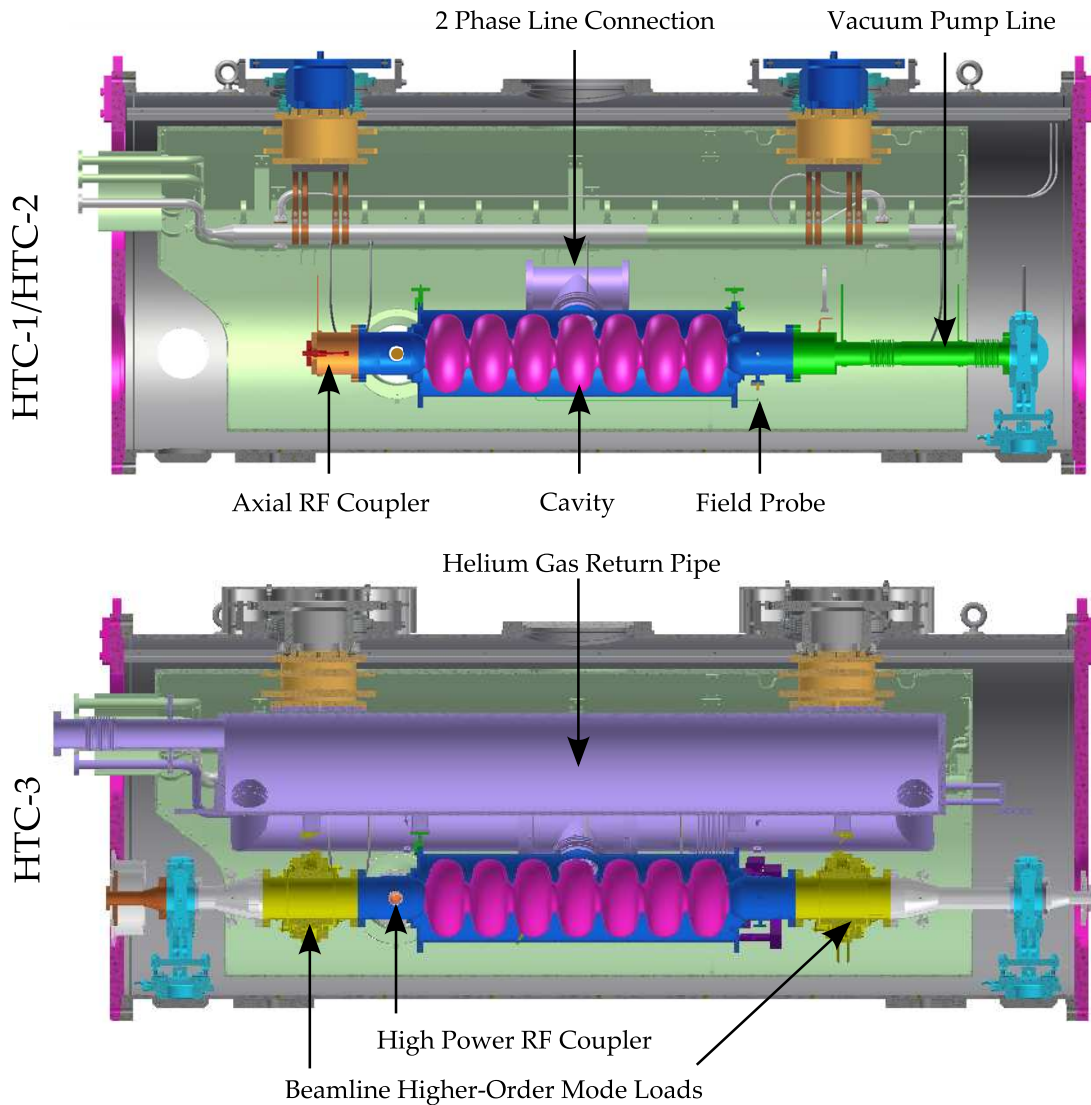
Figure 4.11: Longitudinal cross-sections of the HTC configuration in various experimental phases. Top: Instrumentation in HTC-1 and -2. The main difference is that HTC-2 incorporated a side-mounted high power RF coupler. Bottom: HTC-3 including the beamline HOM absorbing loads.

as well as preliminary investigations into the coupling between the high power coupler and higher-order modes.

HTC-3 reconfigures the assembly, removing the axial power coupler and adding two broadband beamline HOM absorbers–one on each end of the cavity. Meeting gradient and quality factor specifications in this final test would

demonstrate the feasibility of all the main systems needed to fabricate a full main linac ERL cryomodule.

Success in the HTC experimental program would demonstrate the viability of the technology required for the Cornell ERL, and provide evidence that all higher-order modes are strongly damped so that the linac would be able to support current in excess of 100 mA through the linac.

4.3.3   HTC-1

Horizontal Installation

Following the vertical test, a helium jacket was welded to the outside of the cavity. Before welding, six Cernox temperature sensors were permanently fixed to the outer cavity surface. The sensors were located on the top and bottom of each end cell, and the top and bottom of the center cell. During the welding process, the interior remained under vacuum to preserve the cleanliness of the SRF surface. Network analyzer measurements before and after attaching the helium jacket indicated that the stress of welding did not change the fundamental mode resonance frequency and field profile of the cavity.

After welding the helium jacket to the cavity, the cavity was high-pressure rinsed, and an axial probe with $Q_{ext} \sim 9 \times 10^{10}$ to the fundamental mode was installed at one end of the cavity. The Q_{ext} of the coupler was chosen to be higher than in the vertical test to help reduce RF losses on the coupler which could introduce errors into the measurement of the cavity's intrinsic quality factor. A side mounted field probe, with $Q_{ext} \sim 3 \times 10^{11}$ to the fundamental mode,

was installed. This field probes was on the side of the cavity opposite to the fundamental power coupler. The first field probe port(Probe A) points in the same direction as the side mounted coupler, and the second field probe port (Probe B) is rotated 90°.

After finishing the clean assembly in a class 10 cleanroom, the 7-cell cavity was prepared to be mounted in a cavity string. The cavity string was installed on a rail system that incorporated precision machined surfaces for alignment. Photographs of the assembly process are presented in Figure 4.12.
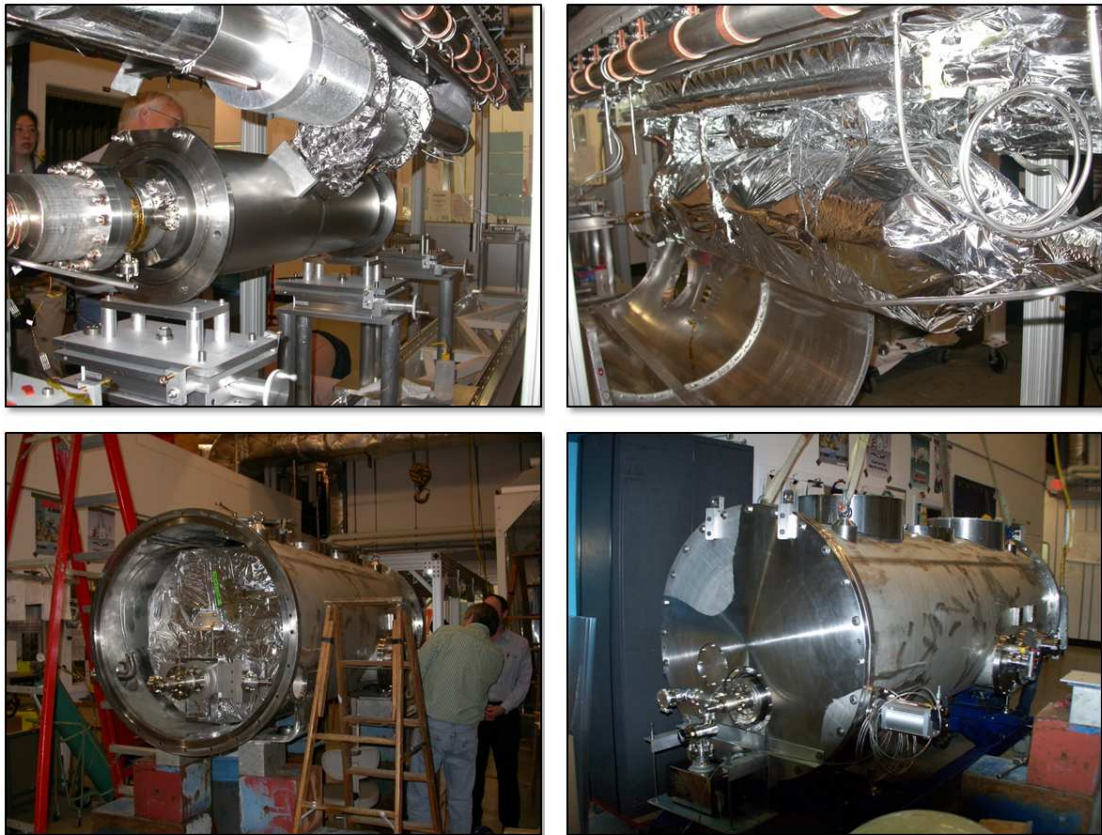
Figure 4.12: Top left: 7-cell cavity in helium jacket attached to two-phase helium supply line. Top right: Cavity cold mass wrapped in superinsulation. Bottom left: Entire cold mass inserted into cryomodule vacuum vessel. Bottom right: Completed cryomodule prepared for transport to the accelerator tunnel for testing.

The cavity's helium jacket was connected to a 2-phase helium supply line, running the length of the cryomodule. This pipe supplies helium to the cavity while maintaining a head of liquid and gas. A slow tuner based on the Saclay-I design, [MCD+90] was installed (see Figure 4.13) to adjust the cavity's frequency and enable damping of microphonics via fast piezoelectric actuators.
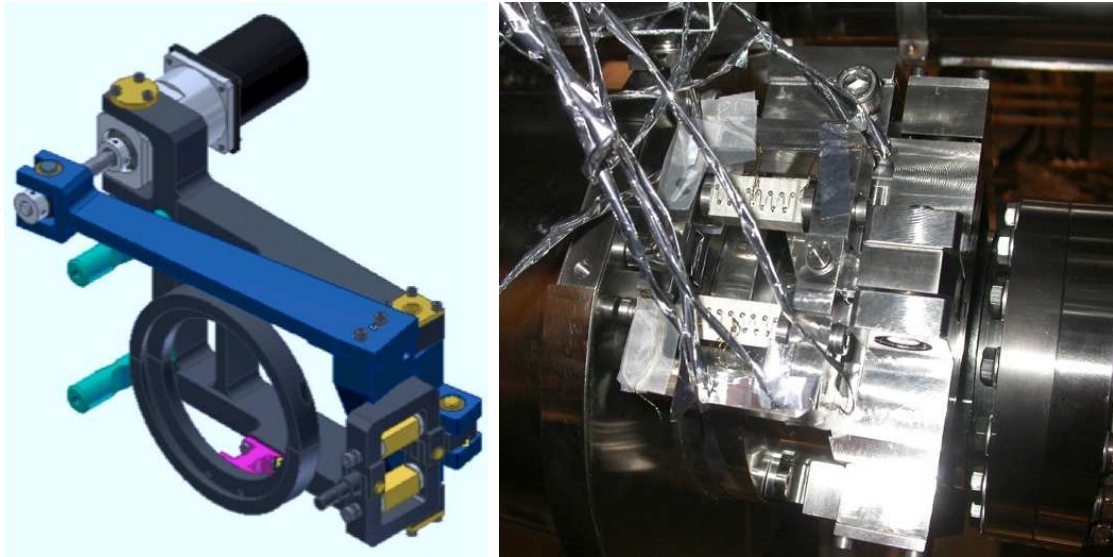
Figure 4.13: CAD model and assembled frequency tuner used in the HTC experiments.

The cavity-helium jacket assembly was enclosed in a CryoPerm® magnetic shield, and then wrapped in multi-layer insulation to reduce the radiative heat input from the 80 K helium lines to the cold mass at 1.8 K. The cavity system and helium supply were enclosed in an 80 K thermal shield, which was then surrounded by a Mu-metal magnetic shield and additional layers of multi-layer insulation. The entire assembly was rolled into the cryomodule enclosure, and the stainless steel vessel was sealed, and moved to a radiation shielded accelerator tunnel. In the tunnel, a cryogenic system supplying liquid helium was connected to the cryomodule, and the cavity was cooled from 300 K to 4.2 K (the temperature of liquid helium at atmospheric pressure). During cool down,

the temperature gradient across the cavity was less than 0.4 K/m, with peak temperature differences between the cavity end cells of 0.3 K.

Stainless Steel Vacuum Vessel
Mu-metal Magnetic Shield
Multi-layer Insulation
80 K Shield
Multi-layer Insulation
Helium Gas Return Pipe
2 K, 2-Phase Line

80 K Helium
5 K Helium
2.0 K Helium
1.8 K Helium
Helium Gas (return)

RF Coupler
7-Cell Cavity
CryoPerm Sheild
Multi-Layer Insulation
Cooldown Input Line
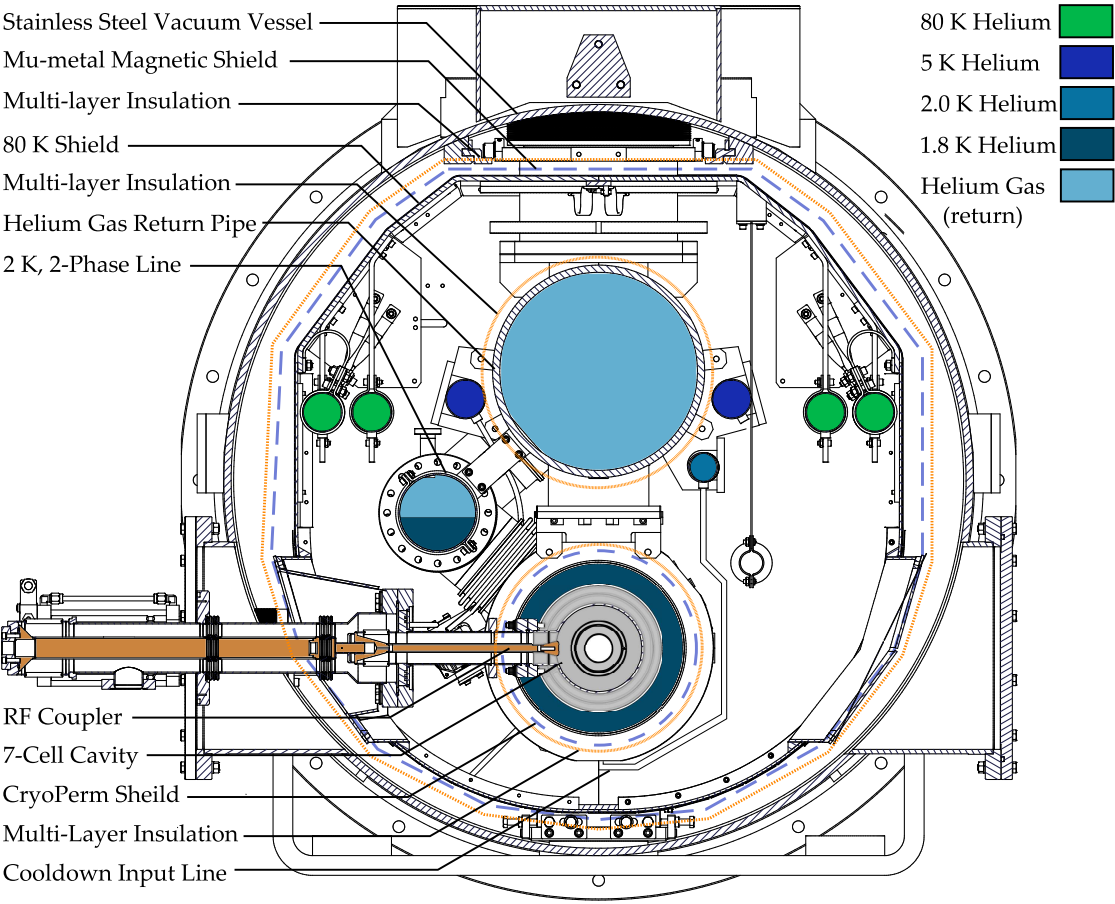
Figure 4.14: Transverse cross-section of the HTC at the input coupler plane.

A network analyzer was used to measure the frequencies of the modes within the fundamental passband. These frequencies can be compared with those obtained during room temperature field-flatness measurements by scaling the frequencies such that the π-mode frequencies agree. The passband frequency comparison is presented in Table 4.2.

Mode	Scaled Bead-Pull [MHz]	HTC-1 Network Analyzer [MHz]	Δf [kHz]
$1\pi/7$	1274.772	1274.726	46.2
$2\pi/7$	1278.234	1278.197	36.6
$3\pi/7$	1283.573	1283.544	29.4
$4\pi/7$	1289.209	1289.194	14.6
$5\pi/7$	1294.801	1294.792	9.29
$6\pi/7$	1298.449	1298.451	-1.60
$7\pi/7$	1299.879	1299.879	0.000

Table 4.2: Frequencies of the modes in the fundamental passband from the scaled field-flatness measurement and in HTC-1. The slight discrepancy in values can either arise from small shape changes during the welding of the helium vessel to the cavity or from handling. The correspondence between the two frequency measurements suggest the cavity field flatness was preserved in HTC-1.

Quality Factor Determination

For HTC-1, the intrinsic quality factor of the cavity was measured both with standard RF methods and calorimetrically. Benchmarking the calorimetric methods is essential since later measurements will use RF couplers with relatively low Q_{ext} and so will not be able to accurately Q_0 via RF methods. The calorimetric methods relied on the dissipated power in the cavity walls acting as a heater, and measuring either the rate of change of the helium level or helium gas exhaust to determine the power input into the helium bath.

Fundamental Mode Qualification via RF Measurements

The quality factor of the cavity was characterized using an analog phase-locked loop system to perform RF measurements as illustrated in Figure 4.15. The phase-lock loop system tracks the cavity's resonant frequency by using a phase detector to produce a voltage proportional to the difference between the cavity's

resonant frequency and the output of the frequency synthesizer.[6] This voltage is used to modulate the synthesizer's output frequency.
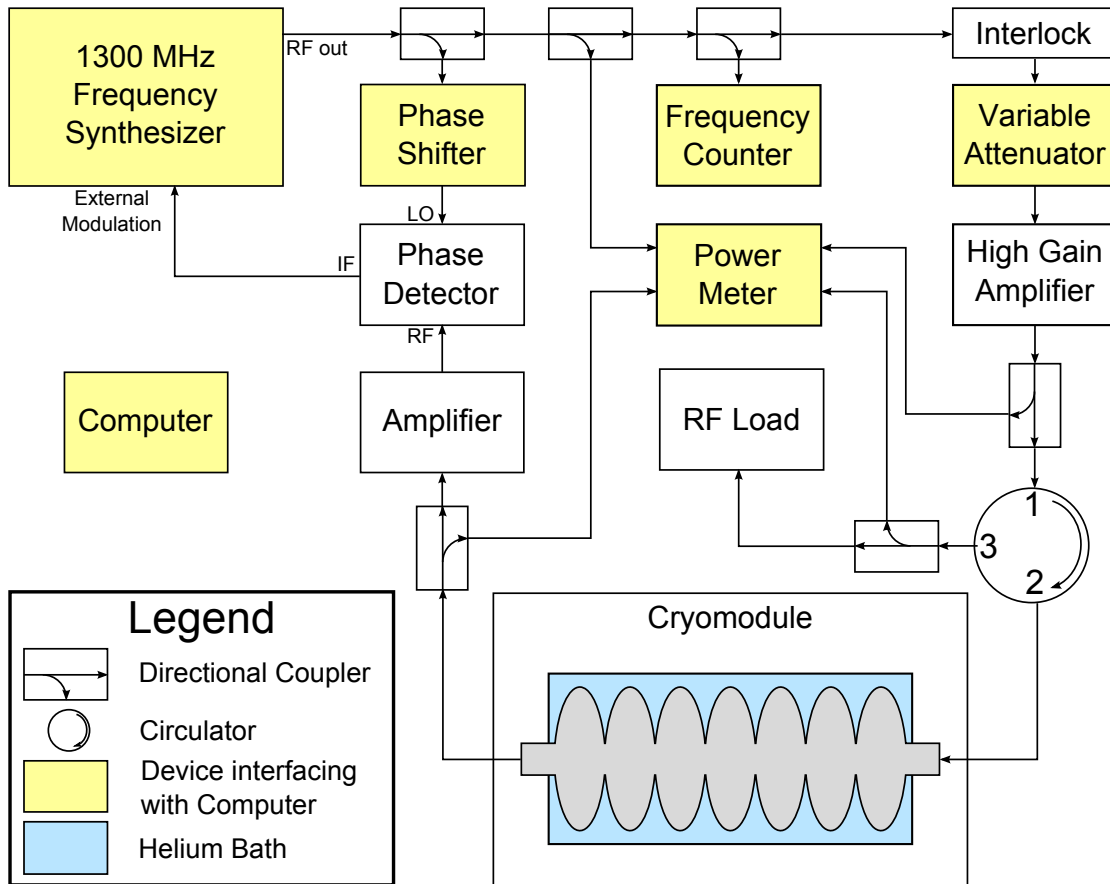
Figure 4.15: Block diagram of the analog RF (phase-locked loop) system used to measure the quality factor of prototype 7-cell cavity ERL 7.1 in the HTC-1 experiment. The phase detector produces a voltage that is a function of the difference between cavity frequency and synthesizer output. This voltage is used to modulate the RF output, tracking the cavity's resonant frequency. The interlock is part of a personnel protection system ensuring that RF power can only be turned on when the experimental area has been secured.

During the cool down to 1.6 K, Q_0 vs temperature was measured at 5 MV/m accelerating gradient. Because there was no chemistry or heat treatment of the cavity between the vertical test and HTC-1, one would expect the only change in

---

[6]Strictly speaking, the voltage output difference between the drive and cavity phase is $V = \phi_{\text{drive}} - \phi_{\text{transient}} = \Delta\phi + \phi_{\text{offset}}$, where $\Delta\phi = \tan^{-1}(\Delta f / f_{1/2})$ and Δf is the frequency change and $f_{1/2} = f_0/(2Q_0)$.

SRF properties would be the residual resistance which is sensitive to the magnetic environment of the cryomodule. Thus the SRF properties of the cavity were again fit with SRIMP. The data with the resulting fit is plotted in Figure 4.16 and the fit parameters are presented in Table 4.3.
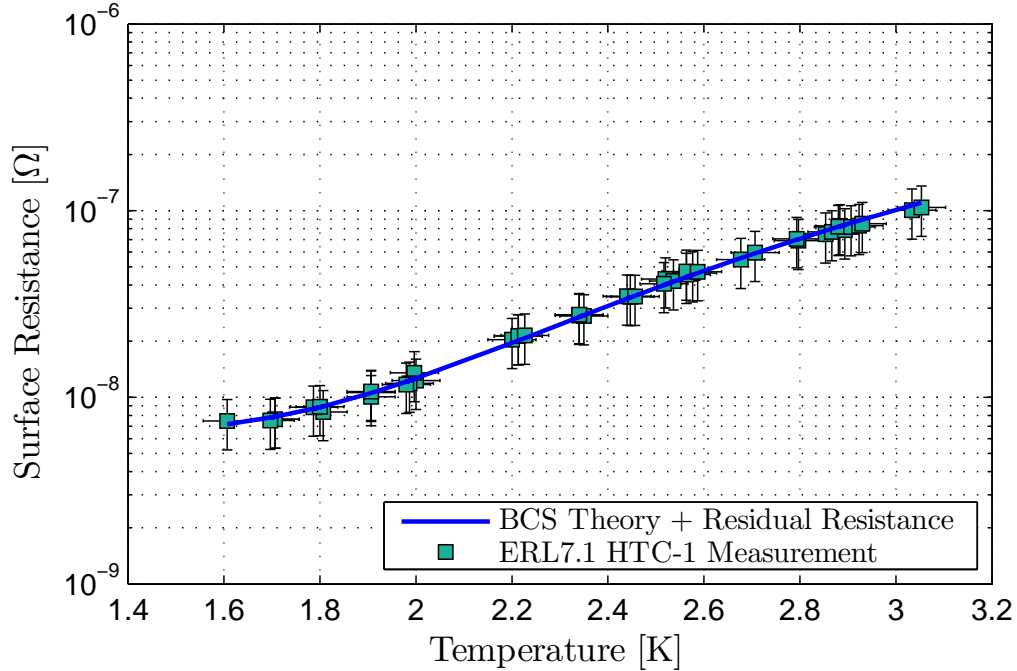
Figure 4.16: Surface resistance vs temperature for ERL 7.1 measured in HTC-1. Properties of the RF layer, which are displayed in Table 4.3, are consistent with vertical test measurements with a reduced residual resistance (see Figure 4.10 and Table 4.1).

As expected, the SRF parameters from the vertical test agree with HTC-1 results very well. The energy gap and the electronic mean free path, which directly yields κ_{GL}, are consistent between the two tests, but the residual resistance decreased by approximately 50%. This is likely due to a smaller quantity of trapped flux in the cavity walls in the HTC-1 measurements. Possible causes of this decline could be factors such as better magnetic shielding or smaller thermal gradients (either spatially or temporally) during the transition through T_c.

The origin of the reduced residual resistance will be investigated in sec-

Input Parameter	Value	Unit
Frequency	1300	MHz
T_c	9.20	K
λ_L	39.00	nm
ξ_0	38.00	nm
Fit Parameter	Value	Unit
E_g	3.905 ± 0.023	—
ℓ_{tr}	23.72 ± 10.55	nm
R_0	6.37 ± 0.33	$n\Omega$
Calculated Result	Value	Unit
λ_{tr}	1.413 ± 0.629	—
$R(\lambda_{tr})$	1.036 ± 0.260	—
λ_{GL}	42.08 ± 5.48	nm
ξ_{GL}	18.39 ± 0.09	nm
κ_{GL}	2.29 ± 0.60	—
$c(\kappa_{GL})$	1.11 ± 0.04	—

Table 4.3: Superconducting properties of ERL 7.1's RF surface layer in the HTC-1 experiment. The input parameters are the same as in the vertical test (shown in Table 4.1). The only significant difference between the tests is the lower residual resistance measured in HTC-1.

tion 4.3.3, as well as possible methods to maximize this effect. In the next section, methods and results from calorimetric measurements of the intrinsic quality factor will be discussed.

Calorimetric Measurements of Q_0 in HTC-1

During cavity operation, RF power is dissipated in the cavity walls and is removed via the liquid helium system. By knowing the field level in the cavity, the stored energy in the cavity, U, can easily be determined and the cavity's intrinsic quality factor can be calculated by measuring the dissipated power and using Equation 1.9.

Two calorimetric methods were used to measure Q_0. In both methods, a fixed

amount of helium was stored in the cryomodule, by closing the liquid helium supply valve and the cavity and an additional heater were used to evaporate helium from the system. The pressure, which fixes the temperature of the bath, was maintained constant by varying the speed of the pump at the helium exhaust port. In both methods, it is essential to separate out the static heat leak to the cryogenic system from warm sources via conduction and radiation, from the heat generated by RF operation of the cavity.

The first method measured the height of the liquid helium in the two-phase pipe with a 4 inch long level stick (refer to Figure 4.14). With knowledge of the cross-sectional area of the supply pipe, the density and latent heat of helium at the given temperature, the energy per volume required to evaporate the liquid helium stored in the bath can be determined. Measuring the rate of change of the level stick directly yields the power dissipated into the bath.

It is challenging to obtain reliable measurements of helium level in the cryomodule with a helium level stick. One challenge is that superfluid helium exhibits a creeping behaviour, wherein a film of the fluid (known as the "Rollin Film"[7]) will move from cold areas to warm ones. [RS39] This tends to cause the measured value of the helium level to be higher than its real value.

This challenge was overcome by noting reproducible "notches" in the helium level stick reading. Using these values were found to yield Q_0 values consistent with RF results, as well measuring a static heat leak consistent with helium gas meter measurements. While no robust explanation currently exists to show why these "notches" exist and can be used to obtain accurate measurements, one hypothesis is that the superconducting wires used in the level stick

---

[7]The film's nomenclature is derived from the name of the discoverer, Dr. B. V. Rollin, and is not, as some wags have described it, a description of how the film seems to be "rolling" uphill.
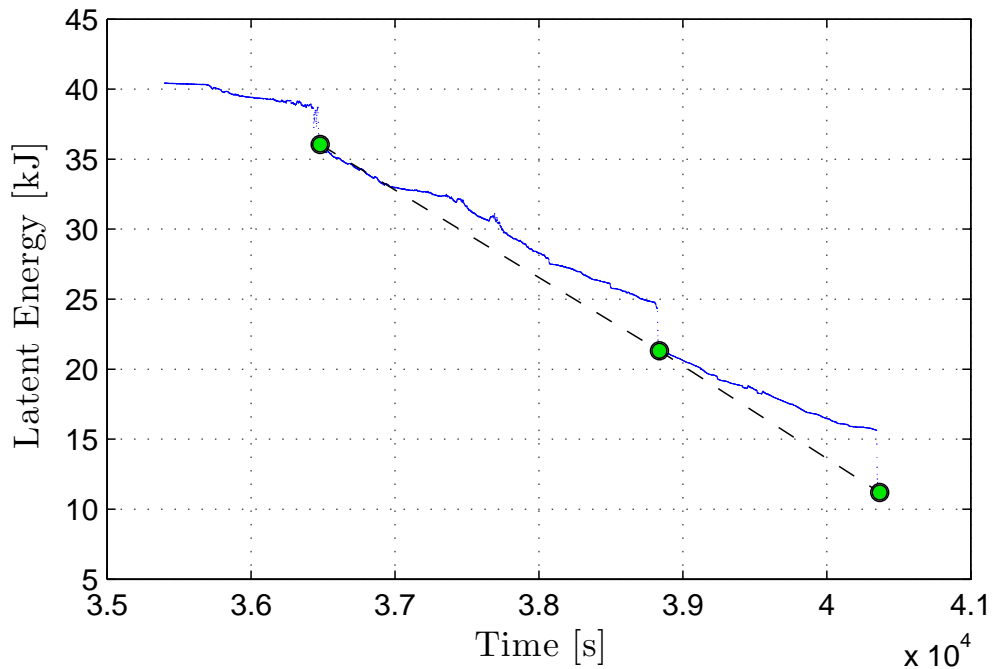
Figure 4.17: Latent energy in the two-phase supply pipe as a function of time, measured by a helium level stick. The blue points represent the level stick data, green circles mark the "notches" which occur at reproducible energy points, and the black dashed line shows the determined boil-off rate of the helium. During this measurement, there was no RF power in the cavity, and a heater attached to the helium supply pipe was run at 5.5 W. The level stick measurement yields dissipated bath power of 6.4 ± 0.3 W. The difference between reading and measurement is due to a heat input present regardless of operating condition, known as the static heat load.

have irregular cross-sectional area, leading to certain places that the film pools when its weight becomes too large to support a vertical film. A plot showing typical notches and how they were used to measure power dissipation is presented in Figure 4.17.

The second calorimetric method measured the mass flow of helium exhausted from the cryogenic pumps. Using the specific heat, density, and thermal integrals of helium from cryogenic temperatures to room temperature, the energy per unit volume stored in the gas can be calculated. The volumetric rate
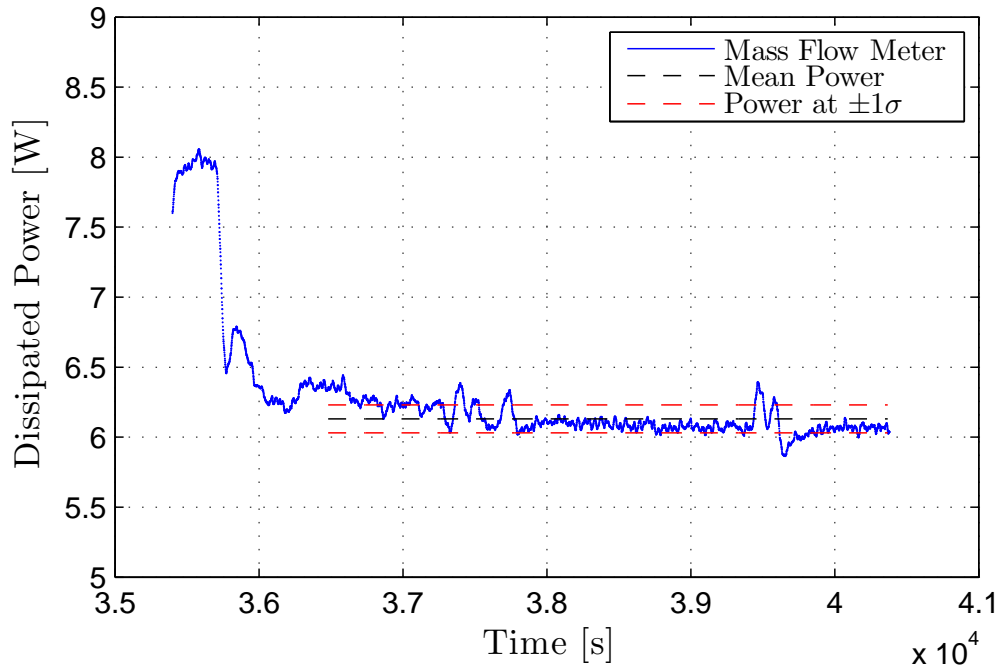
Figure 4.18: Dissipated power measured by a mass flow meter as a function of time under a constant 5.5 W heat load. There is a settling time of approximately 60 s by the cryogenic system before steady state measurements can occur. The data range used to determine dissipated power of 6.2 ± 0.2 W is the same as extreme time points denoted by the green dots in Figure 4.17. Difference between heater power and measured dissipated power is due to the static heat load.

of change yields the power dissipated into the cryogenic bath. In HTC-1, a mass flow meter was used, whose measurements are shown in Figure 4.18. In HTC-2 it was found that a residential gas meter gave more accurate measurements, which are presented in Figure 4.19. It is clear from comparing Figures 4.17, 4.18, and 4.19, the gas meter method provides a more precise measurement of the dissipated power in the bath. Thus it was relied on for measurements in HTC-2 and HTC-3.

Measurements of the static heat load using both the mass flow meter and the level stick methods yield values of 27.5 ± 2.5 W at 80 K, 1.3 ± 0.5 W at 5 K, and 1.5 ± 0.5 W at 1.8 K. [VFG⁺12] These values are consistent with the estimated
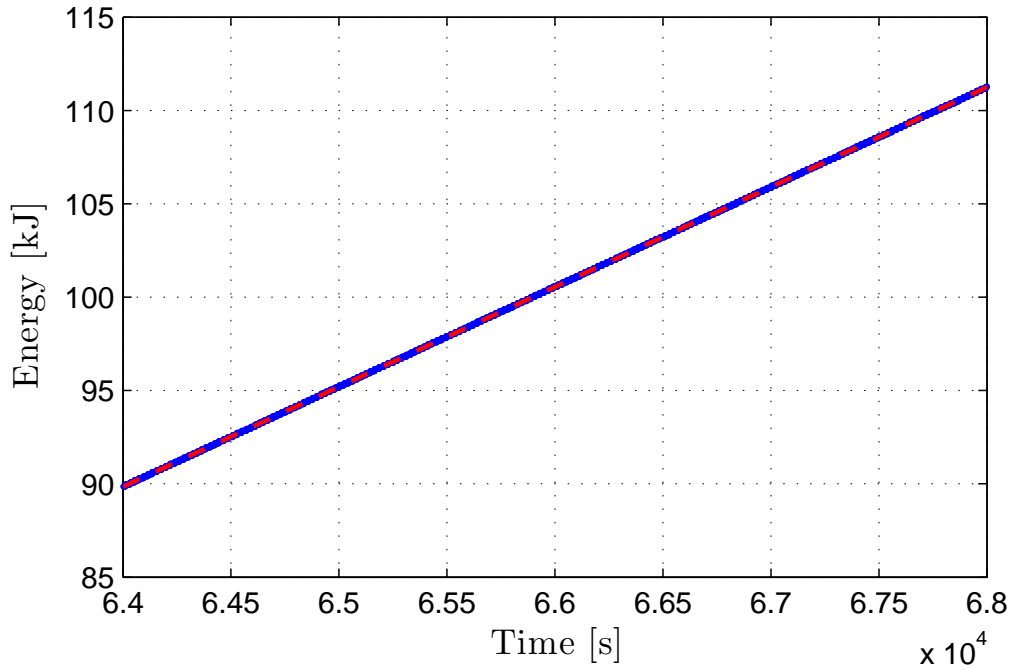
Figure 4.19: Energy measured by the gas meter as a function of time under a constant 4.5 W heat load. The blue points represent the gas meter data, and the red line is a least squares fit yielding the dissipated power of 5.4 ± 0.1 W. Difference between heater power and measured dissipated power is due to the static heat load.

static heat leak at 1.8 K of ~2 W, validating the cryomodule design.

Calorimetric measurements of the quality factor of the cavity at 1.8 K are compared with RF measurements in Figure 4.20. These measurements were made by filling the helium supply pipe ~70% full, and closing the helium input valve. First, a heater at a constant power and the cavity at a fixed field level was used to boil off helium in the cryomodule until only ~15% remained in the pipe. The helium was refilled, and the measurement redone with only the heater on. The power difference between the two runs is interpreted as the dissipated power from the cavity and can be used in Equation 1.9 to directly yield Q_0.

The quality factors measured by both RF and calorimetric methods were con-
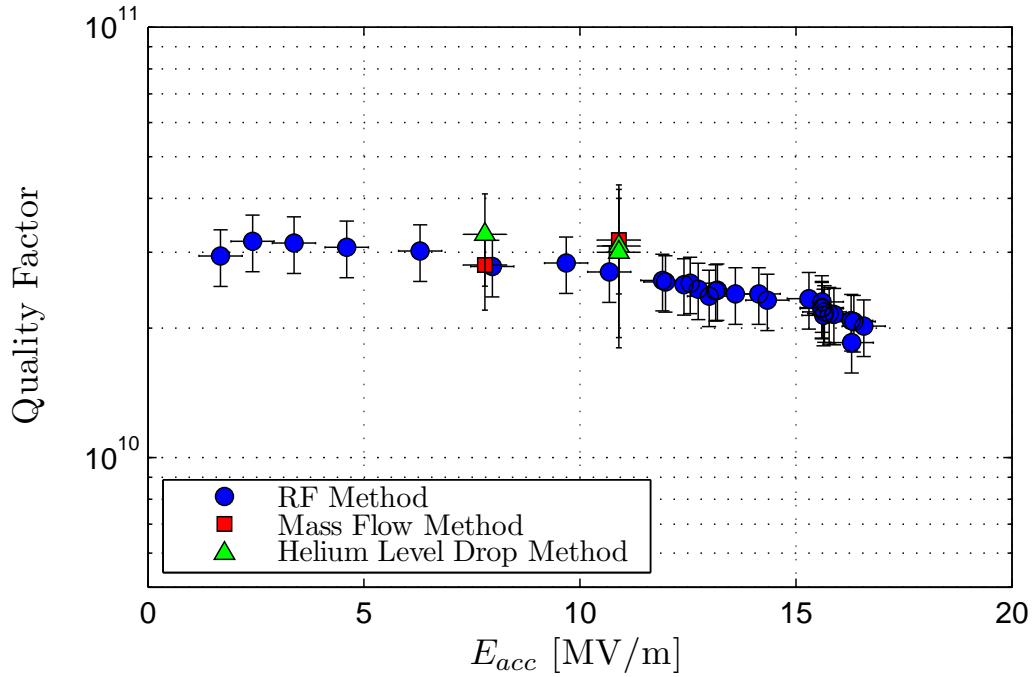
Figure 4.20: Q_0 vs E_{acc} measurement at 1.8 K for the initial cool down of HTC-1. RF measurements are compared with the two calorimetric methods of measuring Q_0 and shown to be consistent.

sistent with one another. The large uncertainty in the calorimetric method is due to the uncertainty in the static heat load, and from the fact that determining Q_0 relies on a difference measurement. The consistency between the two methods demonstrated that calorimetric measurements are reliable, an essential result for subsequent HTC experiments.

Thermal Cycling Effects on Quality Factor

The initial Q_0 measurements at 16.2 MV/m showed 1.8 K values slightly exceeding the 2×10^{10} design specification, arising entirely from a lower residual resistance. Previous work has shown that the Meissner effect is incomplete in pure Nb samples, which contributes to residual resistance through trapped magnetic flux, [AKK12] so the high level of magnetic shielding in the HTC gives high

initial Q_0 by lowering R_0.

In general, the only established method of improving the quality factor by reducing the surface resistance of the SRF layer of a structure is by chemical or high temperature thermal treatment, which would require a time intensive and expensive disassembly, processing step, and reassembly. However, preliminary studies at other laboratories suggested that Q_0 could be increased by thermally cycling the cryomodule's temperature with the cavity in situ. [KNV$^+$09] This is an attractive avenue to explore, because thermally cycling a cryomodule is a quick and inexpensive task, and increases in Q_0 directly reduce the operational cost of the machine. To this end, HTC-1 was used to further explore the effect of thermal cycling to temperatures below 300 K on Q_0.

A thermal cycle consists of slowly raising the temperature of the cavity to a temperature near or above T_c, and then slowly cooling back down to operational temperatures between 1.6 and 2.0 K. Gradients over the cavity during cool down are approximately 0.3 K/m, and the slow cool down rate is 0.4 K/hr. A schematic demonstrating how the cooldown process is executed in the HTC is presented in Figure 4.21.

As mentioned, stray magnetic fields contribute to residual resistance of the SRF surface layer. It has also been shown that quenching a cavity can lead to trapped magnetic flux in the cavity walls, which would contribute to the residual resistivity term of the superconductor. [KP97] In HTC-1, The quality factor before and after quench was measured, as well as after two thermal cycles to 10 K, and one to 100 K. Finally, we thermally cycled and cooled through T_c as quickly as possible to determine whether this would have a deleterious effect on surface resistance. The results are shown in Figure 4.22.
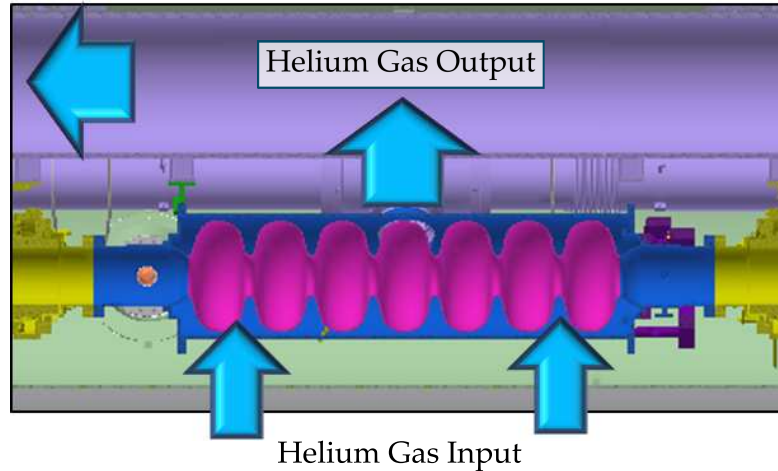
Figure 4.21: Schematic of the cooldown process in the HTC. Helium gas flows symmetrically around the cavity from two inputs at the bottom of the helium jacket. Helium is exhausted through a chimney above the center of the cavity to the two-phase line and helium gas return pipe where it is recovered.

The Q_0 vs E_{acc} measurements did not show degradation between the initial cool down and after quenching the cavity several times. After the first cycle to 10 K, the cavity's quality factor improved by ~20%, and a second low temperature cycle to 12 K yielded an additional ~20% improvement in Q_0.

It was hypothesized that due to a slow leak in the cavity's vacuum system, there could be gasses condensed on the RF surface, contributing to the residual resistance. Since most gasses are not mobile below 77 K, the cavity was thermally cycled to 100 K and retested. The Q_0 achieved in this measurement was ~50% higher than that obtained in the initial cool down, reaching $Q_0 = (3.0 \pm 0.3) \times 10^{10}$ at 1.8 K and 16.2 MV/m. Within experimental certainty, this result was consistent with the post 12 K cooldown. A subsequent fast cool down did not degrade the quality factor.

These results demonstrate that it is possible to improve the quality factor of a cavity simply by cycling through T_c several times maintaining small thermal
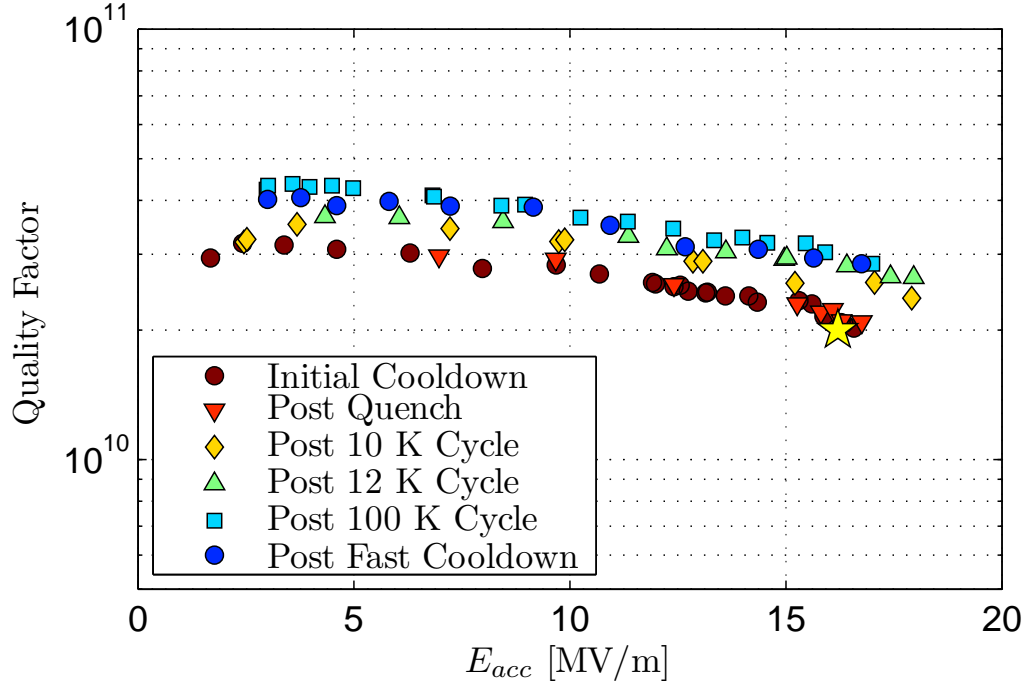
Figure 4.22: Q_0 vs E_{acc} measurements at 1.8 K before and after thermally cycling the cavity. The star denotes the Q_0 specification at 1.8 K. The Q_0 at design gradient increased by ~50% after thermally cycling to low temperatures. There was no significant degradation after the fast cool down. For visual clarity, 10% error bars in Q_0 have been suppressed.

gradients, both spatially and temporally. The HTC-2 and HTC-3 experiments continued investigating thermal cycling, and are discussed in section 4.3.4 and section 4.3.5.

Figures of Merit from HTC-1 Experiment

After the 100 K thermal cycle, Q_0 vs E_{acc} was measured at 1.6 and 1.8 K, and is presented in Figure 4.23. The cavity exceeded Q_0 design specifications by 50% at 1.8 K, and achieved a world record at that time for fundamental mode Q_0 for a multicell cavity installed in a horizontal cryomodule with $Q_0 = (6.1 \pm 0.6) \times 10^{10}$ at 1.6K and 5 MV/m. [VLF+14] At fields just below the quench field

of 17.3 MV/m, there was radiation detected along the beam axis of the cavity of 1-2 R/hr. This suggests the possibility of a low level of surface contaminants introduced during cavity assembly after the final HPR.
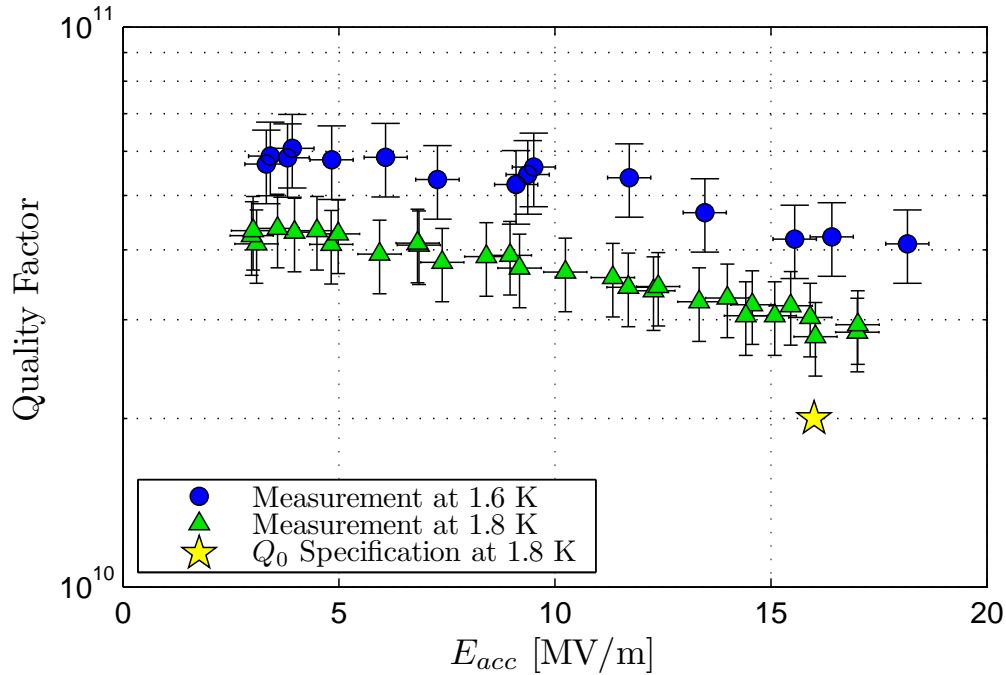
Figure 4.23: Final Q_0 vs E_{acc} measurements at 1.6 and 1.8 K for HTC-1. The star denotes the Q_0 specification at 1.8 K. The cavity exceeded Q_0 at 1.8 K and design gradient by 50% and set a world record Q_0 at 1.6 K and 5 MV/m of $(6.1 \pm 0.6) \times 10^{10}$.

The success of the HTC-1 cavity measurement demonstrated that quality factors do not necessarily degrade between vertical tests and horizontal ones, as illustrated in Figure 4.24. Because the same superconducting parameters described the BCS portion of the surface resistance, the only difference between the tests were a smaller residual resistance in HTC-1.

The reduced residual resistance between the vertical test and HTC-1 results could be due to better magnetic shielding, or the thermal cycling regimen. Figure 4.25 presents measurements of the ambient magnetic flux on the surface of the cavity's helium jacket cavity during cooldown. Notice the significant
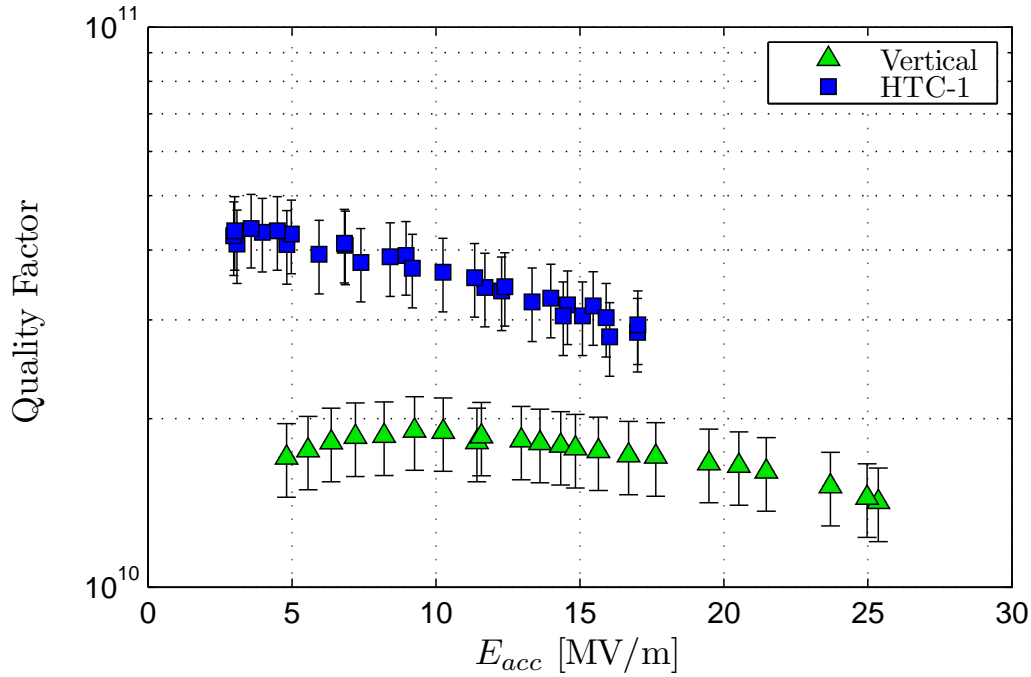
Figure 4.24: Comparison of Q_0 vs E_{acc} between vertical test and HTC-1 at 1.8 K. Measurements in HTC-1 show much higher Q_0, due to lower residual resistance, than in the vertical test even though no surface treatment was done between measurements.

changes in the ambient magnetic flux changes during cooldown.

Ambient magnetic flux can pin to impurity sites in a superconductor, trapping magnetic flux and increasing residual resistance. [VBB+92] The authors of [VBB+92] present a phenomenological result applicable to SRF cavities relating the residual resistance, R_0, the ambient magnetic field, B_{ext}, the upper critical field of the superconductor, B_{c_2}, and the normal state resistance, R_n, according to

$$R_0 = R_n \cdot \frac{B_{ext}}{B_{c_2}}. \tag{4.1}$$

Reasonable values for R_n of 1.3 GHz niobium resonators are between 1.5 and 1.8 mΩ. [PKH98] Generally speaking, B_{c_2} is not known for a superconducting cavity, but it is reasonable to assume $B_{c_2} = 400$ mT (see Table 2.2). The ambient
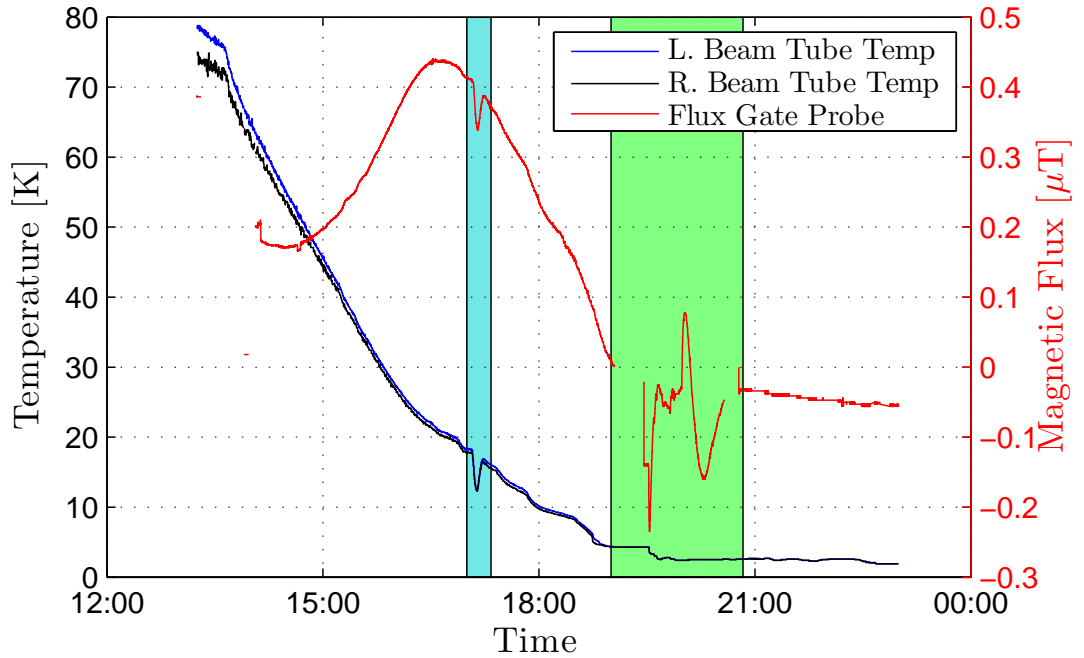
Figure 4.25: Fluxgate magnetometer measurement during HTC cooldown. Temperature sensors on each beam tube recorded the temperature during cooldown. The light blue region highlights a time period in which the helium valve was set incorrectly. The light green region marks the time that the field reversed polarity, requiring reconfiguration of the analog inputs, which was completed just before 21:00 hours.

flux during the transition through T_c in the HTC experiments was $0.2\,\mu$T, corresponding to residual resistance due to trapped flux of (0.8 ± 0.2) nΩ. This can be compared with ambient flux of $5 - 10\,\mu$T in the vertical test (R_0 between 1.8 and 4.5 nΩ). Application of Equation 4.1 with the measured magnetic flux does not account for the entire residual resistance observed in the vertical and horizontal tests.

The sign change of the measured flux during cooldown hints that there may be thermal currents[8] in the cryomodule during cooldown. Currents inside the

---

[8]The Seebeck effect describes how temperature gradients influence the local current density via $\mathbf{J} = \sigma(-\nabla V - S\nabla T)$, where S is the thermopower of the material. [Ash76]

structure can produce magnetic fields, but since the fluxgate probe is outside the helium vessel, the fields measured by the magnetometer may not be representative of the the local magnetic flux at the surface of the cavity.

While the HTC is optimized to achieve small thermal gradients during cooldown, non-zero thermal gradient induced currents may contribute to the cavity's residual resistance in addition to the ambient flux inside the cryomodule. One hypothesis is that thermal currents may be reduced during successive thermal cycles, leading to the reduction in R_0. This effect is further studied in HTC-2.

The next stage of experiments investigated whether the same performance could be repeated for the more complicated assembly, needed in an actual accelerator environment.

4.3.4 HTC-2

Following the success of HTC-1, the cryomodule was disassembled, and the cavity received an HPR to remove any residual surface contaminants. The cavity was then cleanly reassembled with the same procedure as described in section 4.3.3.

Instead of the axial coupler used in the vertical test and HTC-1, for HTC-2 a high power side mounted coupler was installed on the cavity (refer to Figure 4.11 and Figure 4.14 for high power coupler location in the HTC). It can couple 5 kW of power to the cavity and has a fixed nominal external quality factor, Q_{ext}, of 6.5×10^7. [BBB+11] The coupler consists of two main parts: a cold

coaxial coupler (< 80 K), a warm coupler section (> 80 K) with a room temperature coaxial transition to a rectangular waveguide. A computer aided design (CAD) model of the coupler design is presented in Figure 4.26.
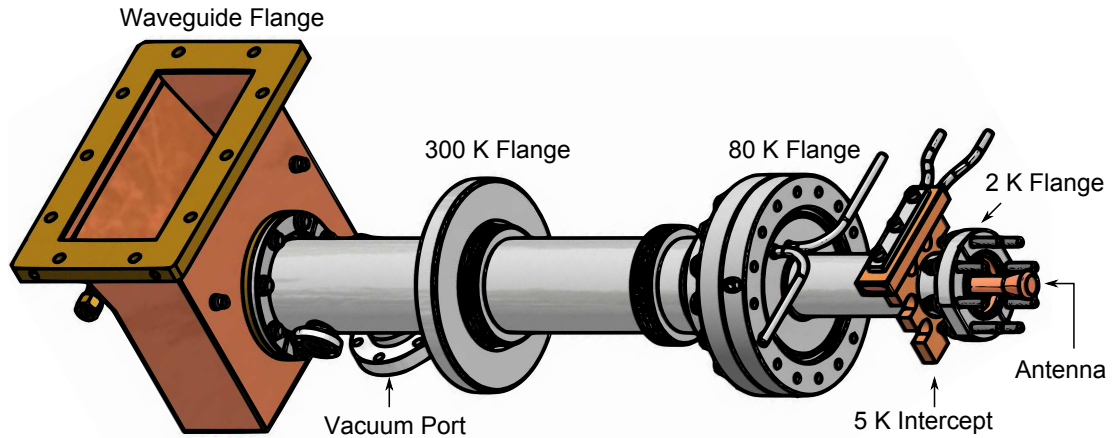
Figure 4.26: CAD model of the high power RF coupler used in the HTC-2 and HTC-3 experiments.

The coupler's 2K flange is directly connected to the 7-cell cavity's power input port. This design choice ensures that the antenna orientation does not change during cool down. [VB09] To provide flexibility, there are two bellow sections between the 80 K and 300 K flanges that allow the coaxial line's orientation to shift up to 10 mm during cool down. The 80 K intercept is cooled with high pressure gaseous helium.

The RF system used in the HTC-1 experiment was an phase-lock loop based system that tracked the fundamental mode resonance frequency. In operation, the ERL will instead operate at a fixed frequency, and vary the power level of the amplifier to keep the cavity's field level constant. This requires a different system to drive the cavity and maintain field stability. A simplified block diagram of this low-level RF (LLRF) system is presented in Figure 4.27.

Since the large over-coupling to the cavity prevented accurate determina-
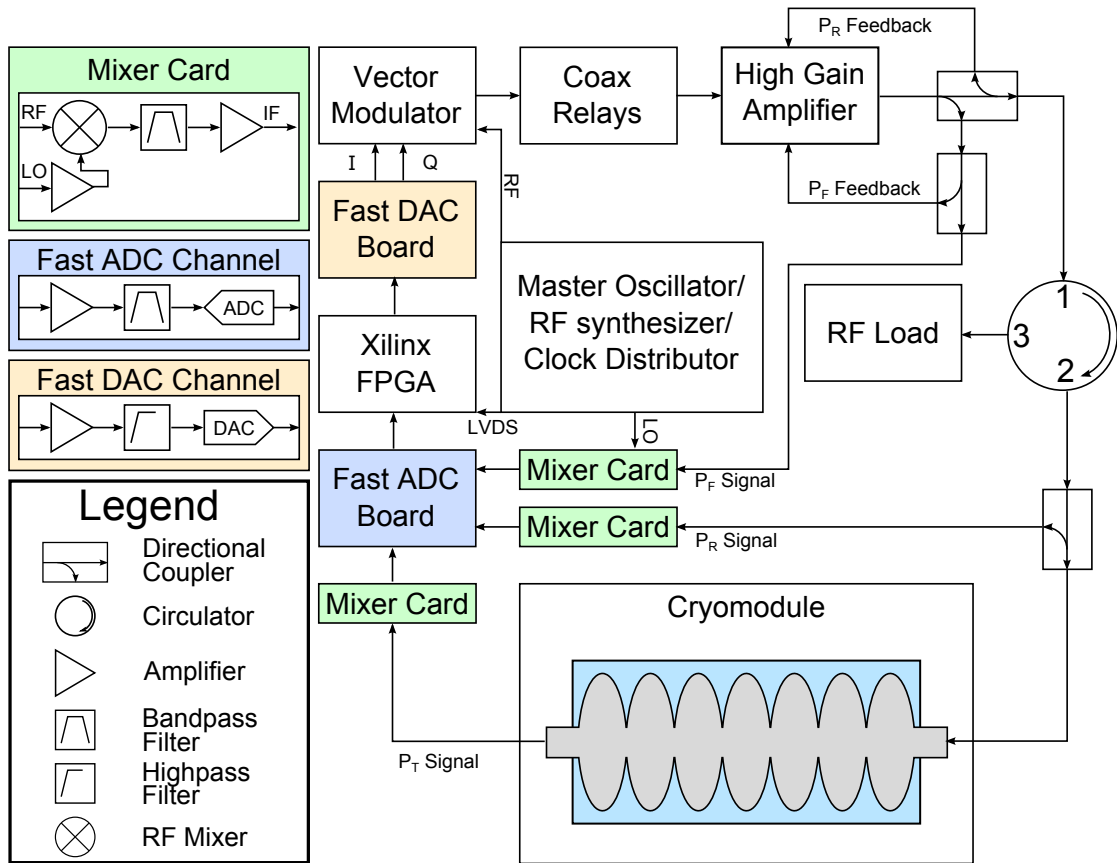
Figure 4.27: Simplified block diagram of the low-level RF system system used to maintain the cavity at constant voltage in the HTC-2 and HTC-3 experiments. The master oscillator outputs 1300 MHz RF power as well as timing signals to the ADC, DAC, and FPGA boards. Each mixer receives a LO input of 1287.5 MHz from the master oscillator (for visual clarity only one such input has been drawn). Using the transmitted (P_T) RF signal, corrections to the in-phase (I) and quadrature (Q) portion of the RF signal are computed in th FPGA and passed to the vector modulator.

tion of the quality factor via RF methods, only calorimetric methods were used. Measurements of the static heat load of the cavity at the three operating temperatures were performed and are presented in Table 4.4. These static heat load measurements show that the high power coupler does not significantly increase the static heat load, as designed.

As in HTC-1, Q_0 vs E_{acc} was measured at 1.6, 1.8, and 2.0 K (see Figure 4.28).

Temperature [K]	Level Stick Method Heat Load [W]	Gas Meter Method Heat Load [W]
1.6	1.0 ± 0.4	1.0 ± 0.2
1.8	1.5 ± 0.4	2.0 ± 0.2
2.0	2.6 ± 0.4	2.2 ± 0.2

Table 4.4: Static heat load measurements made in HTC-2.

Initial measurements showed a lower Q_0 than was achieved in HTC-1, with the 1.8 K Q_0 at design gradient 25% below design specification. The level stick and gas meter methods yielded consistent Q_0 values.
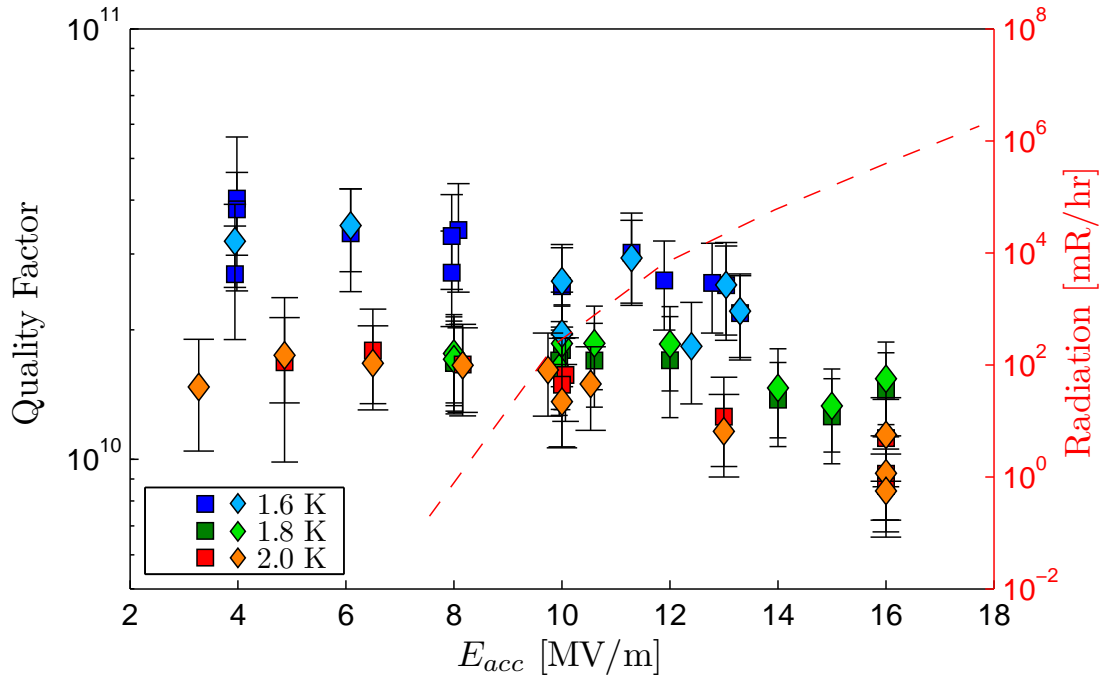
Figure 4.28: Q_0 vs E_{acc} measurements for the initial cool down of HTC-2. Square (□) markers denote measurements made by the level stick method, and diamonds (◊) show results from gas meter based measurements. The red dotted line marks radiation levels with values corresponding to the right axis. Radiation was measured at a gamma probe out side the cryomodule placed along the beam axis. The cavity's pre-thermal cycling 1.8 K Q_0 is below design specification.

The lower Q_0 was accompanied by high levels of radiation, with the first detectable x-rays beginning at gradients above 7.5 MV/m. Gamma probes

mounted at each end of the cryomodule along the beam tube measured x-ray doses above 2 kR/hr, and a neutron detector measured 3×10^3 neutrons/hr at the coupler end of the cryomodule. Because the highest radiation was highest at the gamma probe closest to the high power coupler, it is likely that source of electrons was from the end cell far from the coupler. Electrons were likely field emitted from the cell surface and were accelerated through the structure, striking the wall of the cryomodule and releasing x-rays and neutrons. Generally, electrons arise from small conducting dust particles that serve as a field emitters, which comes from a sub-optimal assembly procedure.

Thermal Cycling Effects on Quality Factor

As in HTC-1, investigations into thermal cycling's effect on Q_0 was continued during the HTC-2 experiment. Since HTC-1 had already demonstrated that thermal cycling can be beneficial, the next step was to determine the temperature at which benefits first begin. Initially, two thermal cycles were performed to low temperatures (15 K). Benefits in HTC-1 were observed from both low temperature and high temperature cycles, so following the low temperature thermal cycles two additional high temperature thermal cycles were performed, the first to 100 K and the second to 300 K. Finally a thermal cycle to a temperature below T_c was performed, to test whether flux can tunnel out of the superconducting bulk, an idea which has been tested in samples, [VKK13] but never confirmed in a superconducting cavity.

The results of thermal cycling on the cavity's Q_0 (measured at 1.8 K) are presented in Figure 4.29. In this plot, data obtained with the level stick and gas meter have been averaged. The most benefit was obtained after the first thermal

178

cycle to 15 K, which increased Q_0 at design gradient from 1.4×10^{10} to 1.9×10^{10}. The subsequent 15 K cycle yielded $Q_0(E_{acc} = 16.2 \text{ MV/m}, 1.8 \text{ K}) = 2.0 \times 10^{10}$.
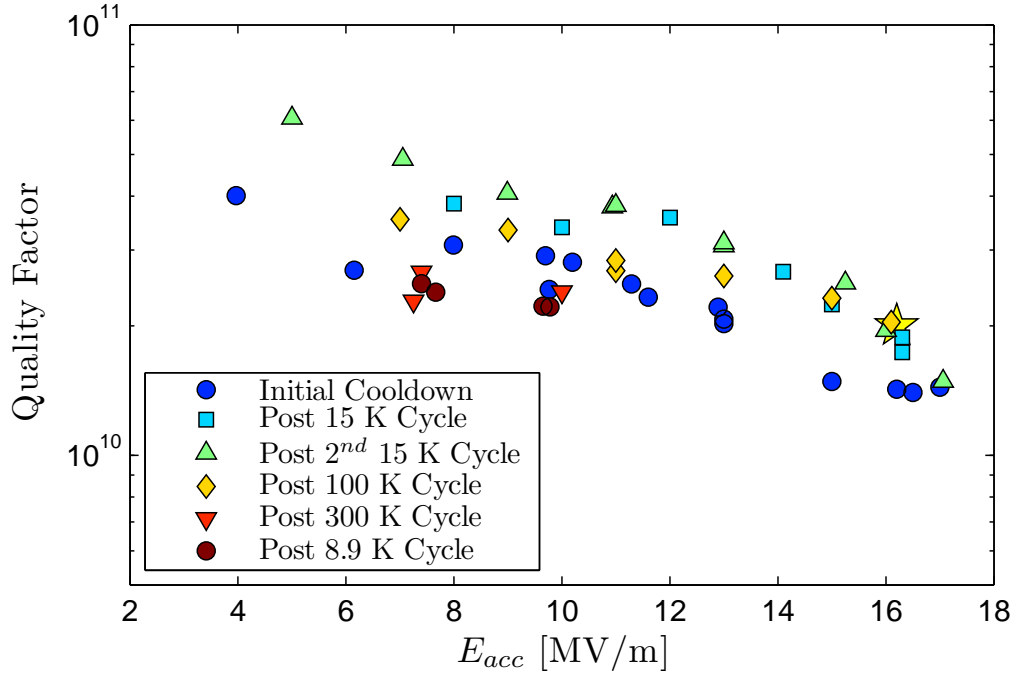
Figure 4.29: Q_0 vs E_{acc} measurements at 1.8 K before and after thermally cycling the cavity in the HTC-2 experiment. The star denotes the Q_0 specification at 1.8 K. The most benefit in reduced surface resistance (higher Q_0) was obtained after the first 15 K thermal cycle. For visual clarity, 20% error bars in Q_0 have been suppressed.

The high temperature thermal cycles were intended to explore whether adsorbed gas was contributing to the high radiation levels produced during cavity operation. By increasing the temperature to 100 K, elements that cling to the cryogenic surface at cryogenic temperatures revert to their gaseous state and can be removed by turbo pumps. Residual gas analyzer measurements showed the removal of H_2O, N_2, O_2, and Ar during the 100 K cycle. Subsequent Q_0 measurements demonstrated that the mid-field (~16 MV/m) quality factor continued to slightly improve, while the low field Q_0 slightly degraded. These changes, however, were not outside of experimental uncertainty, suggest-

ing that residual gasses play no significant role in the thermal cycling effect.

A complete warmup to 300 K was performed to see if the thermal cycle benefits were cumulative, or if they had to be redone for each cool down from room temperature. Unfortunately, during the cool down process there was a small vacuum leak causing the cavity pressure to increase from 1×10^{-7} Torr to 2×10^{-4} Torr. Additional pumping was added to the cavity vacuum space, and the cycle continued. At 1.8 K, the cavity performance was consistent with the measurements during the initial cool down, though high radiation levels prevented operating the cavity at accelerating gradients above 10 MV/m, implying the benefit of thermal cycling is lost when the cavity is returned to room temperature.

Since the cavity performance after the 300 K cool down was similar to the initial cool down, the effect of the maximum temperature reached during a cycle could be directly compared. In this case, a cycle to below 9 K was performed, wherein the cavity temperature was maintained between 8 and 8.9 K for 40 minutes, and then returned to 1.8 K. With this cycle, no improvement in the quality factor was observed. This suggests that thermal cycling benefits occur when reaching maximum temperatures above T_c but well below room temperature. [VEF+13]

Possible explanations for the reduction in residual resistance include removing adsorbed gasses from the surface of the conductor or thermoelectric effects changing the amount of trapped flux in the superconductor.

If gasses were the source of the residual resistance, increasing temperatures to about 15 K is not a high enough temperature for them to become mobile and

dissociate from the cavity surface. Thus, it is unlikely that adsorbed gases are the driving force behind the phenomena.

Figures of Merit from HTC-2 Experiment

The figures of merit for the HTC-2 test were taken as the Q_0 vs E_{acc} points from the post 100 K thermal cycle, which was the last HTC-2 measurement able to cover the entire gradient range without exceeding administratively set radiation limits. The data is plotted in Figure 4.30.
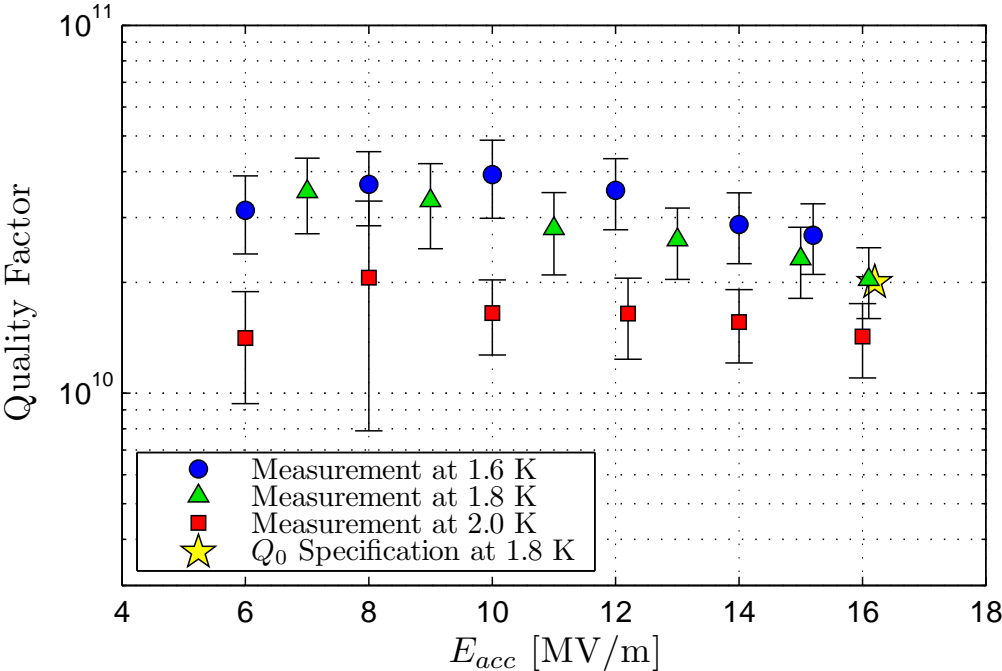
Figure 4.30: Q_0 vs E_{acc} measurements at 1.6, 1.8 and 2.0 K in HTC-2. The cavity met the Q_0 specification. The cavity did not quench at high fields, but was instead administratively limited because of high levels of radiation.

During operation, radiation levels reached 10 kR/hr at probes placed outside the cryomodule along the beam axis, and could not be mitigated through quench processing. Thus, although the design specification was achieved, be-

fore proceeding with the fully equipped cryomodule in HTC-3, chemical processing was required to remove the source of field emission in the end cell far from the input power coupler.

4.3.5 HTC-3

Following the HTC-2 experiment, the cryomodule was disassembled and the cavity received a 5 μm BCP with the intent of removing the source of field emission from the cavity surface followed by a 120°C heat treatment for 48 hr and a single HF rinse, oxide regrowth step. [RGBO13] The cavity was then high pressure rinsed and assembled into the cryomodule along with two beam-line higher-order mode loads (see bottom of Figure 4.11 for reference).

The part of the HOM loads that absorbs RF energy is made of a SiC loaded ceramic[9], [Coo06] which is brazed to a tungsten fixture that attaches directly to the cavity flange. The HOM loads serve not only to damp higher-order modes, but also as bellows connecting the main linac cavities (see Figure 4.31). The absorbers are designed to extract up to 200 W of HOM power for frequencies up to 150 GHz. [ECH+13]

The loads have two points that are thermally anchored. The first is the 5 K intercept right after the stainless steel bellows. Because the HOM load is directly connected to the cavity flange, and the cavity will operate at 1.8 K, anchoring the HOM load at 5 K helps to reduce the conduction losses to the liquid helium bath. The second anchor point is the cooling tube apparatus (nominally at 80 K) that removes the HOM power.

---

[9]It is a commercially available material with the trade name of Coorstek® SC-35.
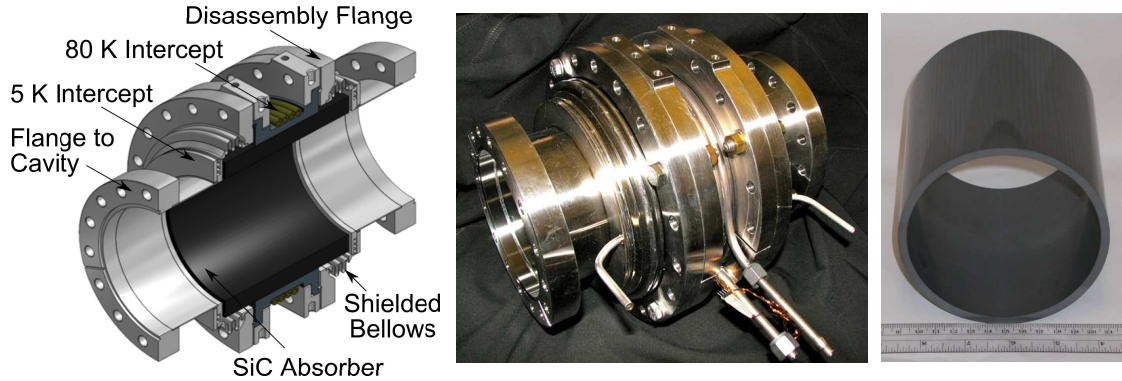
Figure 4.31: Left: Half-plane cut CAD model of the higher-order mode load used in the HTC-3 experiment. Middle: Fabricated HOM load assembly. Right: Ring of SiC absorber prior to brazing into HOM load assembly.

The material properties of the ceramic have been measured from 1–12 GHz, yielding $\mu = \mu_0$, and $\epsilon = [(50 \pm 10) - (28 \pm 7)]\epsilon_0$, via methods developed by V. Shemelin. [VSP05, SB10] The resistivity of the HOM absorbers was measured and found to be on the 10 kΩ scale at 160 K, and increase sharply with decreasing temperature. At 80 K, the resistivity is large, but should still prevent load charging from the beam.

The absorbers were placed under vacuum and showed out-gassing < 10^{-7} Torr·L/s. [ECH+13] A challenge with this material is that the properties are known to vary with production runs, so the values quoted are only reliable for the loads installed in HTC-3.

Prior to installing the HOM loads onto the cavity flanges, the absorbers were methanol rinsed and allowed to air dry. They were attached to the cavity, the high power input coupler was installed, and the cryomodule was moved back to the accelerator tunnel for qualification testing. The cavity was then slowly cooled from room temperature to 2 K.

Temperature [K]	Gas Meter Method Heat Leak [W]
1.6	2.0 ± 0.3
1.8	2.4 ± 0.3
2.0	1.4 ± 0.3

Table 4.5: Static heat leak measurements made in HTC-3 using the gas meter.

As in HTC-2, the Q_0 measurements are all calorimetric in HTC-3. Both the static heat leak and Q_0 measurements relied on the gas meter method, since it is more accurate than the level stick. The static heat leak measurement for HTC-3 are presented in Table 4.5, and are similar to those measured in HTC-1 and -2, demonstrating that the HOM loads to not cause a significant static heat load. The conduction losses to 2 K are significantly reduced due to the presence of 5 K intercepts between the absorber and the HOM holder beam tube.

The external quality factor of the input coupler and field probe was measured with a network analyzer. Port 1 of the network analyzer was connected to the input coupler and port 2 to field probe A, and scattering parameters S_{11}, S_{21} and S_{22} were measured. The Q_L of the entire structure is related to the cavity's intrinsic quality factor, Q_0, and coupler and probe's external quality factor, Q_{ext}^C and Q_{ext}^P by

$$\frac{1}{Q_L} = \frac{1}{Q_0} + \frac{1}{Q_{ext}^C} + \frac{1}{Q_{ext}^P}, \tag{4.2}$$

where S_{ij} are measured in absolute power levels. [Ves] Since Q_0 and Q_{ext}^P are much larger than Q_{ext}^C, we can set those terms to zero and set the measured value of $Q_L = 4.96 \times 10^7$, equal to Q_{ext}^P.

The coupling of the field probe can be determined with the relationship

$$Q_{ext}^P = \frac{4Q_{ext}^C}{S_{21} - S_{11}/2 - S_{22}/2}. \tag{4.3}$$

Scattering parameter measurements yielded a value of $Q_{ext}^P = 3.22 \times 10^{11}$.

The forward and transmitted power levels, P_f and P_t respectively, can be used to determine the cavity voltage, V, by knowing the R/Q of the fundamental mode (387 Ω), and using Equation 1.40 and Equation 1.41 with P_F measured at the input coupler and P_t at the field probe A. [Lie01]
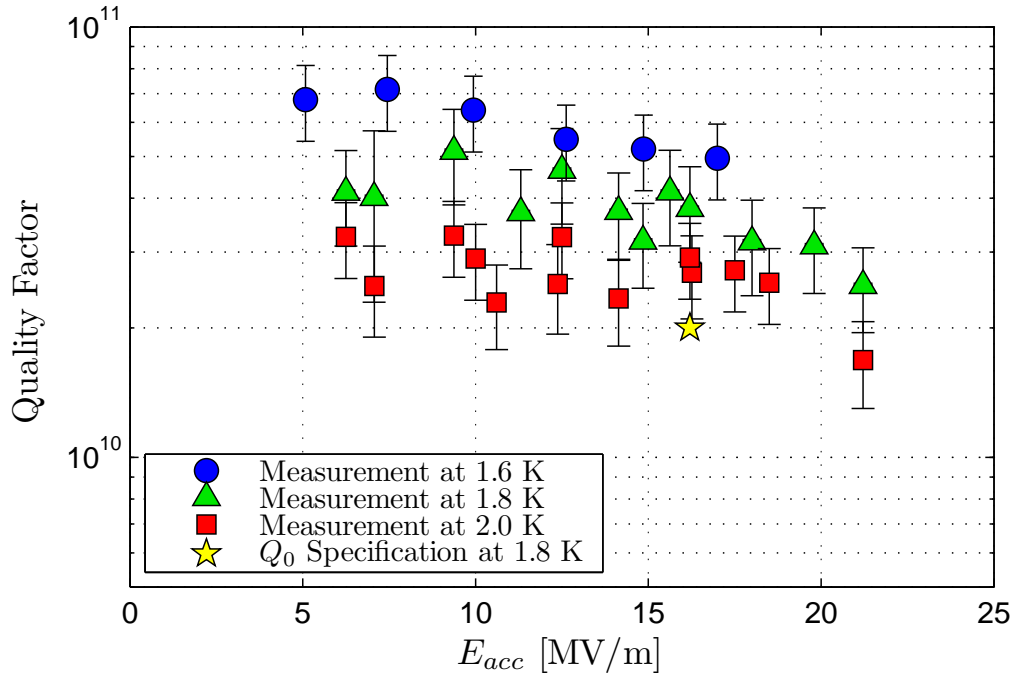
Figure 4.32: Q_0 vs E_{acc} measurements for the initial cool down of HTC-3, measured via the gas meter. The quality factor exceeded design specification, even at 2.0 K. At 1.6 K, $Q_0 = (7.0 \pm 1.2) \times 10^{10}$, exceeding the world record set previously in HTC-1 (see Figure 4.23).

The quality factor vs accelerating gradient was measured at all three temperatures, using the gas meter method, with results plotted in Figure 4.32. The quality factor exceeded design specification, even at 2.0 K. At the proposed ERL operating temperature of 1.8 K, the cavity reached $(4 \pm 0.5) \times 10^{10}$. The low field Q_0 at 1.6 K broke the record set in HTC-1, with a value of $(7 \pm 1.2) \times 10^{10}$. The radiation at high fields was less than 1 R/hr.

The Q_0 of the fully outfitted cavity in HTC-3 exceeded design specification by a factor of 2, meaning the cavity's surface has extremely small surface resistance. At 1.6 K, the BCS resistance is small, and R_s is dominated by residual resistance. The lowest surface resistance achieved in the initial cool down was only ~4 nΩ which is already better than the residual resistance obtained after thermal cycling in HTC-1 of roughly 6 nΩ (see Table 4.3).

One difference in surface preparation between HTC-1 and HTC-3 is the HF rinse after 120°C heat treatment. It is known that the heat treatment lowers the BCS component of resistance while increasing the residual resistance. The HF rinse helps to reduce the residual resistance, resulting in very high Q_0 structures. [RGBO13] Thus whether thermal cycling could reduce the residual resistance below this already very low value is an interesting question.

Thermal Cycling Effects on Quality Factor

Due to time constraints, only a single thermal cycle could be performed during the HTC-3 experiment. Since HTC-2 demonstrated no benefit by thermally cycling to below 9 K, and both HTC-1 and HTC-2 showed benefit from a 15 K thermal cycle, it was decided to perform the thermal cycle to a maximum temperature just above T_c.

The thermal cycle was performed, holding the cavity temperature above T_c for about 30 minutes, and reaching a peak temperature of 10.1 K, as shown in Figure 4.33. During cool down, the peak-to-peak temperature difference across the cavity was 0.2 K, giving a maximum thermal gradient of 0.25 K/m. As shown in as the cavity transitioned through T_c, the temperature was decreasing
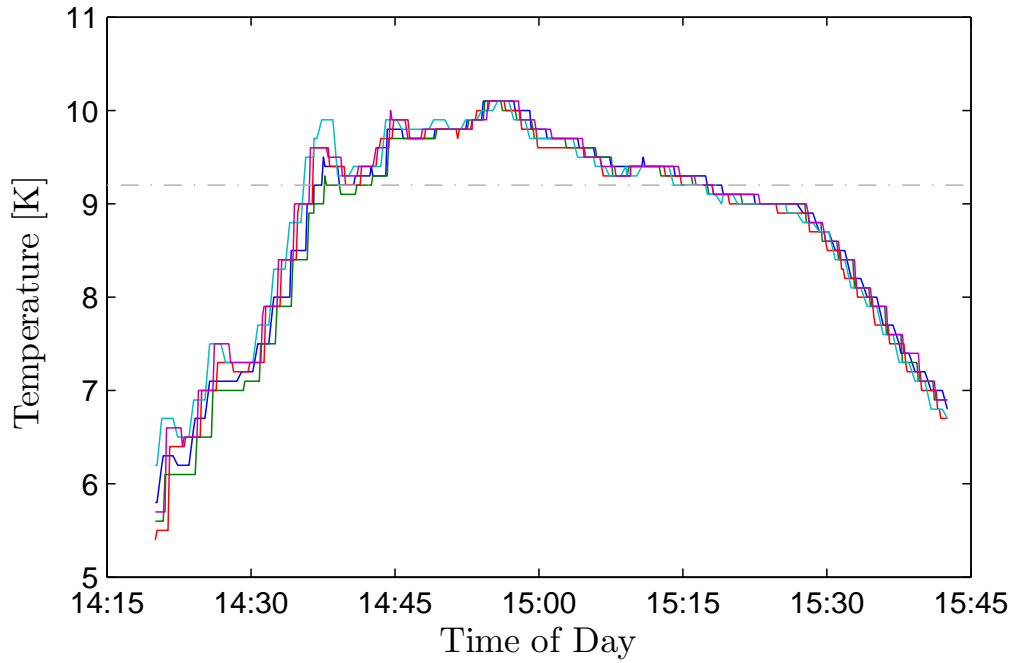
Figure 4.33: Cavity temperature vs time during 10 K cycle of HTC-3. The solid colored lines show the temperature sensors on the cavity center and end cells. The gray dashed line marks the cavity's nominal critical temperature of 9.2 K. The spatial and temporal thermal gradients going through T_c were 0.25 K/m and 0.4 K/hr respectively.

at a rate of 0.4 K/hr. After the cavity temperature decreased below 9.0 K, the rate of cooling was increased to 8 K/hr until the cavity reached 4.2 K. After refilling the cryomodule with liquid helium, the temperature was returned to 2.0 K, at an average rate of 2 K/hr.

Following the thermal cycle, Q_0 vs E_{acc} measurements were performed at all three standard temperatures. The results of the Q_0 measurements following the thermal cycle are presented in Figure 4.34, which compares the results before thermal cycling with the data taken after the 10 K cycle. A significant change in Q_0 was observed due to the thermal cycle. The cavity's Q_0 again exceeded the world record set in HTC-1, reaching quality factors above 1×10^{11} at 1.6 K. The measurements were performed with both the digital LLRF system at lower
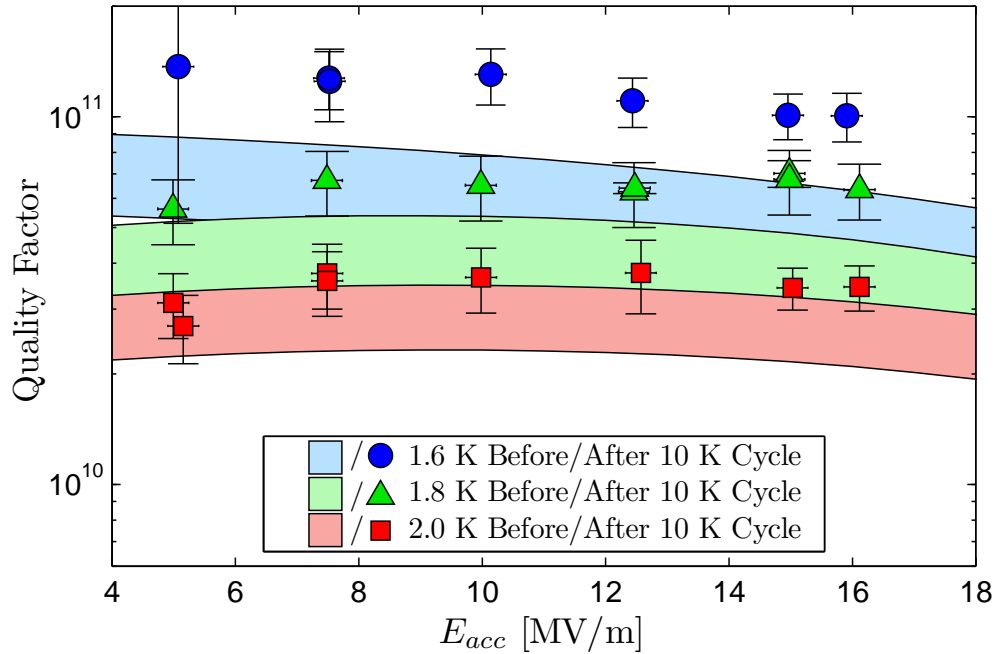
Figure 4.34: Q_0 vs E_{acc} measurements before and after thermally cycling HTC-3 above 10 K. The filled regions correspond to the Q_0 measurements (with errors) made during the initial cool down from Figure 4.32, and the markers show the Q_0 after the thermal cycle.

fields and the phase-locked loop system at-mid fields.

The reproducible nature of Q_0 increase with thermal cycling in all three HTC assemblies is an important result.

Using the Q_0 data at low fields (~5 MV/m), taken at 1.6-2.0 K, the reduction in residual resistance of the cavity's RF surface layer can be calculated using SRIMP. Material parameters for the superconducting layer consistent with measurements are presented in Table 4.6. A plot of the data and the corresponding fits are shown in Figure 4.35.

The material properties of the cavity's surface layer giving rise to BCS resistance are identical within measurement uncertainty between the vertical test, HTC-1 and HTC-3. The only statistically significant difference between the mea-

Cool down:	Initial	Post 10 K	
Input Parameter	Value	Value	Unit
Frequency	1300	1300	MHz
T_c	9.20	9.20	K
λ_L	39.00	39.00	nm
ξ_0	38.00	38.00	nm
Fit Parameter	Value	Value	Unit
E_g	3.887 ± 0.058		—
ℓ_{tr}	24.74 ± 23.77		nm
R_0	3.20 ± 0.34	1.34 ± 0.14	nΩ
Calculated Result	Value	Value	Unit
λ_{tr}	1.355 ± 1.303		—
$R(\lambda_{tr})$	1.035 ± 0.557		—
λ_{GL}	41.59 ± 11.51		nm
ξ_{GL}	18.61 ± 0.14		nm
κ_{GL}	2.24 ± 1.24		—
$c(\kappa_{GL})$	1.11 ± 0.09		—

Table 4.6: Surface superconducting properties extracted from measurements of ERL 7.1 in the HTC-3 experiment. The same energy gap and mean free path was used to fit both sets of data, allowing the residual resistance to vary between runs.

surements arises from disparities in residual resistance. Though residual resistances decreased in all measurements over thermal cycles, in HTC-3, the residual resistance decreased by about 66% from 3.2 nΩ to 1.3 nΩ after the 10 K thermal cycle. This is a remarkable result when one considers that typical residual resistances for cavities in cryomodules are between 5-15 nΩ. The fundamental mode Q_0 measurements of ERL 7.1 are the best ever achieved in a cryomodule.

Additional thermal cycling measurements would be interesting to perform, unfortunately further thermal cycling investigations were not possible due to limited laboratory resources.
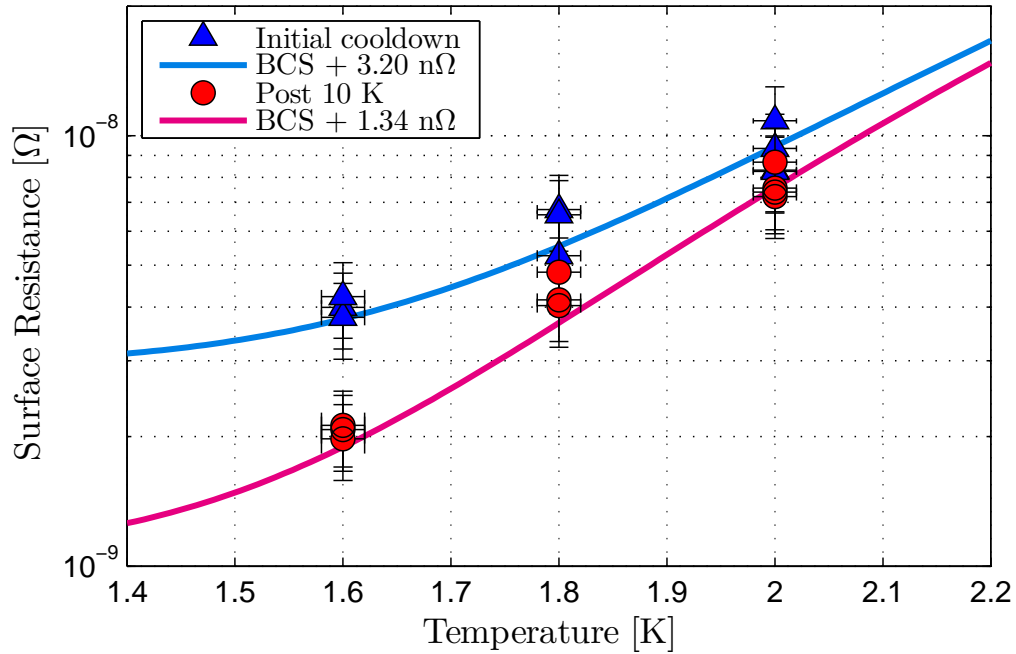
Figure 4.35: R_s vs temperature measurements before and after thermally cycling ERL 7.1 to 10 K in HTC-3. The markers denote measured values and the lines are obtained from SRIMP with the material parameters listed in Table 4.6.

Figures of Merit from HTC-3 Experiment

After the thermal cycle, the cavity's intrinsic quality factor was measured out to the maximum achievable fields with the analog phase locked loop RF system. Accelerating gradients up to 21 MV/m were obtained before being limited by available RF power. The final Q_0 vs E_{acc} figures of merit from the HTC-3 test are displayed in Figure 4.36.

At the proposed operating temperature of 1.8 K, the cavity reached a quality factor of $(6.3 \pm 1.0) \times 10^{10}$ at 16.2 MV/m, exceeding the design specification by a factor of three. Even at fields up to 21 MV/m, the Q_0 had not decreased to below 4×10^{10}. Typically, there is a strong Q-slope observed in Nb cavities treated with BCP just above this field. It was not possible to measure Q_0 at gradients larger
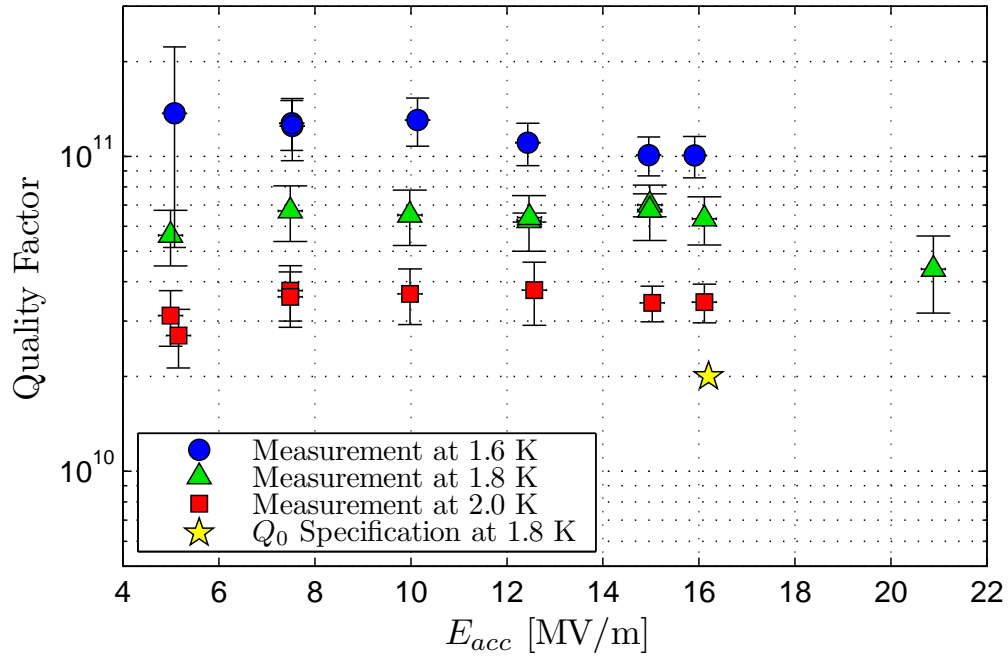
Figure 4.36: Final Q_0 vs E_{acc} curves for ERL 7.1 in HTC-3. At the operating accelerating gradient and temperature, the cavity's Q_0 exceeds design specification by a factor of three, reaching 6×10^{10}. Accelerating gradients of 21 MV/m were achieved.

than this due to lack of available RF power.

4.3.6 Review of HTC Fundamental Mode Q_0 Studies

The series of HTC experiments demonstrated that the prototype ERL cavity can have a very high quality factor in a realistic particle accelerator environment. As Table 4.7 demonstrates, it is possible to consistently decrease the residual resistance of a superconducting structure in a cryomodule by about 3 ± 1 nΩ by thermal cycling the cavity in situ. The fact that the installation of a side mounted high power coupler and HOM loads were able to be done cleanly–as evidenced by the cavity's very low residual resistance–shows that it is reasonable to deploy

this technology on a larger scale in the main linac cryomodule project.

Stage	ΔR_0 [nΩ]	Increase in Q_0 [%]	Best Temperature Cycle [K]
HTC-1	4.5	33	12
HTC-2	4.6	24	15
HTC-3	1.9	44	10

Table 4.7: Reduction in residual resistance in the three HTC experiments due to thermal cycling, assuming the difference in initial and best Q_0(16.2, 1.8 K) is due to decrease in R_0. The third column records the peak temperature reached in the thermal cycle responsible for the greatest reduction in residual resistance. Though the thermal cycle in HTC-3 resulted in a smaller reduction in R_0 than in the other cases, its initial R_0 was much smaller, yielding a much higher Q_0 after cycling.

It was clearly demonstrated that very high Q_0 of the fundamental mode is achievable in a fully equipped cryomodule, more than tripling the design specification of 2×10^{10} at the operating temperature and gradient. Even at 2.0 K Q_0 exceeds 3×10^{10} at the operating gradient, a remarkable result in itself. The applicability of this result is clear when considering that the LCLS-II design requires $Q_0(2.0 \text{ K}) \geq 2.7 \times 10^{10}$, and this measurement is the first to demonstrate the feasibility of this specification in a cryomodule.

Finally, the fact that a quality factor of 1.0×10^{11} was obtained at 16 MV/m opens up the possibility of operating the ERL at a different temperature if this can be replicated on a large number of cavities.

This result has important implications for future large-scale SRF projects. As discussed in subsection 1.4.2, new light sources benefit primarily from high quality factors at medium gradients. For example, reproducing the results of $Q_0(16.2 \text{ MV/m}, 1.8 \text{ K})=6 \times 10^{10}$ would reduce the cost of the LCLS-II by 25-30%, relative to a Q_0 of 1×10^{10}. In addition, the extremely high Q_0 at 1.6 K opens up the possibility of operating a CW linac at 1.6 K for additional cost savings.

With the fundamental mode properties far exceeding design specification, the remaining question is whether the higher-order modes that can potentially cause beam breakup effects at high currents have been sufficiently damped.

4.4   Higher-order Mode Measurements

The higher-order mode properties of the 7-cell cavity will determine whether or not the full linac can support the 100 mA beam current that is the Cornell ERL's operational design specification. The HOM spectra was measured at each stage of the HTC experiment to systematically the damping of the HOMs by the RF input coupler and beamline HOM absorbers. The main differences between the experiments that influence the HOM properties are summarized in Table 4.8.

Stage	RF input method	HOM absorbers
HTC-1	On-axis coupler	none
HTC-2	High-power input coupler	none
HTC-3	High-power input coupler	2 SiC loaded ceramic absorbers

Table 4.8: Summary of the key elements incorporated in each iteration of the horizontal test cryomodule experiments. The fundamental mode couples to the on-axis input coupler with $Q_{ext} = 9 \times 10^{10}$ and the high-power coupler with $Q_{ext} = 5 \times 10^7$. In all cases the field probe was weakly coupled to the fundamental mode with $Q_{ext} = 3 \times 10^{11}$.

The cavity's HOM spectrum was measured in each HTC experiment using a network analyzer to drive the cavity from the RF input coupler and measure the excitation at a field probe A.[10] The scans were performed with an IF bandwidth of 30 Hz while searching for the HOM passbands, and reduced as needed to get a large signal-to-noise ratio. The scan frequency step size was varied from

---

[10]This probe couples to the fundamental mode with $Q_{ext} \sim 3 \times 10^{11}$.

1 kHz/step for a broad scan to 1 Hz/point for modes with very large loaded quality factors. The scattering parameter S_{21} was measured as a function of frequency and yields the properties of higher-order modes.

The most important figures of merit come from the HOM spectra of HTC-3, since this will characterize the performance of the HOM absorbers, which are not present in HTC-1 or HTC-2. Still, the spectra from the first two experiments serve as a point of comparison to determine the efficiency of the absorbing material in a realistic accelerator environment.

A final verification of HOM damping in HTC-3 is done with a beam to search for any possible HOM having a large Q_L and (R/Q) which might have been missed in network analyzer measurements.[11]

4.4.1   Methods to Extract Resonance Properties from Spectra

There are several methods to extract the properties of higher-order modes from spectral measurements of the cavity's scattering matrix. Two techniques were implemented. The first fits the amplitude of S_{21} with a Lorentzian function, using the resonant frequency and quality factors as tuning parameters. The second uses the complex phase information of S_{21} to fit phase vs frequency near an HOM, extracting the same information as in the Lorentzian case.[12] The derivation of the equations is based on a circuit model of an HOM in the cavity.

A cavity containing a single HOM can be modeled as a transmission line

---

[11]This is possible if a HOM is trapped in the center of a cavity, having very weak coupling to the probes used to measure a transfer function.

[12]While complex scattering parameter measurements could be used to fit the resonance curve directly, it is useful to use the amplitude formulation, since this technique is applicable when using spectrum analyzers, which lack phase information.

connected to an RLC circuit. [PA98] To determine the transfer function that will be observed by the network analyzer, consider the simplified system of a voltage source varying sinusoidally at an angular frequency ω connected to a series RLC circuit as shown in Figure 4.37.
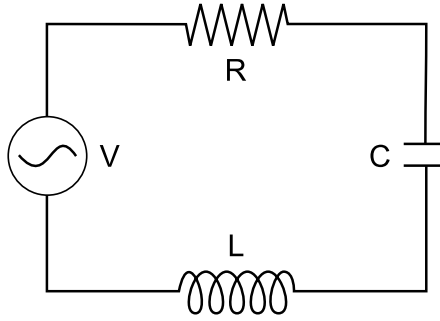
Figure 4.37: HOM in cavity modelled as a series RLC circuit driven by a voltage source, V, having sinusoidal time dependence.

The transfer function, measured across the resistor, of the RLC circuit driven at an angular frequency ω is given by

$$H(\omega) \equiv \frac{V_R}{V} = \frac{R}{R + \frac{1}{i\omega C} + i\omega L} = \frac{R}{R + i\left(\omega L - \frac{1}{\omega C}\right)}, \tag{4.4}$$

where V_R is the voltage across the resistor.

Equation 4.4 can be written in terms of the squared amplitude and phase to yield the following relations:

$$|H(\omega)|^2 = \frac{R^2}{R^2 + \left(\omega L - \frac{1}{\omega C}\right)^2}, \tag{4.5}$$

$$\tan(\phi) \equiv \frac{\Im\left\{H(\omega)\right\}}{\Re\left\{H(\omega)\right\}} = \frac{\omega L - \frac{1}{\omega C}}{R}. \tag{4.6}$$

Note that $\phi \equiv \arg[H(\omega)]$.

These two expressions yield different methods of obtaining the frequency and loaded quality factor of an HOM in the cavity with a network analyzer trace. In the first, one can rewrite Equation 4.5

$$|S_{21}|^2 (\omega) = \frac{\left|S_{21}(\omega_0)\right|^2}{Q_L^{-2} + \left(\frac{\omega}{\omega_0} - \frac{\omega_0}{\omega}\right)^2},$$
(4.7)

using the definition $\omega_0 = 1/\sqrt{LC}$ and $Q_L^2 = L/(R^2C)$, [Poz05] and which will be referred to as the Lorentzian method. An example of fitting a resonance with the Lorentzian method is presented in Figure 4.38. The Lorentzian fit successfully
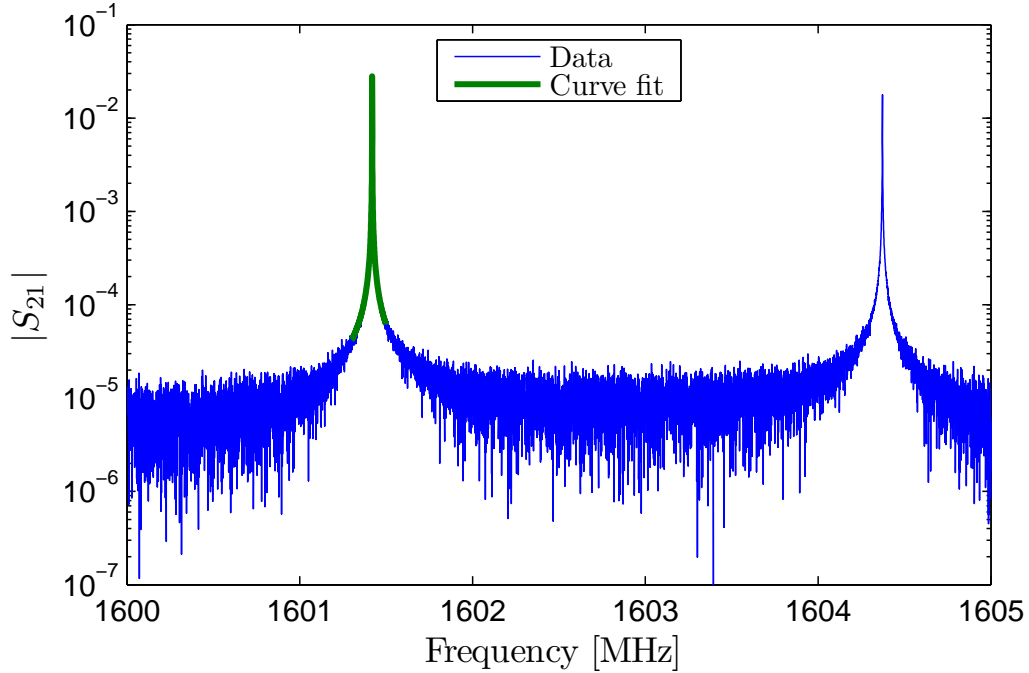
Figure 4.38: A Lorentzian fit of the lowest frequency dipole HOM measured in the HTC-1 experiment. Network analyzer data is in blue, and the thicker green line is the curve fit. This HOM has a resonant frequency of 1601.419 MHz and $Q_L = 7.97 \times 10^6$. The resonance on the right is the other polarization of the mode. The modes are not degenerate due to broken symmetry.

extracted the parameters from the HOM in Figure 4.38, determining a frequency of 1601.419 MHz and $Q_L = 7.97 \times 10^6$. The Q_L of the mode is high, because this

data is from the HTC-1 test, which did not have HOM absorbers, leaving the HOMs mostly undamped.

A simple transformation of Equation 4.6 yields the phase as a function of angular frequency according to

$$\phi(\omega) = \phi_0 + \tan^{-1}\left[Q \cdot \left(\frac{\omega}{\omega_0} - \frac{\omega_0}{\omega}\right)\right] \tag{4.8}$$

where ϕ_0 is a parameter introduced to account for the fact that the transmission line connected to the cavity can introduce a phase shift. [PA98] This method of determining the quality factor is referred to as the phase fit method, and an example of the fit is shown in Figure 4.39.

The phase fit method successfully extracted the parameters from the HOM shown in Figure 4.39, determining a frequency of 1671.091 MHz and $Q_L = 1.05 \times 10^4$. The mode was measured in the HTC-2 experiment, which does not have HOM absorbers.

Using both the Lorentzian method and the phase fit method, Q_L values can be cross-checked for consistency. A more complete description of the implementation of the Lorentzian and phase fit methods are discussed in Appendix B.

4.4.2 Higher-Order Mode Properties in the HTC Experiments

The HOM transfer function of ERL 7.1 was measured in HTC-1 from 1.5 to 6.0 GHz and is presented in Figure 4.40. [VL12] Modes below approximately 3600 MHz have large signal-to-noise ratios. Above this frequency, the combination of a large number of low Q_L HOMs raise the noise floor significantly, making it difficult to identify individual mode properties. There were no higher-
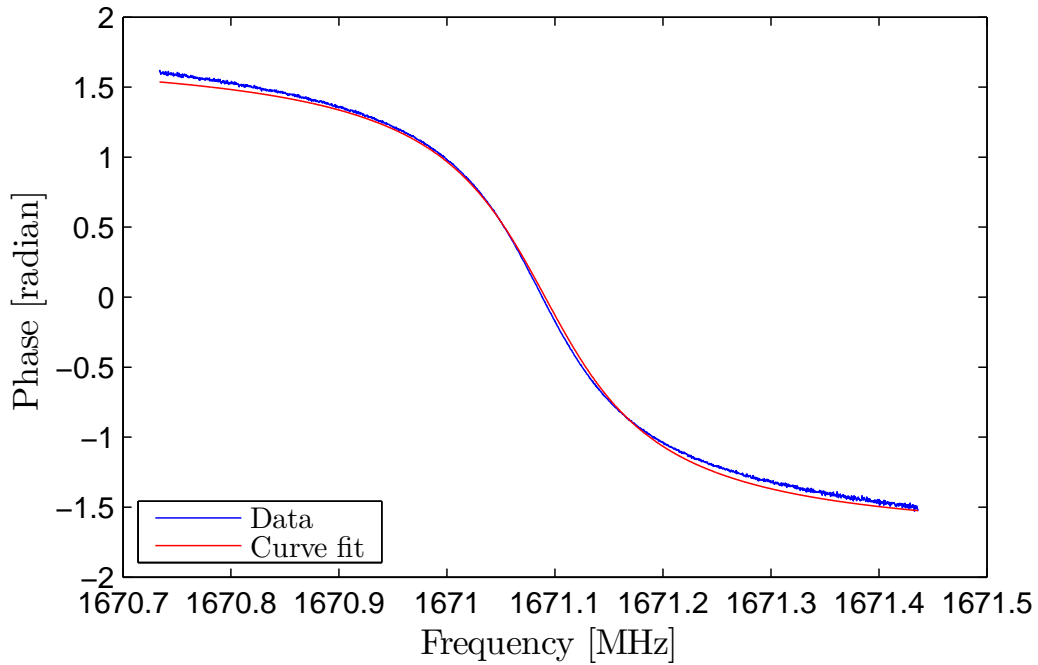
Figure 4.39: A phase fit of a HOM in the lowest dipole passband measured in the HTC-2 experiment. Network analyzer data is in blue, and the red line is the curve fit. This HOM has a resonant frequency of 1671.091 MHz and $Q_L = 1.05 \times 10^4$.

order mode absorbers in HTC-1, so the Q_Ls of the modes are much higher than when HOM dampers are present in the HTC-3 experiment.
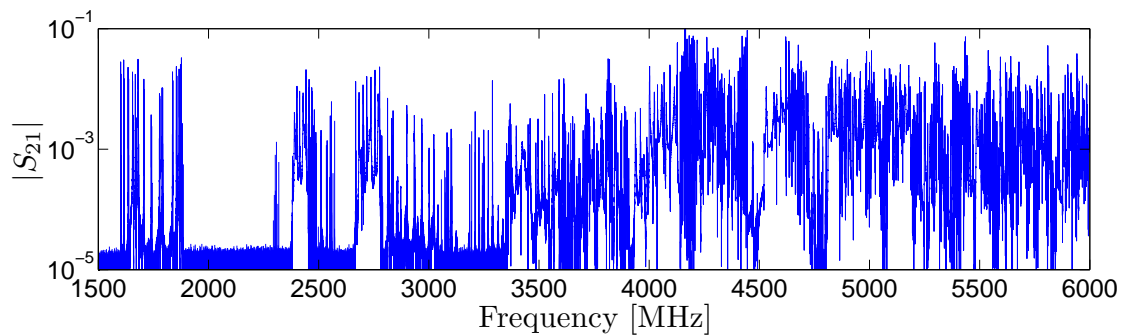
Figure 4.40: Network analyzer measurement of $|S_{21}|$ from 1.5 to 6.0 GHz in HTC-1. The cavity's temperature during the measurement was maintained at 1.8 K. Spectra was taken using an axial probe as input and field probe A as output.

Several features of the cavity can readily be determined from the spectra.

The first is the face that there are no monopole modes within 1.5 MHz of the first two harmonics of 2.6 GHz.[13] This is important, because a high Q_L monopole mode at a harmonic of the bunch frequency would result in resonant excitation of this mode and overload the HOM absorbers. [BBB+11]

In the spectra, it is possible to readily identify various dipole, quadrupole, sextupole and octupole modes. The first instance of passbands containing these modes (along with other modes with similar frequencies) is presented in Figure 4.41. The dipole modes are recognizable as two modes very close in frequency with similar HOM properties. While in a cylindrically symmetric structure their frequencies would be identical, symmetry breaking features such as the side coupler port introduces small perturbations that lead to frequency splitting. Similarly quadrupole, sextupole and octupole modes can be identified by 4, 6 or 8 resonances near a central frequency, though symmetry makes some of these modes degenerate.

Because HTC-1 uses an axial field probe to drive the cavity, the structure is close to azimuthally symmetric and modes can be computed with a 2.5D electromagnetic code such as CLANS. The modes were simulated up to 3.6 GHz–the frequency at which the signal to noise ratio was large enough to extract HOM properties–and compared with experimental measurements. The comparison between modes in HTC-1 and the CLANS results are shown in Figure 4.42.

Measurements of the HOM spectra are found to agree in frequency, but show some discrepancy in quality factor. The first few quadrupole, sextupole and octupole passbands have modes with frequency below the cutoff frequency of the beam tubes, resulting in small coupling to the HOM loads. This will not

---

[13]The ERL operates at 1.3 GHz with bunches spaced by 180°, making the repetition rate 2.6 GHz.
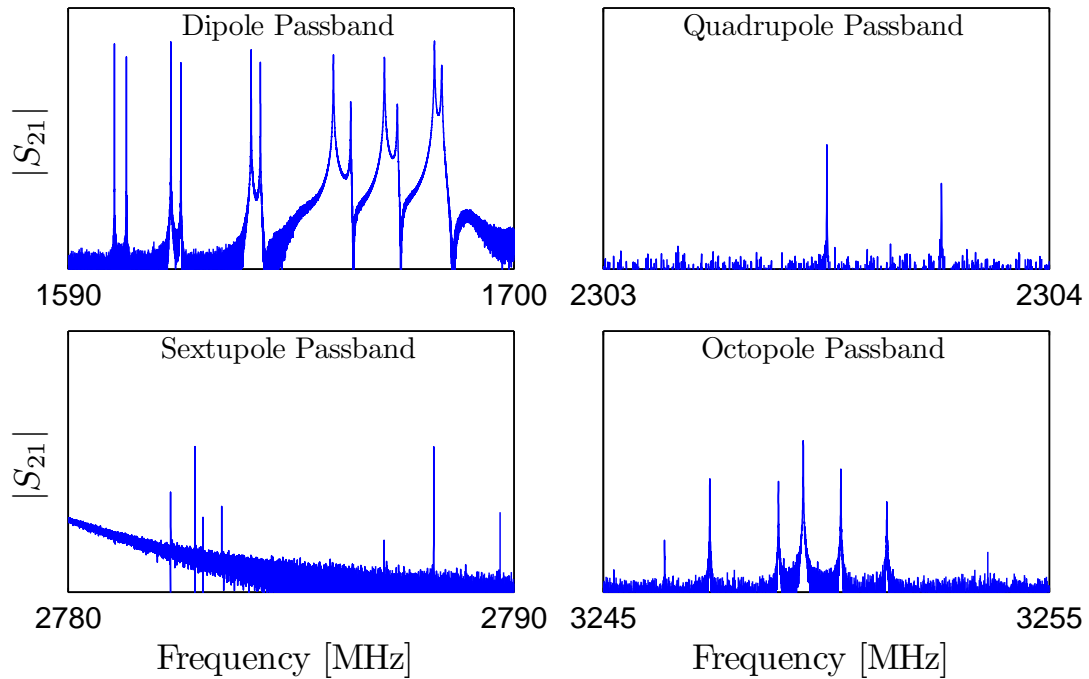
Figure 4.41: The lowest frequency passbands containing dipole, quadrupole, sextupole and octopole modes in HTC-1. Some axis labels have been suppressed for visual clarity. All vertical axes show $|S_{21}|$ on a logarithmic scale ranging from 10^{-5} to 10^{-1}, and the horizontal axis represents frequency in megahertz.

cause an issue, because their effect on the threshold current is small.

The first dipole passband, agrees very well between simulations and measurements, as do subsequent dipole passbands. For some dipole modes, and many of the quadrupole and higher azimuthal order modes, the measured quality factors are even lower than the values obtained from simulations. What is essential to note is that, as designed, all monopole and dipole modes propagate out of the cavity through the beam pipe, as evidenced by the Q_L values between 10^4 and 10^6, where as trapped modes should have Q_L between 10^7 and 10^9. In the fully outfitted cryomodule, these modes would be strongly damped by the higher-order mode loads at each end of the cavity. The HOM measurements thus suggest that the cavity design was successful in avoiding trapped modes.
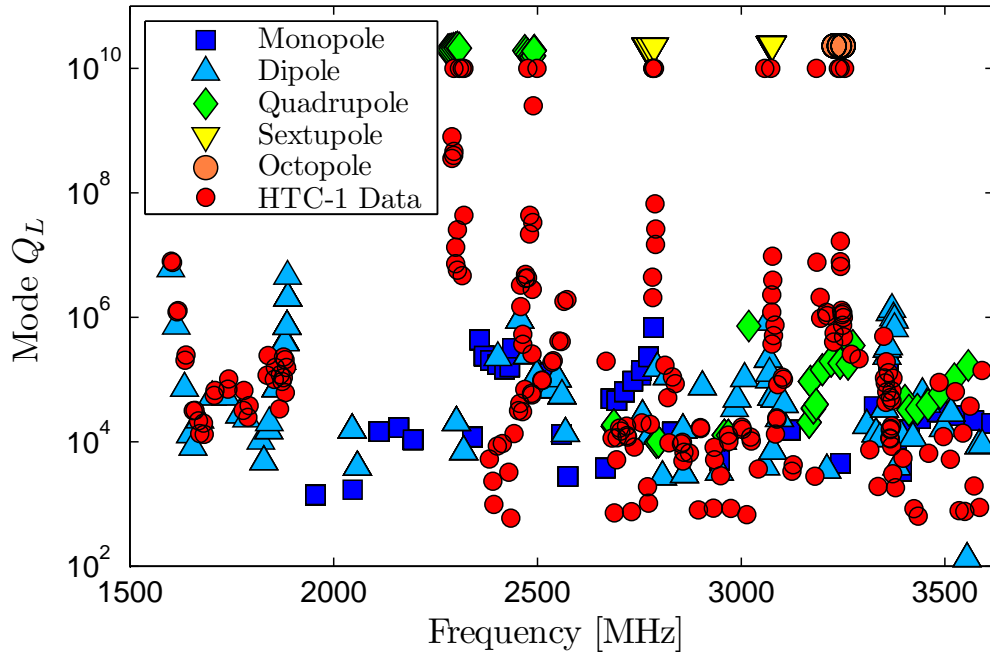
Figure 4.42: Q_L vs frequency for simulated and measured HOMs in HTC-1. The named modes (monopole, dipole, …) are obtained from CLANS simulations, and the small red circles denote spectral measurements obtained by the Lorentzian method.

This key result is the first validation of the HOM design of the cavity.

There are several potential causes of this lower Q_L phenomena. Mode mixing of quadrupole modes (and modes with higher order azimuthal variations) in the cavity to beam pipe transitions can couple these modes with propagating modes in the beam pipes, yielding a lower Q_L. [Gol97] Furthermore, the simulated case assumes a perfectly symmetrical cavity with perfect field flatness. The real cavity has small, but non-zero shape imperfections within specifications, leading to some degree of change of the HOM field distribution in the end cells that can cause changes in Q_L. Finally, symmetry breaking factors such as the input coupler port can change the HOM spectrum and were not taken into account in the 2D HOM simulations.

Some quadrupole, sextupole and octopole modes have very high Q_L, as expected, since they are below cutoff frequency.[14] These modes will not lead to beam breakup effects.

The next step was to investigate whether the RF input coupler would effect damping of the HOM spectra. In HTC-2, the same HOM measurement was performed, except this time using the side mounted coupler to drive the cavity. A comparison of the two spectra obtained in HTC-1 and HTC-2 is presented in Figure 4.43. Due to time constraints, only frequencies up to 3600 MHz were measured, though this is not an issue because according to simulations, the strongest HOMs limiting the threshold current are below this maximum frequency.
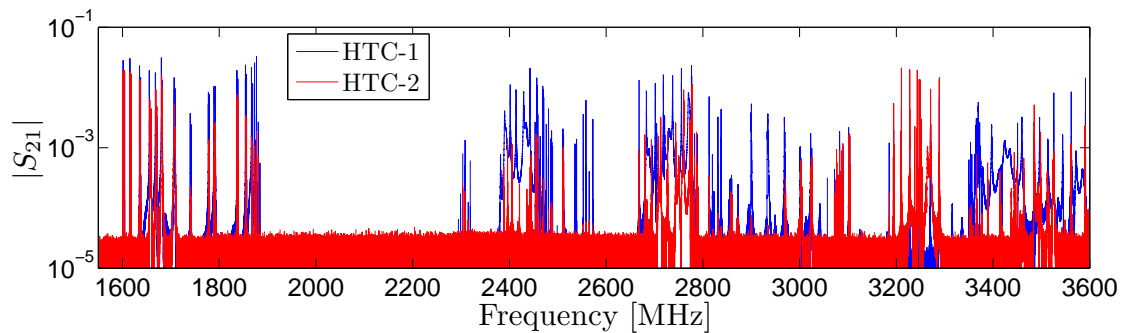
Figure 4.43: Comparison of measurements of $|S_{21}|$ from 1.5 to 3.6 GHz between the HTC-1 and HTC-2 experiments. The cavity's temperature during the measurement was maintained at 1.8 K. The HTC-1 spectrum was taken using an axial probe as input, where as in HTC-2 the input probe was the side mounted coupler. Both measurements used field probe A as output. The HOMs in HTC-2 have Q_L values close to those in HTC-1, which are high due to the lack of RF absorbing loads.

The spectra measured during the HTC-2 experiment shows HOMs at the

[14]Cutoff frequency is the lowest frequency mode that can propagate without attenuation. For a cylindrical beam tube with radius r, the cutoff frequency is given by $f_c = \frac{c}{2\pi} \cdot \frac{x_{mn}}{r}$, for TM modes and $f_c = \frac{c}{2\pi} \cdot \frac{x'_{mn}}{r}$ for TE modes. (Recall x_{mn} and x'_{mn} are the zeros of the Bessel function and it's derivative, respectively.)

same frequencies as in HTC-1, with similar Q_Ls. This suggests that the RF coupler is providing minimal damping to the mode, consistent with ACE3P simulations as illustrated in Figure 4.44.
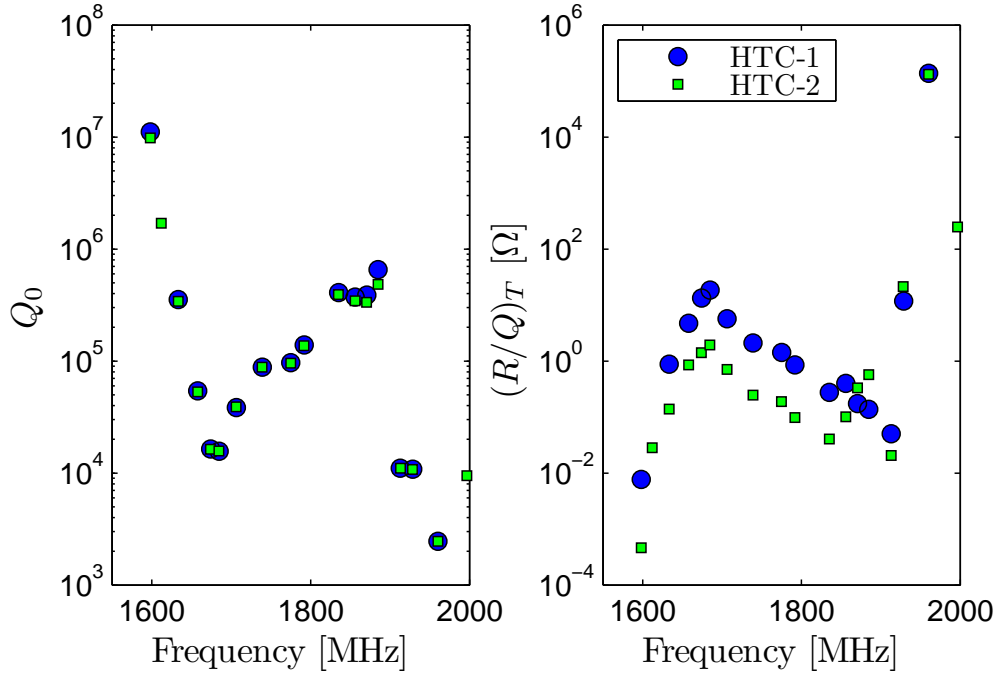
Figure 4.44: ACE3P simulations of low frequency dipole modes in HTC-1 and HTC-2 presenting Q_L and $(R/Q)_T = (R/Q)'_\perp$. Simulations predict that there is not a strong HOM coupler interaction for the lowest dipole passbands. The mode at 1960 MHz with high $(R/Q)'_\perp$ would not exist in a full cryomodule as it is created by the presence of the axial coupler. Damping is only provided by stainless steel beampipe sections.

In HTC-3, the cavity setup was again reconfigured, this time adding two beamline higher-order mode absorbing loads to either end of the cavity. The spectral measurement of the cavity in this configuration allows a final verification of the HOM damping scheme of the ERL main linac cavity with beamline HOM loads. The spectrum of HTC-3 was measured up to 5500 MHz and is presented in Figure 4.45.

For comparison, the spectrum between HTC-1 and HTC-3 is presented in
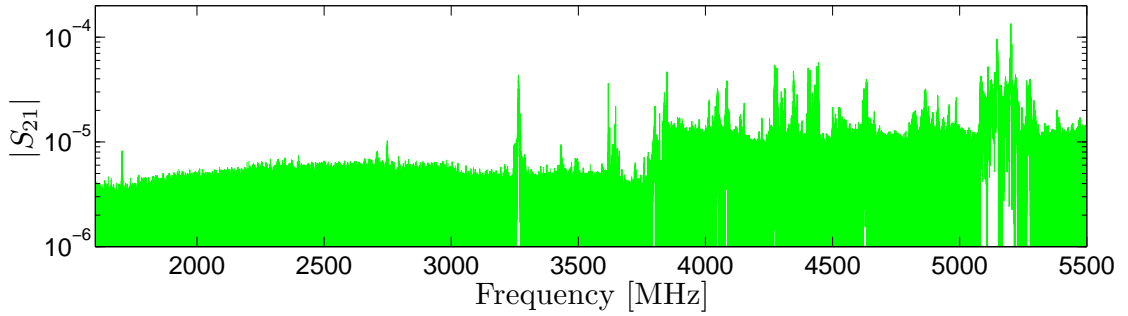
Figure 4.45: Measurement of $|S_{21}|$ from 1.5 to 5.5 GHz of ERL 7.1 in HTC-3. The cavity's temperature during the measurement was maintained at 1.8 K. Spectra was taken using the side mounted RF coupler as input and field probe A as output. The transmitted signal level is much lower than in HTC-1 or HTC-2 measurements due to the presence of strongly damping RF absorbing loads.

Figure 4.46. The noise floor below 3600 MHz is reduced by more than an order of magnitude between the HTC-1 and HTC-3 measurements, which can be attributed to the RF absorbers. There are also significantly fewer modes that are able to be measured, due to the strong damping, showing that the beamline absorbers efficiently provide broadband damping of HOMs.
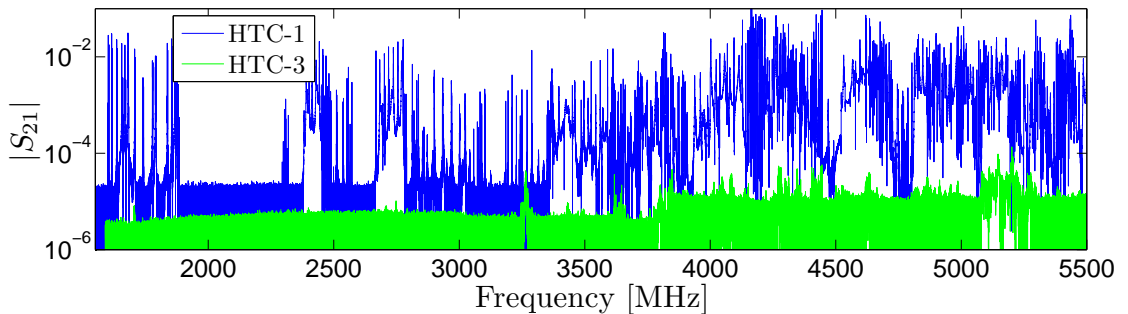
Figure 4.46: Comparison of $|S_{21}|$ spectra between HTC-1 and HTC-3 from 1.5 to 5.5 GHz. The cavity's temperature during the measurement was maintained at 1.8 K. The lack of very high Q_L resonances in the HTC-3 measurement demonstrates the efficacy of the beamline HOM absorbing scheme.

Figure 4.47, Table 4.9, and Table 4.10 present the properties of HOM modes measured in HTC-3. The frequencies agree with simulations, but loaded qual-

ity factors predicted by electromagnetic codes are larger than measured values. Possible causes of this behavior could arise from machining variation between the real geometry and the idealized CAD model, or differences in simulated HOM material properties. Nevertheless, spectral measurements performed in HTC-3 are taken in realistic accelerator environment and demonstrate that HOMs have been strongly damped, having Q_Ls on the order of $10^2 - 10^3$. The exceptional HOM damping provides further evidence that the cavity design was successful and that HOMs should not limit threshold current through the Cornell ERL to under the 100 mA design value.
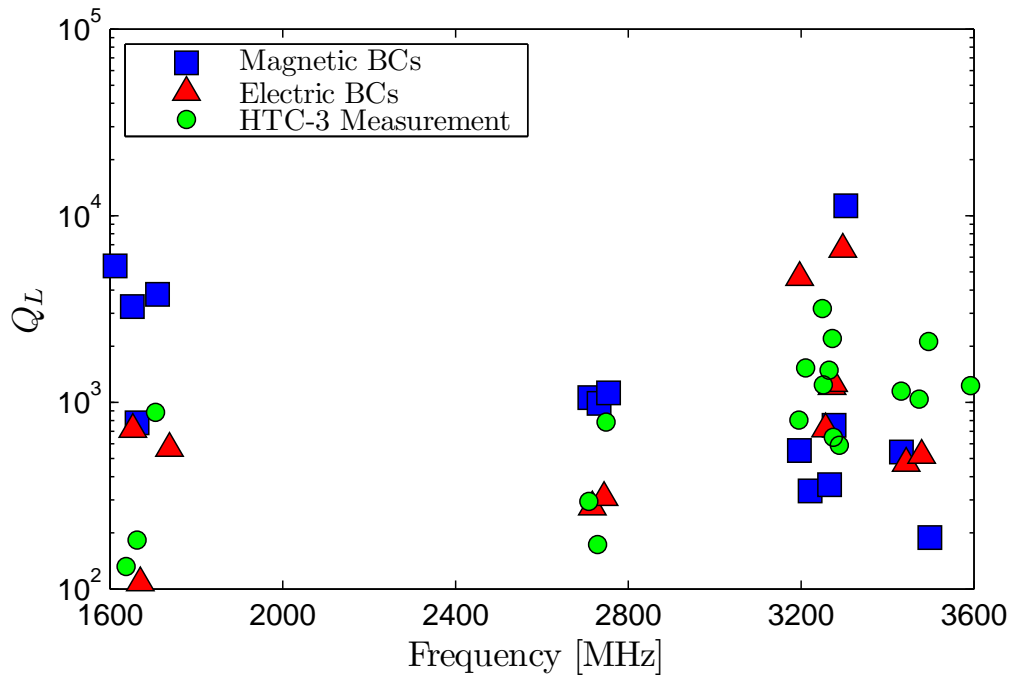
Figure 4.47: ACE3P simulations of HOMs in HTC compared with network analyzer measurements. Simulations modelling both lossy RF absorbers and absorbing boundary conditions simultaneously cannot be currently solved with Omega3P, so lossy absorbers were modelled, but the symmetry plane of the HOM loads and the rectangular waveguide were set to either electric or magnetic boundary conditions. This difference in modelling partly accounts for differences in quality factor between the measurements and simulations, but both show that HOMs are strongly damped in the fully equipped cryomodule.

f_0 [MHz]	Q_L	f_0 [MHz]	Q_L	f_0 [MHz]	Q_L	f_0 [MHz]	Q_L
1637.4117	1.32e2	3630.3944	1.04e6	3809.0307	1.90e3	4039.1344	2.68e3
1662.6128	1.83e2	3630.9727	5.27e5	3813.9569	1.97e5	4047.5938	9.40e2
1705.3440	8.86e2	3636.4594	1.56e6	3816.1146	3.16e3	4061.6825	1.68e3
2708.4012	2.95e2	3640.0009	2.87e2	3819.9457	1.16e5	4074.0674	1.01e3
2728.9106	1.73e2	3642.0975	9.67e4	3825.6921	1.12e5	4079.8158	2.59e3
2748.6406	7.84e2	3643.6910	7.14e4	3831.8272	1.34e3	4081.3894	2.03e3
3194.9459	8.05e2	3647.0764	1.59e5	3832.1174	9.24e5	4084.5994	1.46e3
3210.6628	1.53e3	3647.9088	1.13e5	3838.7176	2.57e3	4088.8181	1.46e3
3248.9539	3.18e3	3647.9211	6.27e4	3841.9901	3.93e3	4094.0225	1.13e3
3251.6725	1.24e3	3652.5325	3.30e4	3843.0820	2.29e3	4104.3871	2.40e3
3264.5710	1.49e3	3660.8575	4.76e3	3848.9038	2.00e3	4120.6256	1.05e3
3272.2906	2.20e3	3671.0948	2.04e3	3890.8351	5.15e3	4123.7216	7.03e2
3274.7617	6.51e2	3723.3290	8.51e2	3897.6500	6.52e2	4137.6914	1.04e3
3288.4388	5.89e2	3738.0247	6.98e2	3910.0731	1.49e3	4140.3136	5.22e3
3431.7733	1.15e3	3745.0022	6.33e2	3940.6970	1.42e3	4146.3533	2.73e3
3473.2295	1.04e3	3758.9201	4.26e3	3946.5141	2.62e3	4149.4583	3.46e4
3495.4240	2.12e3	3765.6838	3.76e2	3953.5589	5.80e2	4152.3073	3.34e4
3592.1809	1.23e3	3775.2054	4.62e3	3975.1453	1.72e3	4156.2950	1.13e4
3617.9073	9.90e5	3780.5399	1.87e3	4009.5183	9.06e2	4161.5823	1.30e3
3618.7104	1.46e3	3801.0156	1.49e3	4014.5007	5.66e3	4169.9621	3.32e3
3620.8522	1.80e5	3806.3779	7.78e4	4027.1821	5.06e3	4209.7840	2.32e5
3623.8689	1.17e6	3806.6699	1.48e5	4033.9365	7.10e3	4211.9027	5.09e3

Table 4.9: List of higher-order mode properties measured in HTC-3 (1 of 2).

4.5 HTC Testing with Beam

The HTC was installed in the Cornell ERL injector cryomodule beam line, and initial tests of the structure with high current electron beam began in Fall 2013. The objective of the experiment is to obtain a beam based measurement of HOM properties, by exciting HOMs in the cavity with an off-axis beam. [VBLM12]

Following the methodology discussed in [Far98] and [Bab01], for a bunch repetition frequency, f_b, a HOM resonating at f_λ is excited by modulating the bunch charge of the beam such that

$$q_n = q_0 \left[1 + a_{\mathrm{mod}} \sin \left(2\pi n f_{\mathrm{mod}} / f_b + \phi_{\mathrm{mod}} \right) \right]. \tag{4.9}$$

f_0 [MHz]	Q_L	f_0 [MHz]	Q_L	f_0 [MHz]	Q_L	f_0 [MHz]	Q_L
4222.0821	5.25e3	4360.1906	6.01e5	4608.1083	2.79e3	5101.1750	8.15e2
4240.2149	1.27e3	4361.4271	8.12e5	4618.5077	3.53e3	5120.7471	1.06e3
4252.3711	2.56e3	4363.8028	2.25e5	4624.0194	9.09e2	5124.2376	3.70e2
4270.6968	2.48e3	4364.0928	3.51e5	4630.6343	3.24e3	5128.5368	3.19e3
4272.3209	1.71e3	4364.3107	2.52e5	4633.2581	4.55e3	5133.6280	5.41e2
4274.3014	1.62e3	4378.3186	1.02e3	4637.0098	7.96e3	5146.9068	2.31e8
4280.9319	4.02e3	4398.9551	2.00e4	4643.8466	8.93e2	5146.9176	1.48e3
4285.2373	1.02e3	4403.8105	1.07e4	4647.9963	3.44e3	5147.1788	4.18e7
4290.1072	6.81e3	4406.4509	7.45e3	4652.8069	2.22e3	5153.4109	1.82e2
4298.1488	8.93e3	4408.7920	7.41e3	4660.0017	1.38e3	5159.2464	1.58e3
4302.2109	4.03e3	4411.4590	5.79e3	4664.0712	2.85e3	5180.3810	1.77e3
4304.7651	3.16e3	4413.0309	4.04e3	4862.3381	1.52e3	5191.1296	9.47e2
4306.9543	2.56e3	4421.1265	2.04e3	4864.2321	8.06e2	5191.1552	9.78e2
4312.0252	3.40e3	4431.1266	3.37e3	4876.1753	8.94e2	5205.4070	1.28e3
4325.9090	1.04e3	4439.4375	4.51e3	4911.7936	1.26e9	5222.4223	3.92e2
4337.2107	3.00e3	4444.9807	1.25e4	4958.9102	9.20e2	5229.3143	3.57e2
4340.3413	2.79e3	4500.9464	3.72e2	5081.4665	2.19e3	5232.8550	1.87e2
4346.4202	2.41e3	4524.9740	3.52e3	5083.8145	3.48e3	5266.6578	1.02e3
4355.9786	4.28e5	4536.5189	1.75e3	5092.5883	9.62e2	5292.0479	1.63e3
4359.8050	4.57e3	4551.5090	9.35e2	5098.4083	3.29e2	5292.1057	1.70e3
4360.0847	3.70e5	4554.6667	1.75e3	5098.8585	3.31e2	—	—

Table 4.10: List of higher-order mode properties measured in HTC-3 (2 of 2). Simulations of the high Q_L modes at 4911 mode and 5147 MHz predict that these are decapole and sextupole modes respectively. They have high quality factors because they are below cut-off frequency of the beam pipe.

is the nth bunch charge, where q_0 is the average bunch charge, a_{mod} is the modulation amplitude, f_{mod} and ϕ_{mod} are the modulation frequency and initial phase, respectively. Mode resonance occurs when $f_{\text{mod}} = |f_\lambda - m f_b|$ for an integer m.

Bunches with energy $\mathcal{E}$ entering a cavity with position offset x_{offset} will be kicked by the resonant mode over a range of angles. A BPM downstream at a distance d_{BPM} will then encounter bunches with a maximum spread in offsets

$$\Delta_{\text{BPM}} \approx \frac{c}{\pi} a_{\text{mod}} \, x_{\text{offset}} \, d_{\text{BPM}} \, q_0 \, f_b \, \frac{q}{\mathcal{E}} \frac{(R/Q)_{\perp,\lambda} \, Q_\lambda}{f_\lambda}, \quad (4.10)$$

allowing the $(R/Q)_\perp$ to be measured (q is the charge of the electron). After driv-
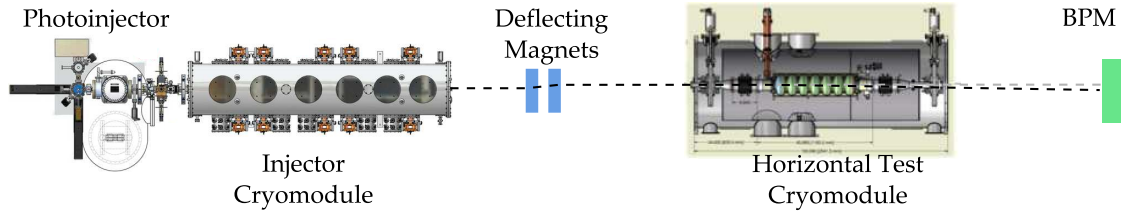
Figure 4.48: Schematic of the beam-based HOM measurement (not to scale). An electron beam (black dotted line) is produced via photo-emission and accelerated in the injector cryomodule section. The beam is transported parallel to the beam-axis by deflecting magnets. As the beam passes through the HTC a HOM deflects it from the nominal path (gray dotted line), where the maximum displacement is measured by a beam-position monitor (BPM).

ing the mode resonantly and turning off the beam, the Q_L of the mode can be determined. Finally, spectrum analyzer measurements allow the frequency of the mode to be determined.

In practice HOM measurements are conducted by using an off-axis beam to excite a HOM in the cavity, then turning off the electron beam. After a short time, a probe beam is passed through the cavity, and the maximum deflection at the beam position monitor is used in Equation 4.10.

So far, no dipole modes have been found above the noise floor of the measurement, though the influence of HOMs on the beam has been seen by observing several quadrupole modes in the first two passbands, with Q_L in the 10^7 range (consistent with simulations). Measurements will continue to search for strong HOMs, but these measurements add further confidence that the cavity design was successful at strongly damping HOMs.

Initial high current beam operation has passed 25 mA of current through the HTC, and found that all modes are strongly damped, and show no significant heating of the HOM loads. This is a record for for current through a linac, and

supplies further confidence that the cavity design and fabrication was successful.

4.6 Mechanical Considerations

Mechanical vibrations can couple to electromagnetic fields, a phenomena known as microphonics, which was first observed in work with normal conducting resonators. [KSS67] As discussed in subsection 3.3.1, the coupler kick to a beam is strongly dependent on the detuning of the cavity from microphonics. Power requirements increase to maintain a constant cavity voltage when liquid helium bath pressure fluctuations and other vibration sources change the resonant frequency of the cavity (see Figure 4.49). [PL12c] For these reasons it is important to characterize the level of microphonics present in the cavity and ensure they are within the Cornell ERL design specification of ±20 Hz peak detuning.

Measurements of the microphonics levels for ERL 7.1 installed in the HTC is presented in Figure 4.50, demonstrate that peak detuning is within the design specifications. [PL12a] In addition, both the slow frequency tuner and fast piezo-electric tuner were tested and found to operate with very low hysteresis, which is important for cavity frequency control. [PL12a] Studies of Lorentz force detuning of the cavity and sensitivity to pressure fluctuations found agreement between simulations and measurement. [PL12b] All mechanical systems functioned properly and within specification, validating the cryomodule design.
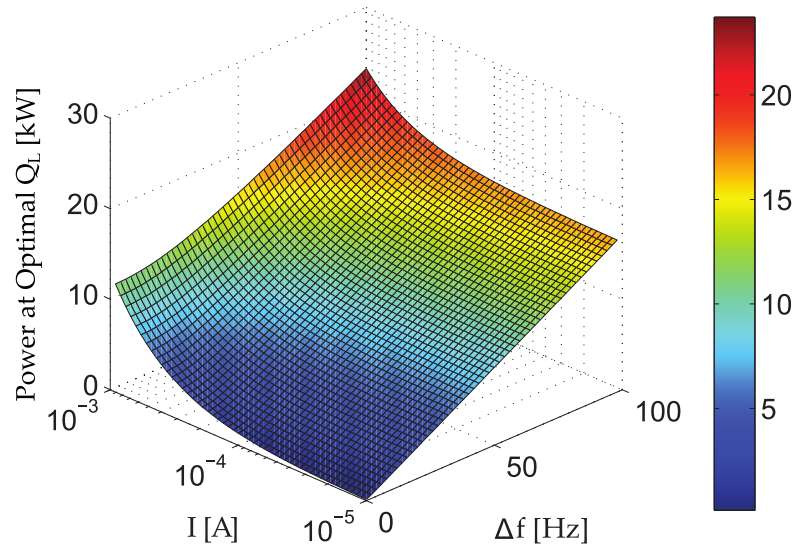
Figure 4.49: Power required to maintain a fixed cavity voltage for varying beam current, I, and cavity detuning, Δf, at optimal RF input coupling, Q_L. (Reproduced from [PL12c])

4.7 Conclusions

The Cornell ERL main linac prototype 7-cell cavity has been fabricated to within design tolerances (±0.5 mm) and successfully tested with a horizontal test cryomodule in three stages, HTC-1, -2 and -3. The final stage incorporated all the systems necessary for the main linac cryomodule, including a side mounted high power RF input coupler and beam line HOM loads.

The main linac cavity ERL 7.1 exceeded fundamental mode Q_0 design specifications in each of the HTC experiments. Temperature cycling helped to improve the quality factor of the cavity by about 50%, and measurements from HTC-2 suggest that temperatures must be increased above 8.9 K for benefit to be realized. A world record quality factor for a multicell cavity installed in a horizontal cryomodule was set in HTC-3 with $Q_0(T = 1.6 \text{ K}) = (10.0 \pm 1.8) \times 10^{10}$.

The higher-order mode spectrum and was successfully measured and found
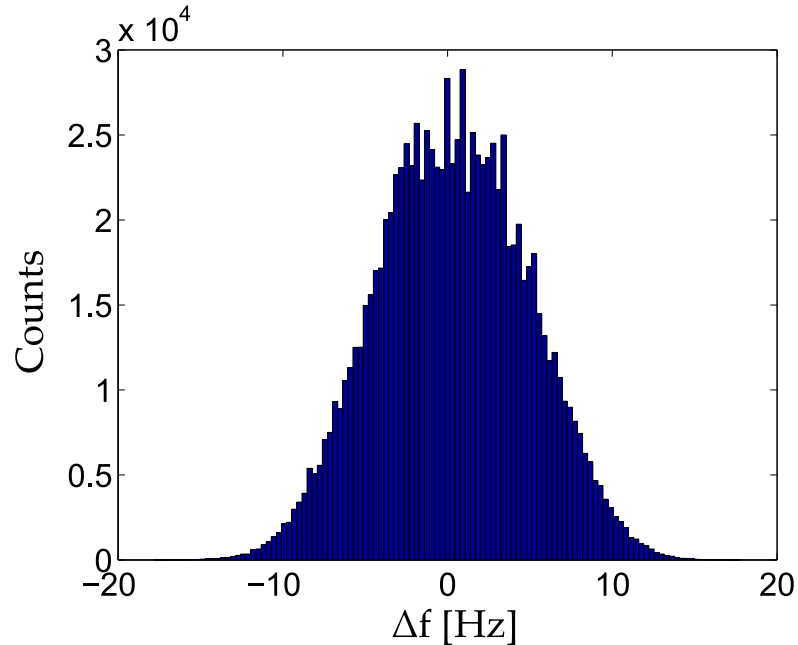
Figure 4.50: Histogram of microphonics in the HTC over 500 s with 10^6 samples. The peak detuning was 17.8 Hz with an RMS detuning of 4.6 Hz. (Reproduced from [PL12a])

to be consistent with expected machining variation. Simulations and experimental results in HTC-3 confirm that HOMs in the cavity are strongly damped, with dipole Q_L between 10^2 and 10^4. The measured values of Q_L are strongly damped by the absorbers suggesting that the optimized baseline cavity design, which minimized the effect of strong HOMs, was maintained in the prototype 7-cell.

All three measurements of the scattering parameter find no monopole modes near harmonics of 2600 MHz. If the beam could resonantly drive an HOM on one of these resonances, the resulting HOM power could overload the HOM absorber. Fortunately, frequency domain measurements show that the design was successful in avoiding this danger.

The initial beam test confirmed excellent HOM damping with no dipole

mode having a high $(R/Q) \cdot Q$ found as of this writing. In addition, the cavity supports beam current in excess of 25 mA, a record in a CW linac.

In conclusion, the prototype 7-cell cavity ERL 7.1 was shown to exceed all design specifications and should deliver excellent performance as the driver for the main linac of Cornell's Energy Recovery Linac.

CHAPTER 5

FINAL SUMMARY

This thesis has presented research pushing back three frontiers of SRF science: Gradient, CW beam power, and Quality Factor.

On the first frontier, this thesis demonstrates that the superheating field fundamentally limits the maximal surface magnetic field on superconducting niobium structures, not the lower critical field, B_{c_1}, as has sometimes been suggested. For typical surface preparation of niobium cavities used in large scale accelerators, (electropolish, or buffer chemical polish, followed by a 120°C heat treatment), surface magnetic fields of 200 mT at 0 K is the ultimate limit set by the superheating field, though this may be improved slightly via material treatment making the surface layer nearly type-I. Already, there are hints that this ultimate surface field limit is being reached in accelerating structures. [KCG+12, RAG+11] Theoretical and experimental results agree: niobium is reaching its highest sustainable gradients.

To make further progress on this frontier, new materials should be developed as a replacement for niobium. Theoretical work has demonstrated that the use of Nb_3Sn in superconducting accelerating structures could double the maximum gradient. [CS08, Pos13b] To this end, Cornell has a research and development program ongoing to fabricate Nb_3Sn structures and initial results are encouraging, demonstrating surface fields in excess of B_{c_1}. [Pos13a] With continued research and development of Nb_3Sn, a new generation of higher gradient machines is on the horizon.

Progress has also been made on the CW beam power frontier. Prior to this

213

work, the maximal measured current in an ERL was 9 mA, before being limited by beam breakup effects. [Ten06] Initial simulations suggested that beam breakup due to trapped dipole modes could occur at currents much less than the 100 mA specification needed for the Cornell ERL. Work presented in this thesis on designing an optimized, robust cavity with strongly damped higher-order modes has shown that an ERL consisting of realistic cavities can support threshold current of over 300 mA. The findings of this thesis demonstrate that an improvement factor of 30 in beam breakup current is achievable in SRF CW linacs.

Advances have also been made in intrinsic cavity quality factor, the final frontier. The proposed design specification for the Cornell ERL main linac cavities of reaching $Q_0 = 2 \times 10^{10}$ at 1.8 K and 16.2 MV/m has been more than tripled, obtaining Q_0 above 6×10^{10} at the same operating gradient and temperature in a fully outfitted cryomodule. Moreover, a multi-cell cryomodule world record has been set for niobium cavities, reaching values in excess of 1×10^{11}. Routine production of cavities reproducing this result would allow for operation of the ERL at 1.6 K with substantial energy savings.

In closing, SRF science has demonstrated the capacity to produce workhorse CW linear particle accelerators able to push to higher average beam currents, and with higher efficiently than any other accelerating technology. The hope is that this thesis has helped to make the future of SRF just a little brighter.

APPENDIX A

LENGTH SCALES AND PARAMETERIZATION IN

SUPERCONDUCTIVITY THEORY

A.1 Definitions

There are several definitions of length scales within the various formulations of superconductivity. This section collects these definitions, equations, and relationships from several sources, and is intended to serve as a quick reference.

As stated by McNiff et. al., BCS theory characterizes superconductors with 4 independent parameters. [OMFB79] One possible parameter selection of which could be the low temperature surface resistivity, ρ, normal-state electronic specific heat coefficient, γ_e, the superconducting transition temperature, T_c, and the Fermi-surface area, S. These parameters are presented in Table A.1. Next, various length scales are presented, along with their physical interpretation, in Table A.2. Finally, mathematical constants and functions necessary to evaluate superconducting parameters in this appendix are presented in Table A.3.

Parameter	Symbol	Unit
Low temperature resistivity*	ρ	$\Omega \cdot$ cm
Electronic specific-heat coefficient*	γ_c	erg cm^{-3} K^{-2}
Critical temperature	T_c	K
Conduction-electron density	n	cm^{-3}
Fermi-surface area	S	cm^{-2}
Fermi-surface area normalization	$S_F \equiv 4\pi(3\pi^2 n)^{2/3}$	cm^{-2}
The electronic charge	ε	esu
Fermi-velocity	v_F	cm s^{-1}
Cooper-pair binding energy at 0 K	$2\Delta(0)$	erg

Table A.1: Physical parameters used in the theory of superconductors.
*Values are taken in the normal conducting state.

Symbol	Interpretation	Equation
ℓ_{tr}	Normal-conducting electronic mean free path. Characterizes the "cleanliness" ($\ell_{tr} \to \infty$) or "dirtiness" ($\ell_{tr} \to 0$) of a superconductor. [MS69]	Eq. A.1 [OMFB79]
ξ_0	BCS coherence length of a clean superconductor. Rough spatial extent of Cooper pairs. [Son98]	Eq. A.3 [OMFB79]
ξ_{GL}	Coherence length used in Ginzburg-Landau theory. The length scale over which the superconducting order parameter fluxuates. Roughly the radius of one flux quantum near the upper critical field of a Type-II superconductor. [Kit86]	Eq. A.13 [Kit86]
ξ_S	Coherence length used in SRIMP. [Hal70b]	Eq. A.19 [Hal70b]
λ_L	London penetration depth, measuring decay constant of magnetic field within the bulk of a clean superconductor. [Kit86]	Eq. A.6 [OMFB79]
λ_{GL}	Ginzburg-Landau penetration depth, characterizing the extent of order parameter penetration into superconducting bulk. [Kit86]	Eq. A.15 [OMFB79]

Table A.2: Characteristic length scales in the theory of superconductivity.

Parameter	Symbol	Definition	Value
Euler's number	e	$\sum\limits_{n=0}^{\infty} \dfrac{1}{n!}$	2.718
Euler-Mascheroni Constant	γ	$\lim\limits_{n\to\infty}\left(\sum\limits_{k=1}^{n}\dfrac{1}{k} - \ln(n)\right)$	0.577
—	e^{γ}	—	1.781
Zeta-function	$\zeta(s)$	$\sum\limits_{n=1}^{\infty}\dfrac{1}{n^s}$	—
—	$\zeta(3)$	—	1.202
Gamma function	$\Gamma(z)$	$\int_0^{\infty} t^{z-1}e^{-t}\,dt$	—
Digamma function	$\psi(z)$	$\dfrac{d}{dz}\ln\Gamma(z)$	—

Table A.3: Numerical functions and constants used in this appendix. Values are truncated at three decimal places.

A.2 Reference Equations

The following equations are presented in exact form when available, and also with numerical approximations accurate to three significant figures.

The normal-conducting electronic mean free path is given by [OMFB79]

$$\ell_{tr} = 9 \times 10^{11} (3\pi^2)^{1/3} \frac{\hbar}{\varepsilon^2 \rho (n^{2/3} S / S_F)} \tag{A.1}$$

$$= \frac{1.27 \times 10^4}{\rho_{\Omega \cdot cm} (n^{2/3} S / S_F)} \text{ cm.} \tag{A.2}$$

The BCS coherence length is [OMFB79]

$$\xi_0 = \frac{\hbar v_F}{\pi \Delta} \tag{A.3}$$

$$= \frac{e^\gamma}{(3\pi)^{1/3}} k_B \frac{n^{2/3} S / S_F}{\gamma_c T_c} \tag{A.4}$$

$$= 7.95 \times 10^{-17} \frac{n^{2/3} S / S_F}{\gamma_c T_c} \text{ cm,} \tag{A.5}$$

where the first definition comes from [Kit63, page 193].

London penetration depth at zero temperature is [OMFB79]

$$\lambda_L = \frac{3\pi^{1/2}}{2(3\pi^2)^{2/3}} \frac{\hbar c}{k_B e} \frac{\gamma_c^{1/2}}{n^{2/3} S / S_F} \tag{A.6}$$

$$= 1.33 \times 10^8 \frac{\gamma_c^{1/2}}{n^{2/3} S / S_F} \text{ cm.} \tag{A.7}$$

The Ginzburg-Landau parameters were shown by Gor'kov to be the limiting results of the microscopic theory. [Gor59] As such, the respective coherence lengths and penetration depths can be converted from one form to another. The conversion relies on two functions and a dimensionless parameter introduced by Gor'kov. [Wer69]

The Gor'kov χ function is written in terms of a sum, that can be solved in terms of the digamma function and the zeta function:

$$\chi(z) = \frac{\sum_{v=0}^{\infty}(2v+1)^{-2}(2v+1+z)^{-1}}{\sum_{v=0}^{\infty}(2v+1)^{-3}}, \tag{A.8}$$

$$= \frac{\pi^2 z - 4\left(\gamma + \ln(4) + \psi\left[\frac{1+z}{2}\right]\right)}{7\zeta(3)z^2} \tag{A.9}$$

which is used later in the form of a helper function, $R(z)$ defined as

$$R(z) = (1+z)\chi(z), \tag{A.10}$$

and is plotted in Figure A.1.
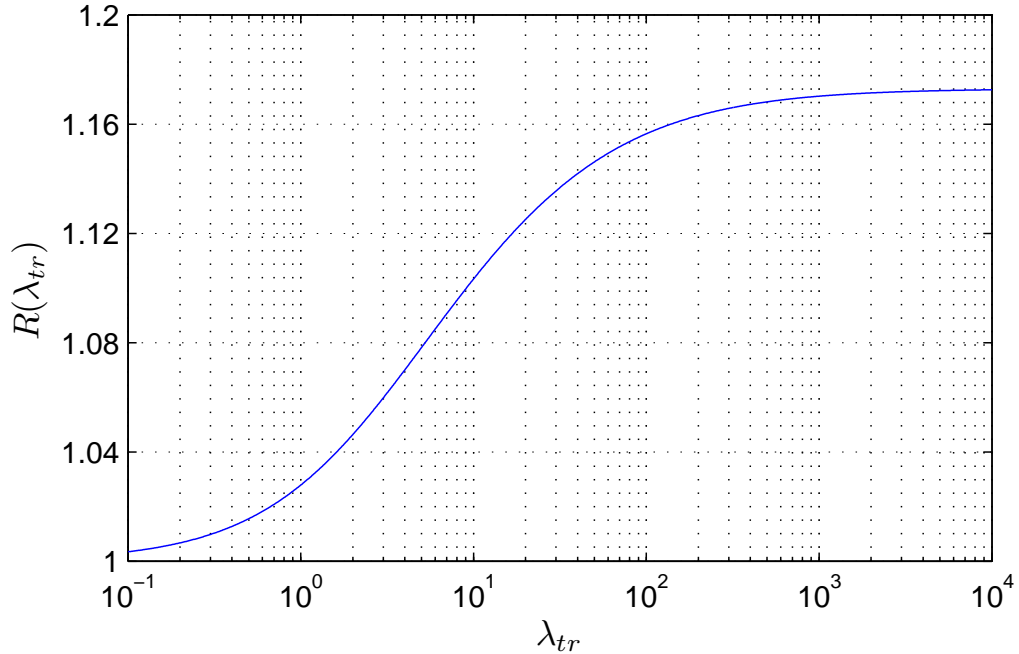
Figure A.1: Plot of $R(\lambda_{tr})$ vs λ_{tr}, showing that R is a slowly varying function that is approximately unity. This function has limiting values $R(0) = 1$ and $R(\infty) = \pi^2/(7\zeta(3)) \approx 1.173$. [Wer69]

These functions use a normalized length parameter λ_{tr} as an argument:

$$\lambda_{tr} = \frac{\pi e^{-\gamma}}{2} \cdot \frac{\xi_0}{\ell_{tr}} \tag{A.11}$$

$$\approx 0.882\frac{\xi_0}{\ell_{tr}}. \tag{A.12}$$

218

The parameters in Ginzburg-Landau theory have temperature dependence written in terms of the reduce temperature $t \equiv T/T_c$, though are only theoretically rigorous results for T near T_c.

The Ginzburg-Landau coherence length is given by [OMFB79]

$$\xi_{GL} = \pi e^{\gamma} \sqrt{\frac{7\zeta(3)}{48}} \sqrt{\chi(\lambda_{tr})} \cdot \xi_0 \cdot \frac{1}{\sqrt{1-t}} \tag{A.13}$$

$$\approx 0.739 \sqrt{\frac{R(\lambda_{tr})}{\xi_0^{-2} + 0.882(\xi_0 \ell_{tr})^{-1}}} \cdot \frac{1}{\sqrt{1-t}} \tag{A.14}$$

Ginzburg-Landau penetration depth is

$$\lambda_{GL} = \frac{\lambda_L}{\sqrt{2R(\lambda_{tr})}} \sqrt{1 + \frac{\pi e^{-\gamma}}{2} \cdot \frac{\xi_0}{\ell_{tr}}} \cdot \frac{1}{\sqrt{1-t}}, \tag{A.15}$$

$$\approx \frac{\lambda_L}{\sqrt{2R(\lambda_{tr})}} \sqrt{1 + 0.882 \frac{\xi_0}{\ell_{tr}}} \cdot \frac{1}{\sqrt{1-t}}. \tag{A.16}$$

The ratio of these length scales yield the celebrated parameter κ_{GL}:

$$\kappa_{GL} \equiv \frac{\lambda_{GL}}{\xi_{GL}}, \tag{2.1 revisited}$$

$$= \frac{e^{\gamma}}{\pi} \sqrt{\frac{24}{7\zeta(3)} \cdot \frac{1}{R(\lambda_{tr})}} \cdot \frac{\lambda_L}{\xi_0} \cdot \left(1 + \frac{\pi e^{-\gamma}}{2} \cdot \frac{\xi_0}{\ell_{tr}}\right), \tag{A.17}$$

$$\approx \frac{0.957}{R(\lambda_{tr})} \cdot \frac{\lambda_L}{\xi_0} \left(1 + 0.882 \frac{\xi_0}{\ell_{tr}}\right). \tag{A.18}$$

The dependence of κ_{GL} on ℓ_{tr} for typical niobium material properties is presented in Figure A.2. It illustrates that after the mean free path is a few times larger than the coherence length, κ_{GL} is only weakly dependent on ℓ_{tr}.

Finally, it is important to be clear about the relationship between the theoretical definitions of the above parameters, and the values that codes use to compute RF surface resistivity of superconductors. A MatLab implementation
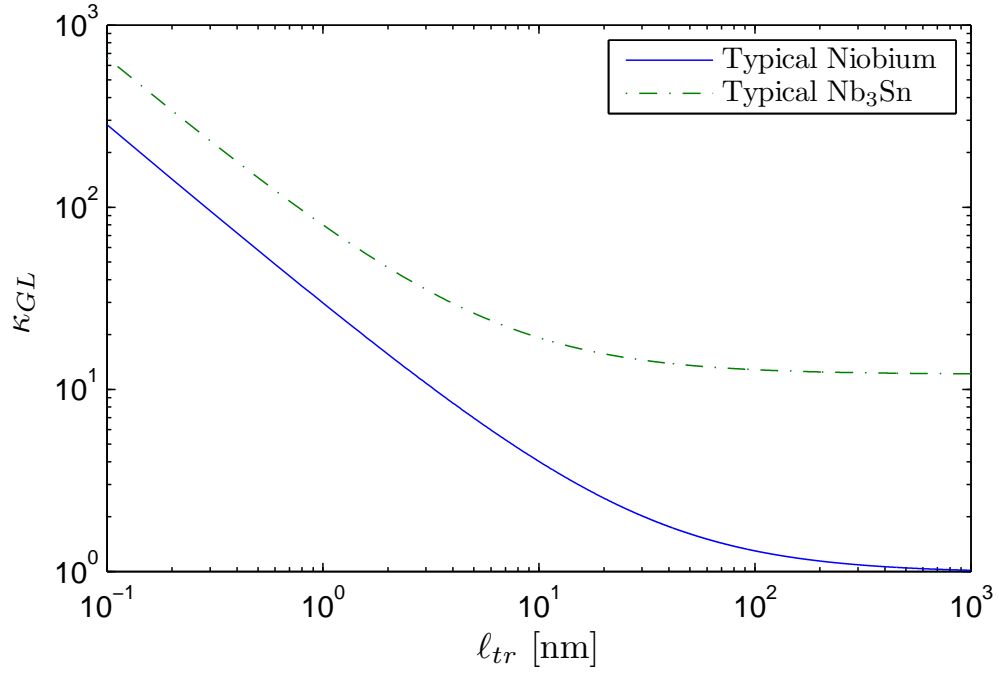
Figure A.2: κ_{GL} vs ℓ_{tr} for typical niobium and Nb$_3$Sn material properties.

of SRIMP [Hal70b] is used to carry out resistivity calculations in the work presented here, taking into account frequency, critical temperature, electronic mean free path, normalized energy gap, London penetration depth, and coherence length. All parameters listed are equivalent to the quantities named above with two exceptions:

SRIMP defines the coherence length to be given by [Hal70b]

$$\xi_S = \frac{\hbar v_F}{2\Delta(0)} = \frac{\pi}{2}\xi_0, \tag{A.19}$$

and instead of normalizing the Cooper-pair energy gap in the standard method, i.e. $E_g = 2\Delta(0)/(k_B T_c)$, SRIMP expects an energy gap, E_S, given by

$$E_S = \frac{\Delta(0)}{k_B T_c}. \tag{A.20}$$

For comparison, the literature lists the normalized energy gap, E_g, of Niobium as 3.84, [MB57] and 3.6. [Per66, BGK59] SRIMP calculations for these ma-

terials would use E_S = 1.92 and 1.8 respectively. SRIMP is discussed in Appendix C.

HIGHER-ORDER MODE FITTING ALGORITHMS

The purpose of this appendix is to describe details of the techniques used in this thesis to extract higher-order mode data from S_{21} measurements of an RF cavity (see section 4.4). Specifically it details preliminary calculations that should be performed before the Lorentzian fit and phase fit methods can be implemented.

B.1 Lorentzian Method

As derived in section 4.4, the Lorentzian function used to fit the magnitude of the HOM spectra is given by

$$|S_{21}|^2(\omega) = \frac{\left|S_{21}(\omega_0)\right|^2}{Q_L^{-2} + \left(\frac{\omega}{\omega_0} - \frac{\omega_0}{\omega}\right)^2}. \qquad (4.7 \text{ revisited})$$

The parameters Q_L and ω_0 are obtained by minimizing the residual sum of squares between the data and prediction from the above equation. The challenge with applying the minimization algorithm is twofold: First, a suitable range in frequency space must be selected. Second, a satisfactory initial condition must be supplied to the optimizer.

Locating peaks is a common task in signal processing. One of the most common techniques is to take the derivative of the signal and note zero crossings. Since data is usually noisy, it is often smoothed data prior to differentiation. Once the location of peaks are known, the peak can be isolated by only considering data above a given noise level or some fraction below the peak. A MatLab

function `findpeaks` is used to locate resonances, [The13b] and a range in frequency of either 1 MHz or half the distance to the next resonance is used as the domain for HOM extraction.

An initial condition can be determined by one of two techniques. The simpler of the two uses the peak value of $|S_{21}|$ as a guess for ω_0, and the frequency difference between ω_0 and the frequency at which the signal drops to one-half of its peak value, $\omega_{1/2}$, is used to determine the guess for Q via the relation

$$Q = \frac{\omega_0}{\omega_{1/2}}. \tag{B.1}$$

The second method relies on estimation theory to use the data set itself to compute an unbiased estimator for variables that parametrically model a signal, $\hat{y}$ that has noise contribution $\hat{w}$. In this paradigm, suppose there is a set of m parameters $\hat{\theta} = [\theta_1 \ldots \theta_m]^T$ that describes a data vector of n samples: $\hat{y} = [y_1 \ldots y_n]^T$. The system is linear if it can be modelled with an $n \times m$ observation matrix $\mathbf{H}$ such that

$$\hat{y} = \mathbf{H}\hat{\theta} + \hat{w}. \tag{B.2}$$

The "best" value of $\hat{\theta}$ in Equation B.2 is defined to be the vector with values having the smallest variance. [Kay93] The variance of $\hat{\theta}$ is bounded from below by the Crámer-Rao Lower Bound, [Cra46] (CRLB) which, when applied to the linear model above, yields the result

$$\hat{\theta} = \left(\mathbf{H}^T\mathbf{H}\right)^{-1} \mathbf{H}^T \hat{y}. \tag{B.3}$$

Equation B.2 can be applied to estimate parameters in the Lorentzian function that depend on an angular frequency vector $\hat{\omega}$ and using the mapping

$\theta_1 = |S_{21}(\omega_0)|$, $\theta_2 = Q_L^{-2}$, and $\theta_3 = \omega_0$ and by rewriting Equation 4.7 revisited in a linear form

$$\hat{z} \equiv \frac{1}{\hat{y}} = \frac{\theta_2}{\theta_1} + \frac{1}{\theta_1}\left(\frac{\hat{\omega}}{\theta_3} - \frac{\theta_3}{\hat{\omega}}\right)^2, \tag{B.4}$$

$$= \underbrace{\left(\frac{\theta_2}{\theta_1} - \frac{2}{\theta_1}\right)}_{\phi_1} + \underbrace{\left(\frac{\theta_3^2}{\theta_1}\right)}_{\phi_2}\hat{\omega}^{-2} + \underbrace{\left(\frac{1}{\theta_1\theta_3^2}\right)}_{\phi_3}\hat{\omega}^2, \tag{B.5}$$

$$= \phi_1 + \phi_2 \cdot \hat{\omega}^{-2} + \phi_3\hat{\omega}^2, \tag{B.6}$$

where vector functions are performed element-wise, i.e. raising the vector to the power p, is written $\hat{y}^p$ and is equivalent to $[y_1^p \ldots y_n^p]^T$. Note that a change of variables has been performed to obtain a linear relation for an estimator $\hat{\phi}$, that is a function of $\hat{\theta}$. The observation matrix $\mathbf{H}$ is then written as

$$(\mathbf{H}) = \begin{pmatrix} 1 & \omega_1^{-2} & \omega_1^2 \\ 1 & \omega_2^{-2} & \omega_2^2 \\ \vdots & \vdots & \vdots \\ 1 & \omega_n^{-2} & \omega_n^2 \end{pmatrix}. \tag{B.7}$$

Applying Equation B.3 to the data set gives the estimate

$$\hat{\phi} = \left(\mathbf{H}^T\mathbf{H}\right)^{-1}\mathbf{H}^T \cdot \hat{z}, \tag{B.8}$$

which can be transformed into the original parameters via

$$\theta_1 = \frac{1}{\sqrt{\phi_2\phi_3}}, \tag{B.9}$$

$$\theta_2 = 2 + \frac{\phi_1}{\sqrt{\phi_2\phi_3}}, \tag{B.10}$$

$$\theta_3 = \left(\frac{\phi_3}{\phi_2}\right)^{1/4}, \tag{B.11}$$

and gives a reasonable initial condition for the optimizer. The benefit of computing an estimator in this fashion is that it is an analytic function of the data, so it can be executed very quickly. An example of applying this method to simulated data is presented in Figure B.1.

Though the estimated resonance in Figure B.1 doesn't fit the curve very well it has several benefits: First, it is an analytic function of the data, allowing for rapid calculation. Second, the quality factor is of the proper order of magnitude, and horizontal and vertical scaling of the curve yield a resonable correspondance to the original signal. Third, this estimator is usually a good initial guess for an optimization-based fit of a resonance.
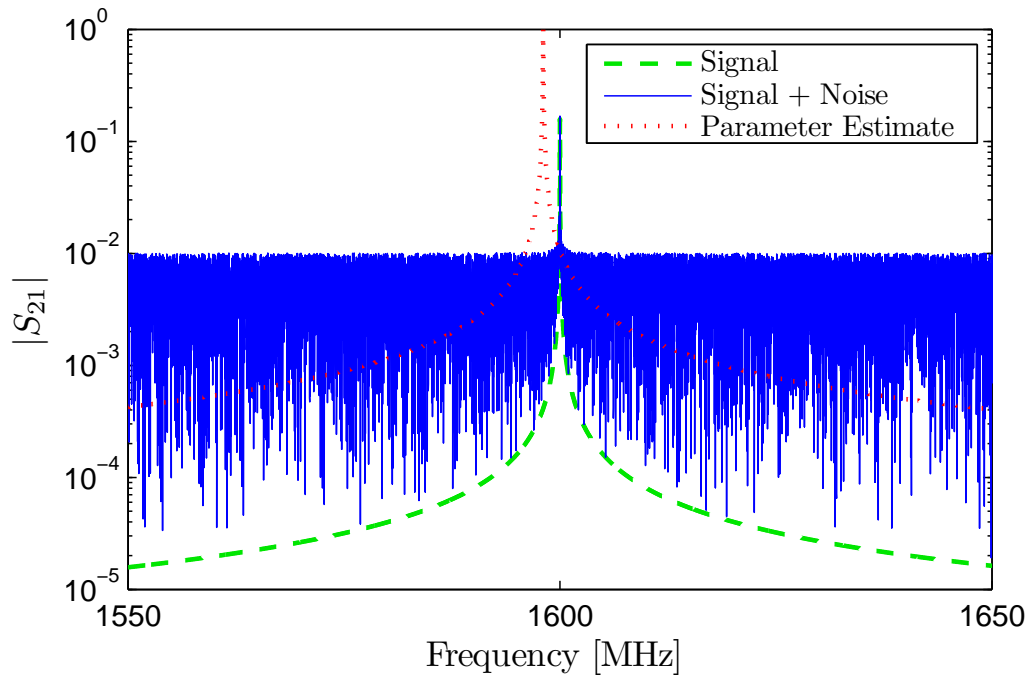
Figure B.1: Estimating parameters of a simulated HOM with noise. The HOM is generated with f_0 = 1600 MHz and Q_L = 10^6. The CRLB yields an estimate of the HOM properties as f_{est} = 1598.1 MHz and Q_{est} = 4.1×10^4, which is a suitable initial condition for the optimizer.

One challenge that arises in trying to curve fit resonance data is that higher-order mode quality factors can vary over several orders of magnitude and, due

to the noise in the signal, the initial condition based on Equation B.1 does not always yield an approximation in the right range (estimation theory generally yields superior intial Q_L values). To ensure the optimizer checks quality factors over a large range, the objective function that was used in the minimizer is given by

$$h(a, b, \omega_0; \hat{\omega}) = \sum \left[\frac{10^{-a}}{\sqrt{10^{-2b} + \left(\frac{\hat{\omega}}{\omega_0} - \frac{\omega_0}{\hat{\omega}} \right)^2}} - \hat{y} \right]^2 . \tag{B.12}$$

The quality factor of the mode is then simply $Q_L = 10^b$.

B.2   Phase Fit Method

If spectral measurements measure phase information as well as magnitude of S_{21}, a second method can be applied to extract HOM properties. The parameters can also be determined from frequency vs phase information via the relation

$$\phi(\omega) = \phi_0 + \tan^{-1} \left[Q \cdot \left(\frac{\omega}{\omega_0} - \frac{\omega_0}{\omega} \right) \right]. \tag{4.8 revisited}$$

This equation can be used with data measured from the network analyzer by noting that the real, $\rho_R(\omega)$, and imaginary, $\rho_I(\omega)$ parts of Equation 4.4, trace out a circle:

$$(\rho_R(\omega) - x_0)^2 + (\rho_I(\omega) - y_0)^2 = R^2, \tag{B.13}$$

where (x_0, y_0) is the center of the circle with radius R in the complex plane. [SMZ89]

To obtain the phase vs frequency information, the data should be translated so that it is centered on the origin, and rotated so that the resonant frequency

intersects the real axis (this allows the extent of the phase data to extend between $\pm\pi/2$, which is the range of $\tan^{-1}(x)$). [PA98] An example of fitting the data and transforming it to yield usable $\phi(\omega)$ data is presented in Figure B.2.
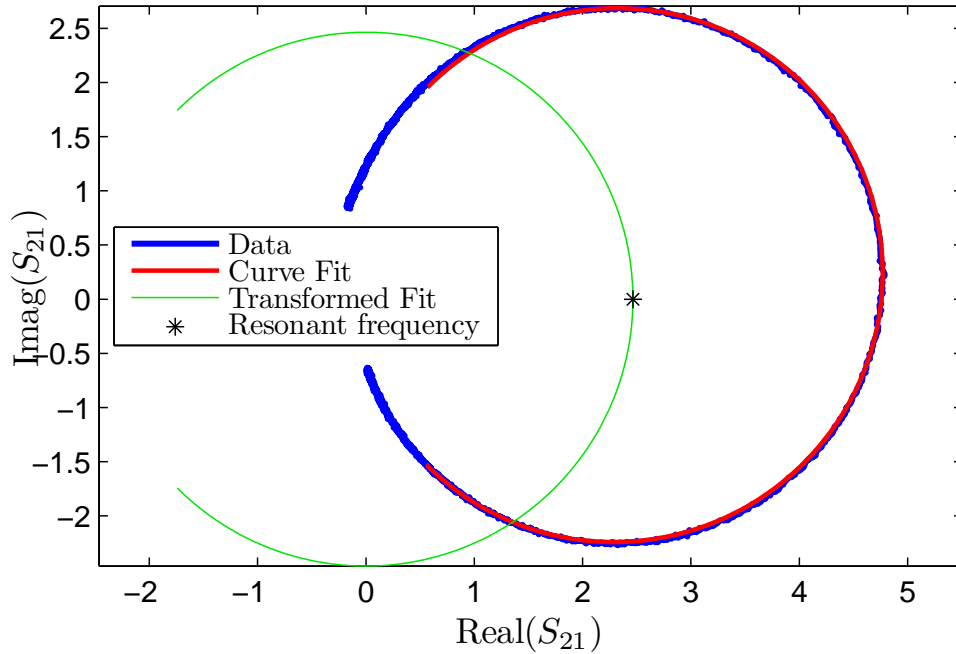
Figure B.2: Illustration of the method to obtain phase vs frequency data from S_{21} measurement. The network analyzer measures real an imaginary parts of S_{21}, and near a resonance, the curves form circles (blue). Curve fitting yields the red curve, which fully parameterizes the circles. Transforming the data yields the green curve which can be used to directly extract the phase as a function of frequency. The black point marks the resonant frequency. Data scale is increased by a factor of 10^3 in both the horizontal and vertical dimensions. Plot adapted from [Gol13].

After obtaining the parameters of the circle traced by the resonance, the phase vs frequency data is obtained from the relationship

$$\tan\phi(\omega) = \frac{\Im(S_{21})}{\Re(S_{21})}.$$

(B.14)

Using Equation 4.8 revisited, the quality factor can be extracted.

Both the Lorentzian and phase fit methods yield comparable values for Q_L

227

for modes having their 3 dB points above the noise floor. In these cases the error in Q_L is typically on the order of 20-30%. [Gol13] With modes having lower signal-to-noise ratios, the measured Q_L can differ by more than 40%. In either case, the most important figure of merit for a mode is the order of magnitude of Q_L, so using both methods provides a cross check of HOM properties, which is essential to predict the performance of the linac.

DETERMINING SURFACE SRF PARAMETERS WITH SRIMP

Quality factor measurements of resonant structures, while helpful from an energy-consumption perspective, are ultimately dependent on the underlying RF surface properties of the superconductor under study. Fundamentally, when an RF field penetrates a superconductor, electrons arrange themselves in such a way to cancel the magnetic field in the bulk, but due to the inertial mass of Cooper pairs, [Coo56] this screening is imperfect. Furthermore, not all the current can be carried by superconducting electrons, so the electronic mean free path of normal conducting electrons leads to a finite conductivity of the superconductor in RF fields. The finite conductivity can be calculated from BCS theory using a code called SRIMP, a code originally developed in FORTRAN by J. Halbritter, [Hal70b] and which is used throughout this thesis to determine SRF properties consistent with measured values of superconductors.

Input	Definition	Value	Unit
T_c	Superconductor's critical temperature	9.2	K
E_S	Normalized energy gap $\Delta(0)/(k_B T_c)$	1.8 - 1.96	–
λ_L	London penetration depth	390	Å
ξ_S	"SRIMP coherence length" $= \pi\xi_0/2$	596.9	Å
RRR	Residual resistivity ratio ($\propto \ell_{tr}$)	–	–
f_0	Frequency of applied RF field	–	MHz
T	Temperature at which to calculate R_{BCS}	–	K

Table C.1: SRIMP input parameters and typical values for high purity niobium. No value has been given for RRR since by definition a clean sample has RRR, $\ell_{tr} \to \infty$.

SRIMP uses six input parameters to calculate the surface impedance of the superconductor, which are discussed in [Hal70b], but also summarized in Table C.1 for ease of reference. SRIMP returns specular and diffuse[1] resistance

---

[1]Specular reflection applies to the case of a pure superconducting material, whereas diffuse

values calculated via BCS theory at a temperature $T < T_c$.

The quality factor and surface resistance of a cavity are related via the geometry factor: $R_s = G/Q_0$. The SRF properties of the surface layer are extracted by finding the parameters that yield the "best fit" to the measured R_s vs T data. Of course, now the challenge is simply to define what constitutes "best," which requires a digression into statistics.

C.1   A Digression into Statistics

Suppose data is taken with negligible error in the independent variable x, but some uncertainty, σ in the dependent variable y, i.e. the nth measurement yields the value $(x_n, y_n \pm \sigma_n)$. Furthermore, assume that the observations are modelled by a function f depending on p unknown parameters $\hat{\beta} = [\beta_1 \ldots \beta_p]$. The "best fit" is defined in the sense of those parameters that minimize

$$\chi^2 \equiv \sum_i \left(\frac{y_i - f\left(\hat{\beta}; x_i\right)}{\sigma_i} \right)^2 = \sum_i w_i \left(y_i - f\left(\hat{\beta}; x_i\right)\right)^2, \qquad \text{(C.1)}$$

where $w_i = 1/\sigma_i^2$, [SW03] and can be obtained using standard optimization techniques, such as the simplex method or the Levenberg-Marquardt algorithm. [Lev44]

Let $\hat{\beta}^*$ minimize Equation C.1 (with a value of χ^{*2}). The problem is to determine the uncertainty of $\hat{\beta}^*$. In general, there is no exact methods to generate confidence intervals for parameters of nonlinear models. [GI94] It is possible to define an *approximate* standard error for each parameter, which approaches the

---

reflection applies to electrons scattering off impurity sites, which accurately models niobium RF resonators that are not necessarily in the clean limit. [Pad09]

standard error as the number of samples increases without bound. The approximate standard error can be calculated from the asymptotic correlation matrix, A, defined as

$$A \equiv \frac{\chi^{*2}}{n-p} \cdot (J^T W J)^{-1},$$
(C.2)

where J is the $n \times p$ Jacobian matrix

$$J = \begin{pmatrix} \dfrac{\partial f\left(\hat{\beta}^*, x_1\right)}{\partial \beta_1^*} & \cdots & \dfrac{\partial f\left(\hat{\beta}^*, x_1\right)}{\partial \beta_p^*} \\ \vdots & \ddots & \vdots \\ \dfrac{\partial f\left(\hat{\beta}^*, x_n\right)}{\partial \beta_1^*} & \cdots & \dfrac{\partial f\left(\hat{\beta}^*, x_n\right)}{\partial \beta_p^*} \end{pmatrix},$$
(C.3)

and W is a diagonal matrix taking into account the relative weights of the data points via $W_{ii} = w_i = 1/\sigma_i^2$. [IBM]

Supposing a two-sided confidence level of $100(1-\alpha)\%$ is desired, the confidence interval of β_j^* is given by

$$C\left[\beta_j^* - t_{1-\alpha/2;n-p} \cdot \sqrt{A_{jj}} \leq \beta_j^* \leq \beta_j^* + t_{1-\alpha/2;n-p} \cdot \sqrt{A_{jj}}\right] \approx 1 - \alpha$$
(C.4)

where $t_{x,\nu}$ is the inverse of Student's cumulative distribution function, [STU08]

$$F(x|\nu) = \int_{-\infty}^{x} \frac{\Gamma\left(\frac{\nu+1}{2}\right)}{\Gamma\left(\frac{\nu}{2}\right)} \frac{1}{\sqrt{\nu\pi}} \left(1 + \frac{t^2}{\nu}\right)^{-\frac{\nu+1}{2}} dt,$$
(C.5)

and A_{ii} is the element of the matrix defined in Equation C.2, and the approximation in Equation C.4 becomes an equality in the limit of infinite observations. [GI94]

C.2 MatLab Code to Fit BCS Data with SRIMP

MatLab code has been developed to obtain the best estimators of SRF parameters given measurements of a superconducting sample, along with their associated errors. The program accepts as input a matrix of observations with each row corresponding to a measurement presented in the following columns: [Temperature (K), Surface Resistance (Ω), Frequency (MHz), {Weight}]. The last column is optional, and if not supplied, the program performs a minimization of the unweighted residual sum of squares.

The program begins by defining the structure used for the curve fit:

```matlab
function sol_param_array = polymorphic_BCS_fit(varargin)
    % Return default parameter array if there are no arguments
    param_array = {
        'Tc',         9.2,      'fix';
        'EnGap',      1.96,     'fix';
        'lonDepth',  390,       'fix';
        'cohLength',380*pi/2,'fix';
        'RRR',        10,       'fix';
        'R0',         10e-9,    'fix';
        'lambda_0',  .16,       'fix';
    };
```

If `polymorphic_BCS_fit` is called without arguments, it will return this cell array. The array can be manipulated by changing the values of the fit parameters, and making them variable by changing the string from `fix` to `var`.

After input validation and various programmatic control flags (not reproduced here), the program minimizes the (weighted) residual sum of squares to obtain estimates for the free variables. The essential elements of this section of the program are: 1) the variables are transformed by taking logarithms, because the objective function exponentiates the input arguments to keep them strictly positive. 2) the optimizer uses the `fminsearch` in the minimization

which implements the simplex method. 3) After optimization, the parameters are mapped back into an array along with the model parameters and residual sum of squares. 4) The statement on line 83 allows the code to be called without running the optimization, but simply to compute the BCS prediction for given model parameters at the temperatures specified by the input matrix.

```matlab
%% Begin program
    % Cycle over param_array to generate input for minimizer.
    % All parameters should be positive, so transform using exp(x)
    fit_guess = [];

    p = 1;  % Counter for free parameters
    for i=1:size(param_array, 1)
        if ~isequal(param_array{i, 3}, 'fix')
            fit_guess(p) = log(param_array{i, 2}); %#ok<AGROW>
            p = p + 1;
        else
            param_array{i, 2} = log(param_array{i, 2});
        end
    end

%% Execute optimization
    if isempty(fit_guess)
        polymorphic_objective([]);
    else
        options = optimset('TolX', 1e-2);
        [fit_results, final_RSS] = fminsearch(...
            @polymorphic_objective, ...
            fit_guess, ...
            options);
    end

    % Now put the results into the original array
    p = 1;
    for i=1:size(param_array,1)
        if isequal(param_array{i, 3}, 'fix')
            param_array{i, 2} = exp(param_array{i, 2});
        else
            param_array{i,2} = exp(fit_results(p));
            param_array{i,3} = 'fit';
            p = p + 1;
        end
    end

    sol_param_array = param_array;
    user_data = get(0, 'UserData');
    if ~exist('final_RSS', 'var')
        RSS = user_data{3};
    end
```

```
110
111        sol_param_array{size(param_array, 1)+1, 1} = user_data{1};
112        sol_param_array{size(param_array, 1)+1, 2} = user_data{2};
113        sol_param_array{size(param_array, 1)+1, 3} = RSS;
```

The next part of the code determines the confidence intervals via the mathematics presented in section C.1. When determining gradients, a step size of 5% of each parameter is used, following Ciovati's method. [Cio05, Appendix A] The confidence level is defined at the beginning of the program (not reproduced here) and is set to 95% by default. The gradient of R_0 does not need to be computed, since by definition, $R_s = R_0 + R_{BCS}$, so $\partial R_s / \partial R_0 = 1$. (The same is true for penetration depth fits, which is discussed more throughly after the code block.)

```
116  %% Compute confidence intervals
117      if p > 1
118          dof = size(data, 1) - (p-1);
119          h = 0.05;    % Derivative step percentage
120          J = zeros(size(data, 1), (p-1));
121          temps = data(:,1);
122          freq = data(1,3);
123          beta_star = cell2mat(sol_param_array(1:5, 2));
124
125          p = 1;
126          for i=1:size(param_array, 1)
127              if ~isequal(sol_param_array{i, 3}, 'fix')
128                  if i <= 5
129                      % Compute the jacobian
130                      beta_star_l = beta_star;
131                      beta_star_h = beta_star;
132                      beta_star_l(i) = beta_star(i)*(1 - h);
133                      beta_star_h(i) = beta_star(i)*(1 + h);
134
135                      % Lower value for derivative
136                      [R_bcs_l, ~, XD_l] = ...
137                          srimp_matlab([beta_star_l; freq], temps);
138                      % Upper value for derivative
139                      [R_bcs_h, ~, XD_h] = ...
140                          srimp_matlab([beta_star_h; freq], temps);
141
142                      switch flag.solve
143                          case 'XD'
144                              numerator = (XD_h - XD_l);
145                          otherwise
146                              numerator = (R_bcs_h - R_bcs_l);
147                      end
```

```matlab
148                    J(:, p) = numerator./(2*h*beta_star(i));
149                elseif i==6 || i==7
150                    % Gradient of R0 and lambda_0 is 1 since
151                    % Rs = R0 + R_bcs(params) and
152                    % XD_meas = lambda_0 + XD(params)
153                    J(:, p) = 1;
154                end
155                p = p+1;
156            end
157        end
158        % Compute asymptotic correlation matrix & conf. interval
159        A = RSS/dof*inv(J'*diag(weights)*J);
160        t_star = tinv(1 - confidence_level/2, dof);
161
162        p = 1;
163        for i = 1:(size(sol_param_array,1) - 1)
164            ap = 0;
165            if ~isequal(sol_param_array{i, 3}, 'fix')
166                ap = sqrt(A(p,p));
167                p = p+1;
168            end
169            sol_param_array{i, 4} = t_star*ap;
170        end
171        sol_param_array{end, 4} = A;
172    end
```

The final section is the objective function used in the minimization. This is written as a subfunction within the body of the main function so that the variables within the main function are within the same scope as the objective function. The objective function can either fit surface resistance as a function of temperature, or if the flag.solve variable is set to the string XD, can also fit the temperature dependent penetration depth of the superconductor. To use this option, the second column of the data matrix should be set to penetration depth measurements in μm. This feature, and its application, will be discussed later.

Essential features of the code for the objective function are that the accuracy of the BCS calculation is set to 10^{-3} (sufficient for the accuracy of the Q_0 measurements that generate the surface resistance data), and that the objective

function uses the weighted sum of squares to compute residuals. The objective function exponentiates the input parameters to implicitly enforce positive BCS parameters. For clarity, parts of the function that used to plot the data and fit during minimization have been removed from the code displayed below.

```matlab
175   %% Generate the objective function
176   function RSS = polymorphic_objective(x)
177       accuracy = 1e-3; %#ok<NASGU>
178
179       % Function to use in computing RSS: log, identity, weights, etc
180       f = @(x) (sqrt(weights).*x);
181
182       % Put guess parameters along with non-guess parameters
183       p = 1;
184       for i = 1:size(param_array)
185           if isequal(param_array{i, 3}, 'fix')
186               p_array{i, 2} = exp(param_array{i, 2});
187           else
188               p_array{i, 2} = exp(x(p));
189               p = p + 1;
190           end
191       end
192
193       % Seperate data for SRIMP call and RSS computation
194       temps = data(:,1);
195       BCS_Data = data(:,2);
196       freqs = data(:,3);
197       data_struct = [cell2mat(p_array(1:5, 2)); freqs(1)];
198       [R_bcs, ~, XD] = srimp_matlab(data_struct, temps);
199
200       % Fit either coherence length or surface resistance
201       switch flag.solve
202           case 'XD'
203               % Change XD from angstrom to um
204               XD = XD*1e-4;
205
206               lambda_0 = p_array{7,2};   % Penetration depth offset
207               RSS_init = (f(XD') - f(BCS_Data + lambda_0) ).^2;
208
209               RSS_init(RSS_init < 1e-20) = 1e-20;
210               RSS = sum(RSS_init);
211           otherwise
212                       R0 = p_array{6,2};
213               RSS_init = (f(R_bcs' + R0) - f(BCS_Data)).^2;
214               RSS = sum(RSS_init);
215       end
216       set(0, 'UserData', {temps, BCS_Data, RSS});
217   end
```

236

C.3   SRIMP Fit Parameter Uncertainty

The code discussed in the previous section allows both temperature dependent surface resistance and penetration depth data to be fit based on BCS parameters. Unfortunately, the estimation is difficult, because of "sloppiness" within the model, which refers to the fact that certain combinations of parameters can be changed without strongly effecting the behaviour of the model. [BHC$^+$04]

This effect can be illustrated by fitting data with some amount of simulated noise. For this example, BCS surface resistance data was generated at temperatures from 1.4 to 4.2 K, with default Nb parameters, and uniformly distributed noise with maximal magnitude of 20% was added to the simulated data. The number of points in the temperature range was also varied from between 11 to 2001. The noisy data was fit with the algorithm described in the previous section by using T_c and E_S as free variables. A plot summarizing the best estimate of T_c and E_S from the data, along with 95% confidence ellipses, is presented in Figure C.1.

Figure C.1 shows that due to the sloppy behaviour of the model, even when the number of observations increases, the estimators does not necessarily converge to their actual values. As the number of observations increases, the confidence intervals shrink, but since the estimators yield consistent results far from their actual values, the confidence intervals are too optimistic. It is important to note that while only two of the nine confidence intervals include the actual point, they are all within 2-3% of the real value. Thus for this example, when fitting T_c and E_S, it is more reasonable to estimate errors at the 3% level rather than those predicted from Equation C.4.

237

The correlation between E_s and T_c is expected. An approximation of the BCS surface resistance, valid at temperatures $T \ll T_c$ is

$$R_{BCS}(T) = \frac{a_0}{T} \ln\left(\frac{2k_B T}{\pi \hbar f}\right) \exp\left(-\frac{\Delta}{k_B T_c} \frac{T_c}{T}\right), \qquad (C.6)$$

where a_0 is a free parameter, and $E_S = \Delta/(k_B T_c)$. [Cio05] Equation C.6 shows that in the low temperature region, it is the product $E_S \cdot T_c$ that controls the exponential contribution to surface resistance, so it is not surprising that the fit is sloppy in regard to this combination of variables.
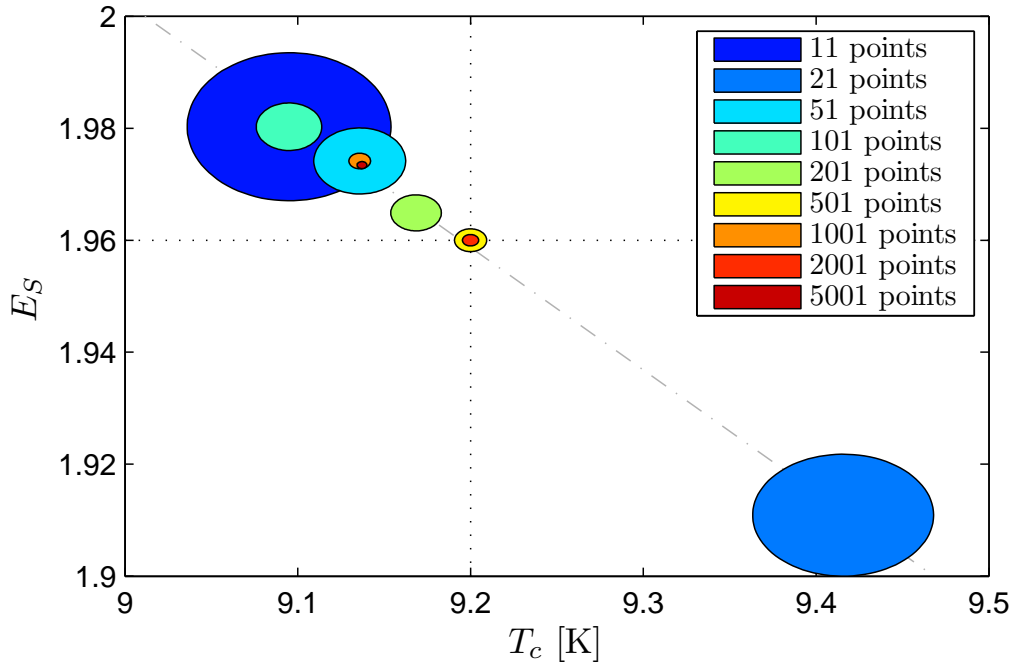

Figure C.1: Sloppiness between T_c and E_S in SRIMP fits, obtained from simulated noisy data ($T_c = 9.2$, $E_S = 1.96$, dotted black lines), over the range 1.4 to 4.2 K. The ellipses mark 95% confidence intervals. As the number of data points increase, the confidence interval decreases, but does not necessarily converge to the "actual" value. The gray dash-dot line shows the dimension that the combination of T_c and E_S can vary without strongly increasing the value of χ^2. Uniformly distributed noise with peak-to-peak amplitude equal to 20% of the ideal value was added to the BCS prediction of R_s given by SRIMP. This noise level is typical of SRF measurements.

The convergence of fits varying RRR (proportional to the electronic mean

free path, ℓ_{tr}) and residual resistance is presented in Figure C.2. Just as in the fit of E_S and T_c, the number of points in the temperature range 1.4 - 4.2 K used to generate the surface resistance according to BCS theory was varied, and uniformly distributed noise with 20% variation was added to the simulated data.
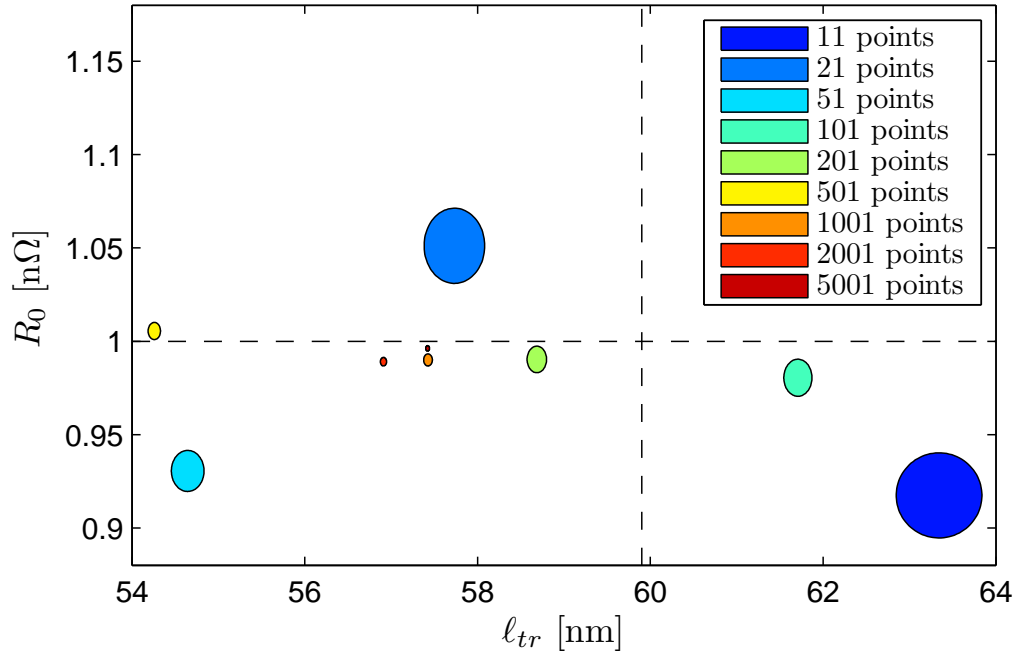

Figure C.2: SRIMP fit convergence with R_0 and ℓ_{tr} as free parameters obtained from simulated noisy data (R_0 = 1 nΩ, ℓ_{tr} = 59.9 nm, dotted black lines), over the range 1.4 to 4.2 K. The horizontal extent of the ellipses marks the 95% confidence interval, but the vertical 95% confidence interval scaling has been increased by a factor of $\tau \approx 6.28\ldots$ for visual clarity. As the number of data points increase, the confidence interval decreases, but does not converge to the real value within uncertainty. There is no correlation between R_0 and ℓ_{tr}, for the case of uniformly distributed noise with 20% relative peak-to-peak magnitude.

Figure C.2 shows that there is no correlation between R_0 and ℓ_{tr}. This is expected because R_0 is an additive constant that is not a parameter of the BCS theory. In the worst cases, with 20% error in the data, R_0 is within 5-8% of its actual value. The electronic mean free path is only correct to within 10%.

To quantify the difference between the propagated error calculated from the asymptotic correlation matrix and the actual difference between fit parameters and the real underlying values, simulations were run varying both the number of points and the noise level. As before, the parameters used to generate BCS data was that of standard Nb, with electronic mean free path of 59.9 nm, and a residual resistance of 1 nΩ. Fits with 2 degrees of freedom were performed, either with R_0 and ℓ_{tr} as free parameters or with E_S and T_c being varied.

In the following figures, an additional factor, ζ has been introduced, that measures by what factor the 95% confidence interval computed via Equation C.4 would have to be increased to include the actual value of the SRF parameter. Mathematically,

$$\zeta_i \equiv \frac{|\beta_i^* - \beta_i|}{t_{0.975;n-p} \cdot \sqrt{A_{ii}}}, \tag{C.7}$$

where in this case β_i^* is the best estimate of the free parameter β_i, and A_{ii} is the diagonal element of the asymptotic correlation matrix corresponding to β_i.

First, fits with only ℓ_{tr} and R_0 as free parameters were performed at three different noise levels. Figure C.3 shows the accuracy of ℓ_{tr} as the number of points in the data sample increases. It is essential to note that even with low numbers of observations, and large noise, ℓ_{tr}^* is accurate to better than 8%. In contrast, ζ is consistently above unity–meaning the confidence interval is underestimated– even for large numbers of points.

The same information for R_0 is displayed in Figure C.4. In this case, the worst case relative error is 9%, but as noise levels decrease, the error can be <1%. As in the case of ℓ_{tr}, ζ does not converge to unity at large number of observations, but remains around 10 for most noise levels.
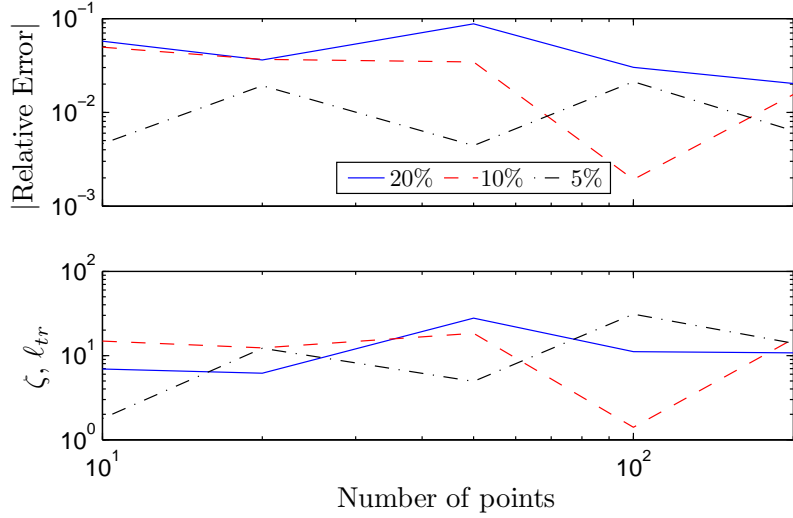
Figure C.3: SRIMP fit relative error of ℓ_{tr} with R_0 and ℓ_{tr} as free parameters obtained from simulated noisy data ($R_0 = 1$ nΩ, $\ell_{tr} = 59.9$ nm), from 1.4 to 4.2 K. Top: Absolute value of relative error in ℓ_{tr}. Bottom: ζ as defined in Equation C.7 as a function of number of data points in the observation for various noise levels. Uniformly distributed noise had relative peak-to-peak magnitude of 5, 10, and 20%.
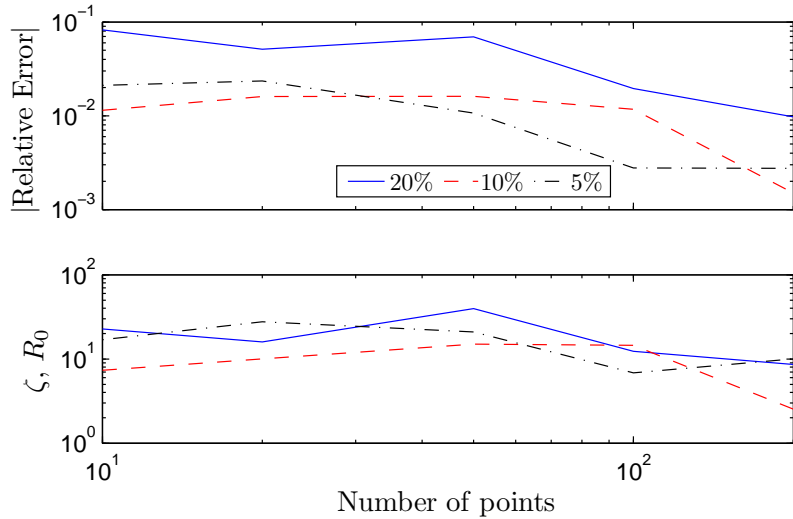

Figure C.4: SRIMP fit relative error of R_0 with R_0 and ℓ_{tr} as free parameters. Top: Absolute value of relative error in R_0. Bottom: ζ as defined in Equation C.7 as a function of number of observations for various noise levels. Uniformly distributed noise had relative peak-to-peak magnitude of 5, 10, and 20%.

Next, fits varying T_c and E_S were performed at three different noise levels. Figure C.5 shows the accuracy of T_c as the number of points in the data sample increases. It is essential to note that even with low numbers of observations, and large noise, T_c^* is accurate to better than 2%. In contrast, the estimate for the confidence interval is consistently more than a factor of 2 too small, even for large numbers of points.
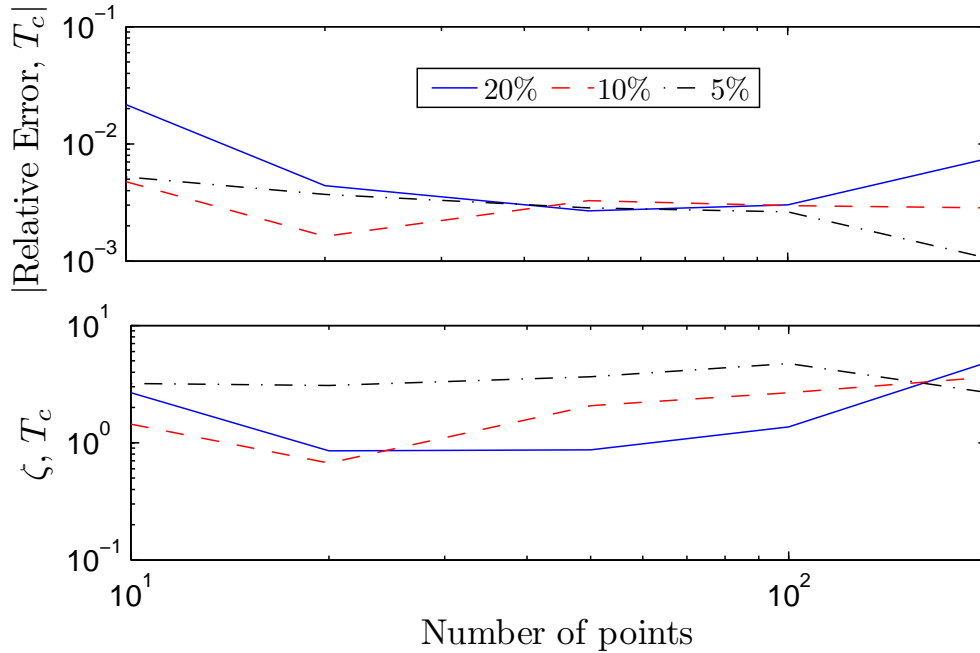

Figure C.5: SRIMP fit relative error of T_c with T_c and E_S as free parameters obtained from simulated noisy data ($R_0 = 1$ nΩ, $\ell_{tr} = 59.9$ nm), from 1.4 to 4.2 K. Top: Absolute value of relative error in T_c. Bottom: ζ as defined in Equation C.7 as a function of number of observations for various noise levels. Uniformly distributed noise had relative peak-to-peak magnitude of 5, 10, and 20%.

The results from fitting E_S is displayed in Figure C.6. In this case, the worst case relative error is $\approx 7\%$, but as noise levels decrease, the error can be within 2%. As in the case of the other parameters investigated, ζ does not converge to unity at large number of observations for E_S.
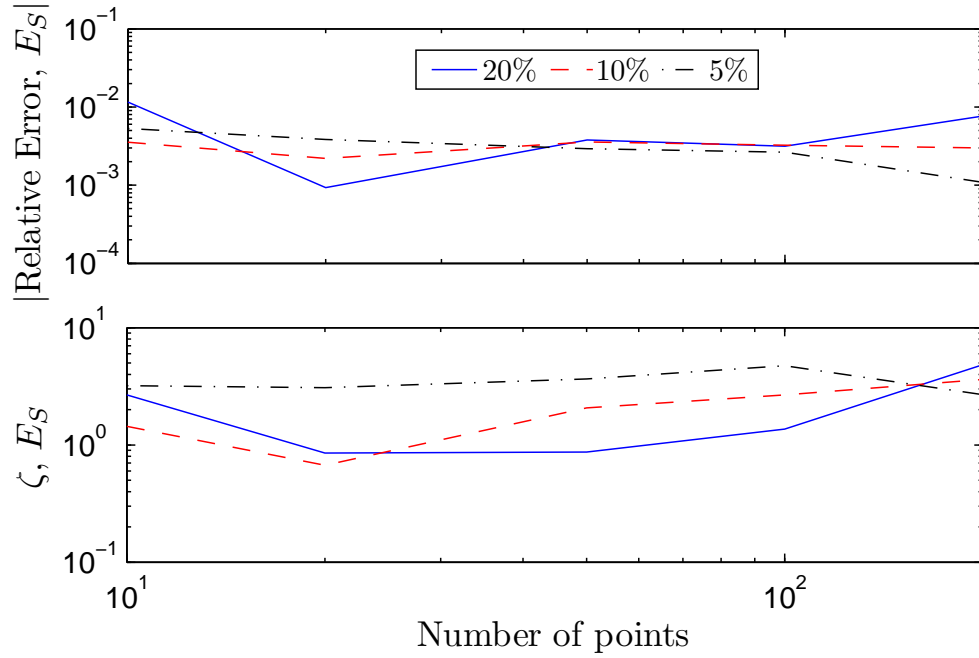
Figure C.6: SRIMP fit relative error of E_S with T_c and E_S as free parameters obtained from simulated noisy data ($R_0 = 1$ nΩ, $\ell_{tr} = 59.9$ nm), from 1.4 to 4.2 K. Top: Absolute value of relative error in E_S. Bottom: ζ as defined in Equation C.7 as a function of number of observations for various noise levels. Uniformly distributed noise had relative peak-to-peak magnitude of 5, 10, and 20%.

The simulations in the four figures demonstrate that the actual accuracy of SRIMP fits is much less than the predicted statistical confidence interval. A contribution to the fact that the confidence intervals do not include the actual value is the fact that the matrix $J \cdot W \cdot J$ is often near singular, so the inverse of the matrix is not accurately computed. In the next section Monte Carlo simulations are performed to determine empirically the accuracy of fit parameters.

C.3.1 Monte Carlo Simulations

As mentioned in the previous section, inverting the matrix needed to compute the asymptotic correlation matrix is sometimes inaccurately performed, since the matrix can be nearly singular. To ameliorate this, confidence intervals were determined empirically via Monte Carlo simulations, and logarithmic weighting of the residual sum of squares was employed. For each combination of free parameters, noise levels, and number of data points, 128 R_s vs T data sets were generated and fit with the algorithm described in section C.2.

Both randomly distributed errors, and systematic errors were investigated. Assuming the "ideal" surface resistance values are given by $\vec{R}_{s,i} = [R_{s,i}(T_1), \ldots, R_{s,i}(T_n)]$, the noisy vector $\vec{R}_{s,n}$ is defined as

$$\vec{R}_{s,n} = [1 + \sigma_R N(0, 1)]\vec{R}_{s,i}, \tag{C.8}$$

for the random errors, where $N(0, 1)$ is normally distributed noise with zero mean and unity variance and σ is the RMS amplitude of the noise.

A systematically noisy signal, $\vec{R}_{s,sys}$, is defined as

$$\vec{R}_{s,sys} = (1 + \Delta_S)\vec{R}_{s,i}, \tag{C.9}$$

where in this case, Δ_S is a systematic shift.

SRIMP Fits with 4-degrees of Freedom

Histograms presenting the distribution of parameter estimates for a fit with 4 degrees of freedom (T_c, E_S, ℓ_{tr} and R_0) of signals with random noise are presented in Figures C.7, C.8, C.9, and C.10. The nominal values of the superconducting RF layer are $T_c = 9.2$ K, $E_S = 1.96$, $\ell_{tr} = 16.7$ nm, $R_0 = 10$ nΩ. The histograms show the resulting best fit parameters for various combinations of the number points taken between 1.4 and 4.2 K and random noise levels.

The histograms demonstrate that in most cases, the mean of the estimates are very close to the actual value of the parameter. There are a few outliers that strongly increase the standard deviation of the estimates. One exception is that the fits of ℓ_{tr} suggest that the underlying distribution is skewed, and has a long, one-sided tail, meaning that a normal distribution may not be a suitable representation of the data. Figure C.11 shows the distribution of ℓ_{tr} compared with a gamma probability distribution.

$$\hat{\beta} \in [T_c, E_S, \ell_{tr}, R_0], \quad \beta_i^* = T_c$$

Figure C.7: Histograms showing the distribution of the best estimate of T_c in 128 Monte Carlo simulations for various relative noise levels and number of data points. The red curve is the best fitting normal distribution, and the green line shows the nominal value of T_c. Horizontal scale has units of Kelvin.

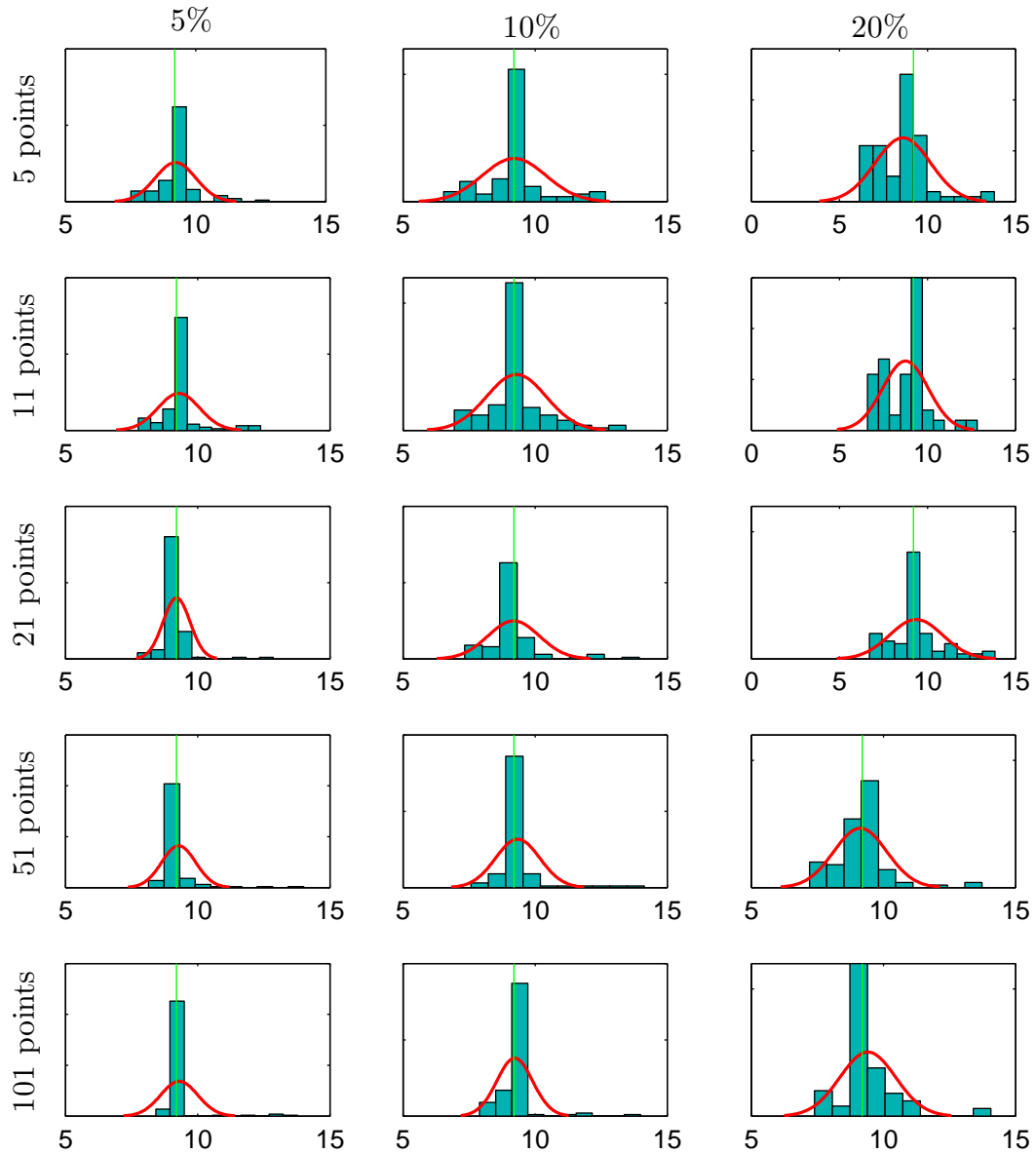$$\hat{\beta} \in [T_c, E_S, \ell_{tr}, R_0], \quad \beta_i^* = E_S$$
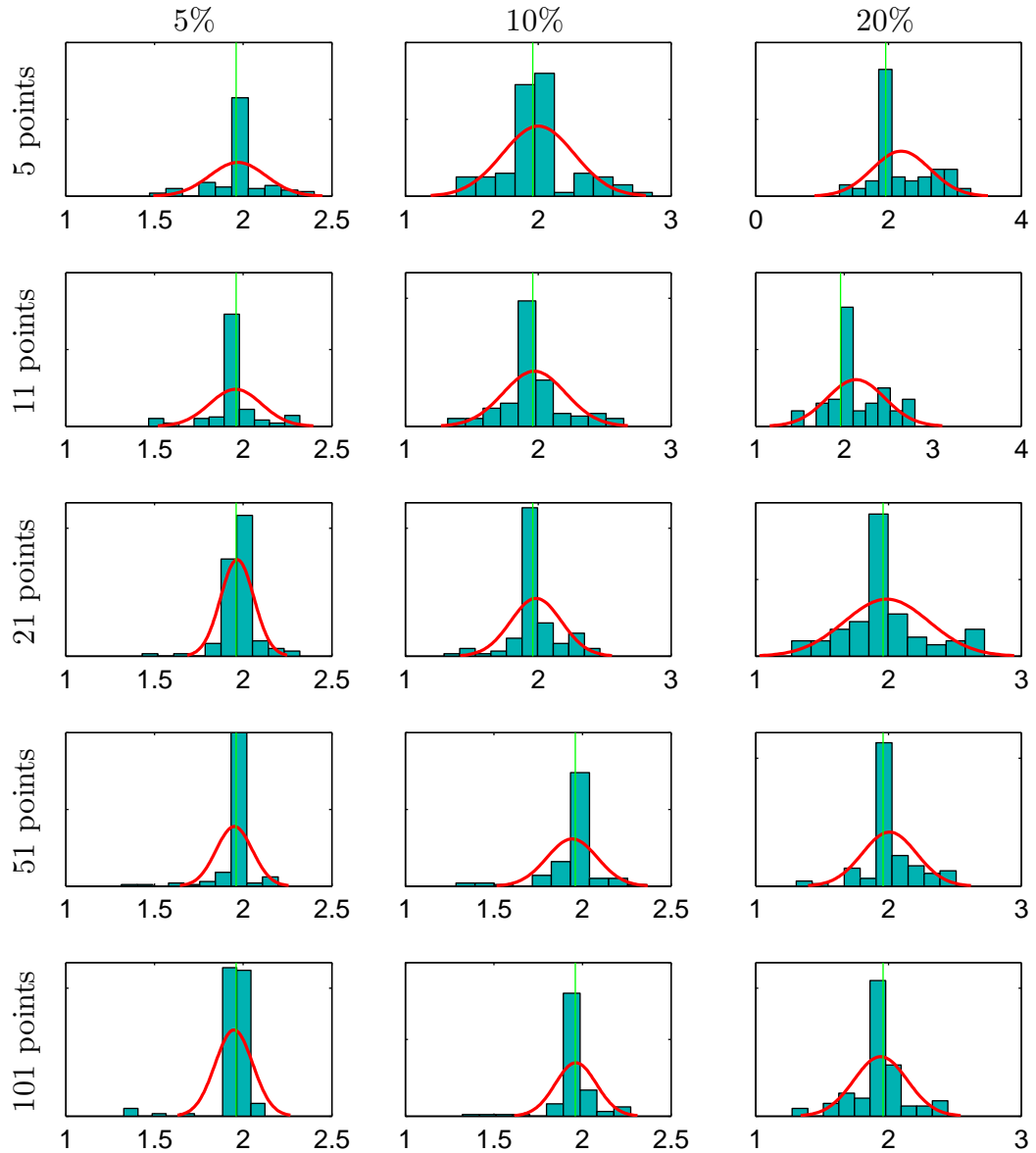
Figure C.8: Histograms showing the distribution of the best estimate of E_S in 128 Monte Carlo simulations for various relative noise levels and number of data points. The red curve is the best fitting normal distribution, and the green line shows the nominal value of E_S.

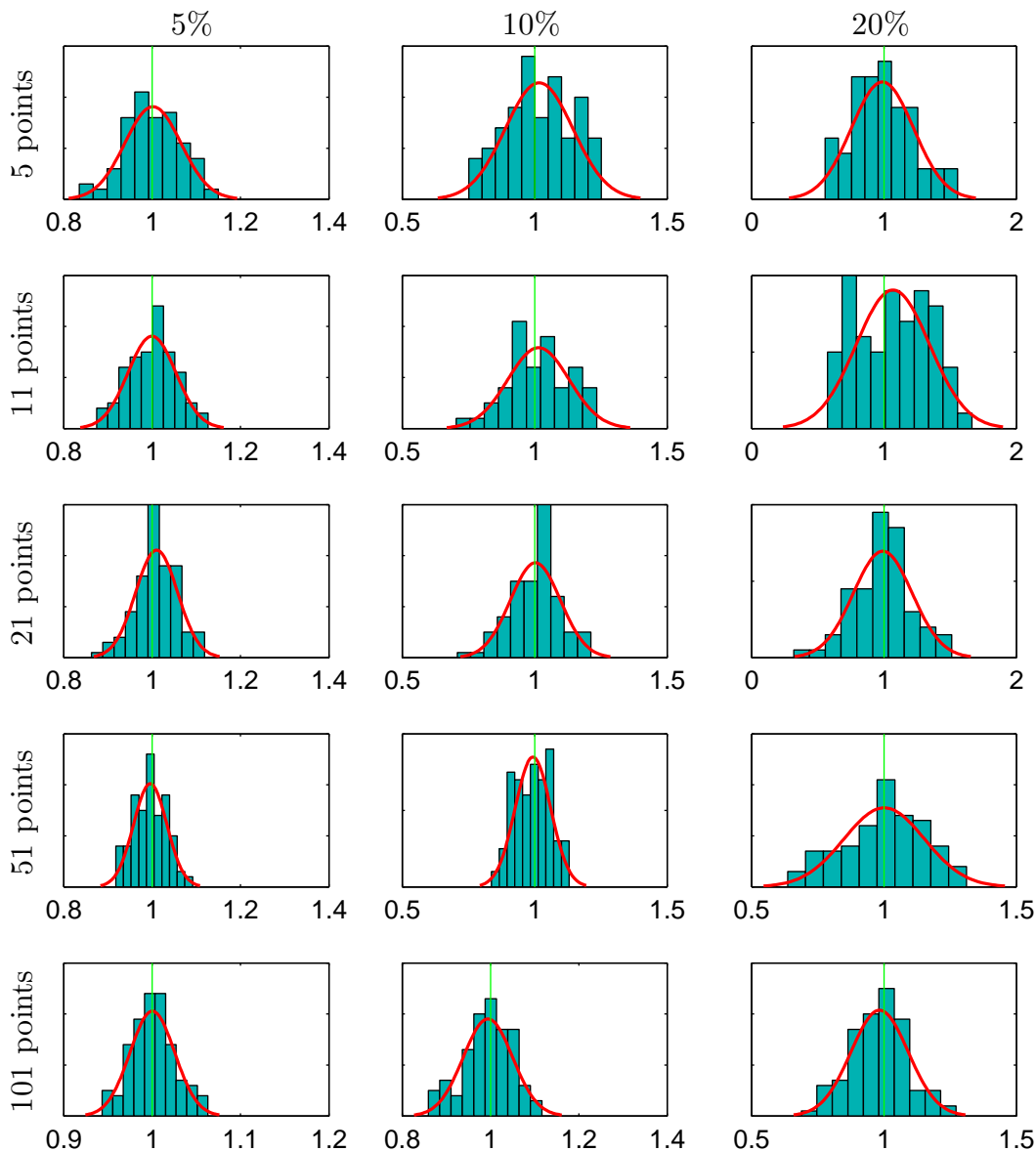$$\hat{\beta} \in [T_c, E_S, \ell_{tr}, R_0], \quad \beta_i^* = R_0$$

Figure C.9: Histograms showing the distribution of R_0 in 128 Monte Carlo simulations for various relative noise levels and number of data points in the measurement. The red curve is the best fitting normal distribution, and the green line shows the nominal value of R_0. Horizontal scale is in nano-ohms.

$$\hat{\beta} \in [T_c, E_S, \ell_{tr}, R_0], \quad \beta_i^* = \ell_{tr}$$

Figure C.10: Histograms showing the distribution of ℓ_{tr} in 128 Monte Carlo simulations for various relative noise levels and number of data points in the measurement. The red curve is the best fitting normal distribution, and the green line shows the nominal value of ℓ_{tr}. Horizontal scale is in nanometers.

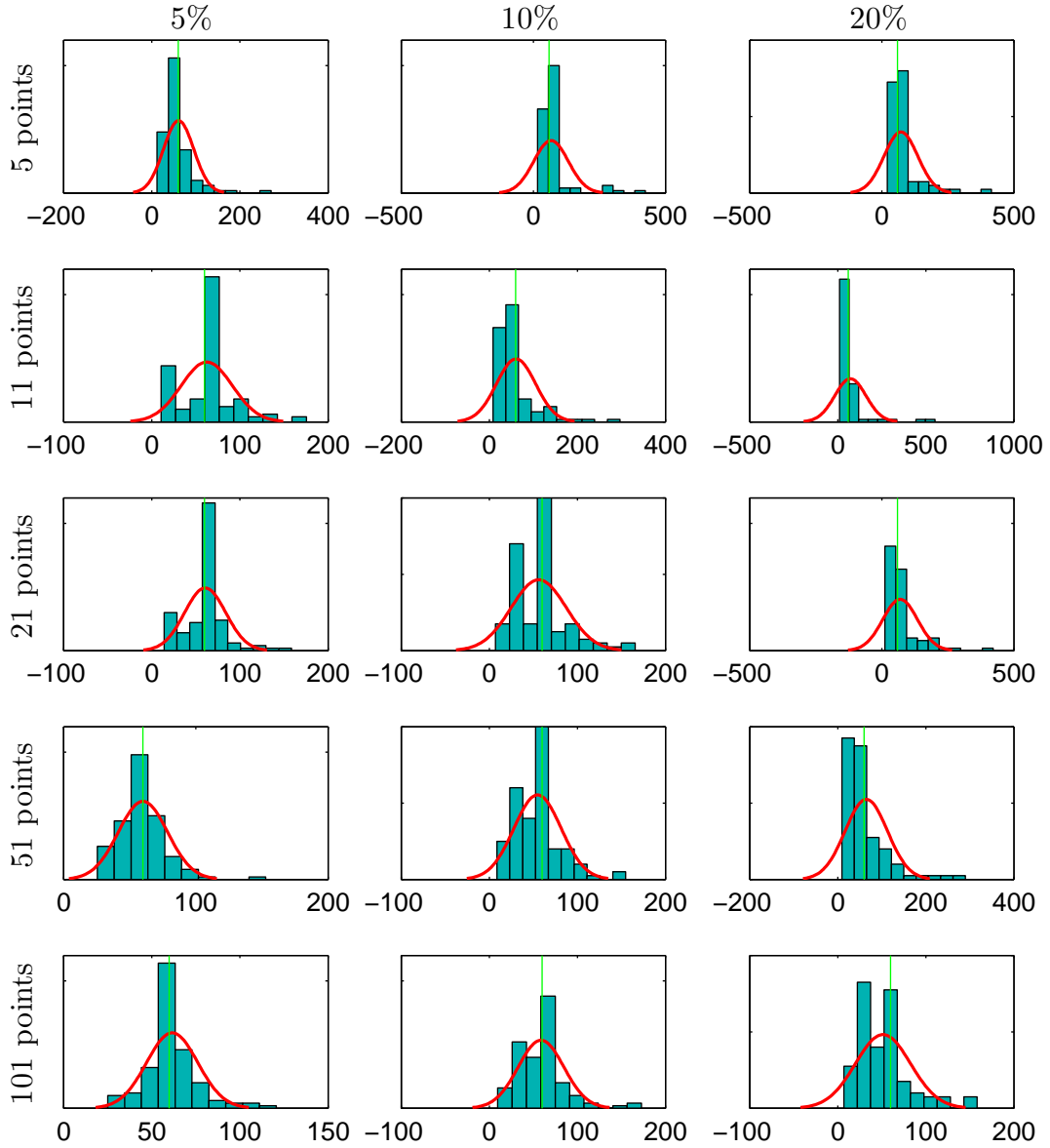$$\hat{\beta} \in [T_c, E_S, \ell_{tr}, R_0], \quad \beta_i^* = \ell_{tr}$$
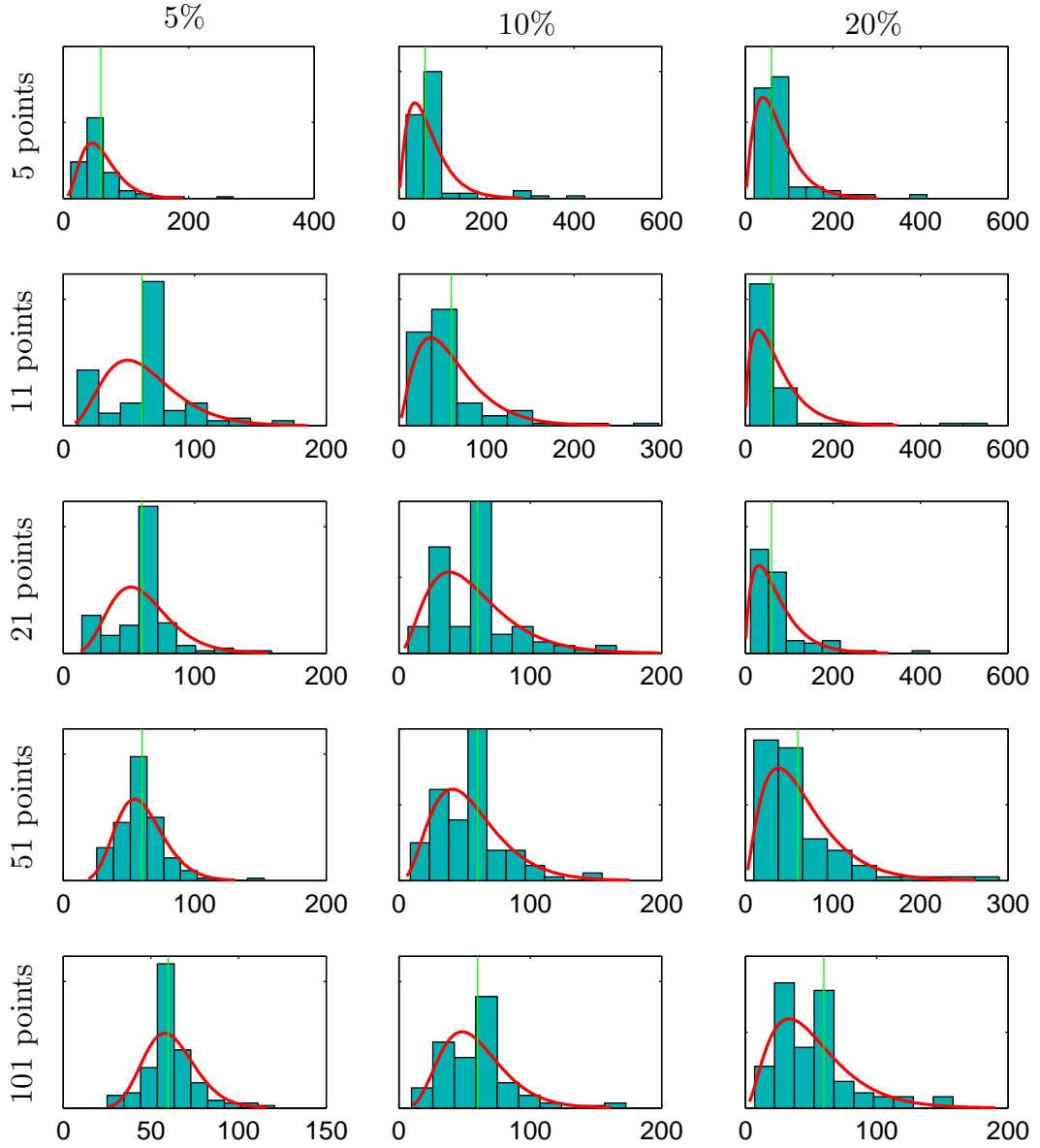
Figure C.11: Histograms showing the distribution of ℓ_{tr} in 128 Monte Carlo simulations for various relative noise levels and number of data points in the measurement. The red curve is the best fitting gamma distribution, and the green line shows the nominal value of ℓ_{tr}. Horizontal scale is in nanometers. Comparison with Figure C.10 suggests that for these simulations a gamma distribution reflects the underlying data better than a normal distribution.

The relative error of each free parameter as a function of number of data points in the sample and random noise level is summarized in Table C.2. For both the histograms in the previous pages, and the table below, points with $\ell_{tr} >$ 500 nm have been eliminated as outliers. This does not effect the underlying physics, because as illustrated in Figure A.2, $\kappa_{GL}(\ell_{tr} > 500$ nm$)$ is within 3% of $\kappa_{GL}(\ell_{tr} \to \infty)$.

Free Parameters	β_i	σ_R [%]	Relative Error [%]				
			Number of Data Points				
			11	21	51	101	201
T_c, E_S ℓ_{tr}, R_0	T_c	5	14.0	13.9	18.1	10.3	9.5
		10	19.8	19.0	22.3	21.9	11.5
		20	20.4	26.5	24.6	18.7	15.3
	E_S	5	10.5	9.8	10.5	6.5	6.3
		10	15.8	14.3	14.2	11.9	7.7
		20	23.1	20.4	18.5	13.1	11.9
	ℓ_{tr}	5	50.3	48.5	39.3	30.9	24.9
		10	75.6	64.5	52.9	46.3	41.6
		20	80.2	91.8	86.2	69.9	50.7
	R_0	5	6.2	5.6	4.6	3.8	2.6
		10	12.3	12.2	9.5	6.8	5.7
		20	23.8	26.4	22.9	15.4	10.8

Table C.2: Uncertainty in SRIMP fit parameters determined by Monte Carlo simulations characteristic of Nb (Nominal values of the superconducting RF layer are T_c = 9.2 K, E_S = 1.96, ℓ_{tr} = 16.7 nm, R_0=10 nΩ). Parameters were fit in 128 simulations at varying noise levels. The value listed in the table is the standard deviation of the best fit variables normalized by the actual value of the parameter, except in the case of ℓ_{tr}, in which case the value is given by the square-root of the variance of the Gamma distribution.

Table C.2 uses the variance of ℓ_{tr} from the gamma distribution (discussed in the next paragraph), instead of a normal distribution to take into account the non-negative nature of the electronic mean free path as well as the fact that if $\xi_0 \lesssim 3\ell_{tr}$, similar physics results from widely differing ℓ_{tr}.

The gamma probability distribution is a continuous probability distribution

defined on the support $x \in [0, \infty)$, characterized by a shape parameter, k and scale parameter, θ, with the form

$$f(k, \theta; x) = \frac{1}{\theta^k \Gamma(k)} x^{k-1} \exp\left(-\frac{x}{\theta}\right), \qquad (C.10)$$

where $\Gamma(k)$ is the gamma function, or generalized factorial function. [Haz88] The mean of this distribution is given by $k\theta$ and the variance is $k\theta^2$.

Systematic errors were also computed by applying Equation C.9 to ideal data with $\Delta_S \in [-0.15, 0.15]$. The results are presented in Figure C.12.
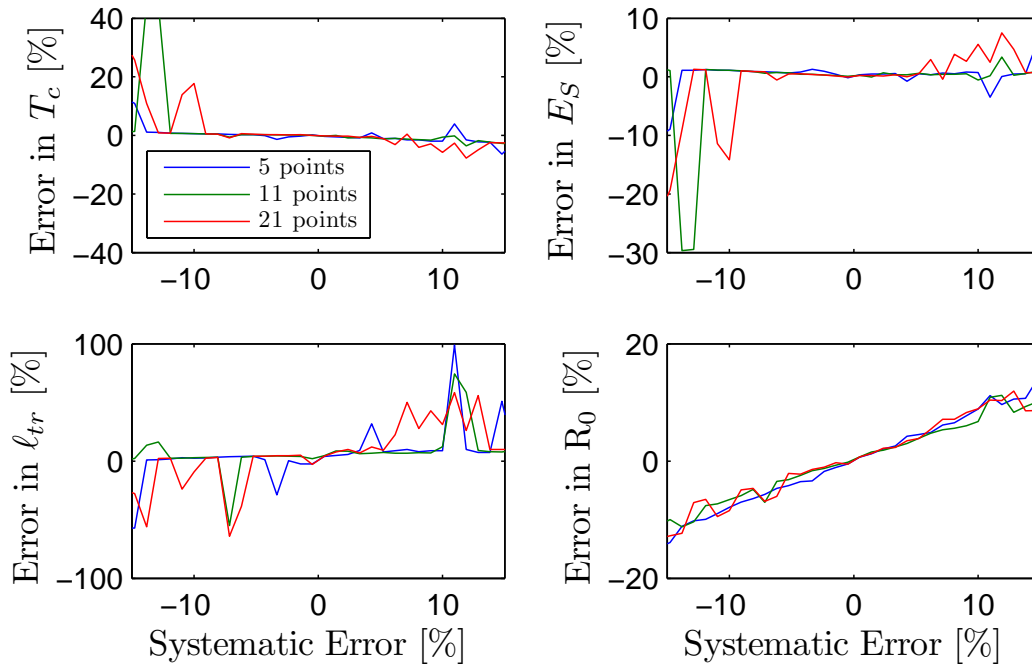

Figure C.12: Relative error in SRIMP fits as a function of systematic error for 4 degrees of freedom for typical niobium. Horizontal axes are the values of Δ_S used in Equation C.9 which range between ±15%. The jagged appearance of the signals is due the fact that the parameters are not uncorrelated.

SRIMP Fits with 3-degrees of Freedom

The HTC experiments in chapter 4 needed to investigate the influence of thermal cycling on material parameters. The critical temperature was well known, so free variables were only energy gap, ℓ and R_0. Monte Carlo simulations were performed around the parameters $E_S = 1.96$, $RRR = 4.0$, $R_0 = 3 \times 10^{-9}\,\Omega$ to determine uncertainties, and the results are tabulated in Table C.3.

Free Parameters	β_i	σ_R [%]	Relative Error [%] Number of Data Points				
			5	11	21	51	101
	E_S	5	0.9	0.6	0.6	0.4	0.3
		10	1.5	1.1	0.8	0.6	0.6
		20	3.1	1.8	1.4	1.4	0.8
E_S	ℓ_{tr}	5	58.0	50.2	46.8	33.2	29.6
ℓ_{tr}, R_0		10	96.1	79.7	52.0	44.5	48.4
		20	88.8	77.5	85.2	82.7	45.6
	R_0	5	5.8	4.6	3.7	2.5	1.6
		10	10.7	9.2	7.5	5.2	3.8
		20	23.6	20.6	14.1	10.9	6.5

Table C.3: Uncertainty in SRIMP fit parameters determined by Monte Carlo simulations characteristic of Nb near parameters characteristic of those measured in the HTC (Nominal values of the superconducting RF layer are $T_c = 9.2$ K, $E_S = 1.96$, $\ell_{tr} = 16.7$ nm, $R_0 = 10$ nΩ). Parameters were fit in 128 simulations at varying noise levels. The value listed in the table is the standard deviation of the best fit variables normalized by the actual value of the parameter, except in the case of ℓ_{tr}, in which case the value is given by the square-root of the variance of the Gamma distribution.

SRIMP Fits with 2-degrees of Freedom

The previous section demonstrated that 3 and 4-parameter fits could yield accurate estimates of superconducting parameters, but sloppiness between the parameters led to large uncertainties, at least for the 4-parameter case between

T_c and energy gap. In the 3-parameter case, the error on mean free path is large, likely due to weak variation of the surface resistance with this parameter. This section explores the uncertainty of parameter estimates from SRIMP fits when only two parameters are varied. Table C.4 presents the relative errors obtained from Monte Carlo simulations of a typical niobium material with various combinations of two free parameters. The values in the table are the standard deviation of best fit fit parameters, divided by the actual value of the parameter.

The effect of systematic errors on parameter estimation was also investigated. Following Equation C.9, surface resistance data was generated with σ varying between ±20%. In all cases, when $\sigma = 0$, the original parameters were found as the best fit, as one would expect. The relative error of the fit parameters for various noise levels are presented in Table C.5 and C.6.

SRIMP Fits with Parameters Typical of Nb$_3$Sn

The Monte Carlo simulations presented in the last few sections used material properties typical of niobium. This section presents results of simulations using material properties characteristic of Nb$_3$Sn, a superconductor which is currently under investigation for use as a next generation material for superconducting structures.

Because the superconducting parameters of Nb$_3$Sn (see Table C.7) are quite different from that of niobium, it is necessary to re-evaluate the fit uncertainties in the new region of parameter space.

In total, 324 random noise simulations were performed at the 5, 10, and 20% relative noise levels with three free parameters, E_S, ℓ_{tr} and R_0, over a tempera-

Free Parameters	β_i	σ_R [%]	Relative Error of β_i^* [%] Number of Data Points				
			5	11	21	51	101
T_c, E_S	T_c	5	10.4	9.8	8.1	5.2	3.8
		10	13.5	10.8	11.3	9.7	7.3
		20	16.0	14.2	14.0	14.0	12.4
	E_S	5	10.6	9.3	7.5	5.1	3.7
		10	14.8	11.7	11.2	8.9	7.0
		20	19.0	17.4	15.5	14.8	11.9
E_S, ℓ_{tr}	E_S	5	1.2	0.8	0.7	0.4	0.3
		10	2.4	1.7	1.3	0.9	0.6
		20	3.1	2.6	2.0	1.5	1.3
	ℓ_{tr}	5	58.0	44.6	34.2	21.4	13.3
		10	136.7	84.4	67.8	45.4	31.5
		20	167.9	144.2	109.9	80.9	62.6
E_S, R_0	E_S	5	0.4	0.3	0.2	0.1	0.1
		10	0.8	0.6	0.4	0.3	0.2
		20	1.7	1.4	0.8	0.5	0.4
	R_0	5	5.4	5.0	4.9	3.2	2.4
		10	13.2	11.7	8.5	6.7	4.9
		20	25.0	23.2	19.0	14.9	9.4
ℓ_{tr}, R_0	ℓ_{tr}	5	18.5	12.7	8.2	6.5	4.6
		10	38.1	25.0	16.6	13.0	8.0
		20	60.9	39.5	34.8	24.1	18.7
	R_0	5	5.9	5.1	4.5	3.0	2.1
		10	11.9	11.0	9.4	6.4	4.3
		20	24.7	25.4	16.9	11.7	8.8

Table C.4: Uncertainty of 2-parameter SRIMP fits determined by Monte Carlo simulations characteristic of Nb (nominal values of the superconducting RF layer are T_c = 9.2 K, E_S = 1.96, ℓ_{tr} = 16.7 nm, R_0=10 nΩ). Parameters were fit in 128 simulations at varying noise levels. The value listed in the table is the standard deviation of the best fit probability distribution normalized by the actual value of the parameter, for typical niobium values.

ture range of 2.0 - 15 K. The values of the nominal superconductor parameters are presented in Table C.7. Histograms of the fits are presented in Figures C.13, C.14 and C.15

The uncertainty from the simulations with random noise results are sum-

Free Parameters	β_i	Δ_S [%]	Relative Error of β_i^* [%]				
			Number of Data Points				
			5	11	21	51	101
T_c, E_S	T_c	-20	35.4	40.0	44.2	47.3	48.2
		-10	10.2	11.2	11.9	12.3	12.7
		-5	4.0	4.0	5.3	5.5	5.3
		5	-2.0	-2.9	-2.1	-3.6	-4.2
		10	-6.3	-7.3	-7.1	-7.4	-7.5
		20	-9.9	-11.6	-12.1	-12.2	-12.7
	E_S	-20	-23.7	-26.3	-28.4	-29.9	-30.4
		-10	-7.9	-8.7	-9.3	-9.6	-10.0
		-5	-3.1	-3.1	-4.3	-4.5	-4.4
		5	1.2	2.3	1.4	3.1	3.7
		10	6.8	6.5	6.2	6.6	6.7
		20	10.0	10.2	10.9	11.1	11.7
E_S, ℓ_{tr}	E_S	-20	2.6	2.6	2.6	2.6	2.5
		-10	1.6	1.0	0.9	1.6	0.9
		-5	0.5	0.5	0.5	0.4	0.5
		5	-0.5	-0.4	-0.5	-0.4	-0.4
		10	-1.1	-0.9	-0.9	-0.8	-0.8
		20	-2.2	-1.7	-1.6	-1.6	-1.6
	ℓ_{tr}	-20	-62.8	-61.7	-61.5	-61.4	-61.4
		-10	-34.5	-33.9	-34.8	-30.3	-35.4
		-5	-13.9	-16.1	-16.3	-16.7	-16.9
		5	12.4	15.7	15.4	16.3	16.3
		10	22.7	31.2	31.9	33.1	33.3
		20	40.7	62.6	64.9	67.0	68.6

Table C.5: Uncertainty of 2-parameter SRIMP fits as a function of systematic error for typical niobium parameters (nominal values of the superconducting RF layer are T_c = 9.2 K, E_S = 1.96, ℓ_{tr} = 16.7 nm, R_0=10 nΩ).

marized in Table C.8, and the effect of systematic errors on the accuracy of fit parameters for Nb$_3$Sn is illustrated in Figure C.16.

The simulation results show that fit uncertainties are much smaller in regions of the parameter space characteristic of Nb$_3$Sn compared with niobium. This is likely due to two factors: First, the electronic mean free path of Nb$_3$Sn is much smaller than of niobium. The "dirty" limit is more sensitive to ℓ_{tr} than the "clean" limit is. For niobium, ℓ_{tr} is often near the minimum of surface resistance,

Free Parameters	β_i	Δ_S [%]	Relative Error of β_i^* [%]				
			Number of Data Points				
			5	11	21	51	101
E_S, R_0	E_S	-20	3.5	3.5	3.5	3.5	3.5
		-10	1.7	1.6	1.6	1.6	1.7
		-5	0.8	0.8	0.8	0.8	0.8
		5	-0.8	-0.8	-0.8	-0.7	-0.8
		10	-1.5	-1.5	-1.4	-1.5	-1.5
		20	-2.8	-2.8	-2.8	-2.8	-2.8
	R_0	-20	-16.5	-13.3	-12.1	-10.6	-10.1
		-10	-7.9	-6.3	-5.5	-5.2	-4.5
		-5	-3.8	-3.0	-2.8	-2.2	-2.3
		5	3.7	2.8	2.5	2.4	2.0
		10	7.9	5.9	5.2	4.2	3.8
		20	15.3	11.7	9.9	8.7	7.7
ℓ_{tr}, R_0	ℓ_{tr}	-20	-59.7	-59.5	-59.6	-59.6	-59.5
		-10	-59.5	-59.5	-59.4	-59.6	-59.8
		-5	-33.4	-33.5	-33.2	-33.8	-33.8
		5	33.0	33.2	33.5	33.7	33.5
		10	69.6	69.6	69.2	69.0	69.8
		20	153.9	154.4	154.3	154.6	154.6
	R_0	-20	-23.7	-27.3	-29.4	-30.9	-31.7
		-10	-10.8	-11.5	-12.1	-12.5	-12.7
		-5	-5.1	-5.0	-5.1	-4.9	-4.9
		5	5.2	4.6	4.6	5.0	4.6
		10	10.3	10.3	10.3	9.5	9.7
		20	19.9	20.0	19.9	20.0	19.7

Table C.6: Uncertainty of 2-parameter SRIMP fits as a function of systematic error for typical niobium parameters (nominal values of the superconducting RF layer are T_c = 9.2 K, E_S = 1.96, ℓ_{tr} = 16.7 nm, R_0=10 nΩ).

introducing only second order effects on surface resistance. Second, about 70% of the superconducting temperature range was sampled in the case of Nb$_3$Sn, opposed to 30% for niobium, strongly constraining the parameters.

Parameter	Value	Unit
T_c	18.0	K
E_S	2.45	-
λ_L	88.5	nm
ξ_S	11.0	nm
ℓ_{tr}	3.79	nm
R_0	9.365	nΩ

Table C.7: Nb$_3$Sn material parameters used in Monte Carlo SRIMP fitting. [Pos]

$$\hat{\beta} \in [E_S, \ell_{tr}, R_0], \quad \beta_i^* = E_S$$
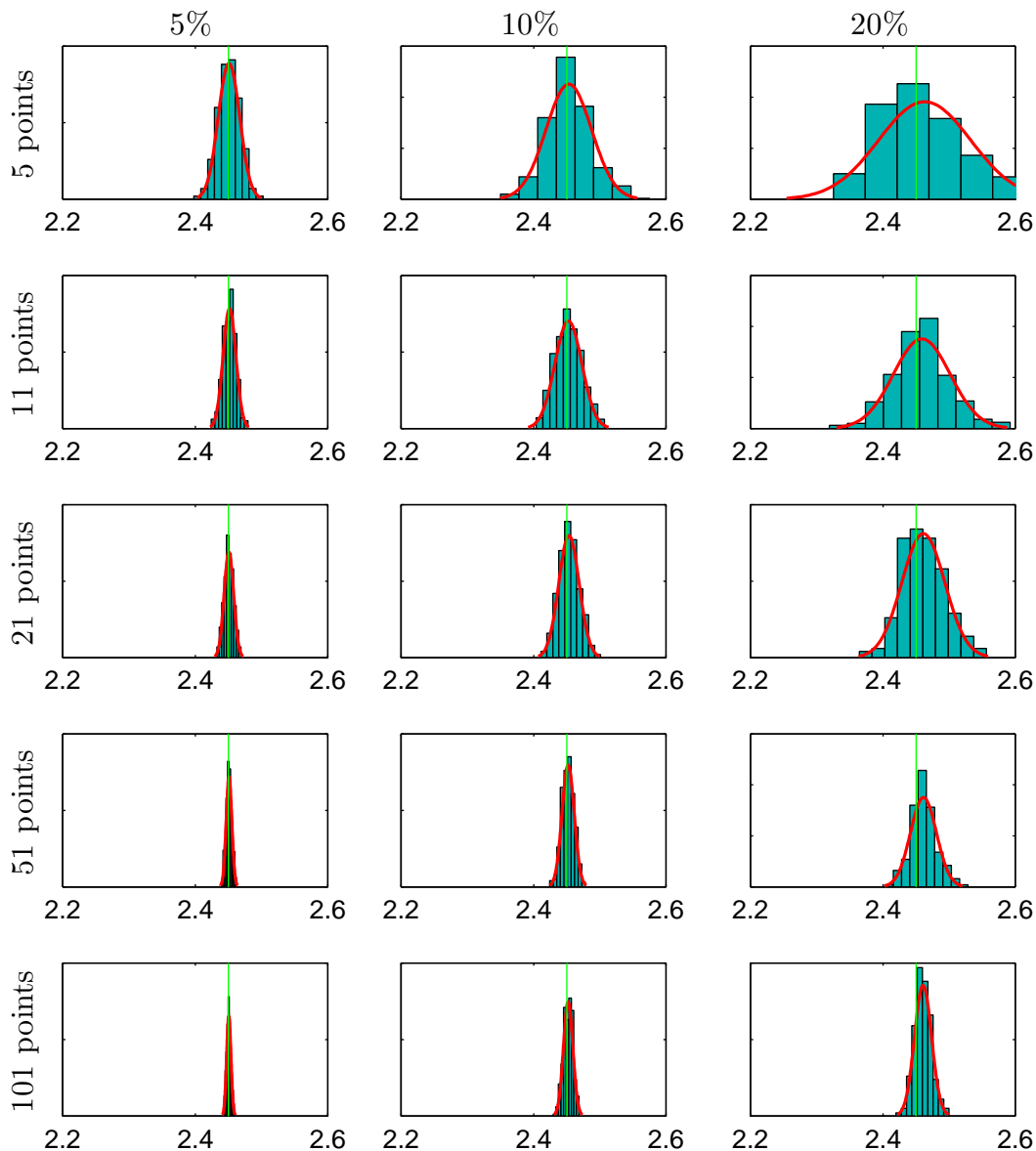
Figure C.13: Histograms showing the distribution of E_S in 324 Monte Carlo simulations of nominal Nb$_3$Sn for various relative noise levels and number of data points in the measurement. The red curve is the best fitting normal distribution, and the green line shows the nominal value of E_S.

$$\hat{\beta} \in [E_S, \ell_{tr}, R_0], \quad \beta_i^* = \ell_{tr}$$
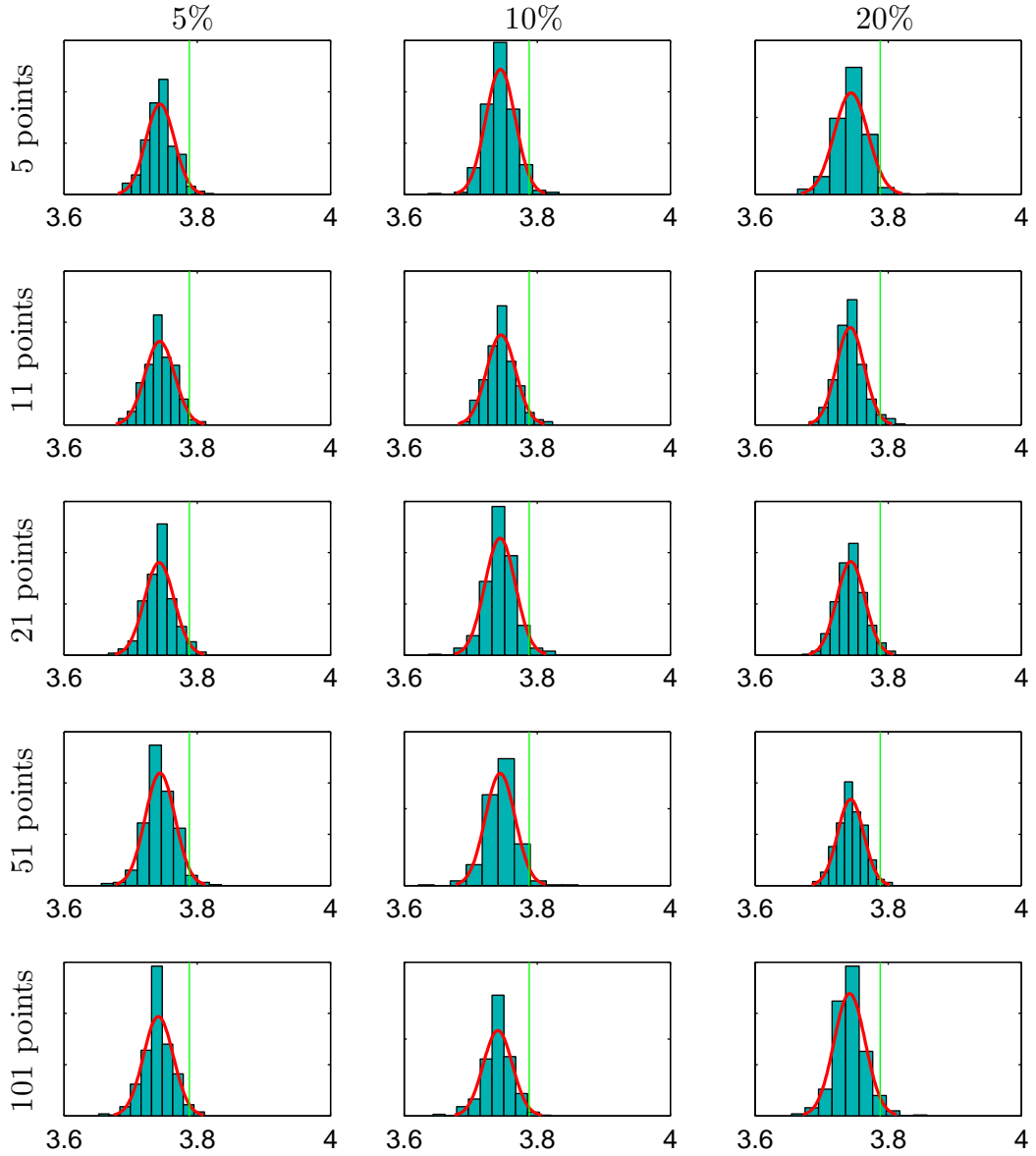
Figure C.14: Histograms showing the distribution of ℓ_{tr} in 324 Monte Carlo simulations of nominal Nb$_3$Sn for various relative noise levels and number of data points in the measurement. The red curve is the best fitting gamma distribution, and the green line shows the nominal value of ℓ_{tr}. Horizontal scale is in nanometers.

$$\hat{\beta} \in [E_S, \ell_{tr}, R_0], \quad \beta_i^* = R_0$$
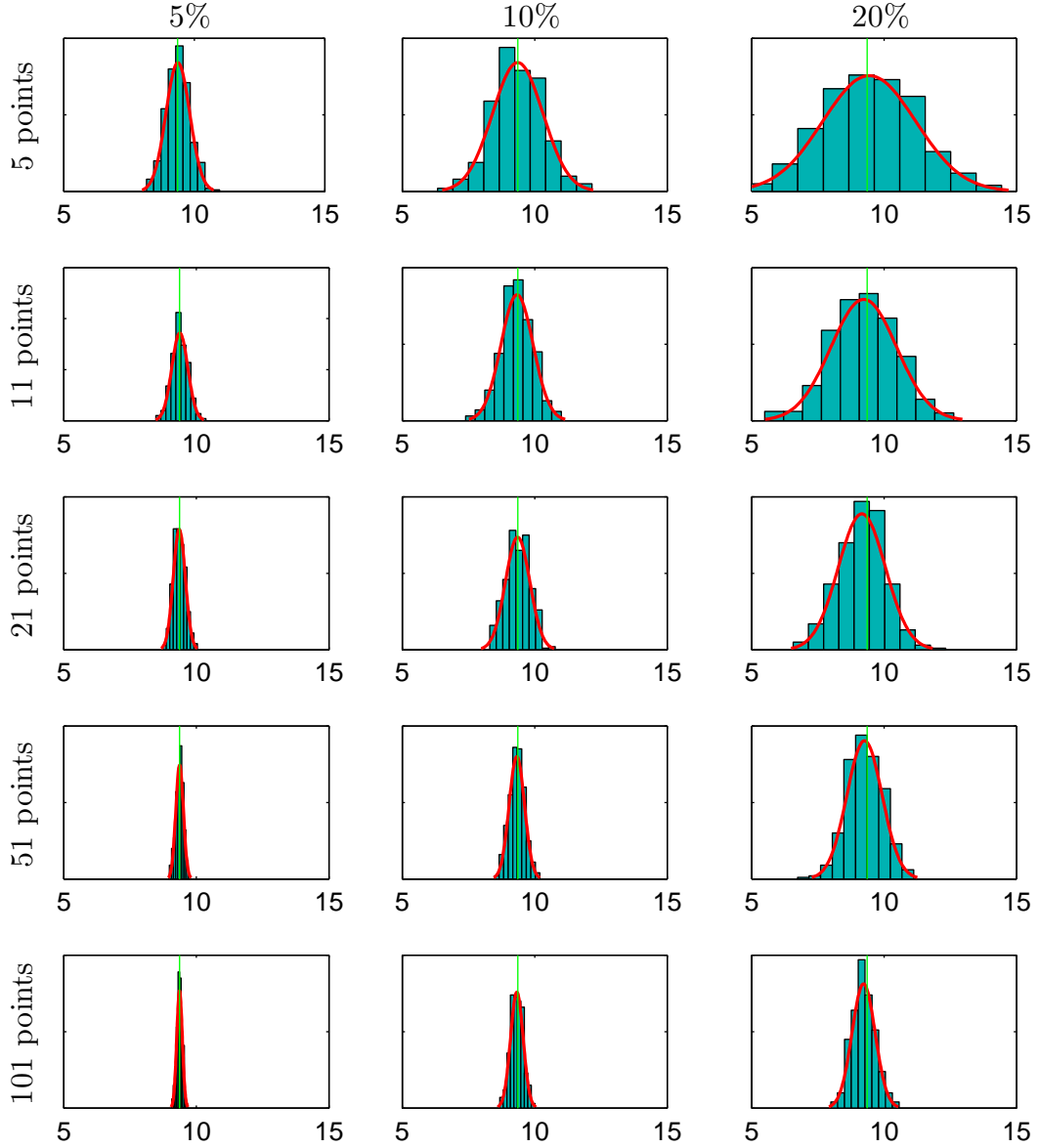
Figure C.15: Histograms showing the distribution of R_0 in 324 Monte Carlo simulations of nominal Nb$_3$Sn for various relative noise levels and number of data points in the measurement. The red curve is the best fitting normal distribution, and the green line shows the nominal value of R_0. Horizontal scale is in nano-Ohms.

Free Parameters	β_i	σ_R [%]	Relative Error [%]				
			Number of Data Points				
			11	21	51	101	201
E_S, ℓ_{tr}, R_0	E_S	5	0.7	0.4	0.3	0.2	0.1
		10	1.5	0.8	0.6	0.4	0.3
		20	3.0	1.7	1.3	0.8	0.5
	ℓ_{tr}	5	1.1	1.1	1.1	1.2	1.2
		10	1.1	1.1	1.2	1.2	1.1
		20	1.2	1.1	1.1	1.1	1.2
	R_0	5	4.5	3.0	2.3	1.5	0.9
		10	9.4	6.6	4.7	3.0	2.3
		20	18.9	11.9	8.6	6.9	4.1

Table C.8: Fit parameter uncertainty determined by 324 Monte Carlo simulations of typical Nb$_3$Sn material properties. Values are the distribution's standard deviations divided by the actual parameter value. Values for ℓ_{tr}, include an additional $\approx$ 0.5% accounting for the difference between the distribution's mean and the actual value of ℓ_{tr}.
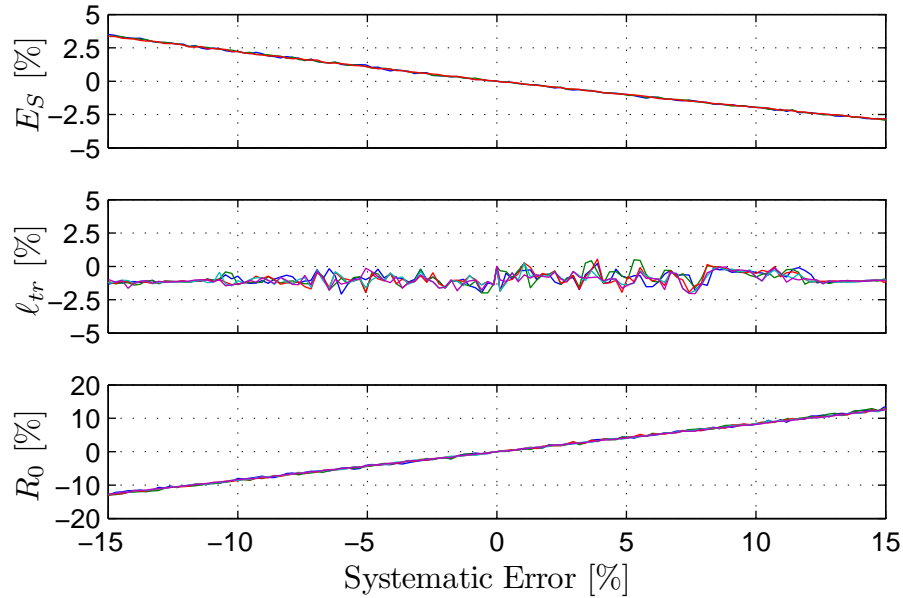
Figure C.16: Relative error in E_S, ℓ_{tr} and R_0 vs systematic error for typical Nb$_3$Sn material parameters.

C.4 Multiple Region Fitting

Section C.3 demonstrated that there is sloppiness in T_c and E_S when fitting R_s vs temperature data. It is possible, however, to gain confidence in T_c by fitting penetration depth, $\lambda(T)$, as function of temperature. This either reduce the number of free parameters in the model or give more confidence in determining T_c, and leads to lower uncertainties in the remaining parameters. From the two-fluid model, [Bar58] one can approximate the temperature dependent penetration depth as

$$\lambda(T) = \lambda_L \sqrt{\frac{1 + \frac{\xi}{\ell}}{1 - \left(\frac{T}{T_c}\right)^4}} - \lambda(T_0) \tag{C.11}$$

where ξ is the coherence length taking into account the electronic mean free path ℓ, and $\lambda(T_0)$ is a fit parameter that sets the penetration depth at a given temperature T_0 (usually around 6-7 K). [Cio05]

The $\lambda(T)$ vs T measurement is performed by tracking the resonant frequency, $f(T)$, of the cavity at a range of temperatures–preferably close to T_c. The penetration depth is then given by the relation

$$\lambda(T) - \lambda(T_0) = \frac{1}{\beta} \left[f(T) - f(T_0) \right], \tag{C.12}$$

where β is a constant dependent on the geometry of the cavity. [Hal70a] Liepe gives the value for the proportionality constant as

$$\beta = \frac{\pi \mu_0 f(T_0)^2}{2G}, \tag{C.13}$$

where G is the geometry factor of the cavity and μ_0 is the permeability of free space. [Lie01] For the ERL 7-cell cavity, with $G = 270$ Ω, typically $\beta \approx 12.4$ kHz/μm. [She, GL13]

Because $\lambda(T)$ is sensitive to the critical temperature, it can be measured accurately by noting the frequency shift near T_c. When data is available, it can be used in combination with R_s data to determine a material's SRF parameters more accurately. This is carried out by applying the algorithm in section C.2 twice–once for R_s and once for $\lambda(T)$–and finding parameters that minimize the weighted sum of both fit's χ^2. The algorithm performing the simultaneous optimization is presented below.

```
1  function sol_array = ...
2          optimize_rs_and_xd(param_array, dat_rs, dat_xd, varargin)
3
4      Tc =          param_array{1,2};
5      EnGap =       param_array{2,2};
6      lonDepth =    param_array{3,2};
7      cohLength=    param_array{4,2};
8      RRR =         param_array{5,2};
9      R0   =        param_array{6,2};
10     lambda_0 =    param_array{7,2};
11
12         % Default weights
13         weight.RS = 1;
14         weight.XD = 1;
15
16     if ~isempty(varargin) && size(varargin,2)==2
17                 weight.RS = varargin{1};
18                 weight.XD = varargin{2};
19     end
20
21     % Run an optimization
22     guess = [ EnGap; RRR; R0; lambda_0 ];
23     [results, final_RSS] = fminsearch(@compute_rss, guess);
24
25     % Put the results into a solution array
26     sol_array = param_array;
27     sol_array{2,2} = results(1);
28     sol_array{5,2} = results(2);
29     sol_array{6,2} = results(3);
30     sol_array{7,2} = results(4);
31     sol_array{8,3} = final_RSS;
32
33     function rss = compute_rss(x)
34         p_array = {...
35             'Tc',         Tc,          'fix';
36             'EnGap',      x(1),        'fix';
37             'lonDepth',   lonDepth,    'fix';
38             'cohLength',  cohLength,   'fix';
39             'RRR',        x(2),        'fix';
```

```
40              'R0',         x(3),          'fix';
41              'Lambda_0', x(4),          'fix';
42              };
43
44          sol_RS = polymorphic_BCS_fit(dat_rs, p_array, 'RS');
45          sol_XD = polymorphic_BCS_fit(dat_xd, p_array, 'XD');
46
47          % Compute a weighting of the two RSS's. (Minimize this)
48          rss = sol_RS{8,3}*weight.RS + sol_XD{8,3}*weight.XD;
49      end
50  end
```

In addition to allowing T_c to be determined accurately, fitting penetration depth near T_c also has been used to determine ℓ_{tr} more accurately than with surface resistance data alone. [GL13, GLG13]

C.5 Conclusion

A superconductor's parameters can be extracted from either R_s vs temperature or $\lambda(T)$ vs temperature data using the fitting algorithms discussed in this appendix. The statistically predicted confidence intervals are too small to include the actual values used to generate validation data. To obtain more accurate confidence intervals, Monte Carlo simulations were performed, and it was demonstrated that for typical measurements (11–51 data points, taken between 1.4 and 4.2 K, with approximately 10% systematic error and 10% random error), the relative uncertainty of the estimated parameters are less than 20%, with the exception of ℓ_{tr} which can have uncertainty of over 80%.

When fitting T_c, E_S, ℓ_{tr} and R_0, at the same time, the electronic mean free path tends to be obtained with poor accuracy. This method should not be used except for cases when there is no prior knowledge of the SRF parameters of the

material, which is seldom the case.

For niobium, more precise results are obtained by only fitting two parameters at a time. Whenever possible, as broad a temperature range as possible should be used. Even greater precision is achievable when both penetration depth data and surface resistance are fit simultaneously.

BIBLIOGRAPHY

[Aad12]   Aad, G et al. Observation of a new particle in the search for the standard model Higgs boson with the ATLAS detector at the LHC. *Physics Letters B*, 716(1):1 – 29, 2012.

[ABB+00]   B. Aune, R. Bandelmann, D. Bloess, B. Bonin, A. Bosotti, M. Champion, C. Crawford, G. Deppe, B. Dwersteg, D. A. Edwards, H. T. Edwards, M. Ferrario, M. Fouaidy, P.-D. Gall, A. Gamp, A. Gössel, J. Graber, D. Hubert, M. Hüning, M. Juillard, T. Junquera, H. Kaiser, G. Kreps, M. Kuchnir, R. Lange, M. Leenen, M. Liepe, L. Lilje, A. Matheisen, W.-D. Möller, A. Mosnier, H. Padamsee, C. Pagani, M. Pekeler, H.-B. Peters, O. Peters, D. Proch, K. Rehlich, D. Reschke, H. Safa, T. Schilcher, P. Schmüser, J. Sekutowicz, S. Simrock, W. Singer, M. Tigner, D. Trines, K. Twarowski, G. Weichert, J. Weisend, J. Wojtkiewicz, S. Wolff, and K. Zapfe. Superconducting tesla cavities. *Phys. Rev. ST Accel. Beams*, 3:092001, Sep 2000.

[Abr70]   Milton Abramowitz. *Handbook of mathematical functions : with formulas, graphs, and mathematical tables*. Dover Publications, New York, 1970.

[Adm13]   U.S. Energy Information Administration. Electric power annual 2011. Online, January 2013. http://www.eia.gov/electricity/annual/pdf/epa.pdf.

[Age99]   OECD Nuclear Energy Agency. *Utilisation and Reliability of High Power Proton Accelerators Workshop Proceedings, Aix-en-Provence, France, 22-24 November 1999*. OECD Publishing, Paris, November 1999.

[AKK12]   S. Aull, O. Kugeler, and J. Knobloch. Trapped magnetic flux in superconducting niobium samples. *Phys. Rev. ST Accel. Beams*, 15:062001, Jun 2012.

[Ash76]   Neil Ashcroft. *Solid state physics*. Holt, Rinehart and Winston, New York, 1976.

[Aue96]   Pertti Auerkari. *Mechanical and physical properties of engineering alumina ceramics*. VTT Technical Research Center of Finland, 1996.

[Bab01]   N. Baboi. *Studies on higher order modes in accelerating structures for linear colliders*. PhD thesis, Deutsches Elektronen-Synchrotron DESY, 2001.

[Bah98]   Marko Bahte. *Materialuntersuchungen an supraleitenden Niob-Proben mit Magnetisierungs- und Suszeptibilitätsmessungen*. PhD thesis, Universität Hamburg, March 1998.

[Bar58]   John Bardeen. Two-fluid model of superconductivity. *Phys. Rev. Lett.*, 1:399–400, Dec 1958.

[BBB+11]   I. V. Bazarov, S. A. Belomestnykh, D. H. Bilderback, M. G. Billing, J. D. Brock, B. W. Buckley, S. S. Chapman, E. P. Chojnacki, Z. A. Conway, J. A. Crittenden, D. Dale, J. A. Dobbins, B. M. Dunham, R. D. Ehrlich, M. P. Ehrlichman, K. D. Finkelstein, E. Fontes, M. J. Forster, S. W. Gray, S. Greenwald, S. M. Gruner, C. Gulliford, D. L. Hartill, R. G. Helmke, G. H. Hoffstaetter, A. Kazimirov, R. P. Kaplan, S. S. Karkare, V. O. Kostroun, F. A. Laham, Y. H. Lau, Y. Li, X. Liu, M. U. Liepe, F. Loehl, L. Cultrera, C. E. Mayes, J. M. Maxson, A. Meseck, A. A. Mikhailichenko, D. Ouzounov, H. S. Padamsee, S. B. Peck, M. A. Pfeifer, S. E. Posen, K. W. Smolenski, P. G. Quigley, P. Revesz, D. H. Rice, U. Sae-Ueng, D. C. Sagan, J. O. Sears, V. D. Shemelin, C. K. Sinclair, D. M. Smilgies, E. N. Smith, C. Spethmann, C. Song, T. Tanabe, A. B. Temnykh, M. Tigner, N. R. A. Valles, V. G. Veshcherevich, Z. Wang, A. R. Woll, Y. Xie, and Z. Zhao. Cornell Energy Recovery Linac Project Definition Design Report. Technical report, Cornell University, Mar 2011.

[BBD+10]   Donald H Bilderback, Joel D Brock, Darren S Dale, Kenneth D Finkelstein, Mark A Pfeifer, and Sol M Gruner. Energy recovery linac (erl) coherent hard x-ray sources. *New Journal of Physics*, 12(3):035011, 2010.

[BBD+12]   S. Baradaran, U. Bergmann, H. Durr, K. Gaffney, J. Goldstein, M. Geuhr, J. Hastings, P. Heimann, R. Lee, and M. Seibert. LCLS-II new instruments workshops report. Technical report, SLAC National Accelerator Laboratory, 2012.

[BCH+99]   D. Boussard, E. Chiaveri, E. Haebel, H.P. Kindermann, R. Losito, S. Marque, V. Rödel, and M. Stirbet. The LHC superconducting cavities. In *Proceedings of the 1999 Particle Accelerator Conference*, 1999.

[BCS57]   J. Bardeen, L. N. Cooper, and J. R. Schrieffer. Microscopic Theory of Superconductivity. *Physical Review*, 106:162–164, April 1957.

[BGK59]   P. A. Bezuglyi, A. A. Galkin, and A. P. Korolyuk. Anisotropy of the absorption coefficients of ultrasonics in superconductors. *SOVIET PHYSICS JETP-USSR*, 9(6):1388–1389, 1959.

[BH04]   I. V. Bazarov and G. Hoffstaetter. Multi-pass beam-breakup: Theory and calculation. In *Proceedings of EPAC04*, Lucerne/CH, 2004.

[BH07]   Brandon Buckley and Georg H. Hoffstaetter. Transverse emittance dilution due to coupler kicks in linear accelerators. *Phys. Rev. ST Accel. Beams*, 10:111002, Nov 2007.

[BHC+04]   K. S. Brown, C. C. Hill, G. A. Calero, C. R. Myers, K. H. Lee, J. P. Sethna, and R. A. Cerione. The statistical mechanics of complex signaling networks: nerve growth factor signaling. *Physical Biology*, 1(3):184, 2004.

[BLP+01]   S. L. Bud'ko, G. Lapertot, C. Petrovic, C. E. Cunningham, N. Anderson, and P. C. Canfield. Boron isotope effect in superconducting MgB$_2$. *Phys. Rev. Lett.*, 86:1877–1880, Feb 2001.

[Bra95]   E. H. Brandt. The flux-line lattice in superconductors. *Reports on Progress in Physics*, 58(11):1465, 1995.

[Bro61]   R. F. Broom. An Upper limit for the Resistivity of a Superconducting Film. *Nature*, 190:992–993, June 1961.

[BS05]   Egor Babaev and Martin Speight. Semi-Meissner state and neither Type-I nor Type-II superconductivity in multicomponent superconductors. *Phys. Rev. B*, 72:180502, Nov 2005.

[CA99]   E. Chojnacki and W. J. Alton. Beamline RF load development at Cornell. In *Proceedings of the 1999 Particle Accelerator Conference*, volume 2, pages 845–847. IEEE, 1999.

[Cam87]   Isodoro E. Campisi. On the Limiting RF Fields in Superconducting Accelerator Cavities. *SLAC AP-58*, 1987.

[Car11]   P. Carriere. Operating notes for BCP of dumbbells. CLASSE Notes, 2011.

[CBJP11]   C Cooper, B Bullock, S Joshi, and A Palczewski. Centrifugal barrel polishing of cavities worldwide. In *15th International Conference on RF Superconductivity, Chicago, IL*, 2011.

[CF84]   I. E. Campisi and Z. D. Farkas. High-Gradient, Pulsed Operation of Superconducting Niobium Cavities. *SLAC AP-16*, 1984.

[Cha99]   Alex Chao. *Handbook of accelerator physics and engineering*. World Scientific, Singapore River Edge, N.J, 1999.

[Chi94]   Yong Ho Chin. User's guide for ABCI version 8.7 (Azimuthal beam cavity interaction). 1994.

[Cho09]   E. Chojnacki. Personal Communication, 2009.

[Cho10]   E. Chojnacki. RF absorber studies at Cornell, including DC conductivity, part 2. Proceedings of 2010 Higher-Order Mode Workshop, Oct 2010.

[CHPS09] Z. A. Conway, D. H. Hartill, H. Padamsee, and E. N. Smith. Defect Location in Superconducting Cavities Cooled with He-II Using Oscillating Superleak Transducers. In *Proceedings of the 2009 Particle Accelerator Conference*, 2009.

[Cio05]   G. Ciovati. *Investigation of the superconducting properties of niobium radio-frequency cavities*. PhD thesis, Old Dominion University, 2005.

[Cio07]   G. Ciovati. Review of high field Q-slope, cavity measurements. In *13th International Workshop on RF Superconductivity*, 2007.

[CKK⁺05] S. Casalbuoni, E.A. Knabbe, J. Ktzler, L. Lilje, L. von Sawilski, P. Schmser, and B. Steffen. Surface superconductivity in niobium for superconducting {RF} cavities. *Nuclear Instruments and Methods in Physics Research Section A: Accelerators, Spectrometers, Detectors and Associated Equipment*, 538(13):45 – 64, 2005.

[Coo56]   L. N. Cooper. Bound Electron Pairs in a Degenerate Fermi Gas. *Physical Review*, 104:1189–1190, November 1956.

[Coo06]   CoorsTek Inc. *CoorsTek Silicon Carbide: Material Properties*, 2006.

[Cra46]   Harald Cramér. *Mathematical methods of statistics*. Princeton University Press, Princeton, 1946.

[CS08]   G. Catelani and James P. Sethna. Temperature dependence of the superheating field for superconductors in the high-κ london limit. *Phys. Rev. B*, 78:224509, Dec 2008.

[DB98]   R. J. Donnelly and C. F. Barenghi. The Observed Properties of Liquid Helium at the Saturated Vapor Pressure. *Journal of Physical and Chemical Reference Data*, 27:1217–1274, November 1998.

[DDBD96]   Andrew J. Dolgert, S. John Di Bartolo, and Alan T. Dorsey. Superheating fields of superconductors: Asymptotic analysis and numerical results. *Phys. Rev. B*, 53:5650–5660, Mar 1996.

[DEG+94]   S. Doebert, R. Eichhorn, H. Genz, H.-D. Graef, R. Hahn, T. Hampel, J. Horn, C. Luettge, H. Loos, K. Ruehl, M. Reichenbach, A. Richter, P. Schardt, V. Schlott, G. Schrieder, E. Spamer, A. Stascheck, A. Stiller, M. Thomas, O. Titze, T. Wesp, and M. Wiencken. Status of the S-DALINAC and experimental developments. In *The Fourth European Particle Accelerator Conference*, 1994.

[DEM+87]   B. Dwersteg, W. Ebeling, W.-D. Moller, D. Renken, D. Proch, J. Sekutowicz, J. Susta, and D. Tong. Superconducting cavities for HERA. In *Proceedings of The Third Workshop on RF Superconductivity*, 1987.

[DeS63]   Warren DeSorbo. Effect of dissolved gases on some superconducting properties of niobium. *Phys. Rev.*, 132(1):107–121, Oct 1963.

[dG65]   P. G. de Gennes. Vortex nucleation in type II superconductors. *Solid State Communications*, 3(6):127 – 130, 1965.

[DG67]   R. Doll and P. Graf. Superheating in cylinders of pure superconducting tin. *Phys. Rev. Lett.*, 19(16):897–899, Oct 1967.

[DGB+11]   D. Dale, S. M. Gruner, J. Brock, D. Bilderback, and E. Fontes. Science at the hard x-ray diffraction limit (xdl2011), part 1. *Synchrotron Radiation News*, 24(6):4–11, 2011.

[DIPK91]   M. Dzenus, K. Iversen, M. Peiniger, and D. Kiehlmann. Produc-

tion of superconducting niobium cavities for cebaf. In *Proceedings of the 1991 Particle Accelerator Conference*, pages 2390–2392 vol.4, 1991.

[DKM01]   B. Dwersteg, D. Kostin, and W. D. Moeller. TESLA RF power couplers development at DESY. In *Proc. of the 10th Workshop on RF Superconductivity, Tsukuba, Japan*, 2001.

[DMM⁺95]   D. Dwersteg, A. Matheisen, W. D. Möller, D. Proch, D. Renken, and J. Sekutowicz. Operating experience with superconducting cavities in the HERA e-ring. In *Proceedings of the 1995 Workshop on RF Superconductivity*, 1995.

[EB64]   F. Englert and R. Brout. Broken symmetry and the mass of gauge vector mesons. *Phys. Rev. Lett.*, 13:321–323, Aug 1964.

[ECC97]   Pascal Elleaume, Oleg Chubar, and Joel Chavanne. Computing 3D magnetic fields from insertion devices. In *Proceedings of the 1997 Particle Accelerator Conference*, volume 3, pages 3509–3511. IEEE, 1997.

[ECH⁺13]   R. Eichhorn, J. Conway, Y. He, G. Hoffstaetter, Y. Li, M. Liepe, T. O'Connell, P. Quigley, J. Sears, V.D. Shemelin, and N. Valles. Cornell's HOM beamline absorbers. In *Proceedings of IPAC 2013*, 2013.

[Eds12]   Alexander Edström. Non-pairwise vortex interactions in ginzburg-landau theory of superconductivity. Master's thesis, KTH, 2012.

[Eil68]   G. Eilenberger. Transformation of Gorkov's equation for type II superconductors into transport-like equations. *Zeitschrift für Physik*, 214(2):195–213, 1968.

[Eis54]   Julian Eisenstein. Superconducting elements. *Rev. Mod. Phys.*, 26:277–291, Jul 1954.

[Emm09]   Paul Emma. First lasing of the LCLS X-ray FEL at 1.5 A. *Proceedings of PAC09*, 2009.

[EP06]   G. Eremeev and H. Padamsee. Change in high field Q-slope by baking and anodizing. *Physica C: Superconductivity*, 441(12):62 –

65, 2006. Proceedings of the 12th International Workshop on RF Superconductivity.

[ES93]   D. A. Edwards and M. J. Syphers. *An introduction to the physics of high energy accelerators*. Wiley, New York, 1993.

[Far84]   Z. D. Farkas. Low Loss Pulsed Mode Cavity Behavior. *SLAC AP-15*, 1984.

[Far98]   S. Fartuokh. A new method to detect the high impedance modes of TESLA cavities. Technical report, CEA/DAPNIA/SEA, 1998.

[Fre68]   R.A. French. Intrinsic type-2 superconductivity in pure niobium. *Cryogenics*, 8(5):301 – 308, 1968.

[FSS66]   D. K. Finnemore, T. F. Stromberg, and C. A. Swenson. Superconducting properties of high-purity niobium. *Phys. Rev.*, 149(1):231–243, Sep 1966.

[GCPS05]   R.L. Geng, C. Crawford, H. Padamsee, and A. Seaman. Vertical electropolishing niobium cavities. In *The 12th International Workshop on RF Superconductivity*, 2005.

[GÉ68]   L. P. Gor'kov and G. M. Éliashberg. Generalization of the Ginzburg-Landau Equations for Non-stationary Problems in the Case of Alloys with Paramagnetic Impurities. *Soviet Journal of Experimental and Theoretical Physics*, 27:328–+, August 1968.

[GEPS07]   R. L. Geng, G. V. Eremeev, H. Padamsee, and V. D. Shemelin. High gradient studies for ILC with single-cell re-entrant shape and elliptical shape cavities made of fine-grain and large-grain niobium. In *Proceedings of PAC07*, 2007.

[GHK64]   G. S. Guralnik, C. R. Hagen, and T. W. B. Kibble. Global conservation laws and massless particles. *Phys. Rev. Lett.*, 13:585–587, Nov 1964.

[GI94]   F.A. Graybill and H.K. Iyer. *Regression analysis: concepts and applications*. An Alexander Kugushev book. Duxbury Press, 1994.

[GL50]   V. L Ginsburg and L. Landau. *Zh. Eksp. Teor. Fiz.*, 20, 1950.

273

[GL13]   D. Gonnella and M. Liepe. High Q_0 studies at Cornell. In *Proceedings of the 16th conference on RF Superconductivity*, 2013.

[GLG13]   D. Gonnella, M. Liepe, and A. Grassellino.   Performance of a FNAL treated superconducting niobium cavity at Cornell. In *Proceedings of the 16th conference on RF Superconductivity*, 2013.

[Gol97]   D. A. Goldberg. Understanding the mixing of higher-order modes of multiply resonant systems. Technical Report LBL Report-39618, Lawrence Berkeley National Laboratory, 1 Cyclotron Road, Berkeley, California 94720, 1997.

[Gol13]   Dan Goldman. Measuring HOM properties in the HTC using multiple methods. August 2013.

[Gor59]   L.P. Gor'kov.   Microscopic derivation of the Ginzburg-Landau equations in the theory of superconductivity. *SOVIET PHYSICS JETP-USSR*, 9(6):1364–1367, 1959.

[GR03]   E. L. Garwin and M. Rabinowitz.   Resistivity Ratio of Niobium Superconducting Cavities. *eprint arXiv:cond-mat/0308266*, August 2003.

[GVL12]   D. Gonnella, N. Valles, and M. Liepe. Automated cavity test suite for Cornell's ERL program.   In *Proceedings of IPAC2012*, pages 2372–2374, 2012.

[HA63]   J. L Harden and V. Arp. The lower critical field in the ginzburg-landau theory of superconductivity. *Cryogenics*, 3(2):105 – 108, 1963.

[Hal79]   E. H. Hall. On a new action of the magnet on electric currents. *American Journal of Mathematics*, 2(3):pp. 287–292, 1879.

[Hal70a]   J. Halbritter. Change of eigenstate in a superconducting RF cavity due to a nonlinear response. *Journal of Applied Physics*, 41(11):4581–4588, 1970.

[Hal70b]   J. Halbritter. Fortran-program for the computation of the surface impedance of superconductors.   *KAROLA - OA-Volltextserver des Forschungszentrums Karlsruhe [http://opac.fzk.de:81/oai/oai-2.0.cmp.S] (Germany)*, 1970.

[Har13]   Michael Hartl.   The   tau   manifesto.   Online:
           http://tauday.com/tau-manifesto.pdf, June 2013.

[Haz88]   Michiel Hazewinkel. *Encyclopaedia of mathematics : an updated and
           annotated translation of the Soviet Mathematical encyclopaedia*. Reidel
           Sold and distributed in the U.S.A. and Canada by Kluwer Aca-
           demic Publishers, Dordrecht Boston Norwell, MA, U.S.A, 1988.

[HB04]   Georg H. Hoffstaetter and Ivan V. Bazarov. Beam-breakup insta-
           bility theory for energy recovery linacs. *Phys. Rev. ST Accel. Beams*,
           7:054401, May 2004.

[HBS07]   Georg H. Hoffstaetter, Ivan V. Bazarov, and Changsheng Song. Re-
           circulating beam-breakup thresholds for polarized higher-order
           modes with optical coupling. *Phys. Rev. ST Accel. Beams*, 10:044401,
           Apr 2007.

[Hei99]   Matthias Hein. *High-temperature superconducting thin films at mi-
           crowave frequencies*. Springer, Berlin New York, 1999.

[Hig64]   Peter W. Higgs.   Broken symmetries and the masses of gauge
           bosons. *Phys. Rev. Lett.*, 13:508–509, Oct 1964.

[Hoc13]   A Hocker. High Q_0 preservation. In *Tesla Technology Collaboration
           on CW SRF*, 2013.

[HP95]   T. Hays and H. S. Padamsee. Determining H_c^{RF} for Nb and Nb_3Sn
           through HPP and Transient Q Analysis. In *7th Workshop on RF
           Superconductivity*, 1995.

[HPR95]   T. Hays, H. S. Padamsee, and R. W. Roth. Response of supercon-
           ducting cavities to high peak power. In *Proceedings of the 1995 U.S.
           Particle Accelerator Conference*, 1995.

[IBM]   IBM Corporation. Parameter estimates and standard errors (non-
           linear regression algorithms). Online.

[Jac98]   John D. Jackson. *Classical Electrodynamics Third Edition*. Wiley,
           third edition, August 1998.

[Kay93]   Steven Kay. *Fundamentals of statistical signal processing*. Prentice-
           Hall PTR, Englewood Cliffs, N.J, 1993.

[KCG+10]   Kwok K., Arno Candel, Lixin Ge, Andreas Kabel, Rich Lee, Zeng-
           hai Li, Cho Ng, Vineet Rawat, and Greg Schussman. Advances in
           parallel electromagnetic codes for accelerator science and devel-
           opment. Technical Report 14349, SLAC, 2010.

[KCG+12]   M. P. Kelly, Z. A. Conway, S. M. Gerbick, M. Kedzie, T. C. Reid,
           R. C. Murphy, and P. N. Ostroumov. Cold testing of supercon-
           ducting 72 MHz cavities for ATLAS. In *Proceedings of LINAC 2012*,
           Tel-Aviv Israel, 2012.

[Kit63]   Charles Kittel. *Quantum theory of solids*. Wiley, New York, 1963.

[Kit86]   Charles Kittel. *Introduction to Solid State Physics*. Wiley, 1986.

[KK35]   W.H. Keesom and A.P. Keesom. New measurements on the spe-
           cific heat of liquid helium. *Physica*, 2(112):557 – 572, 1935.

[KMC+05]   P. Kneisel, G.R. Myneni, G. Ciovati, J. Sekutowicz, and T. Carneiro.
           Performance of large grain and single crystal niobium cavities. In
           Proceedings of the 12th Workshop on RF Superconductivity, 2005.

[KNV+09]   O. Kugeler, A. Neumann, S. Voronenko, W. Anders, J. Knobloch,
           M. Schuster, A. Frahm, S. Klauke, D. Pflückhahn, and S. Rotter-
           dam. Manipulating the intrinsic quality factor by thermal cycling
           and magnetic fields. In *14th International Conference on RF Super-
           conductivity*, 2009.

[KP97]   J. Knobloch and H. Padamsee. Flux trapping in niobium cavities
           during breakdown events. In *Proceedings of SRF 1997*, 1997.

[KSS67]   MM Karliner, VE Shapiro, and IA Shekhtman. Instability in the
           walls of a cavity due to ponderomotive forces of the electromag-
           netic field. *Sov. Phys. Tech. Phys*, 11, 1967.

[Lak13]   Lake Shore Cryotronics, Inc. Hall (magnetic) sensor speci-
           fications. Online, http://www.lakeshore.com/products/Hall-
           Magnetic-Sensors/Pages/Specifications.aspx, 2013.

[Lan65]   L.D. Landau. Collected papers of L. D. Landau. page 546. Gordon
           and Breach, 1965.

[Lev44]   K. Levenberg. A method for the solution of certain non-linear

problems in least squares. *Quarterly of Applied Mathematics*, 2(2):164–168, July 1944.

[LF99]   Pao Lu and Joseph P Foy. Calculation of first sound speed in liquid helium. *Chinese Physics Letters*, 16(4):276, 1999.

[LFF47]   C. T. Lane, Henry A. Fairbank, and William M. Fairbank. Second Sound in Liquid Helium II. *Phys. Rev.*, 71:600–605, May 1947.

[Lie01]   Matthias U. Liepe. *Superconducting Multicell Cavities for Linear Colliders*. PhD thesis, Universität Hamburg, October 2001.

[LK06]   M. Liepe and J. Knobloch. Superconducting RF for energy-recovery linacs. *Nuclear Instruments and Methods in Physics Research A*, 557:354–369, February 2006.

[LL35]   F. London and H. London. The electromagnetic equations of the supraconductor. *Proceedings of the Royal Society of London. Series A, Mathematical and Physical Sciences*, 149(866):pp. 71–88, 1935.

[LLNK09]   L. Lee, Z. Li, C. Ng, and K. Ko. Omega3P: A parallel finite-element eigenmode analysis code for accelerator cavities. Technical Report SLAC-PUB-13529, SLAC National Accelerator Laboratory, 2575 Sand Hill Road, Menlo Park, CA 94025, February 2009.

[M+99]   W. D. Moeller et al. High power coupler for the tesla test facility. In *9th Workshop on RF Superconductivity*, page 577, 1999.

[May09]   C. Mayes. *Energy Recovery Linear Accelerator Lattice Design and Coherent Synchrotron Radiation*. PhD thesis, Cornell University, 2009.

[May11]   C. Mayes. Personal Communication, 2011.

[MB57]   R. W. Morse and H. V. Bohm. Superconducting energy gap from ultrasonic attenuation measurements. *Phys. Rev.*, 108:1094–1096, Nov 1957.

[MCD+90]   A. Mosnier, S. Chel, M. Desmons, B. Hervieu, M. Maurier, B. Phung Ngoc, and A. Veyssiere. MACSE superconducting cavity RF drive system. In *Proceedings of EPAC 1990*, 1990.

[MDK03]   Lia Merminga, David R. Douglas, and Geoffrey A. Krafft. High-current energy-recovering electron linacs. *Annual Review of Nuclear and Particle Science*, 53(1):387–429, 2003.

[Mer68]   J. R. Merrill. Type II Superconductivity Experiment. *American Journal of Physics*, 36:133–136, February 1968.

[MGC63]   B. T. Matthias, T. H. Geballe, and V. B. Compton. Superconductivity. *Rev. Mod. Phys.*, 35:1–22, Jan 1963.

[Mil86]   R.H. Miller. Comparison of standing-wave and traveling-wave structures. In *Linear accelerator conference*, Stanford, CA, USA, June 1986.

[Mit91]   S. Mitsunobu. Superconducting RF activities at KEK. In *Proceedings of SRF 1991*, 1991.

[MK05]   G. R. Myneni and P. Kneisel. Springback in deep drawn high purity niobium for superconductor cavities. In *Materials Science & Technology*, 2005.

[MO33]   W. Meissner and R. Ochsenfeld. Ein neuer effekt bei eintritt der supraleitfhigkeit. *Naturwissenschaften*, 21(44):787–788, 1933.

[Mos89]   A. Mosnier. Developments of HOM couplers for superconducting cavities. In *4th Workshop on RF Superconductivity*, 1989.

[MS67]   J. Matricon and D. Saint-James. Superheating fields in superconductors. *Physics Letters A*, 24:241–242, February 1967.

[MS69]   R. Meservey and B. B. Schwartz. Equilibrium properties: Comparison of experimental results with predictions of the BCS theory. In R. D. Parks, editor, *Superconductivity, Volume 1*, pages 117–191. Marcel Dekker, 1969.

[MT01]   G Materlik and Th. (Editors) Tschentscher. Tesla technical design report. part v. Technical report, 2001.

[MY99]   D.G. Myakishev and V. P. Yakovlev. CLANS2 - a code for calculation of multipole modes in axisymmetric cavities with absorber ferrites. In *Proceedings of PAC 1999*, pages 2775–2777, 1999.

[Myn07]   Ganapati Rao Myneni. Physical and mechanical properties of niobium for SRF science and technology. *AIP Conference Proceedings*, 927(1):41–47, 2007.

[Nat]   National Energy Research Scientific Computing Center (NERSC). Office of Science and U.S. Department of Energy. Contract No. DE-AC02-05CH11231.

[NM75]   V. Novotny and P.P.M. Meincke. Single superconducting energy gap in pure niobium. *Journal of Low Temperature Physics*, 18(1-2):147–157, 1975.

[Nob13a]   Nobel Media AB. Heike Kamerlingh Onnes - Biographical. Web, September 2013.

[Nob13b]   Nobel Media AB. The Nobel Prize in Physics 2013. Web, November 2013.

[OMFB79]   T. P. Orlando, E. J. McNiff, S. Foner, and M. R. Beasley. Critical fields, pauli paramagnetic limiting, and material parameters of Nb_3sn and V_3Si. *Phys. Rev. B*, 19:4545–4561, May 1979.

[Onn]   H. Kamerlingh Onnes. Research Notebooks 56, 57. Kamerlingh Onnes Archive, Boerhaave Museum, Leiden, the Netherlands.

[Onn11]   H. Kamerlingh Onnes. Further experiments with liquid helium. d. on the change of the electrical resistance of pure metals at very low temperatures, etc. v. the disappearance of the resistance of mercury. In Jonhannes Müller, editor, *Royal Netherlands Academy of Arts and Sciences (KNAW)*, volume 14, pages 113–115, May 1911.

[OSB+12]   J. F. Ostiguy, N. Solyak, P. Berrutti, J. P. Carneiro, V. Lebedev, S. Nagaitsev, A. Saini, B. Stheynas, and V. P. Yakovlev. Status of the Project-X CW linac design. In *Proceedings of IPAC 2012*, 2012.

[PA98]   Paul J. Petersan and Steven M. Anlage. Measurement of resonant frequency and quality factor of microwave resonators: Comparison of methods. *Journal of Applied Physics*, 84(6):3392–3402, 1998.

[Pad09]   H. Padamsee. *RF Superconductivity: Volume II: Science, Technology and Applications*. Rf Superconductivity. Wiley, 2009.

[Pal01]   Robert Palais. π is wrong! *The Mathematical Intelligencer*, 23(3):7–8, 2001.

[Pan05]   High Energy Physics Advisory Panel. Discovering the quantum universe. Technical report, United States Department of Energy and the National Science Foundation, 2005.

[PCL$^+$13] S. Posen, G. Catelani, M. U. Liepe, J. P. Sethna, and M. K. Transtrum. Theoretical Field Limits for Multi-Layer Superconductors. *ArXiv e-prints*, September 2013.

[Per66]   John M. Perz. Attenuation of ultrasonic waves of arbitrary polarization and propagation direction in superconductors. *Canadian Journal of Physics*, 44(8):1765–1779, 1966.

[Pip53]   A. B. Pippard. An experimental and theoretical study of the relation between magnetic field and current in a superconductor. *Proceedings of the Royal Society of London. Series A. Mathematical and Physical Sciences*, 216(1127):547–568, 1953.

[PKH98]   H. Padamsee, J. Knobloch, and T. Hays. *RF superconductivity for accelerators*. Wiley, New York, 1998.

[PL11]   S. Posen and M. Liepe. Stochiometric nb$_3$sn in first samples coated at Cornell. In *15th International Conference on RF Superconductivity*, 2011.

[PL12a]   S. Posen and M. Liepe. Measurement of the mechanical properties of superconducting cavities during operation. In *Proceedings of IPAC 2012*, 2012.

[PL12b]   S. Posen and M. Liepe. Mechanical designs of SRF cavities for cw operation - df/dp and stiffening rings theory and measurement. In *Proceedings of IPAC 2012*, 2012.

[PL12c]   S. Posen and M. Liepe. Minimizing helium pressure sensitivity in elliptical srf cavities. In *Proceedings of IPAC2012*, 2012.

[Poo99]   Charles P. Poole. *Handbook of Superconductivity*. Academic Press, 1999.

[Pos]   S. Posen. Personal Communication.

[Pos13a]   S. Posen. First cavity results from the Cornell SRF group's Nb$_3$Sn program. In *Proceedings of NA-PAC 2013*, 2013.

[Pos13b]   S. Posen. SRF cavities beyond niobium: Potential and challenges. In *Proceedings of NA-PAC 2013*, 2013.

[Poz05]   D.M. Pozar. *Microwave Engineering*. Wiley, third edition, 2005.

[PW56]   W. K. H. Panofsky and W. A. Wenzel. Some Considerations Concerning the Transverse Deflection of Charged Particles in Radio-Frequency Fields. *Review of Scientific Instruments*, 27:967, November 1956.

[RAB+95]   T. Raubenheimer, C. Adolphsen, D. Burke, P. Chen, S. Ecklund, J. Irwin, G. Loew, T. Markiewicz, R. Miller, E. Paterson, N. Phinney, M. Ross, R. Ruth, J. Sheppard, H. Tang, K. Thompson, and P. Wilson. Parameters of the SLAC Next Linear Collider. In *Particle Accelerator Conference, 1995., Proceedings of the 1995*, volume 2, pages 698–700 vol.2, 1995.

[RAG+11]   D Reschke, S Aderhold, A Gössel, J Iversen, S Karstensen, D Kostin, G Kreps, A Matheisen, WD Möller, F Schlander, et al. Results on large grain nine-cell cavities at DESY: Gradients up to 45 MV/m after electropolishing. In *15th International Conference on RF Superconductivity*, pages 490–494, 2011.

[Rao09]   Singiresu Rao. *Engineering optimization theory and practice*. John Wiley & Sons, Hoboken, N.J, 2009.

[RGBO13]   A. Romanenko, A. Grassellino, F. Barkov, and J. P. Ozelis. Effect of mild baking on superconducting niobium cavities investigated by sequential nanoremoval. *Phys. Rev. ST Accel. Beams*, 16:012001, Jan 2013.

[ROGP12]   A. Romanenko, J. P. Ozelis, A. Grassellino, and H. Padamsee. Depth distribution of losses in superconducting niobium cavities. In *Proceedings of IPAC2012*, 2012.

[Roh04]   James William Rohlf. *Modern physics from α to Z^0*. Wiley, 2004.

[RR67]   J.C. Renard and Y.A. Rocher. Superheating in pure superconducting niobium. *Physics Letters A*, 24(10):509 – 511, 1967.

[RS39]   B.V. Rollin and F. Simon. On the "film" phenomenon of liquid helium II. *Physica*, 6(2):219 – 230, 1939.

[SAB⁺79]   F. Steglich, J. Aarts, C. D. Bredl, W. Lieke, D. Meschede, W. Franz, and H. Schäfer. Superconductivity in the presence of strong pauli paramagnetism: $CeCu_2Si_2$. *Phys. Rev. Lett.*, 43:1892–1896, Dec 1979.

[SAE⁺13]   T. Saeki, Y. Ajima, K. Enami, H. Hayano, H. Inoue, E. Kako, S. Kato, S. Koike, T. Kubo, S. Noguchi, M. Satoh, M. Sawabe, T. Shishido, A. Terashima, N. Toge, K. Ueno, K. Umemori, K. Watanabe, Y. Watanabe, S. Yamaguchi, A. Yamamoto, Y. Yamamoto, M. Yamanaka, K. Yokoya, Y. Iwashita, F. Yasuda, N. Kawabata, H. Nakamura, K. Nohara, and M. Shinohara. Study on fabrication of superconducting RF 9-cell cavity for ILC at KEK. In *Proceedings of the 2013 International Particle Accelerator Conference*, 2013.

[Sag06]   D. Sagan. Bmad: A relativistic charged particle simulation library. *Nuclear Instruments and Methods in Physics Research A*, 558:356–359, March 2006.

[SB10]   V. Shemelin and S. Belomestnykh. Using a resistive material for HOM damping. In *Proceedings of IPAC 2010*, 2010.

[SBC70]   F.W. Smith, A. Baratoff, and M. Cardona. Superheating, supercooling, surface superconductivity and ginzburg-landau parameters of pure type-i superconductors and their alloys. *Physik der kondensierten Materie*, 12(2):145–192, 1970.

[SBG⁺03]   V. Shemelin, S. Belomestnykh, R. L. Geng, M. Liepe, and H. Padamsee. Dipole-mode free and kick-free 2-cell cavity for the SC ERL injector. In *Proceedings of PAC 2003*, 2003.

[SC12]   V. Shemelin and P. Carriere. Frequency control in the process of a multicell superconducting cavity production. *Review of Scientific Instruments*, 83(4):043304, 2012.

[Sch92]   P. Schmüser. Tuning of multi-cell cavities using bead pull measurements. Technical report, DESY, 1992. SRF920925-10.

[Sch11]   M. Schuh. *Study of Higher Order Modes in Superconducting Acceler-*

ating Structures for Linac Applications. PhD thesis, Ruperto-Carola University of Heidelberg, Germany, June 2011.

[Sek12]   J. K. Sekutowicz. Superconducting elliptical cavities. *ArXiv e-prints*, January 2012.

[SH06]   Changsheng Song and Georg H Hoffstaetter. Longitudinal bbu threshold current in recirculating linacs. Technical report, Cornell University, 2006. http://www.lepp.cornell.edu/~hoff/hoff/papers/ERL06-04.pdf.

[SH07]   Changsheng Song and Georg H Hoffstaetter. Transverse quadrupole bbu threshold current in the cornell x-ray erl. Technical report, Cornell University, 2007. http://www.lepp.cornell.edu/~hoff/hoff/papers/ERL06-04.pdf.

[She]   V. Shemelin. Personal Communication.

[She09a]   V. Shemelin. Comparison of shape of multicell cavity cells. In *14th International Conference on RF Superconductivity*, 2009.

[She09b]   V. D. Shemelin. Suppression of HOMs in a multicell superconducting cavity for Cornell's ERL. In *14th International Conference on RF Superconductivity*, 2009.

[She11]   Valery Shemelin. Corrections of a superconducting cavity shape due to etching, cooling down, and tuning. In *15th International Conference on RF Superconductivity*, volume 10, page 1, 2011.

[Sin12]   W. Singer. Superconducting 1.3 GHz Cavities for European XFEL. In *The XXIII Russian Particle Accelerator Conference*, 2012.

[SKG⁺05]   Jacek Sekutowicz, K Ko, L Ge, L Lee, Zenghai Li, C Ng, G Schussman, Liling Xiao, I Gonin, T Khabibouline, et al. Design of a low loss srf cavity for the ilc. In *Particle Accelerator Conference, 2005. PAC 2005. Proceedings of the*, pages 3342–3344. IEEE, 2005.

[Sla50]   J. C. Slater. *Microwave Electronics*. D. Van Nostrand Company, Princeton, 1950.

[Sla97]   J. P. H. Sladen. Status of superconducting cavities in lep. *Particle Accelerators*, 60(CERN-SL-97-062-RF):15–25, 1997.

[SMZ89]   M.C. Sanchez, E. Martin, and J.-M. Zamarro. New vectorial automatic technique for characterisation of resonators. *Microwaves, Antennas and Propagation, IEE Proceedings H*, 136(2):147–150, 1989.

[Son98]   Jeff E. Sonier. *The Magnetic Penetration Depth and the Vortex Core Radius in Type-II Superconductors*. PhD thesis, University of British Columbia, April 1998.

[SR07]   Tsun-Kong Sham and Richard A. Rosenberg. Time-resolved synchrotron radiation excited optical luminescence: Light-emission properties of silicon-based nanostructures. *ChemPhysChem*, 8(18):2557–2567, 2007.

[STU08]   STUDENT. The probable error of a mean. *Biometrika*, 6(1):1–25, 1908.

[SW03]   G.A.F. Seber and C.J. Wild. *Nonlinear Regression*. Wiley Series in Probability and Statistics. Wiley, 2003.

[TBD$^+$05] C. D. Tennant, K. B. Beard, D. R. Douglas, K. C. Jordan, L. Merminga, E. G. Pozdeyev, and T. I. Smith. First observations and suppression of multipass, multibunch beam breakup in the jefferson laboratory free electron laser upgrade. *Phys. Rev. ST Accel. Beams*, 8:074403, Jul 2005.

[TCS11]   Mark K. Transtrum, Gianluigi Catelani, and James P. Sethna. Superheating field of superconductors within ginzburg-landau theory. *Phys. Rev. B*, 83:094505, Mar 2011.

[Tem08]   Alexander B. Temnykh. Delta undulator for Cornell energy recovery linac. *Phys. Rev. ST Accel. Beams*, 11:120702, Dec 2008.

[Ten06]   C. D. Tennant. *Studies of Energy Recovery Linacs at Jefferson Laboratory*. PhD thesis, College of William and Mary, October 2006.

[TFT87]   Yuzo Kojima Shinji Mitsunobu Hirotaka Nakai Toshiharu Nakazato Shuichi Noguchi Kenji Saito Takaaki Furuya, Kiyomitsu Asano and Tsuyoshi Tajima. The TRISTAN superconducting cavities. In *Proceedings of the Third Workshop on RF Superconductivity*, 1987.

[The13a]   The International Linear Collider Collaboration. The International

Linear Collider Technical Design Report. Volume 3, Part II. Technical report, 2013.

[The13b]   The MathWorks, Inc., 3 Apple Hill Drive, Natick, Massachusetts 01760 USA. *MatLab Documentation Center: findpeaks*, 2013. http://www.mathworks.com/help/signal/ref/findpeaks.html.

[Tig65]   M. Tigner. A possible apparatus for electron clashing-beam experiments. *Nuovo Cim.*, 37:1228–1231, 1965.

[Tin04]   Michael Tinkham. *Introduction to superconductivity*. Dover Publications, Mineola, N.Y, 2004.

[Tis38]   L. Tisza. Transport Phenomena in Helium II. *Nature*, 141:913, May 1938.

[TM80]   A. A. Teplov and M. N. Mikheeva. Parallel critical magnetic fields for superconducting vanadium and technetium films. *Zh. Eksp. Teor. Fiz*, 79:2302–2310, 1980.

[Tra11a]   M. Transtrum. Personal Communication, 2011.

[Tra11b]   M. Transtrum. *Information Geometry for Nonlinear Least-Squares Data Fitting and Calculation of the Superconducting Superheating Field*. PhD thesis, Cornell University, 2011.

[Val12]   N. Valles. High Q cavities at Cornell. In *7th SRF Materials Workshop*, 2012.

[VB09]   V. Veshcherevich and S. Belomestnykh. Input coupler for main linac of Cornell ERL. In *The 14th Internation Conference on RF Superconductivity*, 2009.

[VBB+92]   C Vallet, M Boloré, B Bonin, JP Charrier, B Daillant, J Gratadour, F Koechlin, and H Safa. Flux trapping in superconducting cavities. In *Proc. of the European Particle Accelerator Conference EPAC92*, page 1295, 1992.

[VBLM12]   N Valles, M. Billing, G. HofG. Hoffstaetter. Liepe, and C. Mayes. HOM studies of the cornell ERL prototype cavity in a horizontal test cryomodule. In *Proceedings of IPAC2012*, 2012.

[VCL09]   N. R. A. Valles, Z. A. Conway, and M. Liepe. Exploring the maximum superheating fields of niobium. In *14th International Conference on RF Superconductivity*, 2009.

[vdHAP+07] B. van der Horst, A.Matheisen, B. Petersen, S. Saegebarth, and P. Schilling. Update on cavity preparation for high gradient superconducting multicell cavities at desy. In *The 13th International Workshop on RF Superconductivity*, 2007.

[VEF+13]   N. Valles, R. Eichhorn, F. Furuta, M. Ge, D. Gonnella, Y. He, K. Ho, G. Hoffstaetter, M. Liepe, T. O'Connell, S. Posen, P. Quigley, J. Sears, and V. Veshcherevich. Cornell ERL main linac 7-cell cavity performance in horizontal test cryomodule qualifications. In *Proceedings of IPAC 2013*. CLASSE, 2013.

[Ves]   V. Veshcherevich. Personal Communication.

[VFG+12]   N. Valles, F. Furuta, M. Ge, Y. He, K. M. V. Ho, G. H. Hoffstaetter, M. Liepe, T. O'Connell, S. Posen, P. Quigley, J. Sears, M. Tigner, and V. Veshcherevich. Testing of the main-linac prototype cavity in a horizontal test cryomodule for the Cornell ERL. In *Proceedings of IPAC 2012*, 2012.

[VKK13]   J. Vogt, O. Kugeler, and J. Knobloch. Studies of systematic flux reduction in superconducting Nb. In *Proceedings of IPAC 2013*. Helmholtz-Zentrum fr Materialien und Energie (HZB), 2013.

[VKL11]   N. Valles, D. S. Klien, and M. Liepe. Beam break-up studies for cornell's energy recovery linac. In *15th International Conference on RF Superconductivity*, 2011.

[VL09]   N. Valles and M. Liepe. Seven-cell cavity optimization for Cornell's energy recovery linac. In *14th International Conference on RF Superconductivity*, 2009.

[VL10a]   N. Valles and M. Liepe. Baseline cavity design for Cornell's energy recovery linac. In *International Particle Accelerator Conference*, 2010.

[VL10b]   N. Valles and M. Liepe. Cavity design for Cornell's energy recovery linac. In *Proceedings of IPAC 2010*, 2010.

[VL11]   N. Valles and M. Liepe. Designing multiple cavity classes for the main linac of Cornell's ERL. In *Proceedings of PAC 2011*, 2011.

[VL12]   N. Valles and M. Liepe. HOM studies on the Cornell ERL prototype cavity in a horizontal test cryomodule. In *Proceedings of IPAC 2012*, 2012.

[VLF⁺14]   N. Valles, M. Liepe, F. Furuta, M. Gi, D. Gonnella, Y. He, K. Ho, G. Hoffstaetter, D.S. Klein, T. O'Connell, S. Posen, P. Quigley, J. Sears, G.Q. Stedman, M. Tigner, and V. Veshcherevich. The main linac cavity for cornell's energy recovery linac: Cavity design through horizontal cryomodule prototype test. *Nuclear Instruments and Methods in Physics Research Section A: Accelerators, Spectrometers, Detectors and Associated Equipment*, 734, Part A(0):23 − 31, 2014.

[VLS11]   N. Valles, M. Liepe, and V. Shemelin. Coupler kick studies in Cornells 7-cell superconducting cavities. In *15th International Conference on RF Superconductivity*, Chicago, IL US, 2011.

[VSP05]   M. Liepe V. Shemelin and H. Padamsee. Measurements of ϵ and μ of lossy materials for the cryogenic HOM load. In *Proceedings of PAC 2005*, 2005.

[Wer69]   N. R. Werthamer. The Ginzburg-Landau equations and their extensions. In R. D. Parks, editor, *Superconductivity, Volume 1*, pages 321–370. Marcel Dekker, 1969.

[Wie95]   Helmut Wiedemann. *Particle accelerator physics*. Springer, Berlin u.a, 1995.

[Wil00]   Klaus Wille. *The physics of particle accelerators : an introduction*. Oxford University Press, Oxford New York, 2000.

[Xia97]   Z. Xiaowei. *Parallel electromagnetic field solvers using finite element methods with adaptive refinement and their application to wakefield computation of axisymmetric accelerator structure*. PhD thesis, 1997. Copyright - Copyright UMI - Dissertations Publishing 1997; Last updated - 2010-08-07; First page - n/a; M3: Ph.D.

[XKL⁺11]   L. Xiao, K. Ko, K. Lee, M. Liepe, and N. Valles. Effects of elliptically deformed cell shape in the Cornell ERL cavity. In *15th International Conference on RF Superconductivity*, 2011.

287

[Yak11]   V. Yakolev. Transverse impedance definitions. Personal Communication, 2011.

[YDM77]   T. Yogi, G. J. Dick, and J. E. Mercereau. Critical rf Magnetic Fields for Some Type-I and Type-II Superconductors. *Phys. Rev. Lett.*, 39(13):826–829, Sep 1977.